DISSERTATION

A DIRECT D-BAR RECONSTRUCTION ALGORITHM FOR COMPLEX ADMITTIVITIES IN $W^{2,\infty}(\Omega)$ FOR THE 2-D EIT PROBLEM

Submitted by

Sarah Jane Hamilton

Department of Mathematics

In partial fulfillment of the requirements

For the Degree of Doctor of Philosophy

Colorado State University

Fort Collins, Colorado

Summer 2012

Doctoral Committee:

Advisor: Jennifer L. Mueller

Paul Duchateau
Simon Tavener
Kevin Lear

ABSTRACT

A DIRECT D-BAR RECONSTRUCTION ALGORITHM FOR COMPLEX ADMITTIVITIES IN $W^{2,\infty}(\Omega)$ FOR THE 2-D EIT PROBLEM

Electrical Impedance Tomography (EIT) is a fairly new, portable, relatively inexpensive, imaging system that requires no ionizing radiation. Electrodes are placed at the surface of a body and low frequency, low amplitude current is applied on the electrodes, and the resulting voltage value on each electrode is measured. By applying a basis of current patterns, one can obtain sufficient information to recover the complex admittivity distribution of the region in the plane of the electrodes. In 2000, Elisa Francini presented a nearly constructive proof that was the first approach using D-bar methods to solve the full nonlinear problem for twice-differentiable conductivities and permittivities. In this thesis the necessary formulas to turn her proof into a direct D-bar reconstruction algorithm that solves the full nonlinear admittivity problem in 2-D are described. Reconstructions for simulated Finite Element data for circular and non-circular domains are presented.

TABLE OF CONTENTS

LIST OF FIGURES

1. INTRODUCTION

Electrical Impedance Tomography (EIT) is a noninvasive electronic imaging technique that generates an image of the admittivity distribution inside a domain with very limited prior knowledge of its electrical properties. In practice, electrodes are attached to the exterior of the domain, for example around the perimeter of a human chest, and a set of linearly independent current patterns is applied. The currents penetrate the domain (to various depths), and the resulting voltages on all of the electrodes are measured. In the human body, organs, tissue, bone, etc. have different electrical properties and thus different conductivities and permittivities (see Table 1.1). With EIT, these differences are exploited and the admittivity (conductivity along with permittivity) distribution is reconstructed in the plane of the electrodes using the electrical measurements taken at the surface. Electrical conductivity measures the ease with which a steady current can flow, whereas electrical permittivity measures the ability of a material to store a charge. Mathematically, recovering the admittivity of the interior from measurements of potential and current on the surface is a severely ill-posed inverse problem.

As EIT is a portable, relatively inexpensive, real-time imaging system that requires no ionizing radiation, it is very suitable for bedside monitoring. The medical applications of EIT are varied and include (but are not limited to): diagnosing breast cancer [KINS06, KPH$^+$02, IKK$^+$07], neonatal pulmonary measurement [Pha11], monitoring and evaluating lung function in patients [BBM94, SNM04, FSPS07, VBOM04, FPE09, FHHW02, CGMS05, MCCG06] (this is of particular interest while patients are on respirators in hospitals), and diagnosing pulmonary edema and embolus [SGS94, KNR99, FAS07, ZRBS] just to name a few. David Isaacson and his research group at Rensselaer Polytechnic Institute (RPI) are working with Massachusetts General Hospital in Boston, Massachusetts USA. They are combining EIT simultaneously with mammograms for breast cancer detection [KNSI07]. EIT also has many industrial and engineering applications such as detection of ground-

Tab. 1.1: Conductivity and permittivity values (*in vivo*) for tissues and organs in the human chest [FCI+91, SK57] for 100kHz.

Tissue	Conductivity $\left(\frac{\mathrm{S}}{\mathrm{m}}\right)$	Permittivity $\left(\frac{\mu\mathrm{F}}{\mathrm{m}}\right)$
Blood	0.67	0.05
Liver	0.28	0.49
Cardiac Muscle	0.63 (longitudinal) 0.23 (transversal)	0.88 (average)
Lung	0.10 (expiration) 0.04 (inspiration)	0.44 0.22
Fat	0.036	0.18

water contamination [RDB+96, DRJ98], land mine detection [CMGW06], subsurface flow remediation and monitoring [DR95, DRLN92, RDL+93, SSS30], and nondestructive evaluation [WB95, XPB89].

Using Maxwell's Equations for electromagnetic waves with spatial frequency ω, and assuming linear constitutive relations, one can derive the *admittivity equation*,

$$\begin{aligned} \nabla \cdot (\gamma(z)\nabla u(z)) &= 0, \quad z \in \Omega \subset \mathbb{R}^2 \\ u(z)|_{\partial\Omega} &= f(z), \quad z \in \partial\Omega, \end{aligned} \tag{1.1}$$

a generalized Laplace equation where $u(z)$ is the electric potential

$$\gamma(z) = \sigma(z) + \mathrm{i}\,\omega\epsilon(z),$$

is the admittivity in the interior of the domain Ω, $\sigma(z)$ represents the electrical conductivity of the body, $\epsilon(z)$ is the electrical permittivity of the body, and ω is the spatial frequency of the applied current. A detailed derivation of the admittivity equation and the required boundary conditions may be found in Appendix A.

Applying a known voltage on the boundary $\partial\Omega$,

$$u(z) = f(z), \quad z \in \partial\Omega,$$

corresponds to a Dirichlet boundary condition. Measuring the resulting current density distribution $J(z)$ on the boundary corresponds to

$$\gamma(z)\frac{\partial u}{\partial \nu}(z) = J(z), \quad z \in \partial\Omega,$$

a Neumann boundary condition. Therefore, the electrical measurements performed on the surface of the body correspond to knowledge of the Dirichlet-to-Neumann data $\Lambda_\gamma : f \to \Lambda_\gamma f$ for $\mathrm{Re}(\gamma),\ \mathrm{Im}(\gamma) \in C^1(\Omega),\ f \in H^{1/2}(\partial\Omega)$,

$$\Lambda_\gamma f = \gamma \frac{\partial u}{\partial \nu}\bigg|_{\partial\Omega} \in H^{-1/2}(\partial\Omega), \tag{1.2}$$

where ν denotes the outward pointing unit normal vector to the surface $\partial\Omega$, and u is the unique solution to (1.1) in $H^1(\Omega)$ such that $u|_{\partial\Omega} = f$. The theory requires knowledge of the Dirichlet-to-Neumann map, but in practice current patterns are applied instead of voltages. This is done since the D-N map amplifies noise, whereas the N-D map dampens noise. As we apply a set of linearly independent current patterns, the Neumann-to-Dirichlet map can tell you what voltages will occur for any given current pattern. Physically, the Dirichlet-to-Neumann map Λ_γ tells you what current density distribution will result on the boundary $\partial\Omega$ for any given applied voltage. We often call Λ_γ a voltage to current density map.

Notice that there are two obvious problems that we could be trying to solve in (1.1): recover the electric potential $u(z)$ in the interior (the forward problem), or recover the admittivity $\gamma(z)$ in the interior (the inverse problem). We are interested in solving the latter, which is often called an inverse coefficient problem.

Many advancements have been made in the real valued inverse admittivity problem (commonly called the *inverse conductivity problem*) regarding the existence and uniqueness of solutions as well as reconstruction algorithms since Calderón first posed the inverse conductivity problem in 1980 [Cal80]. These are discussed in Section 2. In 2000, Elisa Francini, [Fra00], extended the real-valued conductivity results of Brown and Uhlmann, [BU97], to complex-valued admittivities which include the electrical permittivity of a body, $\epsilon(z)$. Reconstructing permittivity will allow doctors to diagnose problems that were previously invisible with a conductivity-only approach (e.g., tissue necrosis in transplant organs, distinguishing pathologies in the ICU, such as the difference between a pneumothorax (zero permittivity) and hyperinflation (low non-zero permittivity), both of which have high resistivity).

Francini proved results regarding existence and uniqueness of solutions to the admittivity equation and outlined an approach for solving the inverse problem via a $\bar{\partial}$-method. In this

paper, we identify $\mathbb{R}^2$ with $\mathbb{C}$ so that $z = x + \mathrm{i}\, y$ where $x,\ y \in \mathbb{R}$ and use the standard notations for the ∂_{z} and $\bar{\partial}_{\mathrm{z}}$-derivatives,

$$\partial_{\mathrm{z}} = \frac{1}{2}\left(\frac{\partial}{\partial x} - \mathrm{i}\,\frac{\partial}{\partial y}\right) \qquad\qquad \bar{\partial}_{\mathrm{z}} = \frac{1}{2}\left(\frac{\partial}{\partial x} + \mathrm{i}\,\frac{\partial}{\partial y}\right).$$

Francini transforms the second order partial differential equation (1.1) to a first order system with both ∂ and $\bar{\partial}$ derivatives in z,

$$D\Psi - Q\Psi = 0, \tag{1.3}$$

where

$$D = \begin{pmatrix} \bar{\partial}_{\mathrm{z}} & 0 \\ 0 & \partial_{\mathrm{z}} \end{pmatrix}$$

and

$$Q(z) = \begin{pmatrix} 0 & -\frac{1}{2}\,\partial_{\mathrm{z}}\left(\log(\gamma(z))\right) \\ -\frac{1}{2}\,\bar{\partial}_{\mathrm{z}}\left(\log(\gamma(z))\right) & 0 \end{pmatrix} = \begin{pmatrix} 0 & Q_{12}(z) \\ Q_{21}(z) & 0 \end{pmatrix}.$$

We refer to the matrix $Q(z)$ as a potential due to the analog to the Schrödinger potential. Next, Francini looks for exponentially growing solutions to (1.3) with the following asymptotic behavior:

$$\Psi(z,k) = \begin{pmatrix} e^{\mathrm{i}\,kz} & 0 \\ 0 & e^{-\mathrm{i}\,k\bar{z}} \end{pmatrix} M(z,k), \quad \text{where } k \in \mathbb{C} \text{ and } M \sim \begin{pmatrix} 1 & 0 \\ 0 & 1 \end{pmatrix}, \text{ as } |k| \text{ or } |z| \to \infty.$$

These complex geometrical optics (CGO) solutions are the key to the direct reconstruction algorithm since the potential Q, and hence γ, can be computed directly from the elements of the CGO solutions M (see Theorem 6.2 of [Fra00] or my more computationally practical Theorem 10).

Another key function in the reconstruction algorithm is the *scattering transform*. The scattering transform $S(k)$, a matrix, is a nonlinear Fourier transform of the potential matrix Q defined by

$$S_{12}(k) = \frac{\mathrm{i}}{\pi}\int_{\Omega} e(\xi, -\bar{k}) Q_{12}(\xi) M_{22}(\xi,k)\, d\mu(\xi) \tag{1.4}$$

$$S_{21}(k) = -\frac{\mathrm{i}}{\pi}\int_{\Omega} e(\xi, k) Q_{21}(\xi) M_{11}(\xi,k)\, d\mu(\xi), \tag{1.5}$$

where

$$e(z,k) = e^{\mathrm{i}(zk + \bar{z}k)},$$

and $\mathrm{supp}(Q) \subset \Omega$.

Francini shows that the Dirichlet-to-Neumann map uniquely determines γ, but does not provide a means of computing the scattering transform $S(k)$ from the N-D map Λ_γ. The remaining steps in her nearly constructive proof are to solve a D-bar equation in an auxiliary complex frequency parameter k for the complex geometrical optics solutions M:

$$\bar{\partial}_k M(z,k) = M(z,\bar{k}) \begin{pmatrix} e(z,\bar{k}) & 0 \\ 0 & e(z,-k) \end{pmatrix} S(k), \tag{1.6}$$

and finally to compute the matrix potential Q from the following formula

$$Q(z) = \lim_{k_0 \to \infty} \mu(B_\rho(0))^{-1} \int_{k:|k-k_0|<r} D_k M(z,k)\, d\mu(k), \quad \text{for any } \rho > 0,$$

where

$$D_k M = DM - \mathrm{i}\, k \begin{pmatrix} 1 & 0 \\ 0 & -1 \end{pmatrix} M^{\mathrm{off}},$$

and M^{off} denotes the off-diagonal part of the matrix M.

These steps can be summarized in the following diagram:

$$\Lambda_\gamma \underset{\substack{\text{no formula} \\ \text{in [Fra00]}}}{\xrightarrow{1}} S(k) \xrightarrow{2} M(z,k) \xrightarrow{3} Q(z).$$

The formula provided by [Fra00] for Step 3 is impractical for computation because it requires a large k limit of integrals of the CGO solutions $M(z,k)$ and its derivatives over balls of increasing radii in k. In this thesis, a new formula for the recovery of the matrix potential Q from the CGO solutions M that only involves only knowledge of $M(z,0)$ (i.e. one value of k) and is very suitable for computation is derived (see Theorem 10).

Step 1 was partially completed by Alan Von Herrmann [Von09]. He showed the existence of an exponentially growing solution, u_1, to the admittivity equation $\nabla \cdot (\gamma \nabla u) = 0$, and the existence of a second exponentially growing solution u_2 was proved in [HHMV12] where

$$u_1 \sim \frac{e^{\mathrm{i}\, kz}}{\mathrm{i}\, k} \quad \text{and} \quad u_2 \sim -\frac{e^{-\mathrm{i}\, k\bar{z}}}{\mathrm{i}\, k} \quad \text{for } z \in \mathbb{C} \text{ and } k \in \mathbb{C} \setminus 0.$$

Boundary integral equations for these solutions involving the Dirichlet-to-Neumann map Λ_γ were established (Theorem 31 of [Von09] and [HHMV12]),

$$\begin{aligned} u_1(z,k) &= \frac{e^{\mathrm{i}\, kz}}{ik} - \int_{\partial\Omega} G_k(z-\zeta)\,(\Lambda_\gamma - \Lambda_1)\, u_1(\zeta,k)\, dS(\zeta) \\ u_2(z,k) &= -\frac{e^{-\mathrm{i}\, k\bar{z}}}{ik} - \int_{\partial\Omega} G_k(-\bar{z}+\bar{\zeta})\,(\Lambda_\gamma - \Lambda_1)\, u_2(\zeta,k)\, dS(\zeta) \end{aligned}$$

for all $k \in \mathbb{C}\backslash 0$, $z \in \mathbb{C}$, and $\gamma = 1$ on $\partial\Omega$ where $G_k(z)$ is the Faddeev Green's function, [Fad66].

The work [Von09] did not, however, include a formula connecting the exponentially growing solutions to the scattering transform $S(k)$. Integration by parts on the definition of $S(k)$ ((5.43) and (5.44)) reveals that only the traces of the CGO solutions Ψ_{12} and Ψ_{21} are required to evaluate the scattering transforms $S_{12}(k)$ and $S_{21}(k)$ for $k \in \mathbb{C}$. However, the connection between the exponentially growing solutions u_1, u_2 and the entries of Ψ, the CGO solutions,

$$\Psi_{12}(z,k) = \gamma^{1/2}(z)\,\bar{\partial}_{\mathrm{z}}\,u_2(z,k) \quad \text{and} \quad \Psi_{21}(z,k) = \gamma^{1/2}(z)\,\partial_{\mathrm{z}}\,u_1(z,k)$$

requires the computation of the ∂_{z} and $\bar{\partial}_{\mathrm{z}}$ derivatives of u_1 and u_2. This is not possible since the D-N map only provides knowledge of u_1 and u_2 on $\partial\Omega$.

In this thesis, formulas for the CGO solutions Ψ_{12} and Ψ_{21} on the boundary that connect u_1 and Ψ_{21} as well as u_2 and Ψ_{12}, completing the direct reconstruction algorithm are established. The steps are then:

$$\Lambda_\gamma \underset{1}{\longrightarrow} u_1|_{\partial\Omega},\ u_2|_{\partial\Omega} \underset{2}{\longrightarrow} \Psi_{12}|_{\partial\Omega},\ \Psi_{21}|_{\partial\Omega} \underset{3}{\longrightarrow} S(k) \underset{4}{\longrightarrow} M(z,0) \underset{5}{\longrightarrow} Q(z) \underset{6}{\longrightarrow} \gamma(z).$$

Each of these steps will be explained in detail in Chapters 5 and 6.

The numerical implementation of these steps for simulated Finite Element voltage data is presented. This constitutes the first direct nonlinear reconstruction method for complex admittivities in EIT. To verify the validity of the inverse solver, the forward problem (1.3) was also solved for $M(z,k)$. The scattering transform $S(k)$ as subsequently computed, solved the $\bar{\partial}_k$-equation (1.6) solved to recover $M(z,0)$, the matrix potential $Q(z)$ recovered from Theorem 10 using the CGO solutions $M(z,0)$, and finally the admittivity $\gamma(z)$ was reconstructed via the Generalized Cauchy Integral Formula. These verifications are tantamount to implementing Francini's results with the improved equation for the matrix potential Q. Solving the forward problem (1.3) has proved invaluable in testing the reconstruction formulas that we derived as well as the numerical implementation. While time consuming, the payoff has been enormous.

In this thesis we examine how to solve the inverse admittivity problem in 2-D using a direct $\bar{\partial}$-solver approach. The remainder of this thesis is organized as follows. Chapter 2

provides an overview of the major theoretical developments in the EIT problem as well as various reconstruction approaches for numerically solving the inverse problem. Chapter 3 describes Elisa Francini's proof in greater detail. In Chapter 4, we solve the forward $D_k M = QM$ problem (1.3) for a prescribed admittivity γ that will prove useful when testing the full inverse solver. In Chapter 5, the theory behind the full reconstruction algorithm is presented. Chapter 6 contains the numerical implementation of the full inverse solver. Chapter 7 presents the modifications necessary to implement the complete inverse solver on non-circular domains. As a test case, we examine chest-shaped phantoms. Chapter 8 concludes the thesis with a summary of future work and directions. For the reader's convenience, two appendices are included. Appendix A gives a detailed derivation of the admittivity equation from first principles. Appendix B presents the Finite Element formulation of the Forward Admittivity Problem (1.1) that is needed to generate the Dirichlet-to-Neumann map corresponding to a constant admittivity (which is needed in the first step of the reconstruction algorithm as well as to generate the simulated voltage data to test the algorithm). The results of the reconstruction algorithm on simulated data on a disk have been submitted in the article [HHMV12].

2. LITERATURE REVIEW

Following Calderón's seminal paper in 1980, [Cal80], many advancements have been made regarding existence and uniqueness of the solution γ and the associated regularity requirements. These developments have spurred much research to develop practical reconstruction algorithms. In this section we describe some of the major contributions to both the theoretical and computational aspects of the inverse admittivity problem.

2.1 Theoretical Advancements

Alberto Calderón, who is often credited with the emergence of EIT due to his seminal work in 1980 [Cal80], was inspired by geophysical applications. He was working in the area of oil prospection and wondered if the differences in conductivities of marine sand, granite, bedrock, etc. could be determined from measurements taken on the surface. Calderón examined whether the conductivity, σ (not including permittivity), could be uniquely determined from knowledge of the voltage-to-current density map, Λ_σ (the D-N map). Specifically, does $\Lambda_{\sigma_1} = \Lambda_{\sigma_1}$ imply $\sigma_1 = \sigma_2$? He showed that the linearization of the map, $\sigma \to \Lambda_\sigma$, uniquely determines the conductivity. In addition, he provided the reader with a direct reconstruction algorithm for the linearized case which employs Fourier transforms. However, as the range of the linearized map is not closed, this does not answer the more general problem.

Following Calderón's paper, many theoretical advancements have been made. The following is a brief description of some of the major contributions, but it is inevitably incomplete. See, for example, [CBKM08, Uhl99, AP06] for a more complete listing. In 1984, Kohn and Vogelius showed that a smooth conductivity, $\sigma \in C^\infty(\overline{\Omega})$, and all its derivatives can be determined uniquely on the boundary $\partial\Omega$ [KV84]. In a followup paper in 1985, [KV85], they extended their results to piecewise analytic conductivities. In 1986, Sylvester and Uhlmann showed uniqueness for near constant, smooth conductivities in the interior of a two-dimensional domain Ω [SU86].

Progress then stalled slightly for the two dimensional problem, while advancements were made for $\mathbb{R}^n$, $n \geq 3$. In 1987, Sylvester and Uhlmann proved global uniqueness for smooth isotropic conductivities, $\sigma \in C^\infty(\overline{\Omega})$ where $\Omega \subset \mathbb{R}^n$ for $n \geq 3$ (but not the planar case $n = 2$). In 1988, Nachman et al. [NSU88] relaxed the smoothness condition to $\sigma \in W^{2,\infty}(\Omega)$ for $n \geq 3$; then in [Nac88] the smoothness was relaxed further to $\sigma \in C^{1,1}(\bar{\Omega})$ and locally uniform Lipshitz boundary $\partial\Omega$. Currently, the result by Brown and Torres [BT03], which relaxes the smoothness condition to conductivities with in $W^{3/2,p}$ for $p > 2n$, is the sharpest known result for $n \geq 3$.

It was not until 1996 that the global uniqueness question was answered in two dimensions. Nachman proved uniqueness for $\sigma \in W^{2,p}(\Omega)$ for $p > 1$ and Lipschitz boundary, [Nac96]. Nachman's proof required transforming the conductivity equation ((1.1) with $\epsilon = 0$) to the Schrödinger equation. His proof was constructive in nature and outlined a direct reconstruction method involving $\bar{\partial}$-methods. The $\bar{\partial}$-methods originated in evolution equations and inverse scattering. The methods first appeared in the work by Gardner et al. [GGKM67] on the Korteweg-de Vries (KdV) equation. Beals and Coifman later used the $\bar{\partial}$-approach in inverse scattering theory [BC80, BC85, BC86]. In 1997, Brown and Uhlmann [BU97], further reduced the smoothness assumption on σ to conductivities in $W^{1,p}(\Omega)$ for $p > 2$ by re-writing the second order conductivity equation as a first order system. Their proof was also constructive in nature and again used $\bar{\partial}$-methods. In 2006, Astala and Päivärinta [AP06] removed all regularity constraints on the conductivity so that all that is required is $\sigma \in L^\infty(\Omega)$. Their proof was constructive, used $\bar{\partial}$-methods, and involved transforming the conductivity equation to the Beltrami equation and then using a transport equation to move the solution from outside the domain Ω, inside. One might think this is where the story ends; however, mathematicians are still pushing the envelope, and Astala, Lassas, and Päivärinta are currently working on removing the boundedness condition on the conductivity [ALP11]!

The works cited above all require $\gamma = \sigma$ to be real valued. In 2000, Elisa Francini, [Fra00], extended the work of Brown and Uhlmann [BU97] to complex valued conductivities (also called admittivities) $\gamma(z) = \sigma(z) + \mathrm{i}\omega\epsilon(z)$ for small permittivity ϵ, where $\mathrm{Re}(\gamma),\ \mathrm{Im}(\gamma) \in W^{2,\infty}(\Omega)$. Francini's proof was also constructive in nature, missing only

a viable connection to the voltage data. In 2008, Bukhgeim [Buk08] used Carleman estimates to show that a real valued Schrödinger potential in $W^{2,p}$ for $p > 2$ can be uniquely determined from Cauchy data. He claims that the results extend to complex conductivities (admittivities) as well without the smallness condition on the permittivities that is required by Francini, i.e. for $\mathrm{Re}(\gamma),\ \mathrm{Im}(\gamma) \in L^\infty(\Omega)$. However, his proof is not constructive.

The majority of the results above are for isotropic conductivities. Regarding anisotropic conductivities, it turns out that if two anisotropic conductivities produce the same voltages at the boundary, then the conductivities differ by a diffeomorphism. For results involving anisotropic conductivities, see [ALP05, SU03, Syl90]. Another popular area of work involves detecting inclusions, see [IIN$^+$07, IS00, IS04, UW08]. When the uniqueness requirement for the conductivity is relaxed it becomes possible to hide an object. Much research has been done regarding techniques for electromagnetic invisibility cloaking: see [GLU03b, GLU03a, LTU03, GKLU07, GLU09].

2.2 Reconstruction Algorithms

Existence and uniqueness results are wonderful, but in practice we would like to be able to use those results to create an image for diagnostic purposes. The reconstruction problem is a severely ill-posed inverse problem, since very small differences in the measured boundary data can correspond to drastically different interior conductivity/admittivity distributions [Ale98]. The following is a brief overview of the main types of reconstruction algorithms as well as some major contributions. Again, this list is inevitably incomplete. Table 2.1 summarizes the following methods.

2.2.1 Linearization Methods

Linearization of the (nonlinear) Dirichlet-to-Neumann map, Λ_γ, is only valid when the admittivity differs very slightly from a known distribution. The method that Calderón presented in [Cal80] is a linearization based approach and has been implemented on simulated data in [II89, IC91, CII90] as well as experimental data [BM08, BKIS08]. Other common linearization methods include moment methods [AS91] and backprojection methods [BB90, BT91, SV90, KWT83]. In 1990, Simske et al. formally introduced a one-step

Tab. 2.1: Comparison of classes of reconstruction algorithms for EIT

Algorithm Class	Nonlinear	Fast	Parallelizable	Convergence Theory
Linearization-based	No	Yes	No	No
Output least squares	Yes	No	No	No
Statistical Inversion	Yes	No	No	No
Layer Stripping	Yes	Yes	No	No (unstable)
D-bar	Yes	Yes	Yes	Yes

Newton-Raphson algorithm called NOSER [Sim87, CIN+90]. Other one-step Newton methods include [BM04, Blu97, MIN99].

2.2.2 Iterative Nonlinear Methods

There are a multitude of iterative methods to approximate the solution to the full nonlinear problem. Murai and Kagawa presented an iterative Finite Element approach [MSI02a] that was based on the sensitivity/lead theorem [Ges71, Leh72]. Edic et al. [EIS+98] and Jain et al. [JIEN97] use a multiple step Newton-Raphson method to approximate the solution to the complex valued inverse admittivity problem. Output least-squares methods include [Bor01, BBP96, Dob92, DS94, DBABP99, KB92, VVSK99a] among many more, and iterative Newton's methods include [YWT87, HWWT91]. These methods are widely used, but no convergence theory has been established, and therefore they may converge to local, rather than global, minima. Kalman filter approaches take time dependence into consideration [TGLA04, VKK98, HWWT91, MAF+10]. While many of these iterative methods are promising, their efficiencies depend on if, and how quickly, they can converge which can add considerable computational cost.

2.2.3 Direct Nonlinear Methods

Solution of the inverse conductivity problem via Bayesian inversion was first proposed by Kaipio et al. [KKSV00]. Their approach uses Markov chain Monte-Carlo integration and appears to be very promising; see, e.g., [HVWV02, RWW04]. However, the computational

time and cost is large.

Layer stripping is a direct nonlinear method that reconstructs the admittivity in each layer working in from the boundary [SCII91, Syl92, Yag87]. While this method provides decent reconstructions for simulated data, it has proved to be unstable with experimental data. However, the method does work well for reconstructing γ on the boundary. The instability is introduced as we move through each successive layer of the domain.

Another very promising class of algorithms can be classified as $\bar{\partial}$-methods (also called D-bar methods), which are direct and solve the full nonlinear problem. Nachman's constructive proof in 1996 outlined a $\bar{\partial}$ based reconstruction algorithm [Nac96] for conductivities in $W^{2,p}$ for $p > 1$. In 2000, Siltanen et al. [SMI00] presented the first $\bar{\partial}$ reconstructions of radially symmetric conductivity distributions based on Nachman's proof. Since then, more intricate conductivity distributions have been considered: high contrast conductivity distributions [SMI01, MS03], simulated phantom chests with conductivity values similar to those in real patients [MSI02b, KLMS09], experimental tank data for phantom chests [IMNS04, Mur07, MM09] and experimental human chest data [IMNS06, DM10, MM09]. A regularization strategy was established in [KLMS09] for the full nonlinear algorithm which constitutes the only proof of a global regularization strategy for a nonlinear inverse problem.

In his Ph.D thesis [Knu02], Kim Knudsen studied the Brown-Uhlmann $\bar{\partial}$-reconstruction method for $\sigma \in W^{1,p}$, $p > 2$, that was outlined in [BU97]. He derived the missing formulas needed to complete the nearly constructive proof and implemented the algorithm (see also [KT04]). While the accuracy of the reconstructions were comparable to those produced with the Nachman approach, the initial boundary integral that provides the connection to the data is very sensitive to noise. Knudsen has continued working with $\bar{\partial}$-methods now moving into three dimensions [BKM11, DHK11]. Very recently, the $\bar{\partial}$ reconstruction algorithm presented by Astala and Päivärinta [AP06] for bounded L^∞ conductivities was implemented by Astala et al. [AMPS10, AMP$^+$11].

As of yet, no one else has presented direct $\bar{\partial}$ reconstructions for complex admittivities (see our recent paper [HHMV12]). This Ph.D. project involves doing just that. In this thesis, the missing details of the $\bar{\partial}$-proof for complex admittivities with $\mathrm{Re}(\gamma),\ \mathrm{Im}(\gamma) \in W^{2,\infty}(\Omega)$ as presented by Francini [Fra00] are filled in and the algorithm is implemented for $W^{2,\infty}(\Omega)$ phantoms as well as phantoms with sharp organ boundaries ($L^\infty(\Omega)$).

3. OVERVIEW OF FRANCINI'S APPROACH

We aim to complete and implement Francini's nearly constructive proof, as outlined in [Fra00], for a complex admittivity

$$\gamma(z) = \sigma(z) + \mathrm{i}\,\omega\epsilon(z) \quad z \in \Omega,$$

where $\sigma(z)$ is the real valued electrical conductivity, $\omega = 2\pi f$ is a positive constant dependent on a spatial frequency f of the applied current, $\epsilon(z)$ is the real valued electrical permittivity, and $\Omega \subset \mathbb{R}^2$ is a bounded open domain with a Lipschitz boundary (a regularity condition). For the rest of the paper we assume that there exist positive constants σ_0 and E such that

$$\sigma(z) > \sigma_0, \quad z \in \Omega \subset \mathbb{R}^2 \tag{3.1}$$

and

$$\|\sigma\|_{W^{1,\infty}(\Omega)},\ \|\epsilon\|_{W^{1,\infty}(\Omega)} \leq E. \tag{3.2}$$

We extend σ and ϵ from Ω to all of $\mathbb{R}^2$ such that $\sigma \equiv 1$ and $\epsilon \equiv 0$ outside a ball with fixed radius containing Ω, and (3.1) and (3.2) hold for all of $\mathbb{R}^2$. In fact, all that is required is that γ is constant outside that ball of fixed radius; for convenience we look at the case where $\gamma \equiv 1$.

The constructive proof presented in [Fra00] only requires $\mathrm{Re}(\gamma),\ \mathrm{Im}(\gamma) \in W^{1,\infty}(\Omega)$ but in a few places she requires $\mathrm{Re}(\gamma),\ \mathrm{Im}(\gamma) \in W^{2,\infty}(\Omega)$. Thus, the complete proof is only valid for $\mathrm{Re}(\gamma),\ \mathrm{Im}(\gamma) \in W^{2,\infty}(\Omega)$. In order to attain the original reduction in the regularity requirement on γ, the admittivity equation (1.1) is reduced to a first order system involving ∂_z and $\bar{\partial}_z$ derivatives as follows.

Let u be a solution of

$$\nabla \cdot \gamma(z)\nabla u(z) = 0 \quad \text{for } z \in \Omega \subset \mathbb{R}^2. \tag{3.3}$$

Then the vector

$$\begin{pmatrix} v \\ w \end{pmatrix} = \gamma^{1/2} \begin{pmatrix} \partial_{\mathrm{z}}\, u \\ \bar{\partial}_{\mathrm{z}}\, u \end{pmatrix}, \tag{3.4}$$

solves the system

$$D \begin{pmatrix} v \\ w \end{pmatrix} - Q \begin{pmatrix} v \\ w \end{pmatrix} = 0, \tag{3.5}$$

where D is the operator

$$D = \begin{pmatrix} \bar{\partial}_{\mathrm{z}} & 0 \\ 0 & \partial_{\mathrm{z}} \end{pmatrix},$$

and Q is the matrix potential

$$Q = \begin{pmatrix} 0 & -\frac{1}{2}\,\partial_{\mathrm{z}} \log \gamma(z) \\ -\frac{1}{2}\,\bar{\partial}_{\mathrm{z}} \log \gamma(z) & 0 \end{pmatrix}. \tag{3.6}$$

It can be verified that (3.4) solves (3.5) with a short computation:

$$\begin{aligned} D \begin{pmatrix} v \\ w \end{pmatrix} - Q \begin{pmatrix} v \\ w \end{pmatrix} &= \begin{pmatrix} \bar{\partial}_{\mathrm{z}} & 0 \\ 0 & \partial_{\mathrm{z}} \end{pmatrix} \begin{pmatrix} v \\ w \end{pmatrix} \\ &\quad - \begin{pmatrix} 0 & -\frac{1}{2}\,\partial_{\mathrm{z}} \log \gamma(z) \\ -\frac{1}{2}\,\bar{\partial}_{\mathrm{z}} \log \gamma(z) & 0 \end{pmatrix} \begin{pmatrix} v \\ w \end{pmatrix} \\ &= \begin{pmatrix} \bar{\partial}_{\mathrm{z}}\, v + \frac{1}{2}\,[\partial_{\mathrm{z}} \log \gamma(z)]\, w \\ \partial_{\mathrm{z}}\, w + \frac{1}{2}\,\left[\bar{\partial}_{\mathrm{z}} \log \gamma(z)\right] v \end{pmatrix}. \end{aligned} \tag{3.7}$$

Using (3.3) and (3.4),

$$\begin{aligned} \bar{\partial}_{\mathrm{z}}\, v + \frac{1}{2}\,[\partial_{\mathrm{z}} \log \gamma(z)]\, w &= \bar{\partial}_{\mathrm{z}} \left(\gamma^{1/2}\, \partial_{\mathrm{z}}\, u\right) + \frac{1}{2}\,[\partial_{\mathrm{z}} \log \gamma(z)] \left(\gamma^{1/2}\, \bar{\partial}_{\mathrm{z}}\, u\right) \\ &= \frac{1}{2}\gamma^{-1/2} \left(\bar{\partial}_{\mathrm{z}}\, \gamma\right) (\partial_{\mathrm{z}}\, u) + \gamma^{1/2}\, \bar{\partial}_{\mathrm{z}}\, \partial_{\mathrm{z}}\, u + \frac{1}{2}\gamma^{-1/2} \left(\bar{\partial}_{\mathrm{z}}\, u\right) (\partial_{\mathrm{z}}\, \gamma) \\ &= \frac{1}{2\gamma^{1/2}} \left[\left(\bar{\partial}_{\mathrm{z}}\, \gamma\right) (\partial_{\mathrm{z}}\, u) + \left(\bar{\partial}_{\mathrm{z}}\, u\right) (\partial_{\mathrm{z}}\, \gamma)\right] + \frac{1}{4}\gamma^{1/2} \Delta u \\ &= \frac{1}{4\gamma^{1/2}} \left[\nabla \gamma \cdot \nabla u + \gamma \Delta u\right] \\ &= \frac{1}{4\gamma^{1/2}} \left[\nabla \cdot \gamma \nabla u\right] \\ &= \frac{1}{4\gamma^{1/2}} [0] \\ &= 0. \end{aligned}$$

Similarly,

$$\begin{aligned}
\partial_{\mathrm{z}} w + \frac{1}{2}\left[\bar{\partial}_{\mathrm{z}} \log\gamma(z)\right] v &= \partial_{\mathrm{z}}\left(\gamma^{1/2}\,\bar{\partial}_{\mathrm{z}}\, u\right) + \frac{1}{2}\left[\bar{\partial}_{\mathrm{z}} \log\gamma(z)\right]\left(\gamma^{1/2}\,\partial_{\mathrm{z}}\, u\right) \\
&= \frac{1}{2}\gamma^{-1/2}\left(\partial_{\mathrm{z}}\,\gamma\right)\left(\bar{\partial}_{\mathrm{z}}\, u\right) + \gamma^{1/2}\,\partial_{\mathrm{z}}\,\bar{\partial}_{\mathrm{z}}\, u + \frac{1}{2}\gamma^{-1/2}\left(\partial_{\mathrm{z}}\, u\right)\left(\bar{\partial}_{\mathrm{z}}\,\gamma\right) \\
&= \frac{1}{2\gamma^{1/2}}\left[\left(\partial_{\mathrm{z}}\,\gamma\right)\left(\bar{\partial}_{\mathrm{z}}\, u\right) + \left(\partial_{\mathrm{z}}\, u\right)\left(\bar{\partial}_{\mathrm{z}}\,\gamma\right)\right] + \frac{1}{4}\gamma^{1/2}\Delta u \\
&= \frac{1}{4\gamma^{1/2}}\left[\nabla\gamma\cdot\nabla u + \gamma\Delta u\right] \\
&= \frac{1}{4\gamma^{1/2}}\left[\nabla\cdot\gamma\nabla u\right] \\
&= \frac{1}{4\gamma^{1/2}}[0] \\
&= 0.
\end{aligned}$$

Notice, that if the admittivity γ is continuous and there exists a positive constant σ_0 such that $\sigma > \sigma_0$, then $\gamma^{1/2}(z)$ and $\log\gamma(z)$ are well defined. Therefore, if u satisfies (3.3), the vector (3.4) solves (3.5). Also notice that, due to the extension of $\gamma \equiv$ constant outside a fixed ball containing Ω, the matrix potential Q has compact support and is in $L^\infty(\mathbb{R}^2)$ by (3.2).

We can represent the entries of the potential matrix $Q(z)$ in many ways. The following will prove useful throughout the rest of the thesis:

$$Q_{12}(z) = -\frac{1}{2}\,\partial_{\mathrm{z}}\log(\gamma(z)) = -\frac{\partial_{\mathrm{z}}\,\gamma(z)}{2\gamma(z)} = -\frac{\partial_{\mathrm{z}}\,\gamma^{1/2}(z)}{\gamma^{1/2}(z)}, \tag{3.8}$$

and similarly,

$$Q_{21}(z) = -\frac{1}{2}\,\bar{\partial}_{\mathrm{z}}\log(\gamma(z)) = -\frac{\bar{\partial}_{\mathrm{z}}\,\gamma(z)}{2\gamma(z)} = -\frac{\bar{\partial}_{\mathrm{z}}\,\gamma^{1/2}(z)}{\gamma^{1/2}(z)}. \tag{3.9}$$

Introducing a complex parameter $k \in \mathbb{C}$, we will now look for a family of exponentially growing solutions, $\Psi(z,k)$, to the system

$$D\Psi(z,k) - Q(z)\Psi(z,k) = 0, \quad z,\ k \in \mathbb{C} \tag{3.10}$$

of the special form

$$\begin{aligned}
\Psi(z,k) &= M(z,k)\begin{pmatrix} e^{\mathrm{i}\,kz} & 0 \\ 0 & e^{-\mathrm{i}\,k\bar{z}} \end{pmatrix}, \quad z,\ k \in \mathbb{C} && (3.11) \\
&= \begin{pmatrix} M_{11}(z,k)e^{\mathrm{i}\,kz} & M_{12}(z,k)e^{-\mathrm{i}\,k\bar{z}} \\ M_{21}(z,k)e^{\mathrm{i}\,kz} & M_{22}(z,k)e^{-\mathrm{i}\,k\bar{z}} \end{pmatrix}, \quad z,\ k \in \mathbb{C}, && (3.12)
\end{aligned}$$

where

$$M(z,k) = \begin{pmatrix} M_{11}(z,k) & M_{12}(z,k) \\ M_{21}(z,k) & M_{22}(z,k) \end{pmatrix} \in \mathbb{C}^{2\times 2},$$

is a complex valued matrix function such that $\|M(z,k) - I\|_{L^p(\mathbb{R}^2)} < \infty$ for some $p > 2$ where I is the 2×2 identity matrix.

Using the exponentially growing solutions M defined by (3.12), we can write the system in (3.10) as

$$\begin{aligned}
\bar{\partial}_{\mathrm{z}}\, M_{11}(z,k) - Q_{12}(z) M_{21}(z,k) &= 0 && (3.13)\\
(\bar{\partial}_{\mathrm{z}} - \mathrm{i}\, k) M_{12}(z,k) - Q_{12}(z) M_{22}(z,k) &= 0 && (3.14)\\
(\partial_{\mathrm{z}} + \mathrm{i}\, k) M_{21}(z,k) - Q_{21}(z) M_{11}(z,k) &= 0 && (3.15)\\
\partial_{\mathrm{z}}\, M_{22}(z,k) - Q_{21}(z) M_{12}(z,k) &= 0. && (3.16)
\end{aligned}$$

In matrix form,

$$\begin{aligned}
\mathbf{0} &= \begin{pmatrix} \bar{\partial}_{\mathrm{z}}\, M_{11} - Q_{12} M_{21} & (\bar{\partial}_{\mathrm{z}} - \mathrm{i}\, k) M_{12} - Q_{12} M_{22} \\ (\partial_{\mathrm{z}} + \mathrm{i}\, k) M_{21} - Q_{21} M_{11} & \partial_{\mathrm{z}}\, M_{22} - Q_{21} M_{12} \end{pmatrix} \\
&= \left[\begin{pmatrix} \bar{\partial}_{\mathrm{z}}\, M_{11} & \bar{\partial}_{\mathrm{z}}\, M_{12} \\ \partial_{\mathrm{z}}\, M_{21} & \partial_{\mathrm{z}}\, M_{22} \end{pmatrix} - \mathrm{i}\, k \begin{pmatrix} 1 & 0 \\ 0 & -1 \end{pmatrix} \begin{pmatrix} 0 & M_{12} \\ M_{21} & 0 \end{pmatrix} \right] - \begin{pmatrix} Q_{12} M_{21} & Q_{12} M_{22} \\ Q_{21} M_{11} & Q_{21} M_{12} \end{pmatrix}
\end{aligned}$$

or equivalently,

$$D_k M(z,k) - Q(z) M(z,k) = 0, \tag{3.17}$$

where

$$D_k M = DM - \mathrm{i}\, k \begin{pmatrix} 1 & 0 \\ 0 & -1 \end{pmatrix} M^{\mathrm{off}},$$

and M^{off} denotes the off-diagonal part of the matrix M. The action of the inverse of the D_k operator on a generic matrix A is given by

$$\begin{aligned}
D_k^{-1} A &= \begin{pmatrix} \bar{\partial}_{\mathrm{z}}^{-1} A_{11} & (\bar{\partial}_{\mathrm{z}} - \mathrm{i}\, k)^{-1} A_{12} \\ (\partial_{\mathrm{z}} + \mathrm{i}\, k)^{-1} A_{21} & \partial_{\mathrm{z}}^{-1} A_{22} \end{pmatrix} \\
&= \frac{1}{\pi} \int_{\mathbb{C}} \begin{pmatrix} \frac{1}{z-\zeta} & 0 \\ 0 & \frac{1}{\bar{z}-\bar{\zeta}} \end{pmatrix} \begin{pmatrix} A_{11}(\zeta) & A_{12}(\zeta) e(z-\zeta, \bar{k}) \\ A_{21} e(z-\zeta, -k) & A_{22}(\zeta) \end{pmatrix} d\mu(\zeta) && (3.18)\\
&= \begin{bmatrix} \frac{1}{\pi z} * A_{11} & \frac{e(z,\bar{k})}{\pi z} * A_{12} \\ \frac{e(z,-k)}{\pi \bar{z}} * A_{21} & \frac{1}{\pi \bar{z}} * A_{22} \end{bmatrix}, && (3.19)
\end{aligned}$$

where $*$ denotes convolution and

$$e(z,k) = e^{\mathrm{i}(zk + \bar{z}\bar{k})}.$$

Francini [Fra00] proved the following theorem guaranteeing existence and uniqueness of CGO solutions $M(z,k)$ to (3.17). For the proof, the reader is referred to the original paper itself [Fra00].

Theorem 1 (Theorem 3.1 of [Fra00]). *Let σ and ϵ satisfy the assumptions* (3.1) *and* (3.2). *There exists a constant ω_0 such that for every $\omega < \omega_0$ and $k \in \mathbb{C}$ there is a unique solution $M(z,k)$ to* (3.17) *satisfying the condition*

$$M(\cdot,k) - I \in L^p\left(\mathbb{R}^2\right) \qquad \text{for some } p > 2.$$

One should note that Francini's approach differs from the approach by Nachman [Nac96], and earlier by Sylvester and Uhlmann [SU86], which both involve transforming the conductivity equation (the real valued admittivity version of (3.3)) to the Schrödinger equation via the change of variables $u = \sigma^{-1/2}\tilde{u}$,

$$-\Delta\tilde{u} + q\tilde{u} = 0, \quad \text{where } q(z) = -\frac{\Delta\left(\sigma^{1/2}(z)\right)}{\sigma^{1/2}(z)}. \tag{3.20}$$

Writing the equation in this form requires the real valued conductivity to be twice differentiable.

In the original approach by Brown and Uhlmann [BU97], for real valued conductivities with one derivative in L^p, the conductivity equation was transformed to a first order system in the same manner as Francini [Fra00]. However, there is an important distinction that needs to be noted. As Brown and Uhlmann were working with real valued conductivities (and no permittivity) their potential matrix, here denoted Q_{BU} to avoid confusion, possessed symmetries that the complex case does not. In particular,

$$Q_{\mathrm{BU}}(z) = \begin{pmatrix} 0 & -\frac{1}{2}\,\partial_{\mathrm{z}}\log(\sigma(z)) \\ -\frac{1}{2}\,\bar{\partial}_{\mathrm{z}}\log(\sigma(z)) & 0 \end{pmatrix} = \begin{pmatrix} 0 & q(z) \\ \overline{q(z)} & 0 \end{pmatrix}$$

where

$$q(z) = -\frac{1}{2}\,\partial_{\mathrm{z}}\log(\sigma(z)).$$

In the complex admittivity case,

$$-\frac{1}{2}\,\partial_{\mathrm{z}}\log(\gamma(z)) \neq \overline{-\frac{1}{2}\,\partial_{\mathrm{z}}\log(\gamma(z))},$$

which leads to the loss of symmetry relations in the CGO solutions $M(z,k)$ and subsequently the scattering transforms $S_{12}(k)$ and $S_{21}(k)$. The end result is that when solving for a complex admittivity coefficient, we are forced to, at times, solve two systems rather than just one. C'est la vie.

3.1 A Brief Summary of Francini's Proof

The scattering transform $S(k)$ is the starting point in Francini's proof; she shows that it is uniquely determined by the Dirichlet-to-Neumann map Λ_γ. This piece of Francini's proof is not constructive.

Theorem 2 (Theorem 5.2 of [Fra00]). *Let Ω be a bounded domain with Lipschitz boundary. Assume that γ_1, $\gamma_2 \in W^{1,\infty}(\Omega)$ and $\Lambda_{\gamma_1} = \Lambda_{\gamma_2}$. Then, we can extend γ_1 and γ_2 to $\mathbb{R}^2 \setminus (\overline{\Omega})$ so that $S_1 = S_2$, where S_1 and S_2 are the scattering matrices associated to γ_1 and γ_2.*

The dependence of the CGO solutions M on the auxiliary complex frequency parameter k is related to the scattering transform through the following $\bar{\partial}_k$ system.

Theorem 3 (Theorem 4.1 of [Fra00]). *Let σ and ϵ satisfy* (3.1) *and* (3.2) *and let M be as in Theorem 1. The map $k \to M(\cdot, k)$ is differentiable as a map into $L^r_{-\beta}$, and satisfies the equation*

$$\bar{\partial}_k M(z,k) = M(z,\bar{k}) \begin{pmatrix} e(z,\bar{k}) & 0 \\ 0 & e(z,-k) \end{pmatrix} S(k), \tag{3.21}$$

where

$$S(k) = \frac{\mathrm{i}}{\pi} \int_{\mathbb{R}^2} \begin{pmatrix} e(z,-\bar{k}) & 0 \\ 0 & -e(z,k) \end{pmatrix} (QM)^{off}(z,k)\, d\mu(z). \tag{3.22}$$

Moreover, for every $p > 2$,

$$\sup_k \|M(z,\cdot) - I\|_{L^p(\mathbb{R}^2)} \leq K_2,$$

where K_2 depends on E, σ_0, Ω, and p.

We solve the matrix of $\bar{\partial}_k$-equations for the matrix of CGO solutions $\Psi(z,k)$ inside the domain Ω. Notice that equation (3.21) involves both $M(z,k)$ and $M(z,\bar{k})$. This slight difference will become important during the numerical implementation of the algorithm.

After solving (3.21) for the CGO solutions $M(z,k)$, Francini proposes solving for the matrix potential $Q(z)$ via the following theorem.

Theorem 4 (Theorem 6.2 of [Fra00]). *For any $\rho > 0$,*

$$Q(z) = \lim_{k_0 \to \infty} \mu(B_\rho(0))^{-1} \int_{k:|k-k_0|<r} D_k M(z,k)\, d\mu(k). \tag{3.23}$$

Unfortunately, this method of recovering $Q(z)$ is computationally impractical as it requires integration of derivatives of the CGO solutions $M(z,k)$, as well as $M(z,k)$ itself, over all $k \in \mathbb{C}$ by taking a large k limit of integrals over balls of increasing radii in k. In this thesis a different formula for this step which requires only knowledge of the CGOs $M(z,0)$ (i.e. $M(z,k)$ for $k = 0$) is derived. A detailed explanation of this formula will follow in Chapter 5.

4. SOLUTION OF THE FORWARD $D_K M = QM$ PROBLEM

In order to evaluate the validity of the inverse solver, the forward $D_k M = QM$ problem (3.17) needs to be solved for the CGO solutions $M(z,k)$, with the asymptotic condition $M(\cdot,k) - I \in L^p(\mathbb{R}^2)$ for some $p > 2$ as presented in Francini [Fra00]. The asymptotic conditions for M correspond to $M_{11}(z,k),\ M_{22}(z,k) \sim 1$ and $M_{12}(z,k),\ M_{21}(z,k) \sim 0$ as $|z| \to \infty$, or $|k| \to \infty$ where $z,\ k \in \mathbb{C}$. Notice that Equation (3.13) is coupled with (3.15) while (3.14) with (3.16). This allows us to solve two separate systems and therefore cut by half the size of our original coupled system (3.17). We instead solve

$$\begin{cases} \bar{\partial}_{\mathrm{z}}\, M_{11}(z,k) - Q_{12}(z) M_{21}(z,k) &= 0 \\ (\partial_{\mathrm{z}} + \mathrm{i}\, k) M_{21}(z,k) - Q_{21}(z) M_{11}(z,k) &= 0 \end{cases}, \tag{4.1}$$

and

$$\begin{cases} (\bar{\partial}_{\mathrm{z}} - \mathrm{i}\, k) M_{12}(z,k) - Q_{12}(z) M_{22}(z,k) &= 0 \\ \partial_{\mathrm{z}}\, M_{22}(z,k) - Q_{21}(z) M_{12}(z,k) &= 0 \end{cases}. \tag{4.2}$$

This chapter describes in detail how to solve this forward problem ((4.1) and (4.2)) for the CGO solutions $M(z,k)$ given a prescribed admittivity distribution $\gamma(z)$. Solving the forward $D_k M = QM$ problem to recover the CGO solutions is important for the following reasons.

- By solving the forward problem for the CGO solutions $M(z,k)$, we were able to generate the first plots of the scattering transform $S(k)$ for a complex admittivity where $\mathrm{Re}(\gamma),\ \mathrm{Im}(\gamma) \in W^{2,\infty}(\Omega)$

$$\begin{aligned} S_{12}(k) &= \frac{\mathrm{i}}{\pi} \int_\Omega e(\xi, -\bar{k}) Q_{12}(\xi) M_{22}(\xi,k)\, d\mu(\xi) \\ S_{21}(k) &= -\frac{\mathrm{i}}{\pi} \int_\Omega e(\xi, k) Q_{21}(\xi) M_{11}(\xi,k)\, d\mu(\xi). \end{aligned}$$

- Those scattering transforms were then used as 'ideal' initial data in the reconstruction algorithm. That is, The validity of the inverse $\bar{\partial}_k$-solver, M to Q formula, and inversion of the $\bar{\partial}_z$ operator to recover γ were tested:

$$\text{scattering data} \to \bar{\partial}_k \text{ eq} \to M \to Q \to \gamma.$$

This can be used to investigate the robustness and stability of the reconstruction method for all but the first step (D-N map to scattering data) of the full reconstruction algorithm.

- We can also use the forward problem to verify the formulas that we derived to determine the value of the CGO solutions $\Psi_{12}(z,k)$ and $\Psi_{21}(z,k)$ for $z \in \partial\Omega$ that use the D-N map and measured or simulated data.

In the forward $D_k M = QM$ problem we will prescribe an admittivity $\gamma(z)$ and solve (4.1)-(4.2) for the corresponding CGO solutions $M(z,k)$. To evaluate our forward $D_k M = QM$ solver for the CGOs $M(z,k)$, we can additionally prescribe functions $M_{11}(z,k)$, $M_{12}(z,k)$, $M_{21}(z,k)$, and $M_{22}(z,k)$ and calculate the resulting right hand side functions,

$$\begin{cases} \bar{\partial}_{\mathrm{z}} M_{11}(z,k) - Q_{12}(z) M_{21}(z,k) &= F_1(z,k) \\ (\partial_{\mathrm{z}} + \mathrm{i}\, k) M_{21}(z,k) - Q_{21}(z) M_{11}(z,k) &= F_3(z,k) \end{cases}, \tag{4.3}$$

and

$$\begin{cases} (\bar{\partial}_{\mathrm{z}} - \mathrm{i}\, k) M_{12}(z,k) - Q_{12}(z) M_{22}(z,k) &= F_2(z,k) \\ \partial_{\mathrm{z}} M_{22}(z,k) - Q_{21}(z) M_{12}(z,k) &= F_4(z,k) \end{cases}. \tag{4.4}$$

We can then use the solver to ensure that we can, in fact, recover the prescribed CGO solutions $M(z,k)$. Later, we can set F_1 through F_4 equal to zero and solve the original forward $D_k M = QM$ problem for non-prescribed CGO solutions $M(z,k)$ (and only a prescribed admittivity γ).

As we will later need to interpolate some of our calculations to new grids, we will solve all problems on a grids created with MATLAB's **meshgrid** function. Therefore, the columns of a matrix correspond to changing the x coordinate whereas the rows correspond to changing the y coordinate, e.g. $M(x_j, y_p, k_\ell) = M(p,j)$ for $k = k_\ell \in \mathbb{C}$.

4.1 Approach 1: Using Finite Differences

We first formulate the forward $D_k M - QM = F$ problem, (4.3) and (4.4), using finite differences.

4.1.1 Solving System I

Let us first examine the system in (4.3). Using centered finite differences to approximate the ∂_z- and $\bar{\partial}_z$-derivatives, the system becomes

$$\begin{aligned} 4hF_1 &= M_{11}(x_{j+1}, y_p, k) - M_{11}(x_{j-1}, y_p, k) + \mathrm{i}\, M_{11}(x_j, y_{p+1}, k) - \mathrm{i}\, M_{11}(x_j, y_{p-1}, k) \\ &\quad -4hQ_{12}(x_j, y_p)\, M_{21}(x_j, y_p, k), \end{aligned} \tag{4.5}$$

$$\begin{aligned} 4hF_3 &= M_{21}(x_{j+1}, y_p, k) - M_{21}(x_{j-1}, y_p, k) - \mathrm{i}\, M_{21}(x_j, y_{p+1}, k) + \mathrm{i}\, M_{21}(x_j, y_{p-1}, k) \\ &\quad +4h\,\mathrm{i}\,kM_{21}(x_j, y_p, k) - 4hQ_{21}(x_j, y_p)\, M_{11}(x_j, y_p, k), \end{aligned} \tag{4.6}$$

for $1 \le j, p \le N$ and h denotes the step size (for convenience we have taken $h_x = h = h_y$). To impose the asymptotic boundary conditions, we need to expand our matrix to include $j, p = 0, N+1$ to accurately describe the derivatives. We will then solve the system on the interior nodes with an adjusted right hand side (of a linear system $Am = b$) that incorporates the boundary condition. Since $M_{21} \sim 0$ no adjustments are needed for the right hand side involving F_3, i.e. we only need to adjust the terms involving F_1. We adjust them as follows,

- $4hF_1(x_1, y_p, k)$ is replaced with $4hF_1(x_1, y_p, k) + 1$ for $p = 1, \ldots, N$
- $4hF_1(x_N, y_p, k)$ is replaced with $4hF_1(x_N, y_p, k) - 1$ for $p = 1, \ldots, N$
- $4hF_1(x_j, y_1, k)$ is replaced with $4hF_1(x_j, y_1, k) + \mathrm{i}$ for $j = 1, \ldots, N$
- $4hF_1(x_j, y_N, k)$ is replaced with $4hF_1(x_j, y_N, k) - \mathrm{i}$ for $j = 1, \ldots, N$.

Thus, the linear system to be solved is:

$$Am_1 = b_1, \tag{4.7}$$

where the matrix A is given by:

$$A = \begin{bmatrix} A_{11} & A_{12} \\ A_{21} & A_{22} \end{bmatrix}.$$

The sub-matrix A_{12} is given by,

$$A_{12} = -4h\ \mathrm{diag}\left(\mathrm{vec}\left(Q_{12}\right)\right), \tag{4.8}$$

where "diag(vec (Q_{12}))" places the elements of Q_{12} (column-wise) on the diagonal of a square $(N^2 \times N^2)$ matrix. Similarly, the sub-matrix A_{21} is given by,

$$A_{21} = -4h \ \mathrm{diag}\left(\mathrm{vec}\left(Q_{21}\right)\right). \tag{4.9}$$

Due to the large and banded nature of A_{11}, the sub-matrix is shown in (4.10) for $N = 4$,

$$\begin{bmatrix}
0 & \mathrm{i} & 0 & 0 & 1 & 0 & 0 & 0 & 0 & 0 & 0 & 0 & 0 & 0 & 0 & 0 \\
-\mathrm{i} & 0 & \mathrm{i} & 0 & 0 & 1 & 0 & 0 & 0 & 0 & 0 & 0 & 0 & 0 & 0 & 0 \\
0 & -\mathrm{i} & 0 & \mathrm{i} & 0 & 0 & 1 & 0 & 0 & 0 & 0 & 0 & 0 & 0 & 0 & 0 \\
0 & 0 & -\mathrm{i} & 0 & 0 & 0 & 0 & 1 & 0 & 0 & 0 & 0 & 0 & 0 & 0 & 0 \\
-1 & 0 & 0 & 0 & 0 & \mathrm{i} & 0 & 0 & 1 & 0 & 0 & 0 & 0 & 0 & 0 & 0 \\
0 & -1 & 0 & 0 & -\mathrm{i} & 0 & \mathrm{i} & 0 & 0 & 1 & 0 & 0 & 0 & 0 & 0 & 0 \\
0 & 0 & -1 & 0 & 0 & -\mathrm{i} & 0 & \mathrm{i} & 0 & 0 & 1 & 0 & 0 & 0 & 0 & 0 \\
0 & 0 & 0 & -1 & 0 & 0 & -\mathrm{i} & 0 & 0 & 0 & 0 & 1 & 0 & 0 & 0 & 0 \\
0 & 0 & 0 & 0 & -1 & 0 & 0 & 0 & 0 & \mathrm{i} & 0 & 0 & 1 & 0 & 0 & 0 \\
0 & 0 & 0 & 0 & 0 & -1 & 0 & 0 & -\mathrm{i} & 0 & \mathrm{i} & 0 & 0 & 1 & 0 & 0 \\
0 & 0 & 0 & 0 & 0 & 0 & -1 & 0 & 0 & -\mathrm{i} & 0 & \mathrm{i} & 0 & 0 & 1 & 0 \\
0 & 0 & 0 & 0 & 0 & 0 & 0 & -1 & 0 & 0 & -\mathrm{i} & 0 & 0 & 0 & 0 & 1 \\
0 & 0 & 0 & 0 & 0 & 0 & 0 & 0 & -1 & 0 & 0 & 0 & 0 & \mathrm{i} & 0 & 0 \\
0 & 0 & 0 & 0 & 0 & 0 & 0 & 0 & 0 & -1 & 0 & 0 & -\mathrm{i} & 0 & \mathrm{i} & 0 \\
0 & 0 & 0 & 0 & 0 & 0 & 0 & 0 & 0 & 0 & -1 & 0 & 0 & -\mathrm{i} & 0 & \mathrm{i} \\
0 & 0 & 0 & 0 & 0 & 0 & 0 & 0 & 0 & 0 & 0 & -1 & 0 & 0 & -\mathrm{i} & 0
\end{bmatrix}, \tag{4.10}$$

and finally the sub-matrix A_{22} is computed by

$$A_{22} = \mathrm{conj}\left(A_{11}\right) + 4hk\,\mathrm{i}\,\mathrm{I}_{N^2}, \tag{4.11}$$

where conj (A_{11}) denotes the complex conjugate of the sub-matrix A_{11}, I_{N^2} is the $N^2 \times N^2$ identity matrix, and $k \in \mathbb{C}$ is a complex number. The vector m_1 is given by

$$m_1 = \begin{bmatrix} M_{11}(x_1, y_1, k) \\ \vdots \\ M_{11}(x_1, y_N, k) \\ M_{11}(x_2, y_1, k) \\ \vdots \\ M_{11}(x_2, y_N, k) \\ \vdots \\ \vdots \\ \vdots \\ M_{11}(x_N, y_1, k) \\ \vdots \\ M_{11}(x_N, y_N, k) \\ M_{21}(x_1, y_1, k) \\ \vdots \\ M_{21}(x_1, y_N, k) \\ M_{21}(x_2, y_1, k) \\ \vdots \\ M_{21}(x_2, y_N, k) \\ \vdots \\ \vdots \\ \vdots \\ M_{21}(x_N, y_1, k) \\ \vdots \\ M_{21}(x_N, y_N, k) \end{bmatrix}, \tag{4.12}$$

or using vectorize ("vec") notation,

$$m_1 = \begin{bmatrix} \mathrm{vec}(M_{11}) \\ \mathrm{vec}(M_{21}) \end{bmatrix}.$$

Finally, the right hand side b_1 is given by

$$b_1 = \begin{bmatrix} 4h\mathrm{vec}(F_1) + V \\ 4h\mathrm{vec}(F_3) \end{bmatrix}, \tag{4.13}$$

where V is the correction for the right hand side that incorporates the boundary condition. For the $N = 4$ example, V is given by

$$V = \begin{bmatrix} 1+\mathrm{i} \\ 1 \\ 1 \\ 1-\mathrm{i} \\ \mathrm{i} \\ 0 \\ 0 \\ -\mathrm{i} \\ \mathrm{i} \\ 0 \\ 0 \\ -\mathrm{i} \\ -1+\mathrm{i} \\ -1 \\ -1 \\ -1-\mathrm{i} \end{bmatrix}. \tag{4.14}$$

4.1.2 Solving System II

We now proceed to the system in (4.4). Using centered finite differences to approximate the ∂_z- and $\bar{\partial}_z$-derivatives, the system similarly becomes

$$\begin{aligned} 4hF_2 &= M_{12}(x_{j+1}, y_p, k) - M_{12}(x_{j-1}, y_p, k) + \mathrm{i}\, M_{12}(x_j, y_{p+1}, k) - \mathrm{i}\, M_{12}(x_j, y_{p-1}, k) \\ &\quad -4h\,\mathrm{i}\,k M_{12}(x_j, y_p, k) - 4hQ_{12}(x_j, y_p) M_{22}(x_j, y_p, k), \end{aligned} \tag{4.15}$$

$$\begin{aligned} 4hF_4 &= M_{22}(x_{j+1}, y_p, k) - M_{22}(x_{j-1}, y_p, k) - \mathrm{i}\, M_{22}(x_j, y_{p+1}, k) + \mathrm{i}\, M_{22}(x_j, y_{p-1}, k) \\ &\quad -4hQ_{21}(x_j, y_p) M_{12}(x_j, y_p, k), \end{aligned} \tag{4.16}$$

for $1 \le j, p \le N$. To impose the asymptotic boundary conditions we again need to expand our matrix to include $j, p = 0, N+1$ in order to accurately describe the derivatives. We will then solve the system on the interior nodes with an adjusted right hand side. Since $M_{12} \sim 0$ no adjustments are needed for the right hand side involving F_2, i.e. we only need to adjust the terms involving F_4. We adjust them as follows,

- $4hF_4(x_1, y_p, k)$ is replaced with $4hF_1(x_1, y_p, k) + 1$ for $p = 1, \ldots, N$
- $4hF_4(x_N, y_p, k)$ is replaced with $4hF_1(x_N, y_p, k) - 1$ for $p = 1, \ldots, N$
- $4hF_4(x_j, y_1, k)$ is replaced with $4hF_1(x_j, y_1, k) - \mathrm{i}$ for $j = 1, \ldots, N$

- $4hF_4\left(x_j, y_N, k\right)$ is replaced with $4hF_1\left(x_j, y_N, k\right) + \mathrm{i}$ for $j = 1, \ldots, N$

The matrix system to be solved is very similar to that of System I and is given by

$$Bm_2 = b_2 \tag{4.17}$$

where the matrix B is given by:

$$B = \begin{bmatrix} B_{11} & B_{12} \\ B_{21} & B_{22} \end{bmatrix}$$

where,

$$B_{11} = \mathrm{conj}\left(A_{11}\right) \tag{4.18}$$

$$B_{12} = A_{21} \tag{4.19}$$

$$B_{21} = A_{12} \tag{4.20}$$

$$B_{22} = A_{11} + 4hk\,\mathrm{i}\,\mathrm{I}_{N^2}. \tag{4.21}$$

Now,

$$m_2 = \begin{bmatrix} \mathrm{vec}\left(M_{22}\right) \\ \mathrm{vec}\left(M_{12}\right) \end{bmatrix}, \tag{4.22}$$

and the right hand side b_2 is given by,

$$b_2 = \begin{bmatrix} 4h\mathrm{vec}\left(F_4\right) + \mathrm{conj}(V) \\ 4h\mathrm{vec}\left(F_2\right) \end{bmatrix}. \tag{4.23}$$

4.1.3 The Test Problem for the Finite Difference Solver

We look at the following test problem to evaluate the results of our finite difference solver for the forward $D_k M - QM = F$ problem (Equations (4.3) and (4.4)).

Admittivity for the Test Problem

To choose an appropriate admittivity function $\gamma(z)$, we modify the ideas outlined in [MS03] and define

$$\gamma(r) := \left(\alpha_1 F_{\mathrm{cond}}(r) + 1\right)^2 + \mathrm{i}\,\omega\left[\left(\alpha_2 F_{\mathrm{perm}}(r) + 1\right)^2 - 1\right], \tag{4.24}$$

to be the admittivity where

$$\sigma(r) := \left(\alpha_1 F_{\mathrm{cond}}(r) + 1\right)^2, \tag{4.25}$$

is the conductivity and

$$\epsilon(r) := (\alpha_2 F_{\text{perm}}(r) + 1)^2 - 1, \tag{4.26}$$

the permittivity. Note that these are radially symmetric functions where $r = \sqrt{x^2 + y^2}$. For the conductivity we use Example 3 of [MS03] so that

$$F_{\text{cond}}(r) = \exp\left\{ \frac{-2(\rho_1^2 + r^2)}{(r+\rho_1)^2(r-\rho_1)^2} \right\}, \quad r \le \rho_1, \tag{4.27}$$

and $F_{\text{cond}}(r) = 0$ if $r > \rho_1$. Then

$$\bar{\partial} F_{\text{cond}}(r) = \frac{2(x + \mathrm{i}\, y)\left(r^2 + 3\rho_1^2\right)}{(r-\rho_1)^3 (r+\rho_1)^3} F_{\text{cond}}, \quad r \le \rho_1, \tag{4.28}$$

and $\bar{\partial} F_{\text{cond}}(r) = 0$ if $r > \rho_1$.

We use Example 2 of [MS03] to define the permittivity as follows,

$$F_{\text{perm}}(r) = \left(r^2 - \rho_2^2\right)^4 \cos\left(\frac{3\pi r}{2\rho_2}\right), \quad r \le \rho_2, \tag{4.29}$$

and $F_{\text{perm}}(r) = 0$ if $r > \rho_2$. Then, for $r \le \rho_2$

$$\bar{\partial} F_{\text{perm}}(r) = (x + \mathrm{i}\, y)\left[4\left(r^2 - \rho_2^2\right)^3 \cos\left(\frac{3\pi r}{2\rho_2}\right) - \frac{3\pi}{4\rho_2 r}\left(r^2 - \rho_2^2\right)^4 \sin\left(\frac{3\pi r}{2\rho_2}\right)\right], \tag{4.30}$$

and $\bar{\partial} F_{\text{perm}}(r) = 0$ if $r > \rho_2$. Notice that $\bar{\partial} F_{\text{perm}}$ is undefined for $r = \sqrt{x^2 + y^2} = 0$ due to division by zero. Numerically, we can deal with this by using the *sinc* function

$$\text{sinc}(r) = \frac{\sin(r)}{r} \approx 1 \ \text{ for } r \text{ very near } 0$$

so that for r close to zero,

$$\bar{\partial} F_{\text{perm}}(r) = (x + \mathrm{i}\, y)\left[4\left(r^2 - \rho_2^2\right)^3 \cos\left(\frac{3\pi r}{2\rho_2}\right) - \frac{1}{2}\left(\frac{3\pi}{2\rho_2}\right)^2 \left(r^2 - \rho_2^2\right)^4\right].$$

Now that we have defined the admittivity $\gamma(r)$, we can form the matrix potential Q by defining Q_{12} and Q_{21} as follows. Recall,

$$Q = \begin{bmatrix} 0 & Q_{12} \\ Q_{21} & 0 \end{bmatrix},$$

where,

$$\begin{aligned} Q_{12}(z) &:= -\frac{1}{2}\,\partial_{\text{z}} \log\left(\gamma(z)\right) = -\frac{\partial_{\text{z}}(\gamma(z))}{2\gamma(z)}, \\ Q_{21}(z) &:= -\frac{1}{2}\,\bar{\partial}_{\text{z}} \log\left(\gamma(z)\right) = -\frac{\bar{\partial}_{\text{z}}(\gamma(z))}{2\gamma(z)}. \end{aligned}$$

Therefore, to define the matrix potential $Q(z)$, we only need to calculate $\partial_{\mathrm{z}}(\gamma(z))$ and $\bar{\partial}_{\mathrm{z}}(\gamma(z))$. Using Equation (4.25) we find,

$$\bar{\partial}_{\mathrm{z}}\,\sigma(r) = 2\alpha_1\,(\alpha_1 F_{\mathrm{cond}}(r) + 1)\,\bar{\partial}_{\mathrm{z}}\,F_{\mathrm{cond}}(r), \tag{4.31}$$

and using Equation (4.26),

$$\bar{\partial}_{\mathrm{z}}\,\epsilon(r) = 2\alpha_2\,(\alpha_2 F_{\mathrm{perm}}(r) + 1)\,\bar{\partial}_{\mathrm{z}}\,F_{\mathrm{perm}}(r). \tag{4.32}$$

Therefore,

$$\begin{aligned}
\bar{\partial}_{\mathrm{z}}\,\gamma(r) &= \bar{\partial}_{\mathrm{z}}\,\sigma(r) + \mathrm{i}\,\omega\,\bar{\partial}_{\mathrm{z}}\,\epsilon(r) \\
&= 2\alpha_1\,(\alpha_1 F_{\mathrm{cond}}(r) + 1)\,\bar{\partial}_{\mathrm{z}}\,F_{\mathrm{cond}}(r) \\
&\quad + 2\alpha_2\,\mathrm{i}\,\omega\,(\alpha_2 F_{\mathrm{perm}}(r) + 1)\,\bar{\partial}_{\mathrm{z}}\,F_{\mathrm{perm}}(r),
\end{aligned} \tag{4.33}$$

and thus the equations for $Q_{12}(z)$ and $Q_{21}(z)$ are fully defined using the calculations performed above and taking the conjugates where appropriate, to obtain the ∂_{z}-derivative instead of the $\bar{\partial}_{\mathrm{z}}$-derivative since $\sigma(z)$ and $\epsilon(z)$ are real valued functions. We avoid the tedium of writing out the explicit terms here.

Defining M_{11} and M_{21} for the Test Problem

We will need both M_{11} and M_{21} in order to calculate the right hand side functions, F_1 and F_3 respectively. We will then solve a "linear" system $Am_1 = b_1$ for m_1, reshape the results into the approximate CGO solutions M_{11} and M_{21} solutions, and compare them to the true functions with which we began. This will give us an idea of how well our solver works.

Let,

$$M_{11}(x,y,k) = \exp\left\{-x^2 - y^2 - 2\,\mathrm{i}\,xy\right\} e_{K11} + 1 \tag{4.34}$$

$$M_{21}(x,y,k) = (1+\mathrm{i})\exp\left\{-x^2 - y^2\right\} e_{K21}, \tag{4.35}$$

where $e_{K11} = \exp\{-k_1^2 - k_2^2 - 2ik_1k_2\}$, $e_{K21} = \exp\{-k_1^2 - k_2^2\}$, and $k = k_1 + \mathrm{i}\,k_2 \in \mathbb{C}$, shown in Figure 4.1. We will need to compute $\bar{\partial}_{\mathrm{z}}\,M_{11}$ and $\partial_{\mathrm{z}}\,M_{21}$ in order to find F_1 and F_3. Short calculations yield,

$$\bar{\partial}_{\mathrm{z}}\,M_{11} = -2\,\mathrm{i}\,y\exp\left\{-x^2 - y^2 - 2\,\mathrm{i}\,xy\right\} e_{K11} \tag{4.36}$$

$$\partial_{\mathrm{z}}\,M_{21} = (1+\mathrm{i})(-x + \mathrm{i}\,y)\exp\left\{-x^2 - y^2\right\} e_{K21}, \tag{4.37}$$

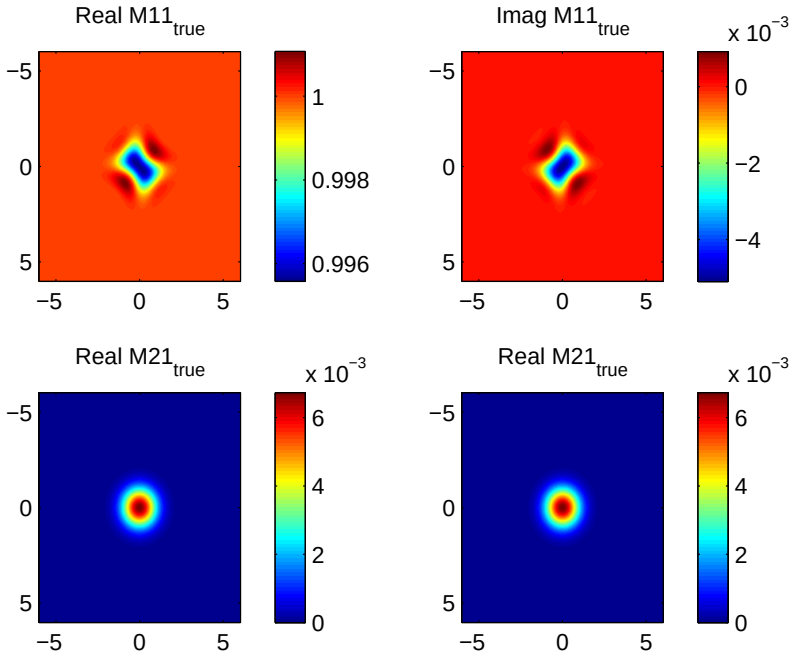

Fig. 4.1: True M's for the test problem using for $k = 1 - 2\,\mathrm{i}$.

which then allow us to fully define

$$\begin{aligned} F_1 &= \bar{\partial}_{\mathrm{z}} M_{11} - Q_{12} M_{21} \\ F_3 &= \partial_{\mathrm{z}} M_{21} + \mathrm{i}\, k M_{21} - Q_{21} M_{11}, \end{aligned}$$

that will be used in the finite difference matrix formulation of the problem.

Defining M_{12} and M_{22} for the Test Problem

For completeness, we check our test problem for the second system (4.2) as well. We will need both M_{12} and M_{22} in order to calculate or right hand side functions, F_2 and F_4 respectively. For simplicity, we let $M_{12} = M_{21}$ and $M_{22} = M_{11}$ from above. We will then solve a system $Bm_2 = b_2$ for m_2, reshape the results into the approximate M_{12} and M_{22} CGO solutions, and compare them to the true functions with which we began. This will give us an idea of how well our forward $D_k M - QM = F$ solver works for the second system.

Let,

$$M_{12}(x, y, k) = (1 + \mathrm{i}) \exp\left\{-x^2 - y^2\right\} e_{K21}, \tag{4.38}$$

where $e_{K21} = \exp\{-k_1^2 - k_2^2\}$ and $k = k_1 + \mathrm{i}\, k_2$. Define

$$M_{22}(x, y, k) = \exp\left\{-x^2 - y^2 - 2\,\mathrm{i}\, xy\right\} e_{K11} + 1, \tag{4.39}$$

where $e_{K11} = \exp\{-k_1^2 - k_2^2 - 2ik_1k_2\}$ and $k = k_1 + \mathrm{i}\, k_2$. We will need to compute $\bar{\partial}_{\mathrm{z}} M_{12}$ and $\partial_{\mathrm{z}} M_{22}$ in order to find F_2 and F_4. Short calculations yield,

$$\bar{\partial}_{\mathrm{z}} M_{12} = -(1 + \mathrm{i})(x + \mathrm{i}\, y) \exp\left\{-x^2 - y^2\right\} e_{K21} \tag{4.40}$$

$$\partial_{\mathrm{z}} M_{22} = -2x \exp\left\{-x^2 - y^2 - 2\,\mathrm{i}\, xy\right\} e_{K11}, \tag{4.41}$$

which then allow us to fully define

$$\begin{aligned} F_2 &= \bar{\partial}_{\mathrm{z}} M_{12} - \mathrm{i}\, k M_{12} - Q_{12} M_{22} \\ F_4 &= \partial_{\mathrm{z}} M_{22} - Q_{21} M_{12}, \end{aligned}$$

which we will be uses in the finite difference matrix formulation of the problem.

Results of the Test Problem

Table 4.1 displays relative errors for $z \in [-6,6]^2$ computed by, for example:

$$\text{Maximum Error for } M_{11} \text{ Real} = \frac{\max\left\{Re\left(M_{11}^{\text{true}} - M_{11}^{\text{apx}}\right)\right\}}{\max\left\{Re\left(M_{11}^{\text{true}}\right)\right\}}$$

Tab. 4.1: Relative Errors for the Test Problem

	Finite Differences
k	$1 - 2\,\mathrm{i}$
N	2^8
Condition Number (A)	1.9559×10^3
Condition Number (B)	3.4982×10^4
Max Error Re(M_{11})	9.5177×10^{-7}
Max Error Im(M_{11})	1.5×10^{-3}
Max Error Re(M_{21})	6.4485×10^{-4}
Max Error Im(M_{21})	7.2353×10^{-4}
Max Error Re(M_{22})	1.1220×10^{-6}
Max Error Im(M_{22})	1.5×10^{-3}
Max Error Re(M_{12})	6.4487×10^{-4}
Max Error Im(M_{12})	7.1655×10^{-4}

Notice that the errors for the finite difference method are very good and therefore we can be confident that our finite difference solver for the forward $D_k M - QM = F$ problem is accurate. Figure 4.2 shows the reconstructions using the finite difference method.

4.2 Approach 2: Using Vainikko's One Grid Method

We can also solve the forward $D_k M = QM$ problem using Vainikko's one grid method as presented in [KMS04]. Here we describe the problem using only one grid (see [KMS04] for details on the two-grid method) and extend it to work with systems. The main idea behind this solution method involves viewing the ∂ and $\bar{\partial}$ inverses as convolutions, then using Fourier transforms to break up the convolution into a product, and using inverse Fourier transforms to finish it off. One should note that the method presented in [KMS04] uses Nachman's solution method to the conductivity problem for twice differentiable conductivities ([Nac96]) and thus was able to exploit certain symmetries that result from considering only real valued conductivities. In particular, solving that problem required only the solution of a single Lippman-Schwinger type equation, rather than two separate systems of

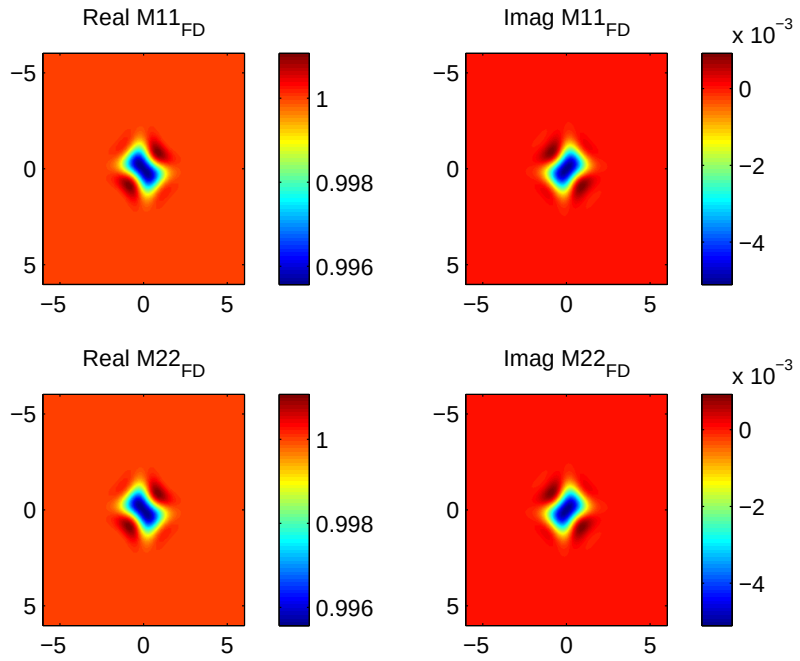

(a) M_{11} and M_{22}

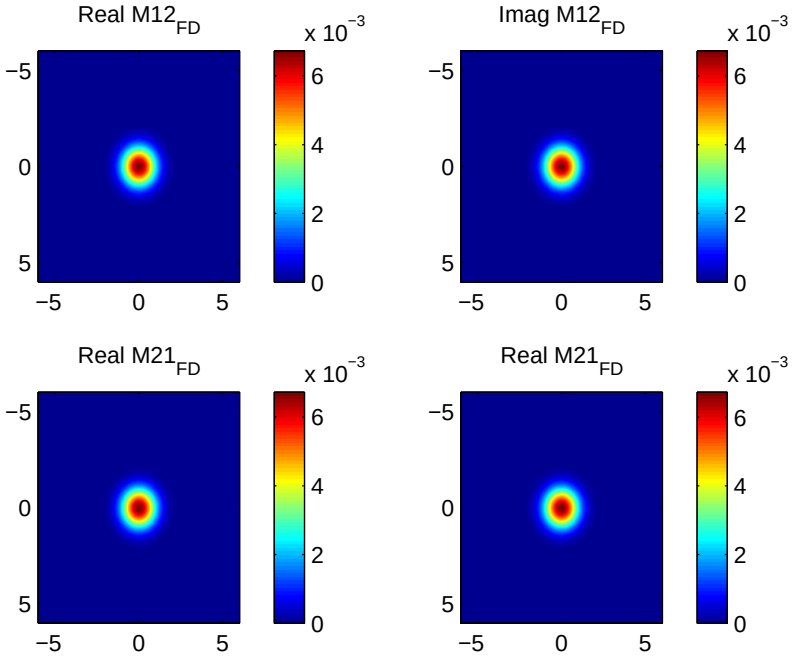

(b) M_{12} and M_{21}

Fig. 4.2: Reconstructions of the M's for the test problem using the Finite Difference Method for $k = 1 - 2\,\mathrm{i}$.

Lippman-Schwinger type equations. As Vainikko's method requires a compact operator, here we will only solve the original forward $D_k M = QM$ problem (not the $D_k M - QM = F$ test problem), i.e. for $F_j = 0$ for $j = 1, \ldots, 4$.

4.2.1 Solving System I

We wish to solve (4.1) where $M_{11}(z,k) \sim 1$ and $M_{21}(z,k) \sim 0$ as $|k|,\ |z| \to \infty$. We invert the $\bar{\partial}_z$ operator using the Generalized Cauchy Integral Formula and use (3.18) to invert the $(\partial_z + \mathrm{i}\, k)$ operator (given in [Fra00]). Using the compact support of Q_{12} and Q_{21} we have,

$$\begin{aligned} M_{11}(z,k) &= 1 + \frac{1}{\pi}\int_\Omega \frac{Q_{12}(\zeta) M_{21}(\zeta,k)}{z-\zeta}\, d\mu(\zeta) \\ \\ M_{21}(z,k) &= \frac{1}{\pi}\int_\Omega \frac{e(z-\zeta,-k) Q_{21}(\zeta) M_{11}(\zeta,k)}{\bar{z}-\bar{\zeta}}\, d\mu(\zeta), \end{aligned}$$

or using convolution

$$\begin{cases} M_{11}(z,k) = & 1 + \frac{1}{\pi z} * [Q_{12}(z) M_{21}(z,k)] \\ \\ M_{21}(z,k) = & \frac{e(z,-k)}{\pi \bar{z}} * [Q_{21}(z) M_{11}(z,k)] \end{cases},$$

where the convolution is only taking place over the finite region Ω as the supports of $Q_{12}(z)$ and $Q_{21}(z)$ are contained in Ω. We can write this as a stacked system,

$$\begin{aligned} \begin{bmatrix} 1 \\ 0 \end{bmatrix} &= \left(\begin{bmatrix} 1 & 0 \\ 0 & 1 \end{bmatrix} - \begin{bmatrix} \frac{1}{\pi z} \\ \frac{e(z,-k)}{\pi \bar{z}} \end{bmatrix} * \left(\begin{bmatrix} 0 & Q_{12}(z) \\ Q_{21}(z) & 0 \end{bmatrix} \begin{bmatrix} M_{11}(z,k) \\ M_{21}(z,k) \end{bmatrix} \right) \right) \\ &= \left(I - G_1 * \left(\tilde{Q}_1 \cdot \right) \right) \tilde{M}_1 \end{aligned} \tag{4.42}$$

where I is the identity matrix

$$G_1 = \begin{bmatrix} \frac{1}{\pi z} \\ \frac{e(z,-k)}{\pi \bar{z}} \end{bmatrix}, \quad \tilde{M}_1 = \begin{bmatrix} M_{11}(z,k) \\ M_{21}(z,k) \end{bmatrix}, \quad \text{and } \tilde{Q}_1 = \begin{bmatrix} 0 & Q_{12}(z) \\ Q_{21}(z) & 0 \end{bmatrix}.$$

Vainikko's method requires that the multiplier function, in our case $\tilde{Q}_1$, be compact which is why we take $F_1 = F_3 = 0$ at the beginning of this section. To implement the solver we will use GMRES and therefore do not need to form the matrix for the operator $\left(I - G_1 * \left(\tilde{Q} \cdot \right) \right)$ explicitly. Rather, we will only need to implement the action of the operator. We will use the simpler form

$$\begin{cases} 1 = & M_{11}(z,k) - \frac{1}{\pi z} * (Q_{12}(z) M_{21}(z,k)) \\ 0 = & M_{21}(z,k) - \frac{e(z,-k)}{\pi \bar{z}} * (Q_{21}(z) M_{11}(z,k)) \end{cases}. \tag{4.43}$$

We will feed GMRES a function that takes a real valued vector (GMRES needs us to separate real and imaginary parts), reshapes the vector into complex matrices for M_{11} and M_{21}, then performs the action of the operator $\left(I - G_1 * \left(\tilde{Q}_1 \cdot\right)\right)$. To perform the convolution we will use Fourier transforms as follows:

$$\frac{1}{\pi z} * (Q_{12}(z)M_{21}(z,k)) = h^2 \,\mathrm{IFFT}\left(\mathrm{FFT}\left(\frac{1}{\pi z}\right) \cdot \mathrm{FFT}\left(Q_{12}(z) \cdot M_{21}(z,k)\right)\right),$$

and similarly

$$\frac{e(z,-k)}{\pi \bar{z}} * (Q_{21}(z)M_{11}(z,k)) \;\; = \;\; h^2 \,\mathrm{IFFT}\left(\mathrm{FFT}\left(\frac{e(z,-k)}{\pi \bar{z}}\right) \cdot \mathrm{FFT}\left(Q_{21}(z) \cdot M_{11}(z,k)\right)\right),$$

where h is the step size of the uniform z grid we are using and $\cdot$ denotes componentwise multiplication. We then separate the real and imaginary parts again and place the CGO solutions M_{11} and M_{21} in an elongated real valued vector which is sent back to GMRES. After GMRES converges to our solution vector, we will need to reshape the elongated vector into the complex matrices $M_{11}(z,k)$ and $M_{21}(z,k)$.

To avoid blurring when using the Fourier transforms, we will evaluate the Green's functions for the $\bar{\partial}_{\mathrm{z}}$ and $\partial_{\mathrm{z}} + ik$ operators, $\frac{1}{\pi z}$ and $\frac{e(z,-k)}{\pi \bar{z}}$ respectively, on a grid twice as large. We then place the functions $Q_{12}(z)M_{21}(z,k)$ and $Q_{21}(z)M_{11}(z,k)$ in the centers of matrices on the enlarged grid padded with zeros around the edges.

4.2.2 Solving System II

We also wish to solve (4.2) where $M_{22}(z,k) \sim 1$ and $M_{12}(z,k) \sim 0$ as $|k|,\ |z| \to \infty$. We invert the ∂_{z} operator using the Solid Cauchy Transform and use (3.18) to invert the $\left(\bar{\partial}_{\mathrm{z}} - \mathrm{i}\, k\right)$ operator. Using the compact support of Q_{12} and Q_{21} we have,

$$M_{22}(z,k) \;\; = \;\; 1 + \frac{1}{\pi}\int_{\Omega} \frac{Q_{21}(\zeta)M_{12}(\zeta,k)}{\bar{z} - \bar{\zeta}}\, d\mu(\zeta)$$

$$M_{12}(z,k) \;\; = \;\; \frac{1}{\pi}\int_{\Omega} \frac{e(z-\zeta,-k)Q_{12}(\zeta)M_{22}(\zeta,k)}{z - \zeta}\, d\mu(\zeta),$$

or using convolution

$$\begin{cases} M_{22}(z,k) = \;\; 1 + \frac{1}{\pi \bar{z}} * [Q_{21}(z)M_{12}(z,k)] \\ \\ M_{12}(z,k) = \;\; \frac{e(z,\bar{k})}{\pi z} * [Q_{12}(z)M_{22}(z,k)] \end{cases},$$

where again the convolution is only taking place over the finite region Ω as the supports of $Q_{12}(z)$ and $Q_{21}(z)$ are contained in Ω. We can write this as a stacked system,

$$\begin{aligned}\begin{bmatrix} 1 \\ 0 \end{bmatrix} &= \left(\begin{bmatrix} 1 & 0 \\ 0 & 1 \end{bmatrix} - \begin{bmatrix} \frac{1}{\pi \bar{z}} \\ \frac{e(z,\bar{z})}{\pi z} \end{bmatrix} * \left(\begin{bmatrix} 0 & Q_{21}(z) \\ Q_{12}(z) & 0 \end{bmatrix} \begin{bmatrix} M_{22}(z,k) \\ M_{12}(z,k) \end{bmatrix} \right) \right) \\ &= \left(I - G_2 * \left(\tilde{Q}_2 \, \cdot \right) \right) \tilde{M}_2 \end{aligned} \tag{4.44}$$

where I is the identity matrix

$$G_2 = \begin{bmatrix} \frac{1}{\pi \bar{z}} \\ \frac{e(z,k)}{\pi z} \end{bmatrix}, \quad \tilde{M}_2 = \begin{bmatrix} M_{22}(z,k) \\ M_{12}(z,k) \end{bmatrix}, \quad \text{and } \tilde{Q}_2 = \begin{bmatrix} 0 & Q_{21}(z) \\ Q_{12}(z) & 0 \end{bmatrix}.$$

This case is computed analogously.

4.3 Comparison of Forward Solvers

From Section 4.1.3, we know that the Finite Difference solver works for the test problem and thus we can use it to compare to solutions of the forward $D_k M = QM$ problem found using Vainikko's method (when the F_j's are zero i.e. when we are not prescribing the CGO solutions $M(z,k)$). Table 4.2 shows the values for the conductivity and permittivity used for these simulations. A twice differentiable conductivity and permittivity were prescribed using the phantom shown in Figure 4.3. Simple admittivities γ, defined by $\gamma = \sigma + \mathrm{i}\,\epsilon$, were used to help us better visualize the permittivity as the imaginary part of γ and not worry about the frequency ω at present.

Recall that to recover the CGO solutions M for a prescribed admittivity, the potential matrix Q is needed and therefore the ∂_z and $\bar{\partial}_z$ derivatives of γ. These derivatives were approximated using centered finite differences for the conductivity σ and permittivity ϵ by creating four additional matrices of values for the admittivity at $\pm h$ and $\pm \mathrm{i}\,h$ and combining them appropriately, where h is the step size of the grid we are using. The boundary condition is zero due to the compact support of the matrix potential Q and therefore no additional compensation is needed to enforce the zero boundary condition.

The results of the Finite Difference and Vainikko solvers for the various k values are shown in Figures 4.4, 4.5, 4.6, 4.7, 4.8, 4.9, 4.10, and 4.11, with $N = 2^7 = 128$ nodes in each of the x and y directions. Notice that the reconstructions using Vainikko's One Grid Method (denoted by V) are very smooth whereas those using Finite Differences (denoted by

Tab. 4.2: The prescribed admittivity for the test problem used to compare the Finite Difference and Vainikko solvers for the forward $D_k M = QM$ problem.

	Conductivity σ	Permittivity ϵ
heart	1.2	0.1
lungs	0.8	$0.0\overline{3}$
background	1	0

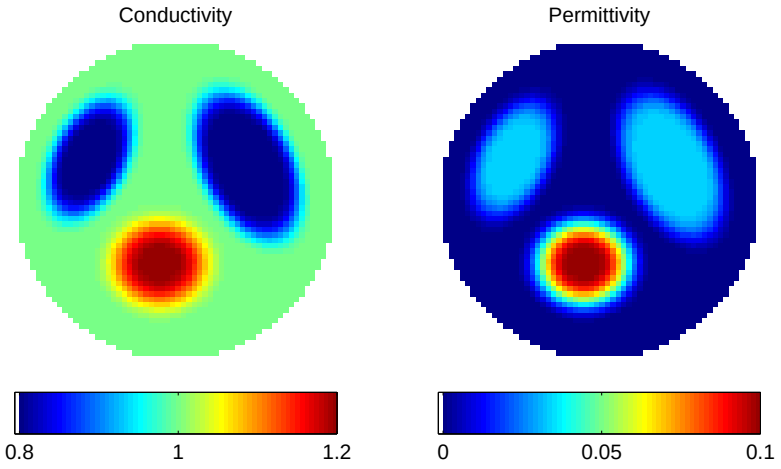

Fig. 4.3: The phantom used in the test problem to compare the Finite Difference and Vainikko solvers for the forward $D_k M = QM$ problem.

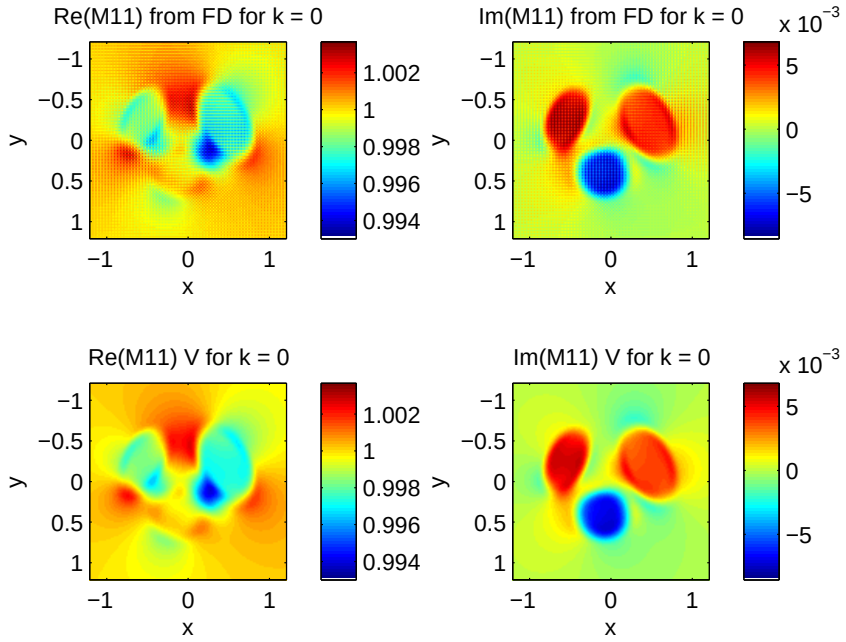

(a) M_{11} for $k = 0$

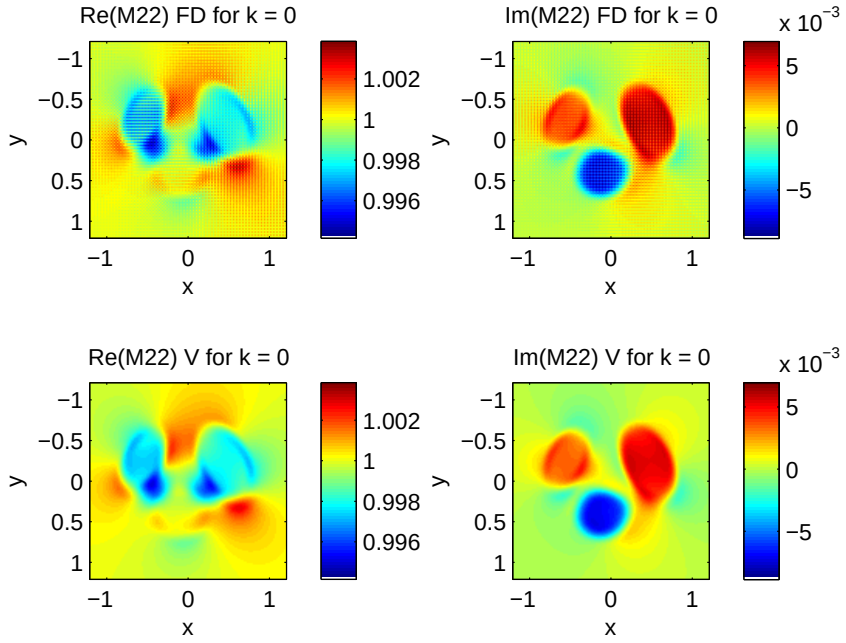

(b) M_{22} for $k = 0$

Fig. 4.4: Comparison of Finite Difference solver (FD) and Vainikko solver (V) for the forward $D_k M = QM$ problem. Figures are shown for M_{11} and M_{22} for $k = 0$.

FD) are not. As later we will need to peel off the values of the M's along the boundary of the unit disc to generate scattering data, we will prefer the smooth solutions of Vainikko's method. In addition, the finite difference solver ranges from 2 to 24 seconds depending on the value of k, compared to the less than 2 seconds required by Vainikko's method. Since the Vainikko solver is accurate and faster than the finite difference solver it is clearly more desirable.

4.4 Boundary Values for the CGO Solutions $M(z,k)$ for the Unit Disc

Plots of the CGO solutions $M(z,k)$ on the boundary of the domain $\partial\Omega$ (here Ω is the unit disc) for the same values of k as above (0, $-0.5+0.2\,\mathrm{i}$, $1-2\,\mathrm{i}$, and $-5+10\,\mathrm{i}$).

The forward $D_k M = QM$ problem was solved using Vainikko's method on a 128 by 128 xy grid, and bilinear interpolation was used to find the values of the CGO solutions $M(z,k)$ for z on the boundary of the unit disc that satisfied $x^2+y^2=1=e^{\mathrm{i}\,\theta}$ for $0 \le \theta < 2\pi$ with 63 theta values using MATLAB. Figures 4.12, 4.13, 4.14, and 4.15 show the plots for $k = 0, -0.5+0.2\,\mathrm{i}$, $1-2\,\mathrm{i}$, and $-5+10\,\mathrm{i}$ respectively (note that these are the same values of k used to plot the CGOs $M(z,k)$ in Figures 4.4-4.11). Notice that as $|k| \to \infty$ the values of the CGO solutions $M_{11}(z,k)$ and $M_{22}(z,k)$ on the boundary of the unit disc approach the constant 1, whereas for $M_{12}(z,k)$ and $M_{21}(z,k)$ tend toward 0 as expected. Additionally, note that the CGO solutions M_{12} and M_{22} oscillate wildly as $|k|$ increases.

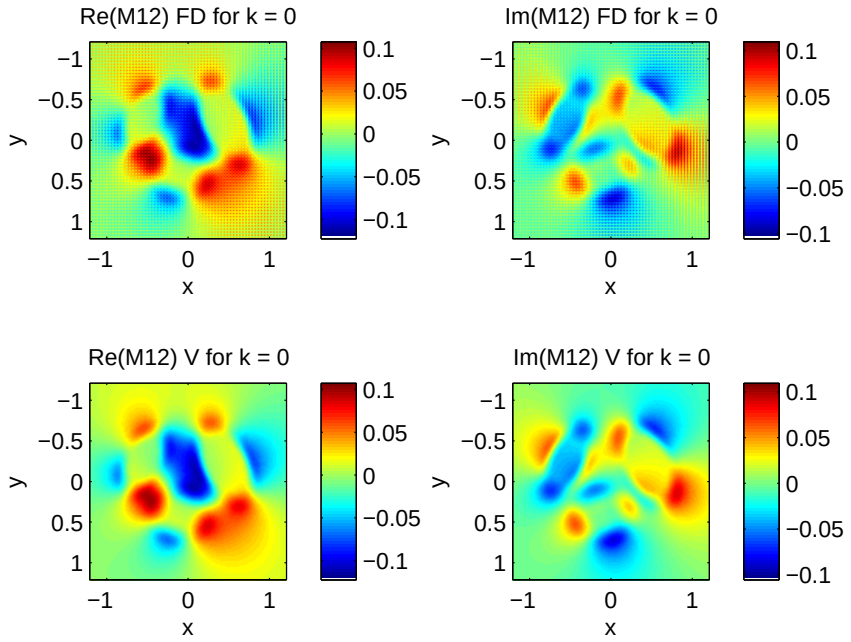

(a) M_{12} for $k = 0$

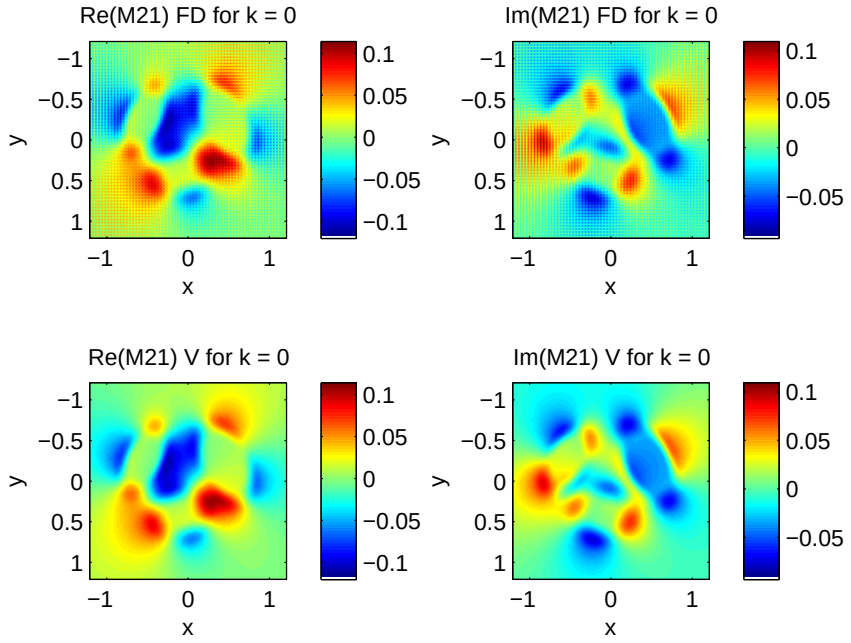

(b) M_{21} for $k = 0$

Fig. 4.5: Comparison of Finite Difference solver (FD) and Vainikko solver (V) for the forward $D_k M = QM$ problem. Figures are shown for M_{12} and M_{21} for $k = 0$.

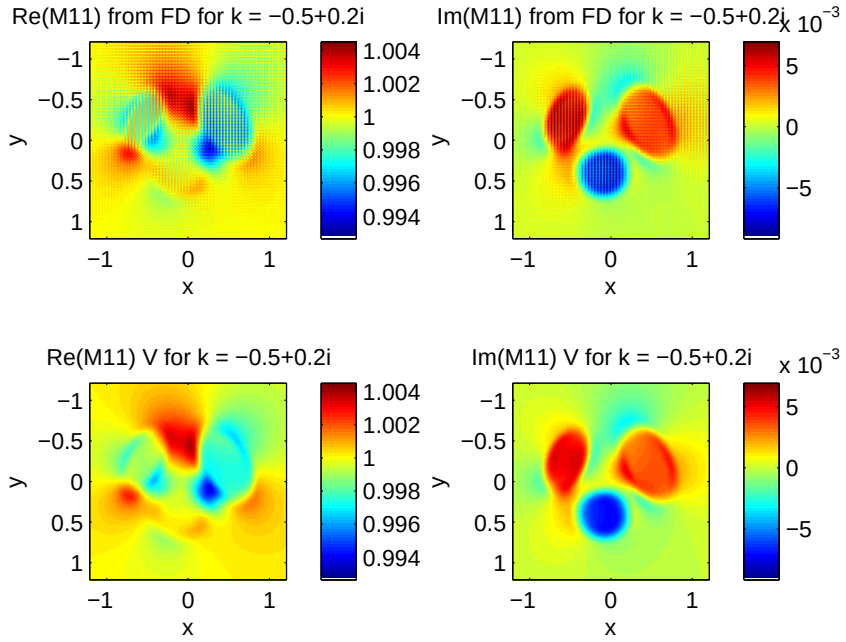

(a) M_{11} for $k = -0.5 + 0.2\,\mathrm{i}$

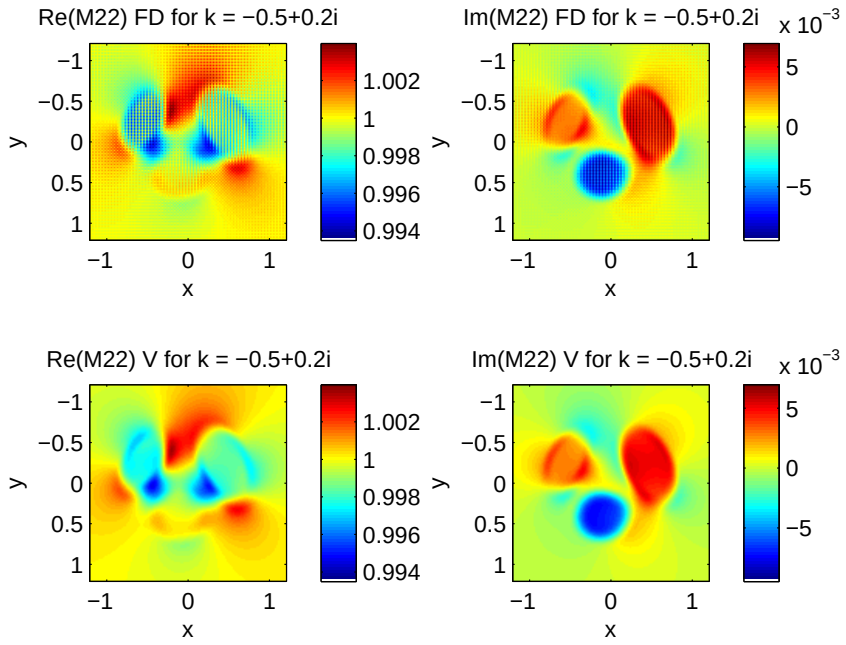

(b) M_{22} for $k = -0.5 + 0.2\,\mathrm{i}$

Fig. 4.6: Comparison of Finite Difference solver (FD) and Vainikko solver (V) for the forward $D_k M = QM$ problem. Figures are shown for M_{11} and M_{22} for $k = -0.5 + 0.2\,\mathrm{i}$.

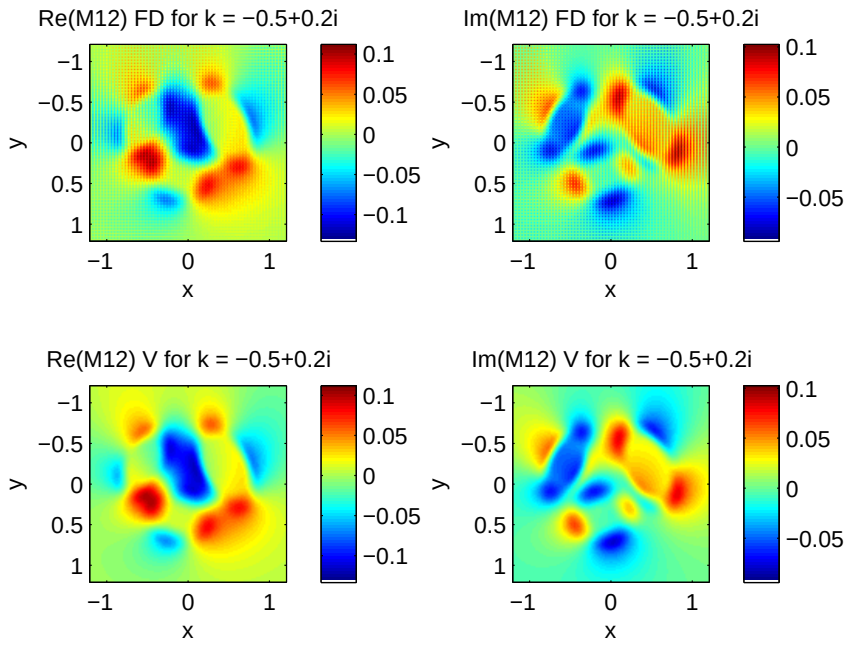

(a) M_{12} for $k = -0.5 + 0.2\,\mathrm{i}$

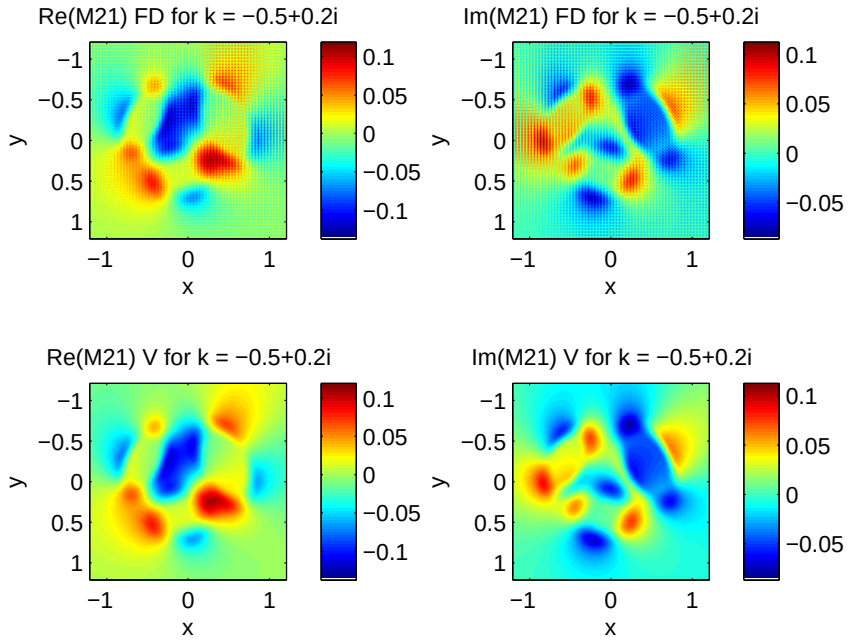

(b) M_{21} for $k = -0.5 + 0.2\,\mathrm{i}$

Fig. 4.7: Comparison of Finite Difference solver (FD) and Vainikko solver (V) for the forward $D_k M = QM$ problem. Figures are shown for Figures are shown for M_{12} and M_{21} for $k = -0.5 + 0.2\,\mathrm{i}$.

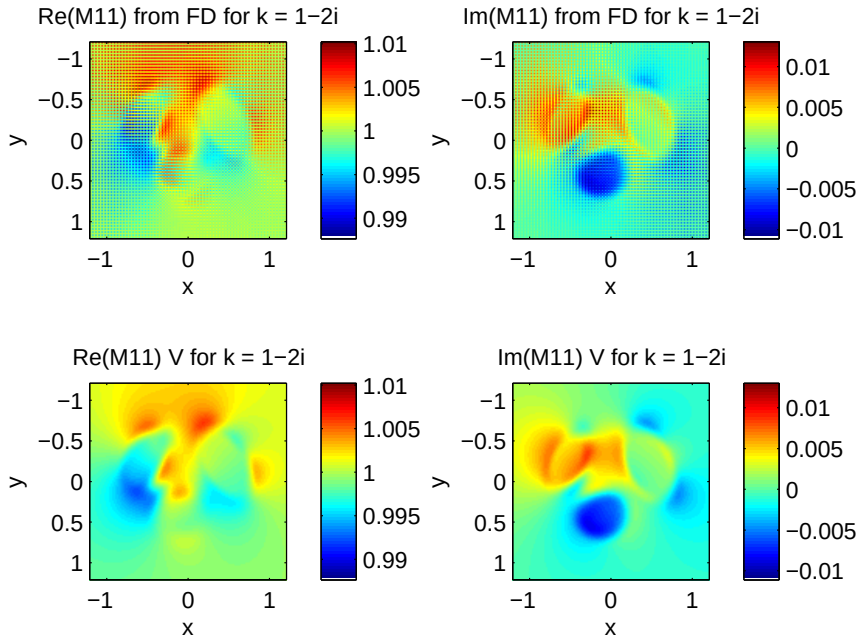

(a) M_{11} for $k = 1 - 2\,\mathrm{i}$

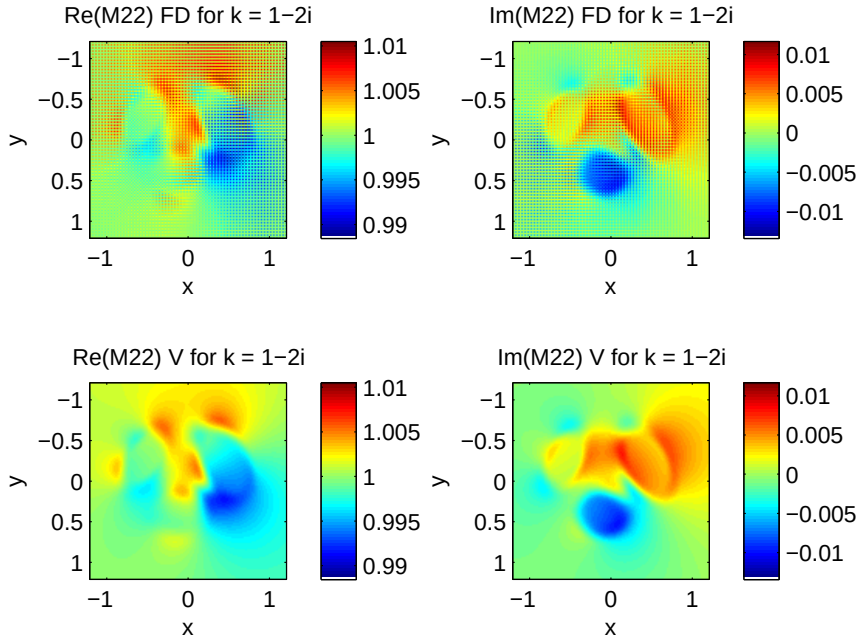

(b) M_{22} for $k = 1 - 2\,\mathrm{i}$

Fig. 4.8: Comparison of Finite Difference solver (FD) and Vainikko solver (V) for the forward $D_k M = QM$ problem. Figures are shown for M_{11} and M_{22} for $k = 1 - 2\,\mathrm{i}$.

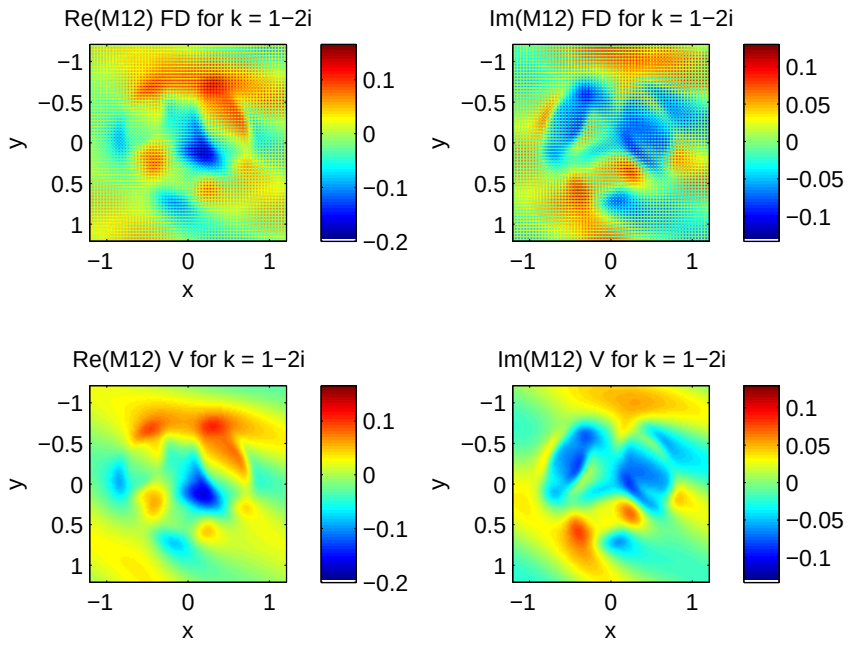

(a) M_{12} for $k = 1 - 2\,\mathrm{i}$

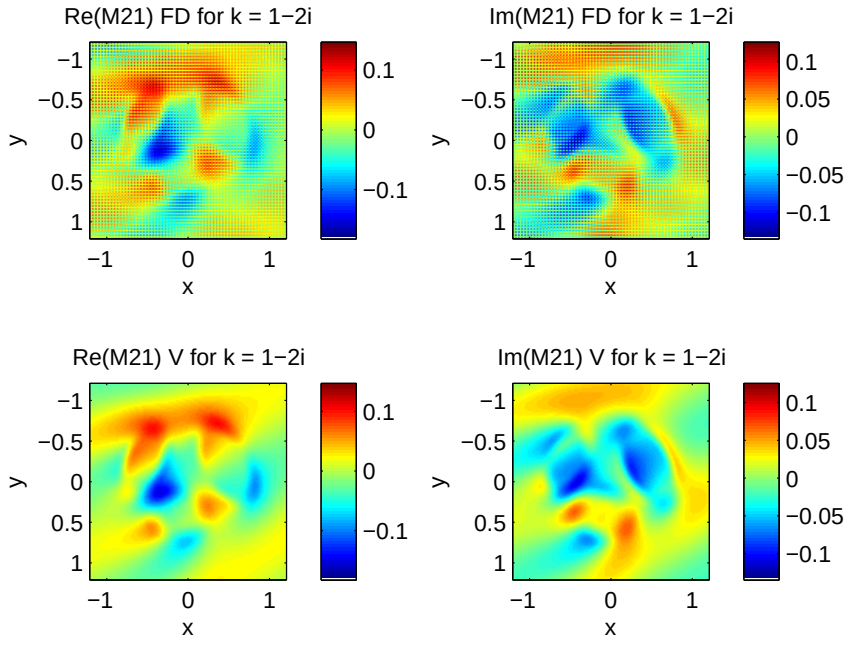

(b) M_{21} for $k = 1 - 2\,\mathrm{i}$

Fig. 4.9: Comparison of Finite Difference solver (FD) and Vainikko solver (V) for the forward $D_k M = QM$ problem. Figures are shown for Figures are shown for M_{12} and M_{21} for $k = 1 - 2\,\mathrm{i}$.

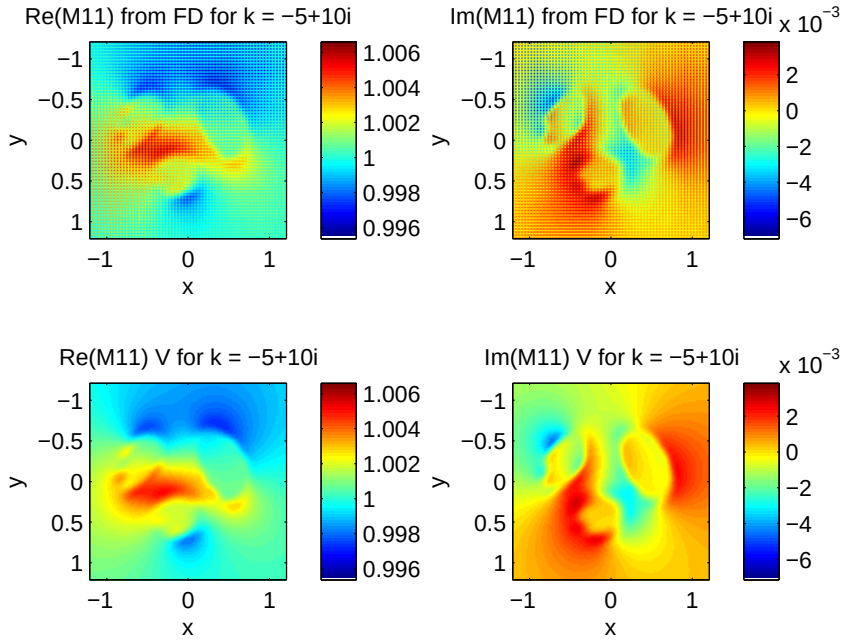

(a) M_{11} for $k = -5 + 10\,\mathrm{i}$

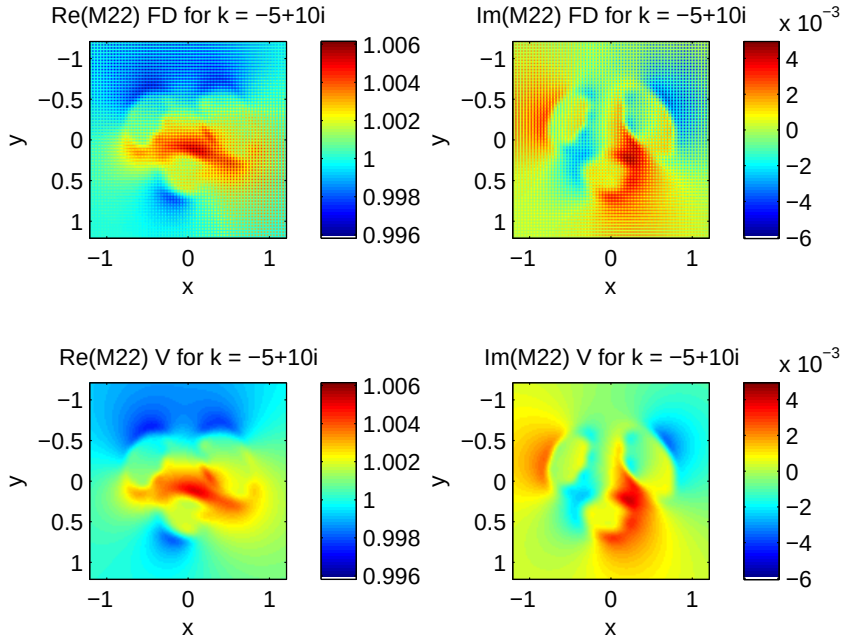

(b) M_{22} for $k = -5 + 10\,\mathrm{i}$

Fig. 4.10: Comparison of Finite Difference solver (FD) and Vainikko solver (V) for the forward $D_k M = QM$ problem. Figures are shown for M_{11} and M_{22} for $k = -5 + 10\,\mathrm{i}$.

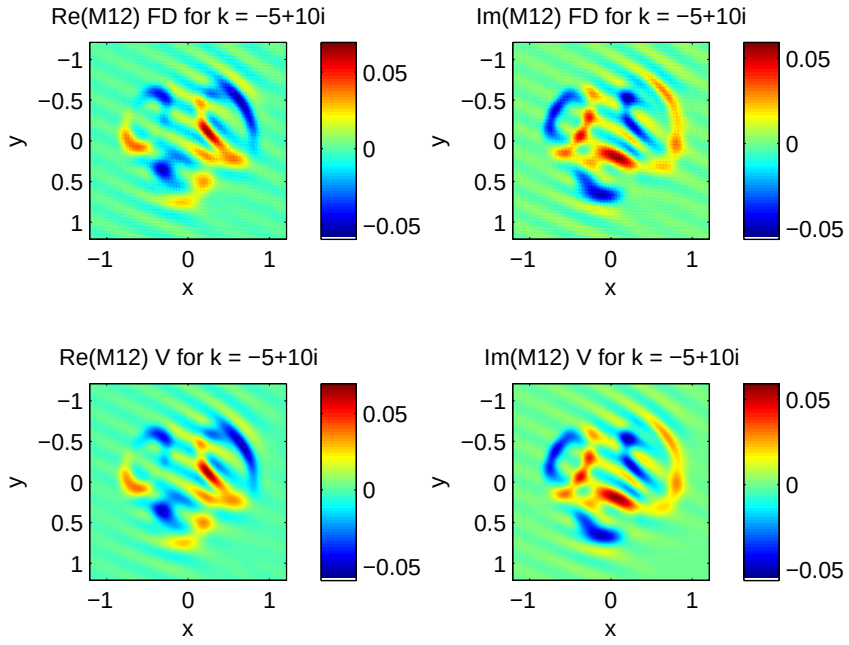

(a) M_{12} for $k = -5 + 10\,\mathrm{i}$

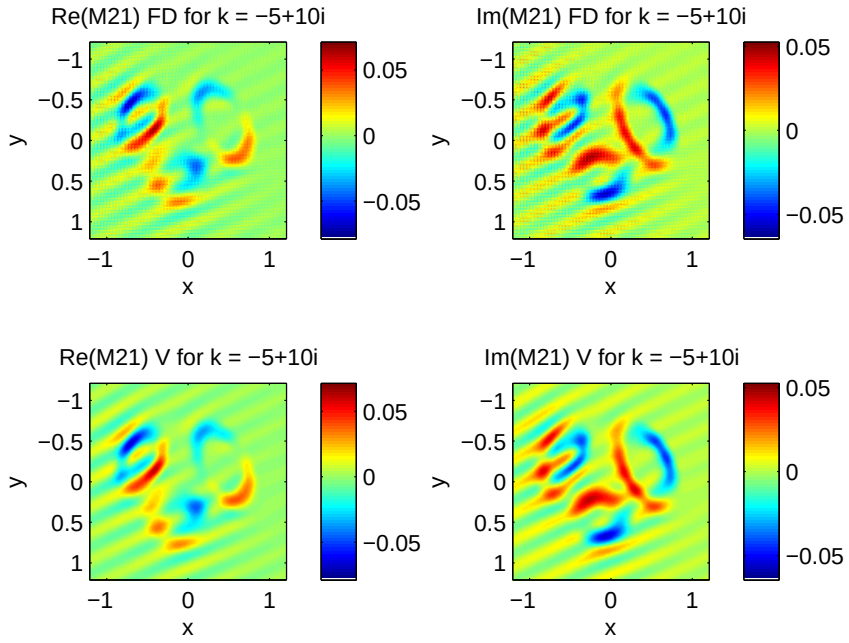

(b) M_{21} for $k = -5 + 10\,\mathrm{i}$

Fig. 4.11: Comparison of Finite Difference solver (FD) and Vainikko solver (V) for the forward $D_k M = QM$ problem. Figures are shown for Figures are shown for M_{12} and M_{21} for $k = -5 + 10\,\mathrm{i}$.

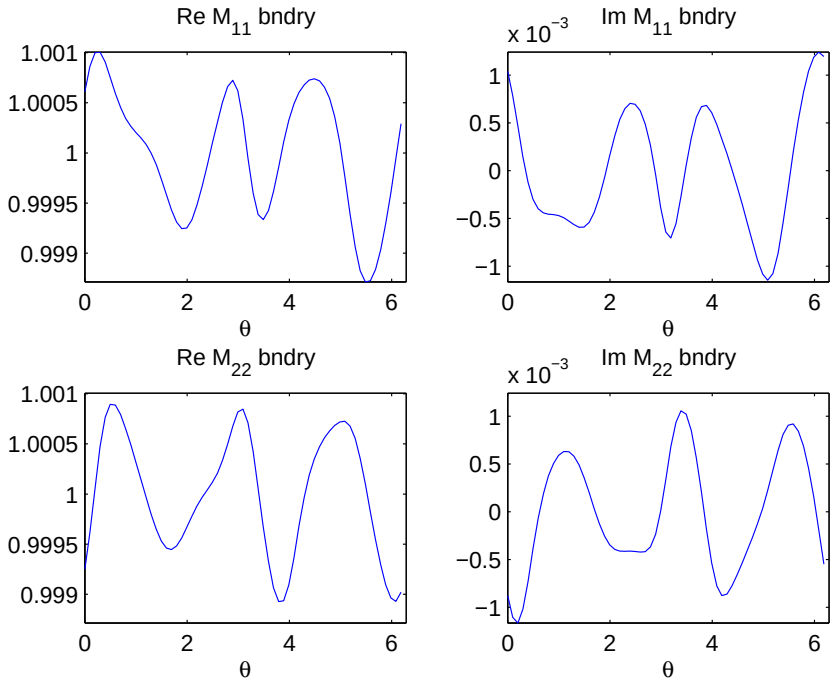

(a) M_{11} and M_{22} for $k = 0$

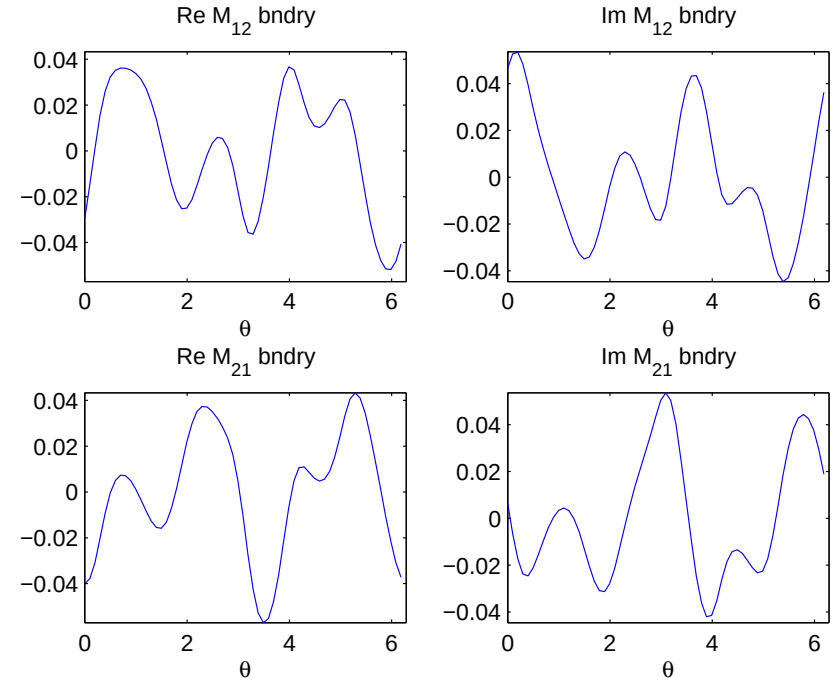

(b) M_{12} and M_{21} for $k = 0$

Fig. 4.12: Plots of M_{11}, M_{12}, M_{21} and M_{22} on the boundary for $k = 0$.

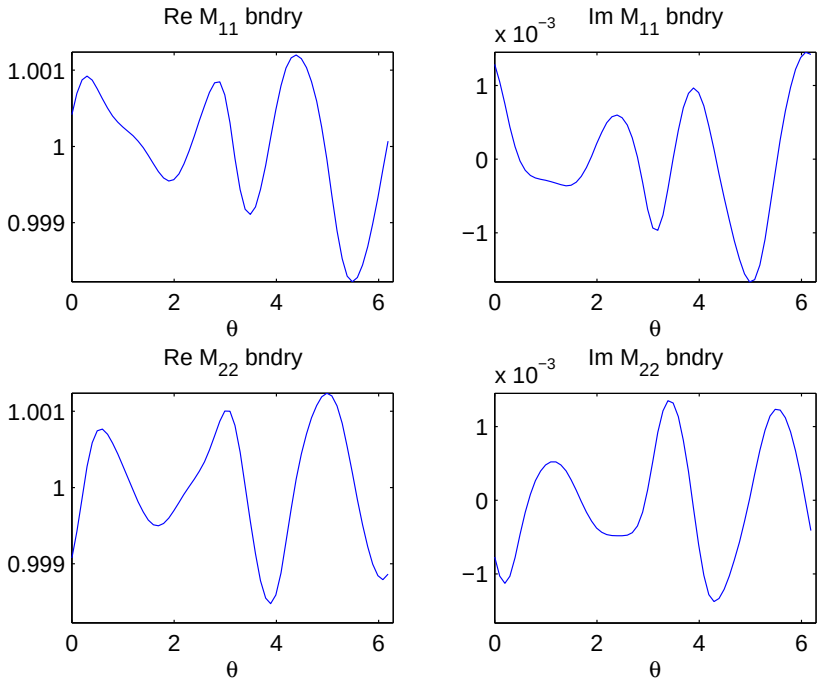

(a) M_{11} and M_{22} for $k = -0.5 + 0.2\,\mathrm{i}$

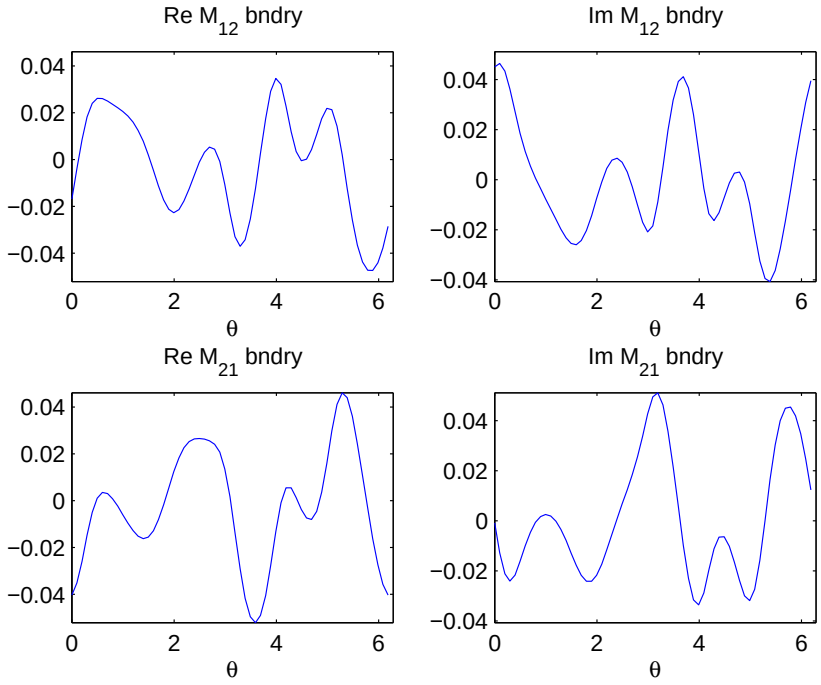

(b) M_{12} and M_{21} for $k = -0.5 + 0.2\,\mathrm{i}$

Fig. 4.13: Plots of M_{11}, M_{12}, M_{21} and M_{22} on the boundary for $k = -0.5 + 0.2\,\mathrm{i}$.

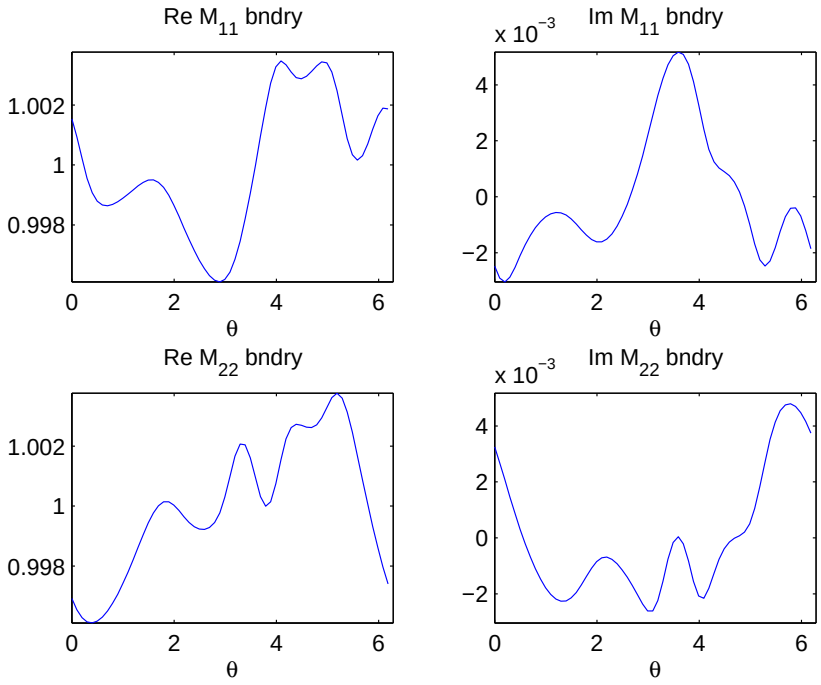

(a) M_{11} and M_{22} for $k = 1 - 2\,\mathrm{i}$

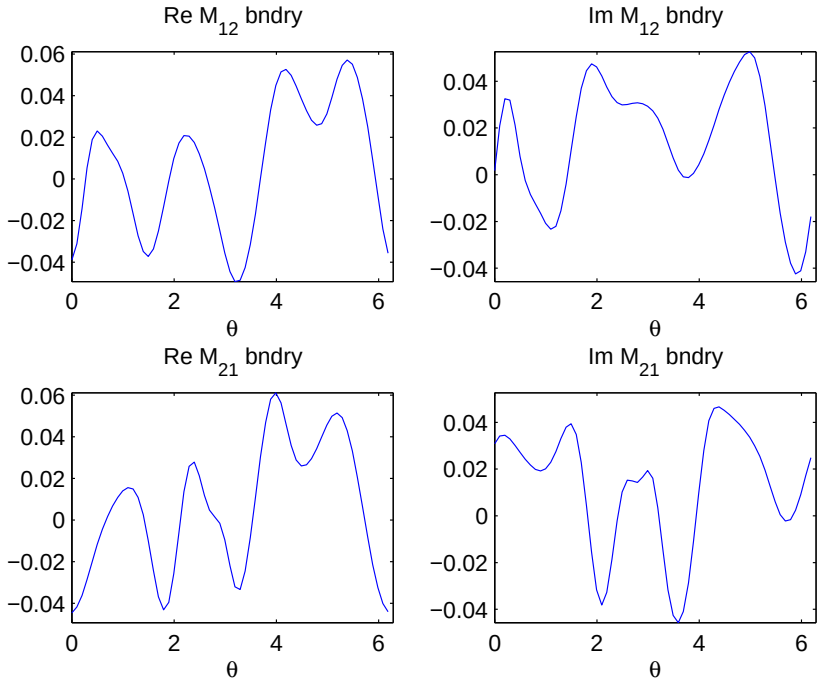

(b) M_{12} and M_{21} for $k = 1 - 2\,\mathrm{i}$

Fig. 4.14: Plots of M_{11}, M_{12}, M_{21} and M_{22} on the boundary for $k = 1 - 2\,\mathrm{i}$.

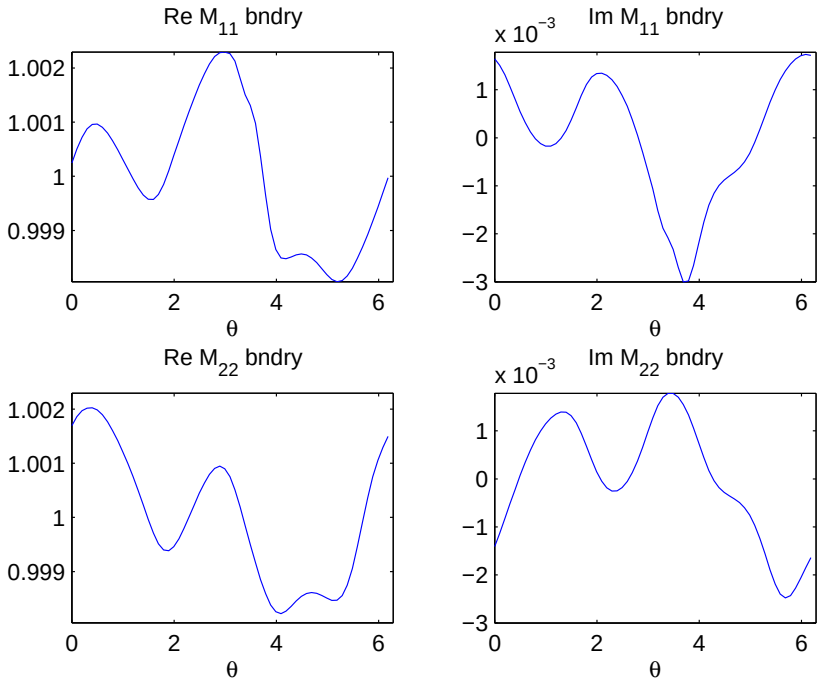

(a) M_{11} and M_{22} for $k = -5 + 10\,\mathrm{i}$

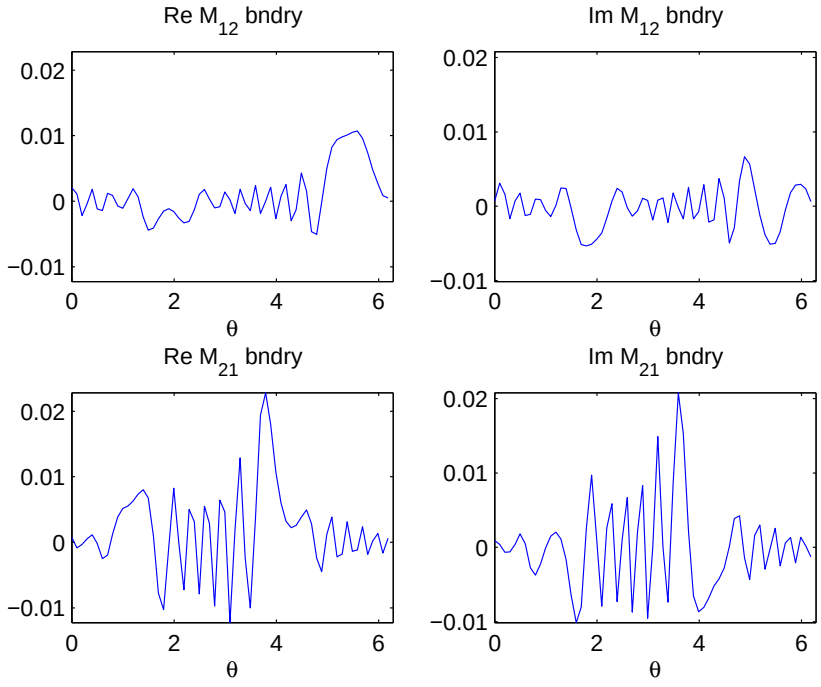

(b) M_{12} and M_{21} for $k = -5 + 10\,\mathrm{i}$

Fig. 4.15: Plots of M_{11}, M_{12}, M_{21} and M_{22} on the boundary for $k = -5 + 10\,\mathrm{i}$.

5. NEW THEORETICAL COMPONENTS TO COMPLETE THE RECONSTRUCTION ALGORITHM

In this chapter the theory behind the missing steps of the full reconstruction algorithm:

$$\Lambda_\gamma \longrightarrow \Psi_{12}|_{\partial\Omega},\ \Psi_{21}|_{\partial\Omega} \longrightarrow S(k) \longrightarrow M(z,0) \longrightarrow Q(z) \longrightarrow \gamma(z),$$

is developed and described in detail. Namely the first step (connecting the CGO solutions Ψ to the D-N data) and a more practical formula for recovering the matrix potential Q from the exponentially growing solutions M are presented.

5.1 Step 1: Connecting the CGO Solutions Ψ to the D-N Data Λ_γ

In the Ph.D thesis of Alan Von Herrmann, [Von09], and our recent paper, [HHMV12], two exponentially growing solutions to the admittivity equation (3.3) are studied. Recall that when Francini re-wrote (3.3) as a first order system, we ended up searching for a 2×2 solution matrix instead of just a vector $(v, w)^T$ as was originally derived. This is due to the fact that there are two solutions to (3.3), unique up to their asymptotic conditions.

Recall that

$$\begin{pmatrix} v \\ w \end{pmatrix} = \gamma^{1/2} \begin{pmatrix} \partial_{\mathrm{z}}\, u \\ \bar{\partial}_{\mathrm{z}}\, u \end{pmatrix}$$

solves the system

$$D \begin{pmatrix} v \\ w \end{pmatrix} - Q \begin{pmatrix} v \\ w \end{pmatrix} = 0.$$

We can think of the matrix of CGO solutions Ψ as two column vectors that correspond to the exponentially growing solutions u_1 and u_2 respectively. Thus,

$$\begin{pmatrix} \Psi_{11} \\ \Psi_{21} \end{pmatrix} = \gamma^{1/2} \begin{pmatrix} \partial_{\mathrm{z}}\, u_1 \\ \bar{\partial}_{\mathrm{z}}\, u_1 \end{pmatrix} \quad \text{and} \quad \begin{pmatrix} \Psi_{12} \\ \Psi_{22} \end{pmatrix} = \gamma^{1/2} \begin{pmatrix} \partial_{\mathrm{z}}\, u_2 \\ \bar{\partial}_{\mathrm{z}}\, u_2 \end{pmatrix}. \tag{5.1}$$

The CGO solutions $\Psi(z, k)$ are key functions in the reconstruction algorithm, however the proof in [Fra00] does not provide a link from these functions to the Dirichlet-to-Neumann data. A useful link can be established through exponentially growing solutions to the

admittivity equation (3.3). For $\gamma - 1$ with compact support contained in Ω, the admittivity equation (3.3) can be studied on all of $\mathbb{R}^2$. If we introduce k as a complex parameter, two distinct exponentially growing solutions, which differ in their asymptotics, u_1 and u_2 exist where $u_1 \sim \frac{e^{ikz}}{ik}$ and $u_2 \sim \frac{e^{-ik\bar{z}}}{-ik}$ in a sense that is made precise in Theorems 5 and 6, where the existence of such solutions is established. After establishing formulas for exponentially growing solutions u_1 and u_2 with connections the the Dirichlet-to-Neumann data, we can then use the relations above to establish formulas for the CGOs Ψ.

5.1.1 Derivation of Formulas for Exponentially Growing Solutions u_1 and u_2

The derivations for the exponentially growing solutions u_1 and u_2, given in our paper [HHMV12], will make use of the following lemma proved in the real case by Nachman [Nac96]; the complex version shown here also holds and was used in [Fra00]. The lemma is also true if $\bar{\partial}_z$ and ∂_z and interchanged. The remainder of the derivation of the formulas for the CGO solutions u_1 and u_2 is quoted from our paper [HHMV12].

Lemma 1 ([Nac96]). *Let $1 < s < 2$ and $\frac{1}{r} = \frac{1}{s} - \frac{1}{2}$.*

1. *If the complex function $v \in L^s(\mathbb{R}^2)$, then there exists a unique complex function $u \in L^r(\mathbb{R}^2)$ such that $(\partial_z + ik)u = v$.*

2. *If the complex function $v \in L^r(\mathbb{R}^2)$ and $\bar{\partial}_z v \in L^s(\mathbb{R}^2)$, $k \in \mathbb{C} \setminus \{0\}$, then there exists a unique complex function $u \in W^{1,r}(\mathbb{R}^2)$ such that $(\partial_z + ik)u = v$.*

3. *If the complex function $v \in L^r(\mathbb{R}^2)$ and $\bar{\partial}_z v \in L^s(\mathbb{R}^2)$, $k \in \mathbb{C} \setminus \{0\}$, then there exists a unique complex function $u \in W^{1,r}(\mathbb{R}^2)$ such that $(\bar{\partial}_z - ik)u = v$.*

The following lemma will also be used in the proofs of Theorems 5 and 6.

Lemma 2 ([Von09]). *For ω sufficiently small and γ satisfying (3.1) and (3.2), the following identities hold:*

$$\bar{\partial}_z(\gamma(z)^{-1/2}M_{11}(z,k) - 1) = (\partial_z + ik)(\gamma(z)^{-1/2}M_{21}(z,k)) \tag{5.2}$$

$$\partial_z(\gamma(z)^{-1/2}M_{22}(z,k) - 1) = (\bar{\partial}_z - ik)(\gamma(z)^{-1/2}M_{12}(z,k)). \tag{5.3}$$

Proof. By the product rule,

$$\begin{aligned}\bar{\partial}_{\mathrm{z}}\left(\gamma(z)^{-1/2}M_{11}(z,k)-1\right) &= \bar{\partial}_{\mathrm{z}}\left(\gamma(z)^{-1/2}\right)M_{11}(z,k)+\gamma(z)^{-1/2}\,\bar{\partial}_{\mathrm{z}}(M_{11}(z,k))\\ &= \gamma(z)^{-1/2}Q_{21}(z)M_{11}(z,k)+\gamma(z)^{-1/2}Q_{12}(z)M_{21}(z,k)\\ &= \gamma(z)^{-1/2}(\partial_{\mathrm{z}}+ik)M_{21}(z,k)+\gamma(z)^{-1/2}Q_{12}(z)M_{21}(z,k).\end{aligned}$$

The second equality utilized (3.8) and (3.9) while the third equality uses (3.13)-(3.16), respectively.

We also have

$$\begin{aligned}(\partial_{\mathrm{z}}+ik)\left(\gamma(z)^{-1/2}M_{21}(z,k)\right) &= \partial_{\mathrm{z}}\left(\gamma(z)^{-1/2}M_{21}(z,k)\right)+ik\gamma(z)^{-1/2}M_{21}(z,k)\\ &= \partial_{\mathrm{z}}\left(\gamma(z)^{-1/2}\right)M_{21}(z,k)+\gamma(z)^{-1/2}\,\partial_{\mathrm{z}}(M_{21}(z,k))\\ &\quad +ik\gamma(z)^{-1/2}M_{21}(z,k)\\ &= \gamma(z)^{-1/2}Q_{12}(z)M_{21}(z,k)+\gamma(z)^{-1/2}(\partial_{\mathrm{z}}+ik)M_{21}(z,k).\end{aligned}$$

This establishes (5.2).

Similarly,

$$\begin{aligned}\partial_{\mathrm{z}}\left(\gamma(z)^{-1/2}M_{22}(z,k)-1\right) &= \partial_{\mathrm{z}}\left(\gamma(z)^{-1/2}\right)M_{22}(z,k)+\gamma(z)^{-1/2}\,\partial_{\mathrm{z}}(M_{22}(z,k))\\ &= \gamma(z)^{-1/2}Q_{12}(z)M_{22}(z,k)+\gamma(z)^{-1/2}Q_{21}(z)M_{12}(z,k)\\ &= \gamma(z)^{-1/2}(\bar{\partial}_{\mathrm{z}}-ik)M_{12}(z,k)+\gamma(z)^{-1/2}Q_{21}(z)M_{12}(z,k).\end{aligned}$$

We also have

$$\begin{aligned}(\bar{\partial}_{\mathrm{z}}-ik)\left(\gamma(z)^{-1/2}M_{12}(z,k)\right) &= \bar{\partial}_{\mathrm{z}}\left(\gamma(z)^{-1/2}M_{12}(z,k)\right)-ik\gamma(z)^{-1/2}M_{12}(z,k)\\ &= \bar{\partial}_{\mathrm{z}}\left(\gamma(z)^{-1/2}\right)M_{12}(z,k)+\gamma(z)^{-1/2}\,\bar{\partial}_{\mathrm{z}}(M_{12}(z,k))\\ &\quad -ik\gamma(z)^{-1/2}M_{12}(z,k)\\ &= \gamma(z)^{-1/2}Q_{21}(z)M_{12}(z,k)+\gamma(z)^{-1/2}(\bar{\partial}_{\mathrm{z}}-ik)M_{12}(z,k).\end{aligned}$$

This establishes (5.3). □

Knudsen establishes the existence of exponentially growing solutions to the conductivity equation in the context of the inverse conductivity problem in [Knu02]. The proofs of the existence of CGO solutions for the admittivity equation and their associated boundary integral equations are in the same spirit as [Knu02].

Theorem 5 ([Von09]). *Let $\gamma(z) \in W^{1,p}(\Omega)$, with $p > 2$ such that σ and ϵ satisfy* (3.1) *and* (3.2)*, and let $\gamma(z) - 1$ have compact support in $W^{1,p}(\Omega)$. Then for all $k \in \mathbb{C} \setminus \{0\}$ there exists a unique solution*

$$u_1(z,k) = e^{ikz}\left[\frac{1}{ik} + w_1(z,k)\right], \tag{5.4}$$

to the admittivity equation in $\mathbb{R}^2$ such that $w_1(\cdot,k) \in W^{1,r}(\mathbb{R}^2)$, $2 < r < \infty$. Moreover, the following equalities hold:

$$(\partial_z + ik)\left[e^{-ikz}u_1(z,k) - \frac{1}{ik}\right] = \gamma^{-1/2}(z)M_{11}(z,k) - 1 \tag{5.5}$$

$$\bar{\partial}_z\left[e^{-ikz}u_1(x,k) - \frac{1}{ik}\right] = \gamma^{-1/2}(z)M_{21}(z,k), \tag{5.6}$$

and

$$\left\| e^{-ikz}u_1(x,k) - \frac{1}{ik}\right\|_{W^{1,r}(\mathbb{R}^2)} \leq C\left(1 + \frac{1}{|k|}\right), \tag{5.7}$$

for some constant C.

Theorem 6 ([HHMV12]). *Let $\gamma(z)$ satisfy the hypotheses of Theorem 5. Then for all $k \in \mathbb{C} \setminus \{0\}$ there exists a unique solution*

$$u_2(z,k) = e^{-ik\bar{z}}\left[-\frac{1}{ik} + w_2(z,k)\right], \tag{5.8}$$

to the admittivity equation in $\mathbb{R}^2$ with $w_2(\cdot,k) \in W^{1,r}(\mathbb{R}^2)$, $2 < r < \infty$. Moreover, the following equalities hold:

$$(\bar{\partial}_z - ik)\left[e^{ik\bar{z}}u_2(z,k) + \frac{1}{ik}\right] = \gamma^{-1/2}(z)M_{22}(z,k) - 1 \tag{5.9}$$

$$\partial_z\left[e^{ik\bar{z}}u_2(z,k) + \frac{1}{ik}\right] = \gamma^{-1/2}(z)M_{12}(z,k), \tag{5.10}$$

and

$$\left\| e^{ik\bar{z}}u_2(z,k) + \frac{1}{ik}\right\|_{W^{1,r}(\mathbb{R}^2)} \leq C\left(1 + \frac{1}{|k|}\right), \tag{5.11}$$

for some constant C.

We will prove Theorem 5; the proof of Theorem 6 is analogous.

Proof. Assume u is a solution of the admittivity equation of the form (5.4), and let $(v,w)^T = \gamma^{1/2}(\partial_z u, \bar{\partial}_z u)^T$ be the corresponding solution to $(D - Q_\gamma)\Psi = 0$. Define the complex

function v via $v(z,k) = \gamma(z)^{-1/2}M_{11}(z,k) - 1$. We will first show there exists a unique complex function $w_1 \in W^{1,r}(\mathbb{R}^2)$, where $r > 2$ such that $(\partial_z + ik)w_1 = v$, for $k \in \mathbb{C} \setminus \{0\}$. Let us rewrite v as follows:

$$v(z,k) = \gamma(z)^{-1/2}\Big[M_{11}(z,k) - 1\Big] + \Big[\gamma(z)^{-1/2} - 1\Big].$$

Let $r > 2$ and $1 < s < 2$ with $\frac{1}{r} = \frac{1}{s} - \frac{1}{2}$. We know by Theorem 4.1 of [Fra00] that there exists a constant $C > 0$ depending on β, σ_0 and p such that $\sup \|M_{11}(z,k) - 1\|_{L^r(\mathbb{R}^2)} \leq C$ for every $r > 2$, and that $\gamma(z)^{-1/2} - 1$ has compact support in $W^{1,r}(\mathbb{R}^2)$. It follows that $v \in L^r(\mathbb{R}^2)$, and by Minkowski's Inequality

$$\|v(z,k)\|_{L^r} = \Big\|\gamma(z)^{-1/2}\Big[M_{11}(z,k) - 1\Big] + \Big[\gamma(z)^{-1/2} - 1\Big]\Big\|_{L^r} \leq C_{r,\gamma},$$

where $C_{r,\gamma}$ depends on r and the bounds on σ and ϵ.

From (3.8) and (3.9),

$$\begin{aligned}
\bar{\partial}_z\, v(z) &= \bar{\partial}_z(\gamma(z)^{-1/2}M_{11}(z,k) - 1) \\
&= (\bar{\partial}_z\, \gamma(z)^{-1/2})M_{11}(z,k) + \gamma(z)^{-1/2}(\bar{\partial}_z\, M_{11}(z,k)) \\
&= \gamma(z)^{-1/2}Q_{21}(z)M_{11}(z,k) + \gamma(z)^{-1/2}Q_{12}(z)M_{21}(z,k) \\
&= \gamma(z)^{-1/2}Q_{21}(z)[M_{11}(z,k) - 1] \\
&\quad + \gamma(z)^{-1/2}Q_{12}(z)M_{21}(z,k) + \gamma(z)^{-1/2}Q_{21}(z)
\end{aligned}$$

We know that $\gamma(z)^{-1/2}Q_{21}(z) \in L^\alpha(\mathbb{R}^2)$ with $1 \leq \alpha \leq p$ since $Q_{12}(z)$ has compact support. It follows that $\gamma(z)^{-1/2}Q_{21}(z) \in L^s(\mathbb{R}^2) \cap L^2(\mathbb{R}^2)$. By the generalized Hölder's inequality and the fact that $\|M_{11}(z,k) - 1\|_{L^s}$ is bounded with $\frac{1}{s} = \frac{1}{r} + \frac{1}{2}$, we have $\bar{\partial}_z\, v(z) \in L^s(\mathbb{R}^2)$ and $\left\|\bar{\partial}_z\, v\right\|_{L^s(\mathbb{R}^2)} \leq K_{r,\gamma}$, where $K_{r,\gamma}$ depends only on r and the bounds on σ and ϵ. Thus, by Lemma 1 (2), there exists a unique solution $w_1(z,k) \in W^{1,r}(\mathbb{R}^2)$ such that

$$(\partial_z + ik)w_1(z,k) = \gamma(z)^{-1/2}M_{11}(z,k) - 1. \tag{5.12}$$

We have by (5.2),

$$\bar{\partial}(\gamma(z)^{-1/2}M_{11}(z,k) - 1) = (\partial_z + ik)\left(\gamma(z)^{-1/2}M_{21}(z,k)\right). \tag{5.13}$$

Taking $\bar{\partial}_z$ of both sides of (5.12) and using (5.13),

$$\begin{aligned}
\bar{\partial}_z\,(\partial_z + ik)\, w_1(z,k) &= \bar{\partial}_z\left(\gamma(z)^{-1/2}M_{11}(z,k) - 1\right) \\
&= (\partial_z + ik)\left(\gamma(z)^{-1/2}M_{21}(z,k)\right).
\end{aligned} \tag{5.14}$$

Using the fact $\bar{\partial}(\partial + ik) = (\partial + ik)\bar{\partial}$, it follows that

$$(\partial_z + ik)\left(\bar{\partial}_z\, w_1(z,k) - \gamma(z)^{-1/2} M_{21}(z,k)\right) = 0. \tag{5.15}$$

Since $\bar{\partial}_z\, w_1(z,k) - \gamma(z)^{-1/2} M_{21}(z,k) \in L^r(\mathbb{R}^2)$, by Lemma 1 (1), we must have

$$\bar{\partial}_z\, w_1(z,k) = \gamma(z)^{-1/2} M_{21}(z,k). \tag{5.16}$$

We now define

$$u_1(z,k) = e^{ikz}\left[w_1(z,k) + \frac{1}{ik}\right], \tag{5.17}$$

then by (5.12)

$$(\partial_z + ik)\left(e^{-ikz}u_1(z,k) - \frac{1}{ik}\right) = (\partial_z + ik)\, w_1(z,k) = \gamma^{-1/2}(z) M_{11}(z,k) - 1,$$

which proves (5.5), and by (5.16)

$$\bar{\partial}_z\left(e^{-ikz}u_1(z,k) - \frac{1}{ik}\right) = \bar{\partial}_z\, w_1(z,k) = \gamma^{-1/2}(z) M_{21}(z,k),$$

which proves (5.6).

The norm estimate given by (5.7) follows by Minkowski's Inequality, the constant C depends on r, the bound on $\gamma - 1$, and the bounds on σ and ϵ. □

Remark: Note that from (5.5)

$$\begin{aligned} \gamma^{-1/2} M_{11}(z,k) - 1 &= (\partial_z + ik)\left(e^{-ikz}u_1(z,k) - \frac{1}{ik}\right) \\ &= \partial_z(e^{-ikz}u_1) + ike^{-ikz}u_1(z,k) - 1 \\ &= e^{-ikz}\,\partial_z\, u_1(z,k) - 1, \end{aligned} \tag{5.18}$$

and from (5.6)

$$\begin{aligned} \gamma^{-1/2} M_{21}(z,k) &= \bar{\partial}_z\left(e^{-ikz}u_1(z,k) - \frac{1}{ik}\right) \\ &= u_1(z,k)\,\bar{\partial}_z\left(e^{-ikz}\right) + e^{-ikz}\,\bar{\partial}_z\, u_1(z,k) \\ &= e^{-ikz}\,\bar{\partial}_z\, u_1(z,k). \end{aligned} \tag{5.19}$$

Thus, we can equivalently rewrite (5.5) and (5.6), respectively, as

$$\gamma^{1/2}(z)\,\partial_z\, u_1(z,k) = e^{ikz} M_{11}(z,k) = \Psi_{11}(z,k) \tag{5.20}$$

$$\gamma^{1/2}(z)\,\bar{\partial}_z\, u_1(z,k) = e^{ikz} M_{21}(z,k) = \Psi_{21}(z,k). \tag{5.21}$$

In a similar manner, we can rewrite (5.9) and (5.10), respectively, as

$$\gamma^{1/2}(z)\,\bar{\partial}_z\, u_2(z,k) = e^{-ik\bar{z}} M_{22}(z,k) = \Psi_{22}(z,k) \tag{5.22}$$

$$\gamma^{1/2}(z)\,\partial_z\, u_2(z,k) = e^{-ik\bar{z}} M_{12}(z,k) = \Psi_{12}(z,k). \tag{5.23}$$

Useful boundary integral equations for the traces of u_1 and u_2 can be derived under the additional assumption that $\gamma \in W^{2,p}$ and $u_1, u_2 \in W^{2,p}$, $p > 1$. The following proposition shows a relationship between the exponentially growing solutions $\psi_S(z,k)$ (when they exist) to the Schrödinger equation

$$(-\Delta + q_S(z))\psi_S(z,k) = 0, \tag{5.24}$$

and the CGO solutions u_1 and u_2 to (3.3). The solution ψ_S to (5.24), where q_S is complex, is asymptotic to e^{ikz} in the sense that

$$w_S \equiv e^{-ikz}\psi_S(\cdot,k) - 1 \in L^{\tilde{p}} \cap L^\infty,$$

where $\frac{1}{\tilde{p}} = \frac{1}{p} - \frac{1}{2}$ and $1 < p < 2$. The question of the existence of a unique solution to (5.24) is addressed for real γ in [Nac96], where it is shown to exist if and (roughly) only if $q_S = \frac{\Delta\gamma^{1/2}}{\gamma^{1/2}}$. The solutions ψ_S will be used to derive the boundary integral equations for u_1 and u_2, but not in the direct reconstruction algorithm.

Lemma 3 ([Von09])**.** *Let $\gamma(z) = \sigma(z) + \mathrm{i}\,\omega\epsilon(z) \in W^{2,p}(\Omega)$, with $p > 2$ such that σ and ϵ satisfy* (3.1) *and* (3.2)*, and let $\gamma(z) - 1$ have compact support in $W^{1,p}(\Omega)$. Let u_1 be the exponentially growing solution to the admittivity equation as given in Theorem 5, and let ψ_S be the exponentially growing solution to the Schrödinger equation* (5.24)*, when it exists. Then*

$$iku_1(z,k) = \gamma^{-1/2}(z)\psi_S(z,k). \tag{5.25}$$

Proof. Note that

$$\begin{aligned} iku_1(z,k) &= e^{ikz}(1 + ikw_1(z,k)) \\ &= e^{ikz}\gamma(z)^{-1/2}\left[\gamma(z)^{1/2} + \gamma(z)^{1/2} ikw_1(z,k)\right] \\ &= e^{ikz}\gamma(z)^{-1/2}\left(1 + \left[\gamma(z)^{1/2} - 1\right] + \gamma(z)^{1/2} ikw_1(z,k)\right), \end{aligned} \tag{5.26}$$

satisfies the admittivity equation with $\gamma(z)^{1/2} - 1 + \gamma(z)^{1/2} ikw_1(z,k) \in W^{1,r}(\Omega)$ for $r > 2$. We also know that when it exists

$$\gamma^{-1/2}(z)\psi_S(z,k) = e^{ikz}\gamma^{-1/2}(z)(1 + w_S(z,k)) \tag{5.27}$$

is also a solution to the admittivity equation with $w_S(z,k) \in W^{1,\bar{p}}(\mathbb{R}^2)$. Hence, these exponentially growing solutions must be equal completing the proof. □

Lemma 4 ([HHMV12]). *Let $\gamma(z) = \sigma(z) + i\omega\epsilon(z) \in W^{2,p}(\Omega)$, with $p > 2$ such that σ and ϵ satisfy* (3.1) *and* (3.2)*, and let $\gamma(z) - 1$ have compact support in $W^{1,p}(\Omega)$. Let u_2 be the exponentially growing solution to the admittivity equation as given in Theorem 6, and let ψ_S be the exponentially growing solution to the Schrödinger equation* (5.24)*, when it exists. Then*

$$-iku_2(z,k) = \gamma^{-1/2}(-\bar{z})\psi_S(-\bar{z},k). \tag{5.28}$$

Proof. From (5.8),

$$\begin{aligned} -iku_2(z,k) &= e^{-ik\bar{z}}(1 - ikw_2(z,k)) \\ &= e^{-ik\bar{z}}\gamma^{-1/2}(-\bar{z})\left(1 + \left[\gamma^{1/2}(-\bar{z}) - 1\right] - \gamma^{1/2}(-\bar{z})ikw_2(z,k)\right) \end{aligned}$$

satisfies the admittivity equation with $[\gamma^{1/2}(-\bar{z}) - 1] - \gamma^{1/2}(-\bar{z})ikw_2(z,k) \in W^{1,r}(\Omega)$ for $r > 2$. From (5.27),

$$\gamma^{1/2}(-\bar{z})\psi_S(-\bar{z},k) = e^{-ik\bar{z}}\gamma^{1/2}(-\bar{z})(1 + w_S(-\bar{z},k))$$

satisfies the admittivity equation with $w_S(-\bar{z},k) \in W^{1,\bar{p}}(\mathbb{R}^2)$. Thus, these exponentially growing solutions must be equal, and so

$$-iku_2(z,k) = \gamma^{-1/2}(-\bar{z})\psi_S(-\bar{z},k)$$

completing the proof. □

Let us recall some terminology arising from [Nac96] before establishing boundary integral equations involving the exponentially growing solutions. Let Λ_σ be the Dirichlet-to-Neumann map when Ω contains the conductivity distribution σ, and Λ_1 the Dirichlet-to-Neumann map for a homogeneous conductivity equal to 1. The Faddeev Green's function $G_k(z)$ is defined by

$$G_k(z) := e^{ikz}g_k(z), \quad -\Delta G_k = \delta, \tag{5.29}$$

where

$$g_k(z) := \frac{1}{(2\pi)^2}\int_{\mathbb{R}^2}\frac{e^{iz\cdot\xi}}{\xi(\bar{\xi}+2k)}d\xi, \quad (-\Delta - 4ik\,\bar{\partial}_z)g_k = \delta, \tag{5.30}$$

for $k \in \mathbb{C}\setminus\{0\}$. In the real-valued case $\gamma = \sigma$, the trace of the function $\psi_S(\cdot,k)$ on Ω satisfies the integral equation [Nac96]

$$\psi_S(z,k) = e^{ikz} - \int_{\partial\Omega} G_k(z-\zeta)(\Lambda_\sigma - \Lambda_1)\psi_S(\zeta,k)dS(\zeta), \quad z\in\partial\Omega, \tag{5.31}$$

where $k \in \mathbb{C}\setminus\{0\}$. The equation (5.31) is a Fredholm equation of the second kind and uniquely solvable in $H^{1/2}(\partial\Omega)$ for any $k\in\mathbb{C}\setminus\{0\}$.

The boundary integral equations for u_1 and u_2 are similar to (5.31).

Theorem 7 ([Von09])**.** *Let $\gamma \in W^{2,p}(\Omega)$ for $p>1$ and suppose $\gamma = 1$ in a neighborhood of $\partial\Omega$. Suppose σ and ϵ satisfy* (3.1) *and* (3.2)*, and let $\gamma(z)-1$ have compact support in $W^{2,p}(\Omega)$. Then for any non-exceptional $k\in\mathbb{C}\setminus\{0\}$, the trace of the exponentially growing solution $u_1(\cdot,k)$ on $\partial\Omega$ is the unique solution to*

$$u_1(z,k) = \frac{e^{ikz}}{ik} - \int_{\partial\Omega} G_k(z-\zeta)(\Lambda_\gamma - \Lambda_1)u_1(\zeta,k)dS(\zeta), \quad z\in\partial\Omega. \tag{5.32}$$

Proof. Let $\frac{1}{p} = \frac{1}{r} - \frac{1}{2}$, where $1<r<2$ and $p>2$. Let $\{\gamma_n\}_{n\in\mathbf{N}} \subset W^{2,r}(\Omega)$ be a sequence converging to $\gamma\in W^{1,p}(\Omega)$. Then by the Sobolev Embedding Theorem, $\{\gamma_n\}_{n\in\mathbb{N}}\subset W^{1,r}(\Omega)$. Let ψ_n be the exponentially growing solutions to the Schrödinger equation with potential $\gamma_n^{-1/2}\Delta\gamma_n^{1/2}$, and u^n be the CGO solutions defined by Theorem 5 to the admittivity equation with admittivity γ_n. Then for each $n\in\mathbb{N}$, the complex γ version of (5.31) holds for non-exceptional $k\in\mathbb{C}\setminus\{0\}$

$$\psi_n(z,k)|_{\partial\Omega} = e^{ikz}|_{\partial\Omega} - \int_{\partial\Omega} G_k(z-\zeta)(\Lambda_{\gamma_n} - \Lambda_1)\psi_n(\zeta,k)dS(\zeta), \tag{5.33}$$

where $\gamma_n = 1$ in the neighborhood of $\partial\Omega$.

It follows by (5.25) that for each complex number $k\neq 0$, and for each $n\in\mathbb{N}$

$$\frac{{\gamma_n}^{-1/2}(z)}{ik}\psi_n(z,k) = u^n(z,k) \to u_1(z,k) \quad \text{in} \quad H^{1/2}(\partial\Omega). \tag{5.34}$$

We claim that for each n, u^n satisfies (5.32). To see this, by (5.25), for $z \in \partial\Omega$,

$$\begin{aligned}
\frac{e^{ikz}}{ik} &- \int_{\partial\Omega} G_k(z-\zeta)(\Lambda_\gamma - \Lambda_1)u^n(\zeta,k)dS(\zeta) \\
&= \frac{e^{ikz}}{ik} - \int_{\partial\Omega} G_k(z-\zeta)(\Lambda_\gamma - \Lambda_1)\frac{{\gamma_n}^{-1/2}(\zeta)}{ik}\psi_n(\zeta,k)dS(\zeta) \\
&= \frac{{\gamma_n}^{-1/2}(z)}{ik}\psi_n(z,k) \\
&= u^n(z,k), \qquad (5.35)
\end{aligned}$$

where we used the fact that $\gamma_n = 1$ in a neighborhood of $\partial\Omega$. Thus, u^n satisfies (5.32) for each $n \in \mathbb{N}$.

We know by Theorem 3.1 of [Fra00] that $M(z,k)$ depends continuously on γ. From (5.34), we can conclude that

$$\int_{\partial\Omega} G_k(z-\zeta)(\Lambda_{\gamma_n} - \Lambda_1)u^n(\zeta,k)dS(\zeta) \mapsto \int_{\partial\Omega} G_k(z-\zeta)(\Lambda_\gamma - \Lambda_1)u_1(\zeta,k)dS(\zeta). \qquad (5.36)$$

Thus, by (5.34), (5.35), and (5.36), we have that $u_1(\cdot,k)|_{\partial\Omega}$ satisfies (5.32). The uniqueness of $u_1(\cdot,k)|_{\partial\Omega}$ follows by Theorem 5. □

An analogous theorem holds for u_2.

Theorem 8 ([HHMV12])**.** *Let $\gamma \in W^{2,p}(\Omega)$ for $p > 1$ and suppose $\gamma = 1$ in a neighborhood of $\partial\Omega$. Suppose σ and ϵ satisfy* (3.1) *and* (3.2)*, and let $\gamma(z) - 1$ have compact support in $W^{2,p}(\Omega)$. Then for any nonexceptional $k \in \mathbb{C} \setminus \{0\}$, the trace of the exponentially growing solution $u_2(\cdot,k)$ on $\partial\Omega$ is the unique solution to*

$$u_2(z,k) = \frac{e^{-ik\bar{z}}}{-ik} - \int_{\partial\Omega} G_k(-\bar{z}+\bar{\zeta})(\Lambda_\gamma - \Lambda_1)u_2(\zeta,k)dS(\zeta), \quad z \in \partial\Omega. \qquad (5.37)$$

Proof. Let p, r, $\{\gamma_n\}_{n\in\mathbf{N}} \subset W^{2,r}(\Omega)$, and ψ_n be as in the proof of Theorem 7. Let u^n be the CGO solutions defined in Theorem 6 to the admittivity equation with admittivity γ_n. Then for each $n \in \mathbb{N}$, for nonexceptional $k \in \mathbb{C} \setminus \{0\}$, evaluating (5.33) at $-\bar{z}$,

$$\psi_n(-\bar{z},k)|_{\partial\Omega} = e^{-ik\bar{z}}|_{\partial\Omega} - \int_{\partial\Omega} G_k(-\bar{z}-\zeta)(\Lambda_{\gamma_n} - \Lambda_1)\psi_n(\zeta,k)dS(\zeta), \qquad (5.38)$$

where $\gamma_n = 1$ in a neighborhood of $\partial\Omega$.

It follows by (5.28) that for each complex number $k \neq 0$, and for each $n \in \mathbb{N}$

$$\frac{{\gamma_n}^{-1/2}(-\bar{z})}{-ik}\psi_n(-\bar{z},k) = u^n(z,k) \to u_2(z,k) \quad \text{in} \quad H^{1/2}(\partial\Omega). \qquad (5.39)$$

We claim that for each n, u^n satisfies (5.37). To see this, by (5.28), for $z \in \partial\Omega$,

$$\begin{aligned}
\frac{e^{-ik\bar{z}}}{-ik} &- \int_{\partial\Omega} G_k(-\bar{z}+\overline{\zeta})(\Lambda_\gamma - \Lambda_1)u^n(\zeta,k)dS(\zeta) \\
&= \frac{e^{-ik\bar{z}}}{-ik} - \int_{\partial\Omega} G_k(-\bar{z}+\overline{\zeta})(\Lambda_\gamma - \Lambda_1)\frac{\gamma_n^{-1/2}(-\overline{\zeta})}{-ik}\psi_n(-\overline{\zeta},k)dS(\zeta) \\
&= \frac{e^{-ik\bar{z}}}{-ik} - \int_{\partial\Omega} G_k(-\bar{z}-\xi)(\Lambda_\gamma - \Lambda_1)\frac{\gamma_n^{-1/2}(\xi)}{-ik}\psi_n(\xi,k)dS(\xi) \\
&= \frac{\gamma_n^{-1/2}(-\bar{z})}{-ik}\psi_n(-\bar{z},k) \\
&= u^n(z,k), \qquad (5.40)
\end{aligned}$$

using the change of variables $-\bar{\zeta} \mapsto \xi$ and the fact that $\gamma_n = 1$ in a neighborhood of $\partial\Omega$. Thus, u^n satisfies (5.37) for each $n \in \mathbb{N}$.

We know by Theorem 3.1 of [Fra00] that $M(z,k)$ depends continuously on γ. From (5.39), we can conclude that

$$\int_{\partial\Omega} G_k(-\bar{z}+\bar{\zeta})(\Lambda_{\gamma_n} - \Lambda_1)u^n(\zeta,k)dS(\zeta) \mapsto \int_{\partial\Omega} G_k(-\bar{z}+\bar{\zeta})(\Lambda_\gamma - \Lambda_1)u_2(\zeta,k)dS(\zeta). \quad (5.41)$$

Thus, by (5.39), (5.40), and (5.41), we have that $u_2(\cdot,k)|_{\partial\Omega}$ satisfies (5.37). The uniqueness of $u_2(\cdot,k)|_{\partial\Omega}$ follows by Theorem 6. □

5.1.2 Determination of the CGO Solutions Ψ_{12} and Ψ_{21} for $z \in \partial\Omega$

Now that we have general formulas for determining $u_1(z,k)$ and $u_2(z,k)$ for $k \in \mathbb{C}\backslash 0$, we can use those formulas to derive the following theorem to determine the traces of the exponentially growing solutions $\Psi(z,k)$ needed for the evaluation of the scattering transform $S(k)$. We use the definition of the scattering transform from [Fra00],

$$S(k) = \frac{\mathrm{i}}{\pi}\int_{\mathbb{R}^2} \begin{pmatrix} e(\xi,-\bar{k}) & 0 \\ 0 & -e(\xi,k) \end{pmatrix} \begin{pmatrix} 0 & Q_{12}(\xi)M_{22}(\xi,k) \\ Q_{21}(\xi)M_{11}(\xi,k) & 0 \end{pmatrix} d\mu(\xi)$$

so that

$$S(k) = \begin{pmatrix} 0 & S_{12}(k) \\ S_{21}(k) & 0 \end{pmatrix}, \qquad (5.42)$$

where, due to the compact support of Q,

$$S_{12}(k) = \frac{\mathrm{i}}{\pi}\int_\Omega e(\xi,-\bar{k})Q_{12}(\xi)M_{22}(\xi,k)\, d\mu(\xi) \qquad (5.43)$$

$$S_{21}(k) = -\frac{\mathrm{i}}{\pi}\int_\Omega e(\xi,k)Q_{21}(\xi)M_{11}(\xi,k)\, d\mu(\xi). \qquad (5.44)$$

We will use the relations given in (3.14) and (3.15),

$$\begin{aligned}(\bar\partial_\xi - \mathrm{i}\,k)M_{12}(\xi,k) &= Q_{12}(\xi)M_{22}(\xi,k)\\ (\partial_\xi + \mathrm{i}\,k)M_{21}(\xi,k) &= Q_{21}(\xi)M_{11}(\xi,k)\end{aligned}$$

and integration by parts for the ∂ and $\bar\partial$ operators,

$$\int_\Omega u\,\bar\partial\, w\; dx\; dy = \frac{1}{2}\int_{\partial\,\Omega} wu(\nu_1 + \mathrm{i}\,\nu_2)dS - \int_\Omega w\,\bar\partial\, u\; dx\; dy, \tag{5.45}$$

$$\int_\Omega u\,\partial\, w\; dx\; dy = \frac{1}{2}\int_{\partial\,\Omega} wu(\nu_1 - \mathrm{i}\,\nu_2)dS - \int_\Omega w\,\bar\partial\, u\; dx\; dy. \tag{5.46}$$

Let us look at S_{12} first,

$$\begin{aligned}S_{12}(k) &= \frac{\mathrm{i}}{\pi}\int_\Omega e(\xi,-\bar k)Q_{12}(\xi)M_{22}(\xi,k)\; d\mu(\xi)\\ &= \frac{\mathrm{i}}{\pi}\int_\Omega e(\xi,-\bar k)(\bar\partial_\xi - \mathrm{i}\,k)M_{12}(\xi,k)\; d\mu(\xi)\\ &= \frac{\mathrm{i}}{2\pi}\int_{\partial\,\Omega} e(\xi,-\bar k)M_{12}(\xi,k)\nu(\xi)\; dS(\xi) - \frac{\mathrm{i}}{\pi}\int_\Omega M_{12}(\xi,k)\,\bar\partial_\xi\, e(\xi,-\bar k)\; d\mu(\xi)\\ &\qquad + \frac{\mathrm{i}}{\pi}\int_\Omega (-\mathrm{i}\,k)e(\xi,-\bar k)M_{12}(\xi,k)\; d\mu(\xi)\\ &= \frac{\mathrm{i}}{2\pi}\int_{\partial\,\Omega} e(\xi,-\bar k)M_{12}(\xi,k)\nu(\xi)\; dS(\xi) - \frac{\mathrm{i}}{\pi}\int_\Omega M_{12}(\xi,k)(-\mathrm{i}\,k)e(\xi,-\bar k)\; d\mu(\xi)\\ &\qquad + \frac{\mathrm{i}}{\pi}\int_\Omega (-\mathrm{i}\,k)e(\xi,-\bar k)M_{12}(\xi,k)\; d\mu(\xi)\\ &= \frac{\mathrm{i}}{2\pi}\int_{\partial\,\Omega} e(\xi,-\bar k)M_{12}(\xi,k)\nu(\xi)\; dS(\xi).\end{aligned} \tag{5.47}$$

Similarly,

$$\begin{aligned}S_{21}(k) &= -\frac{\mathrm{i}}{\pi}\int_\Omega e(\xi,k)Q_{21}(\xi)M_{11}(\xi,k)\; d\mu(\xi)\\ &= -\frac{\mathrm{i}}{\pi}\int_\Omega e(\xi,k)(\partial_\xi + \mathrm{i}\,k)M_{21}(\xi,k)\; d\mu(\xi)\\ &= -\frac{\mathrm{i}}{2\pi}\int_{\partial\,\Omega} e(\xi,k)M_{21}(\xi,k)\overline{\nu(\xi)}\; dS(\xi) + \frac{\mathrm{i}}{\pi}\int_\Omega M_{21}(\xi,k)\,\partial_\xi\, e(\xi,k)\; d\mu(\xi)\\ &\qquad - \frac{\mathrm{i}}{\pi}\int_\Omega (\mathrm{i}\,k)e(\xi,k)M_{21}(\xi,k)\; d\mu(\xi)\\ &= -\frac{\mathrm{i}}{2\pi}\int_{\partial\,\Omega} e(\xi,k)M_{21}(\xi,k)\overline{\nu(\xi)}\; dS(\xi) + \frac{\mathrm{i}}{\pi}\int_\Omega (\mathrm{i}\,k)M_{21}(\xi,k)e(\xi,k)\; d\mu(\xi)\\ &\qquad - \frac{\mathrm{i}}{\pi}\int_\Omega (\mathrm{i}\,k)e(\xi,k)M_{21}(\xi,k)\; d\mu(\xi)\\ &= -\frac{\mathrm{i}}{2\pi}\int_{\partial\,\Omega} e(\xi,k)M_{21}(\xi,k)\overline{\nu(\xi)}\; dS(\xi).\end{aligned} \tag{5.48}$$

Using the definition of CGO solution Ψ this is equivalent to

$$S_{12}(k) = \frac{\mathrm{i}}{2\pi}\int_{\partial\,\Omega} e^{-\,\mathrm{i}\,\xi\bar{k}}\Psi_{12}(\xi,k)\nu(\xi)\,dS(\xi) \tag{5.49}$$

$$S_{21}(k) = -\frac{\mathrm{i}}{2\pi}\int_{\partial\,\Omega} e^{\mathrm{i}\,\xi\bar{k}}\Psi_{21}(\xi,k)\bar{\nu}(\xi)\,dS(\xi). \tag{5.50}$$

Therefore, we only need the traces of $\Psi_{12}(z,k)$ and $\Psi_{21}(z,k)$ to evaluate the scattering transforms $S_{12}(k)$ and $S_{21}(k)$.

Theorem 9. *The traces of the exponentially growing solutions $\Psi_{12}(z,k)$ and $\Psi_{21}(z,k)$ for $k \in \mathbb{C}\setminus 0$ can be determined by*

$$\Psi_{12}(z,k) = \int_{\partial\Omega} \frac{e^{\mathrm{i}\,\bar{k}(z-\zeta)}}{4\pi(z-\zeta)}\delta\Lambda(\zeta)u_2(\zeta,k)\,dS(\zeta) \tag{5.51}$$

$$\Psi_{21}(z,k) = \int_{\partial\Omega} \overline{\left[\frac{e^{\mathrm{i}\,k(z-\zeta)}}{4\pi(z-\zeta)}\right]}\delta\Lambda(\zeta)u_1(\zeta,k)\,dS(\zeta), \tag{5.52}$$

where $\delta\Lambda = \Lambda_\gamma - \Lambda_1$, and u_1 and u_2 are calculated via Equations (5.32) *and* (5.37) *respectively.*

Proof. We use the relations in (5.1) to obtain boundary integral equations for Ψ_{12} and Ψ_{21} for $z \in \partial\Omega$ from Equations (5.32) and (5.37). Let us begin with Ψ_{12}:

$$\begin{aligned}
\Psi_{12}(z,k) &= \gamma^{1/2}(z)\,\partial_{\mathrm{z}}\,u_2(z,k) \\
&= \gamma^{1/2}(z)\,\partial_{\mathrm{z}}\left[\frac{e^{-ik\bar{z}}}{-ik} - \int_{\partial\Omega} G_k(-\bar{z}+\bar{\zeta})\delta\Lambda(\zeta)u_2(\zeta,k)\,dS(\zeta)\right] \\
&= -\gamma^{1/2}(z)\int_{\partial\Omega}\partial_{\mathrm{z}}\left[G_k(-\bar{z}+\bar{\zeta})\right]\delta\Lambda(\zeta)u_2(\zeta,k)\,dS(\zeta).
\end{aligned} \tag{5.53}$$

Similarly,

$$\begin{aligned}
\Psi_{21}(z,k) &= \gamma^{1/2}(z)\,\bar{\partial}_{\mathrm{z}}\,u_1(z,k) \\
&= \gamma^{1/2}(z)\,\bar{\partial}_{\mathrm{z}}\left[\frac{e^{\mathrm{i}\,kz}}{ik} - \int_{\partial\Omega} G_k(z-\zeta)\delta\Lambda(\zeta)u_1(\zeta,k)\,dS(\zeta)\right] \\
&= -\gamma^{1/2}(z)\int_{\partial\Omega}\bar{\partial}_{\mathrm{z}}\left[G_k(z-\zeta)\right]\delta\Lambda(\zeta)u_1(\zeta,k)\,dS(\zeta).
\end{aligned} \tag{5.54}$$

A thorough study of the properties of the Faddeev Green's function G_k and its derivatives is given in [Sil99]. The calculations for the specific derivatives needed here are shown below. By the definition of G_k (5.29)

$$\partial_{\mathrm{z}}\,G_k(-\bar{z}+\bar{\zeta}) = \partial_{\mathrm{z}}\left[e^{ik(-\bar{z}+\bar{\zeta})}g_k(-\bar{z}+\bar{\zeta})\right] = e^{ik(-\bar{z}+\bar{\zeta})}\,\partial_{\mathrm{z}}\,g_k(-\bar{z}+\bar{\zeta}). \tag{5.55}$$

Using the definition of g_k (5.30),

$$\begin{aligned}
\partial_{\mathrm{z}}\, g_k(-\bar{z}+\bar{\zeta}) &= \partial_{\mathrm{z}}\, \frac{1}{(2\pi)^2}\int_{\mathbb{R}^2} \frac{e^{i(-\bar{z}+\bar{\zeta})\cdot\xi}}{\xi(\bar{\xi}+2k)}\, d\xi \\
&= \frac{1}{(2\pi)^2}\int_{\mathbb{R}^2} \frac{\partial_{\mathrm{z}}\left[e^{-(i/2)(\bar{z}\bar{\xi}+z\xi)}\right] e^{i\bar{\zeta}\cdot\xi}}{\xi(\bar{\xi}+2k)}\, d\xi \\
&= \frac{1}{(2\pi)^2}\int_{\mathbb{R}^2} \frac{-(i\xi/2)\, e^{i(-\bar{z}+\bar{\zeta})\cdot\xi}}{\xi(\bar{\xi}+2k)}\, d\xi \\
&= \frac{e^{i(-\bar{z}+\bar{\zeta})\cdot(-2\bar{k})}}{4}\frac{1}{(2\pi)^2}\int_{\mathbb{R}^2} \frac{2e^{i(-\bar{z}+\bar{\zeta})\cdot(\xi+2\bar{k})}}{i\left(\overline{\xi+2\bar{k}}\right)}\, d\xi \\
&= \frac{e^{i(-\bar{z}+\bar{\zeta})\cdot(-2\bar{k})}}{4\pi\left(\overline{-\bar{z}+\bar{\zeta}}\right)} \\
&= -\frac{e^{-ik(-\bar{z}+\bar{\zeta})}e^{-i\bar{k}(-z+\zeta)}}{4\pi(z-\zeta)}, \qquad (5.56)
\end{aligned}$$

by the definition of the inverse Fourier transform and the well known result

$$\mathcal{F}^{-1}\left\{\frac{2}{i\bar{\xi}}\right\}^{\wedge}(z) = \frac{1}{\pi\bar{z}}.$$

Therefore, by (5.55) and (5.56)

$$\partial_{\mathrm{z}}\, G_k(-\bar{z}+\bar{\zeta}) = -\frac{e^{i\bar{k}(z-\zeta)}}{4\pi(z-\zeta)}. \qquad (5.57)$$

The $\bar{\partial}_{\mathrm{z}}$ derivative for Ψ_{21} is calculated in a similar manner,

$$\bar{\partial}_{\mathrm{z}}\, G_k(z-\zeta) = -\overline{\left[\frac{e^{ik(z-\zeta)}}{4\pi(z-\zeta)}\right]}. \qquad (5.58)$$

Substituting the representations for $\partial_{\mathrm{z}}\, G_k(-\bar{z}+\bar{\zeta})$ and $\bar{\partial}_{\mathrm{z}}\, G_k(z-\zeta)$, given in (5.57) and (5.58), back into the equations for Ψ_{12} and Ψ_{21}, given in (5.53) and (5.54) respectively, proves the theorem. □

5.2 Step 4: Recovery of the matrix potential $Q(z)$ from the CGOs $M(z,k)$

After solving the $\bar{\partial}_k$ equation for $M(z,k)$ (3.21), we still need a way to recover the admittivity distribution $\gamma(z)$. Theorem 10 provides a direct relation between the CGO solutions $M(z,0)$ and the matrix potential $Q(z)$. This is the theorem that replaces the large k limit required in Francini's formula (3.23).

Theorem 10. *The entries of the potential matrix $Q(z)$ defined in* (3.6) *can be calculated using only knowledge of the CGO solution $M(z,0)$ via*

$$Q_{12}(z) = \frac{\bar{\partial}_{\mathrm{z}} M_+(Q,z,0)}{M_-(Q,z,0)} \tag{5.59}$$

$$Q_{21}(z) = \frac{\partial_{\mathrm{z}} M_-(Q,z,0)}{M_+(Q,z,0)}. \tag{5.60}$$

where,

$$M_+(Q,z,k) = M_{11}(Q,z,k) + e(z,-k)M_{12}(Q,z,k) \tag{5.61}$$

$$M_-(Q,z,k) = M_{22}(Q,z,k) + e(z,k)M_{21}(Q,z,k). \tag{5.62}$$

Proof. We follow an idea similar to that in [BBR01] and define

$$\begin{aligned} M_+(Q,z,k) &= M_{11}(Q,z,k) + e(z,-k)M_{12}(Q,z,k) \\ M_-(Q,z,k) &= M_{22}(Q,z,k) + e(z,k)M_{21}(Q,z,k). \end{aligned}$$

I use the notation $M_+(Q,z,k)$ and $M_-(Q,z,k)$ to illustrate that M_+ and M_- are only dependent on the Q matrix, not $-Q^T$ as is required in [BBR01]. Therefore,

$$\bar{\partial}_{\mathrm{z}} M_+(Q,z,k) = Q_{12}(z)e(z,-k)\left[M_-(Q,z,k) + \mathrm{i}(k-\bar{k})M_{12}(Q,z,k)\right] \tag{5.63}$$

$$\partial_{\mathrm{z}} M_-(Q,z,k) = Q_{21}(z)e(z,k)M_+(Q,z,k), \tag{5.64}$$

so that

$$\bar{\partial}_{\mathrm{z}} M_+(Q,z,0) = Q_{12}(z)M_-(Q,z,0) \tag{5.65}$$

$$\partial_{\mathrm{z}} M_-(Q,z,0) = Q_{21}(z)M_+(Q,z,0). \tag{5.66}$$

We can verify this:

$$\begin{aligned} \bar{\partial}_{\mathrm{z}} M_+(Q,z,k) &= \bar{\partial}_{\mathrm{z}}\left[M_{11} + e(z,-k)M_{12}\right] \\ &= \bar{\partial}_{\mathrm{z}} M_{11} + e(z,-k)\,\bar{\partial}_{\mathrm{z}} M_{12} + M_{12}\,\bar{\partial}_{\mathrm{z}}\, e^{-\mathrm{i}(zk+\bar{z}\bar{k})} \\ &= \bar{\partial}_{\mathrm{z}} M_{11} + e(z,-k)\left[\bar{\partial}_{\mathrm{z}} M_{12} - \mathrm{i}\,\bar{k}M_{12}\right]. \end{aligned}$$

Equations (3.13) and (3.14) can be written as $\bar{\partial}_{\mathrm{z}} M_{11} = Q_{12}M_{21}$ and $\bar{\partial}_{\mathrm{z}} M_{12} = Q_{12}M_{22} + \mathrm{i}\,kM_{12}$. Using these above we find

$$\begin{aligned} \bar{\partial}_{\mathrm{z}} M_+(Q,z,k) &= Q_{12}M_{21} + e(z,-k)\left[Q_{12}M_{22} + \mathrm{i}\,kM_{12} - \mathrm{i}\,\bar{k}M_{12}\right] \\ &= Q_{12}\left[M_{21} + e(z,-k)M_{22}\right] + \mathrm{i}(k-\bar{k})e(z,-k)M_{12} \\ &= Q_{12}(z)e(z,-k)M_-(Q,z,k) + \mathrm{i}(k-\bar{k})e(z,-k)M_{12}(Q,z,k), \end{aligned}$$

and therefore

$$\begin{aligned}\bar{\partial}_{\mathrm{z}} M_+(Q,z,0) &= Q_{12}(z)e(z,0)M_-(Q,z,0) + \mathrm{i}(0-\bar{0})e(z,-0)M_{12}(Q,z,0)\\ &= Q_{12}(z)M_-(Q,z,0),\end{aligned}$$

which is the desired result. Similarly,

$$\begin{aligned}\partial_{\mathrm{z}} M_-(Q,z,k) &= \partial_{\mathrm{z}}\left[M_{22} + e(z,k)M_{21}\right]\\ &= \partial_{\mathrm{z}} M_{22} + e(z,k)\,\partial_{\mathrm{z}} M_{21} + M_{21}\,\partial_{\mathrm{z}} e(z,k)\\ &= \partial_{\mathrm{z}} M_{22} + e(z,k)\left[\partial_{\mathrm{z}} M_{21} + \mathrm{i}\,kM_{21}\right].\end{aligned}$$

Equations (3.15) and (3.16) give $\partial_{\mathrm{z}} M_{22} = Q_{21}M_{12}$ and $\partial_{\mathrm{z}} M_{21} = Q_{21}M_{11} + \mathrm{i}\,kM_{21}$. Using these relations above results in

$$\begin{aligned}\partial_{\mathrm{z}} M_-(Q,z,k) &= Q_{21}M_{12} + e(z,k)\left[Q_{21}M_{11} - \mathrm{i}\,kM_{21} + \mathrm{i}\,kM_{21}\right]\\ &= Q_{21}(z)\left[M_{12}(Q,z,k) + e(z,k)M_{11}(Q,z,k)\right]\\ &= Q_{21}(z)M_+(Q,z,k),\end{aligned}$$

and

$$\partial_{\mathrm{z}} M_-(Q,z,0) = Q_{21}(z)M_+(Q,z,0),$$

the desired result. The theorem follows directly from Equations (5.65) and (5.66). □

Note: These formulas are advantageous since they are for the original CGO solutions $M(z,k)$ corresponding to the matrix Q and not $-Q^T$ as in [BBR01]. This has the computational advantage of not having to solve the problem for $-Q^T$ in addition to already solving the problem for Q. In addition, the formula to recover the matrix potential Q given in in Theorem 1 (Theorem 6.2 of [Fra00]) is computationally impractical as it requires as large k limit of derivatives of the CGO solutions $M(z,k)$.

5.3 Theoretical BIE Formulas for the CGO solutions $\Psi(z,k)$

In this section additional formulas for the determination of the CGO solutions $\Psi(z,k)$ on the boundary $\partial\Omega$ are presented. The formulas for the entire CGO solution matrix $\Psi(z,k)$ in Section 5.3.1 are derived using a method similar to that of Kim Knudsen in his Ph.D.

thesis [Knu02], but are not practical for numerical implementation. Section 5.3.2 contains formulas for the diagonal CGO solutions entries Ψ_{11} and Ψ_{22}. While the formulas present no issue in implementation, they are not needed in the rest of the algorithm (recall that only the off-diagonal CGO solutions entries Ψ_{12} and Ψ_{21} are needed for the evaluation of the scattering transform $S(k)$), and are therefore only included for their mathematical interest.

5.3.1 Theoretical BIE Formulas for the CGOs $\Psi(z,k)$ - Knudsen Approach

Here the boundary integral equations for the CGO solutions Ψ that were first presented in [Knu02] are described and extended. While these formulas have theoretical value, a practical implementation has previously, [Knu02], proved unstable. Nevertheless, we proceed for their mathematical interest.

Defining a Boundary Relation

Let $\nu = (\nu_1, \nu_2)$ represent the outward facing unit normal vector to the boundary $\partial\Omega$ and therefore $\tau = (-\nu_2, \nu_1)$ denote the unit vector tangent vector to the boundary $\partial\Omega$ (in the traditional counter-clockwise orientation). Let $s : [0, |\,\partial\Omega\,|] \to \partial\Omega$ be the arclength parameterization of the boundary $\partial\Omega$. For $f \in C^1(\partial\Omega)$, $\partial_\tau f = \frac{d}{dt}\left(f(s(t))\right)$ is the derivative of f along the boundary $\partial\Omega$. Define $C_0(\partial\Omega) = \left\{f \in C(\partial\Omega) : \int_{\partial\Omega} f\, d\sigma = 0\right\}$, then on $C_0(\partial\Omega)$ we have

$$(\partial_\tau^{-1} f)(s(t)) := \int_0^t f(s(\tilde{t}))\, d\tilde{t}.$$

Let $u \in C^{2+\epsilon}(\overline{\Omega})$ solve the admittivity equation (3.3) for some $f \in C^{2+\epsilon}$. Then, as we before

$$\begin{pmatrix} v \\ w \end{pmatrix} = \gamma^{1/2} \begin{pmatrix} \partial_{\mathrm{z}}\, u \\ \bar{\partial}_{\mathrm{z}}\, u \end{pmatrix}$$

solves

$$(D - Q) \begin{pmatrix} v \\ w \end{pmatrix} = 0$$

where

$$D = \begin{pmatrix} \bar{\partial}_{\mathrm{z}} & 0 \\ 0 & \partial_{\mathrm{z}} \end{pmatrix}, \quad Q(z) = \begin{pmatrix} 0 & -\frac{1}{2}\,\partial_{\mathrm{z}} \log(\gamma) \\ -\frac{1}{2}\,\bar{\partial}_{\mathrm{z}} \log(\gamma) & 0 \end{pmatrix}.$$

We wish to decompose ∂_z and $\bar{\partial}_z$ at the boundary in the unit normal direction ν and the unit tangential direction τ. Consider, since $\gamma \equiv 1$ on the boundary $\partial\Omega$,

$$
\begin{aligned}
2v &= 2\gamma^{1/2}\,\partial\, u \\
&= (u_x - \mathrm{i}\, u_y) \\
&= (1, -\mathrm{i}) \cdot u \\
&= \|\nu\|_2^2 (1, -\mathrm{i}) \cdot u \\
&= \left(\nu_1^2 + \nu_2^2\right)(1, -\mathrm{i}) \cdot u \\
&= \left(\nu_1^2 + \nu_2^2, -\mathrm{i}\,\nu_1^2 - \mathrm{i}\,\nu_2^2\right) \cdot u \\
&= \left(\nu_1^2 + \nu_2^2 - \mathrm{i}\,\nu_1\nu_2 + \mathrm{i}\,\nu_1\nu_2, -\mathrm{i}\,\nu_1^2 - \mathrm{i}\,\nu_2^2 - \nu_1\nu_2 + \nu_1\nu_2\right) \cdot u \\
&= \left[\left(\nu_1^2 - \mathrm{i}\,\nu_1\nu_2, \nu_1\nu_2 - \mathrm{i}\,\nu_2^2\right) + \left(\nu_2^2 + \mathrm{i}\,\nu_1\nu_2, -\nu_1\nu_2 - \mathrm{i}\,\nu_1^2\right)\right] \cdot u \\
&= \left[(\nu_1 - \mathrm{i}\,\nu_2)(\nu_1, \nu_2) - (\nu_2 + \mathrm{i}\,\nu_1)(-\nu_2, \nu_1)\right] \cdot u \\
&= \left[(\nu_1 - \mathrm{i}\,\nu_2)\nu - (\nu_2 + \mathrm{i}\,\nu_1)\tau\right] \cdot u \\
&= \left[(\nu_1 - \mathrm{i}\,\nu_2)\nu - \mathrm{i}(\nu_1 - \mathrm{i}\,\nu_2)\tau\right] \cdot u \\
&= (\nu_1 - \mathrm{i}\,\nu_2)\nu \cdot u - \mathrm{i}(\nu_1 - \mathrm{i}\,\nu_2)\tau \cdot u \\
&= \bar{\nu}\nu \cdot u - \mathrm{i}\,\bar{\nu}\tau \cdot u \\
&= \bar{\nu}\frac{\partial\, u}{\partial\, \nu} - \mathrm{i}\,\bar{\nu}\frac{\partial\, u}{\partial\, \tau} \\
&= \bar{\nu}\Lambda_\gamma f - \mathrm{i}\,\bar{\nu}\,\partial_\tau\, f \\
&= \left[\bar{\nu}\Lambda_\gamma - \mathrm{i}\,\bar{\nu}\,\partial_\tau\right](f).
\end{aligned}
\tag{5.67}
$$

Similarly,

$$\begin{aligned}
2w &= \gamma^{1/2}\,\bar\partial\, u \\
&= (u_x + \mathrm{i}\,u_y) \\
&= (1,\mathrm{i})\cdot u \\
&= \|\nu\|_2^2(1,\mathrm{i})\cdot u \\
&= \left(\nu_1^2+\nu_2^2\right)(1,\mathrm{i})\cdot u \\
&= \left(\nu_1^2+\nu_2^2+\mathrm{i}\,\nu_1\nu_2-\mathrm{i}\,\nu_1\nu_2, \mathrm{i}\,\nu_1^2+\mathrm{i}\,\nu_2^2-\nu_1\nu_2+\nu_1\nu_2\right)\cdot u \\
&= \left[\left(\nu_1^2+\mathrm{i}\,\nu_1\nu_2, \mathrm{i}\,\nu_2^2+\nu_1\nu_2\right)+\left(\nu_2^2-\mathrm{i}\,\nu_1\nu_2, \mathrm{i}\,\nu_1^2-\nu_1\nu_2\right)\right]\cdot u \\
&= \left[(\nu_1[\nu_1+\mathrm{i}\,\nu_2], \nu_2[\nu_1+\mathrm{i}\,\nu_2])+(-\nu_2[-\nu_2+\mathrm{i}\,\nu_1], \nu_1[-\nu_2+\mathrm{i}\,\nu_1])\right]\cdot u \\
&= \left[[\nu_1+\mathrm{i}\,\nu_2](\nu_1,\nu_2)+[-\nu_2+\mathrm{i}\,\nu_1](-\nu_2,\nu_1)\right]\cdot u \\
&= \left[[\nu_1+\mathrm{i}\,\nu_2]\nu+[-\nu_2+\mathrm{i}\,\nu_1]\tau\right]\cdot u \\
&= [\nu_1+\mathrm{i}\,\nu_2]\nu\cdot u+[-\nu_2+\mathrm{i}\,\nu_1]\tau\cdot u \\
&= [\nu_1+\mathrm{i}\,\nu_2]\Lambda_\gamma f+\mathrm{i}[\nu_1+\mathrm{i}\,\nu_2]\,\partial_\tau f \\
&= \nu\Lambda_\gamma f+\mathrm{i}\,\nu\,\partial_\tau f. \qquad (5.68)
\end{aligned}$$

Equivalently we have

$$\left.\begin{pmatrix} v \\ w \end{pmatrix}\right|_{\partial\Omega} = \frac{1}{2}\begin{bmatrix} \bar\nu & -\mathrm{i}\,\bar\nu \\ \nu & \mathrm{i}\,\nu \end{bmatrix}\left.\begin{bmatrix} \Lambda_\gamma f \\ \partial_\tau f \end{bmatrix}\right| \quad \text{on } \partial\Omega. \qquad (5.69)$$

Inverting (5.69), i.e. solving for $(\Lambda_\gamma f, \partial_\tau f)^T$ on the boundary, gives

$$\begin{aligned}
\left.\begin{bmatrix} \Lambda_\gamma f \\ \partial_\tau f \end{bmatrix}\right|_{\partial\Omega} &= \frac{2}{\bar\nu\mathrm{i}\,\nu-(-\mathrm{i}\,\bar\nu\nu)}\begin{bmatrix} \mathrm{i}\,\nu & \mathrm{i}\,\bar\nu \\ -\nu & \bar\nu \end{bmatrix}\begin{pmatrix} v \\ w \end{pmatrix} \\
&= \begin{bmatrix} \nu & \bar\nu \\ \mathrm{i}\,\nu & -\mathrm{i}\,\bar\nu \end{bmatrix}\begin{pmatrix} v \\ w \end{pmatrix},
\end{aligned}$$

so that

$$\left.\begin{bmatrix} \Lambda_\gamma f \\ \partial_\tau f \end{bmatrix}\right|_{\partial\Omega} = \left.\begin{bmatrix} \nu v+\bar\nu w \\ \mathrm{i}\,\nu v-\mathrm{i}\,\bar\nu w \end{bmatrix}\right|_{\partial\Omega},$$

or

$$\begin{cases} \Lambda_\gamma f|_{\partial\Omega} = & (\nu v+\bar\nu w)|_{\partial\Omega} \\ \partial_\tau f|_{\partial\Omega} = & \mathrm{i}(\nu v-\bar\nu w)|_{\partial\Omega}. \end{cases}$$

Inverting the tangential derivative map,

$$\begin{aligned}\partial_\tau^{-1}\left(\partial_\tau f\right) &= \partial_\tau^{-1}\left(\mathrm{i}(\nu v-\bar{\nu}w)\right)\\ &= \mathrm{i}\int_{\partial\Omega}\left(\nu v-\bar{\nu}w\right)\,d\sigma\\ &= 0,\end{aligned}$$

with the last step following from the fact that we are integrating over a closed loop and therefore $\partial_\tau^{-1}\left(\partial_\tau f\right) = f(s(t)) - f(s(t))$. This gives us $(\nu v - \bar{\nu}w) \in C_0^{1+\epsilon}$. However, we have still yet to fully derive a boundary relation. To do so, we apply the operator $H_\gamma = \Lambda_\gamma\ \partial_\tau^{-1}$ to $\partial_\tau f$ on the boundary,

$$\begin{aligned}H_\gamma\left(\partial_\tau f\right) &= \Lambda_\gamma\,\partial_\tau^{-1}\left(\partial_\tau f\right)\\ &= \Lambda_\gamma f\\ &= \nu v+\bar{\nu}w,\end{aligned}$$

and from above we also have,

$$\begin{aligned}H_\gamma\left(\partial_\tau f\right) &= H_\gamma\left(\mathrm{i}(\nu v-\bar{\nu}w)\right)\\ &= \mathrm{i}\,H_\gamma\left(\nu v-\bar{\nu}w\right).\end{aligned}$$

Therefore,

$$\mathrm{i}\,H_\gamma\left(\nu v-\bar{\nu}w\right) = \left(\nu v+\bar{\nu}w\right) \quad \text{on } \partial\Omega. \tag{5.70}$$

Knudsen defines the space for the boundary relation as

$$\mathcal{BR} = \left\{ (h_1,h_2)\in C^{1+\epsilon}(\partial\Omega)\times C^{1+\epsilon}(\partial\Omega) \;\middle|\; \begin{array}{c}(\nu h_1-\bar{\nu}h_2)\in C_0^{1+\epsilon}(\partial\Omega)\\ \mathrm{i}\,H_\gamma(\nu h_1-\bar{\nu}h_2)=\nu h_1+\bar{\nu}h_2\end{array} \right\}. \tag{5.71}$$

The Cauchy data for the problem in (3.4) is given by

$$C_Q = \left\{ (v,w)|_{\partial\Omega} \;\middle|\; \begin{array}{c}(v,w)\in C^{1+\epsilon}(\overline{\Omega})\times C^{1+\epsilon}(\overline{\Omega})\\ (D-Q)\begin{pmatrix} v\\ w\end{pmatrix}=0\end{array} \right\}.$$

Notice that since

$$\partial_\tau f|_{\partial\Omega} = \mathrm{i}(\nu v-\bar{\nu}w)|_{\partial\Omega},$$

we have

$$u|_{\partial\Omega} = f = \mathrm{i}\,\partial_\tau^{-1}\left(\mathrm{i}(\nu v-\bar{\nu}w)\right)|_{\partial\Omega},$$

so that we can define a solution (v, w) to

$$(D - Q)(v, w)^T = 0,$$

with

$$\begin{pmatrix} v \\ w \end{pmatrix} = \gamma^{1/2} \begin{pmatrix} \partial u \\ \bar{\partial} u \end{pmatrix},$$

and

$$u|_{\partial\Omega} = f = \mathrm{i}\, \partial_\tau^{-1} \left(\mathrm{i}(\nu v - \bar{\nu} w) \right) |_{\partial\Omega}.$$

Knudsen, [Knu02], shows that $\mathcal{BR}$, (5.71), is in fact a complete characterization of the Cauchy data C_Q for the system (3.4). His proof does not rely on the symmetry inherent in his real valued conductivity based matrix potential Q_{BU} and thus our complex admittivity based matrix potential Q presents no challenge to his proof.

Defining the Boundary Integral Equations

Now that we have a boundary relation that involves the Dirichlet-to-Neumann map Λ_γ, we have a connection to the data. However, we still do not have enough information to solve for the exponentially growing solutions Ψ on the boundary. Here we remedy the situation.

Recall the *Cauchy Integral Operator*:

$$\mathcal{S}f(z) = \frac{1}{2\pi\,\mathrm{i}} \int_{\partial\Omega} \frac{f(\tilde{z})}{\tilde{z} - z}\, d\tilde{z}, \quad z \in \mathbb{R}^2 \setminus \partial\Omega, \tag{5.72}$$

which acts as a path integral along the boundary $\partial\Omega$ in the counter-clockwise direction (the traditional positive orientation). If $z \in \partial\Omega$, then the kernel $\frac{1}{\tilde{z}-z}$ is not integrable and we must use principle values to evaluate the integral.

We will also need the well known *Plemelj's Formulae*

$$\lim_{\epsilon \to 0} \mathcal{S}f(z \pm \nu\epsilon) = \mp \frac{1}{2} f(z) + \frac{1}{2\pi\,\mathrm{i}}\, P.V. \int_{\partial\Omega} \frac{f(\tilde{z})}{\tilde{z} - z}\, d\tilde{z}, \tag{5.73}$$

where the boundary integral on the right hand side is evaluated in the sense of principle values.

We will now present and extend the result given in Theorem 3.4.4 of [Knu02] to derive formulas for the CGO solutions Ψ on the boundary. The main idea of the derivation is to consider $z \in \mathbb{C} \setminus \overline{\Omega}$, i.e. the complement of $\overline{\Omega}$, and exploit the asymptotics of Ψ in that region. We will then let z approach the boundary $\partial\Omega$ from the outside and employ *Plemelj's Formulae*.

Lemma 5 (Lemma 3.4.3 of [Knu02]). *Let $r > 2$ and assume that the functions v and w satisfy $(e^{-\mathrm{i}kz}v - 1)$ and $e^{-\mathrm{i}kz}w \in L^r(\mathbb{R}^2)$ respectively. Further assume that $\bar{\partial}_{\mathrm{z}} v$ and $\partial_{\mathrm{z}} w$ in $C^\alpha(\mathbb{R}^2)$ for $0 < \alpha < 1$ are compactly supported in Ω. Then on the boundary, $\partial\Omega$,*

$$\begin{array}{rcl} (I - \mathrm{i}\,\mathcal{S}_k)v & = & 2e^{\mathrm{i}kz} \\ (I + \mathrm{i}\,\overline{\mathcal{S}_k})w & = & 0. \end{array} \tag{5.74}$$

Proof. Let $z \in \mathbb{C}\setminus\overline{\Omega}$, i.e. z in the complement of $\overline{\Omega}$. By definition of the $\bar{\partial}$ and $\bar{\partial}^{-1}$ operators,

$$\begin{aligned} v(z)e^{-\mathrm{i}kz} - 1 &= \frac{1}{\pi}\int_{\mathbb{R}^2} \frac{\bar{\partial}_\zeta \left[v(\zeta)e^{-\mathrm{i}k\zeta} - 1\right]}{z-\zeta}\, d\mu(\zeta) \\ &= \frac{1}{\pi}\int_{\Omega} \frac{\bar{\partial}_\zeta \left[v(\zeta)e^{-\mathrm{i}k\zeta}\right]}{z-\zeta}\, d\mu(\zeta) \\ &= \frac{1}{2\pi}\int_{\partial\Omega} \frac{v(\zeta)e^{-\mathrm{i}k\zeta}}{z-\zeta}\nu\, dS(\zeta) - \frac{1}{\pi}\int_{\Omega} v(\zeta)e^{-\mathrm{i}k\zeta}\,\bar{\partial}_\zeta\left(\frac{1}{z-\zeta}\right)\, d\mu(\zeta), \end{aligned}$$

using the the fact that $\bar{\partial}v$ has compact support in Ω and then integration by parts. Now, as we are only considering z outside of $\overline{\Omega}$, $z - \zeta \neq 0$ for $z \in \Omega$ and thus the second integral over Ω is zero so that

$$v(z)e^{-\mathrm{i}kz} - 1 = \frac{1}{2\pi}\int_{\partial\Omega} \frac{v(\zeta)e^{-\mathrm{i}k\zeta}}{z-\zeta}\nu\, dS(\zeta).$$

We know,

$$d\zeta = \tau\, dS(\zeta) = (\mathrm{i}\,\nu)\, dS(\zeta),$$

and therefore,

$$\nu\, dS(\zeta) = \frac{1}{\mathrm{i}}\, d\zeta.$$

Thus

$$v(z)e^{-\mathrm{i}kz} - 1 = \frac{1}{2\pi\,\mathrm{i}}\int_{\partial\Omega} \frac{v(\zeta)e^{-\mathrm{i}k\zeta}}{z-\zeta}\nu\, d\zeta,$$

and rearranging we find,

$$v(z)e^{-\mathrm{i}kz} + \frac{1}{2\pi\,\mathrm{i}}\int_{\partial\Omega} \frac{v(\zeta)e^{-\mathrm{i}k\zeta}}{\zeta-z}\nu\, d\zeta = 1, \quad z \in \mathbb{C}\setminus\overline{\Omega}.$$

Now, multiply both sides by $e^{\mathrm{i}kz}$ (the asymptotic behavior of v)

$$v(z) + \frac{1}{2\pi\,\mathrm{i}}\int_{\partial\Omega} \frac{v(\zeta)e^{-\mathrm{i}k(\zeta-z)}}{\zeta-z}\nu\, d\zeta = e^{\mathrm{i}kz}, \quad z \in \mathbb{C}\setminus\overline{\Omega},$$

or,

$$v(z) + \frac{1}{2\,\mathrm{i}} \int_{\partial\Omega} v(\zeta)\mathfrak{g}_k(\zeta - z)\nu \; d\zeta = e^{\mathrm{i}\,kz}, \quad z \in \mathbb{C}\setminus\overline{\Omega}, \tag{5.75}$$

where,

$$\mathfrak{g}_k(z) = \frac{1}{\pi z} e^{-\mathrm{i}\,zk}.$$

We will use a modified *Plemelj's Formula*,

$$\lim_{\substack{z\to\partial\Omega \\ \text{outside}}} \left\{ \frac{1}{2\,\mathrm{i}} \int_{\partial\Omega} \phi(\zeta)\mathfrak{g}_k(\zeta - z)\; d\zeta \right\} = -\frac{1}{2}\phi(z) + P.V.\; \frac{1}{2\,\mathrm{i}} \int_{\partial\Omega} \phi(\zeta)\mathfrak{g}_k(\zeta - z)\; d\zeta. \tag{5.76}$$

Now, let z tend toward the boundary $\partial\Omega$ (from the outside) in Equation (5.75) and use (5.76),

$$\begin{aligned}
\lim_{\substack{z\to\partial\Omega \\ \text{outside}}} \left\{ v(z) + \frac{1}{2\,\mathrm{i}} \int_{\partial\Omega} v(\zeta)\mathfrak{g}_k(\zeta - z)\nu \; d\zeta \right\} &= \lim_{\substack{z\to\partial\Omega \\ \text{outside}}} \left\{ e^{\mathrm{i}\,kz} \right\} \\
v(z) + \lim_{\substack{z\to\partial\Omega \\ \text{outside}}} \left\{ \frac{1}{2\,\mathrm{i}} \int_{\partial\Omega} v(\zeta)\mathfrak{g}_k(\zeta - z)\nu \; d\zeta \right\} &= e^{\mathrm{i}\,kz} \\
v(z) + \left(-\frac{1}{2}v(z) + P.V.\; \frac{1}{2\,\mathrm{i}} \int_{\partial\Omega} v(\zeta)\mathfrak{g}_k(\zeta - z)\; d\zeta \right) &= e^{\mathrm{i}\,kz}.
\end{aligned}$$

Multiplying through by 2 and simplifying we have,

$$v(z) - P.V.\; \mathrm{i} \int_{\partial\Omega} \phi(\zeta)\mathfrak{g}_k(\zeta - z)\; d\zeta = 2e^{\mathrm{i}\,kz},$$

or equivalently,

$$(I - \mathrm{i}\,\mathcal{S}_k)\, v(z) = 2e^{\mathrm{i}\,kz}, \tag{5.77}$$

where

$$\mathcal{S}_k f(z) = P.V. \int_{\partial\Omega} f(\zeta)\mathfrak{g}_k(\zeta - z)\; d\zeta. \tag{5.78}$$

We can now consider the corresponding formula for $w(z) \sim 0$ as $|z| \to \infty$,

$$w(z)e^{\mathrm{i}\,\bar{k}\bar{z}} = -\frac{1}{2\pi\,\mathrm{i}} \int_{\partial\Omega} \frac{w(\zeta)e^{\mathrm{i}\,\bar{k}\bar{z}}}{\bar{z} - \bar{\zeta}}\; d\bar{\zeta}.$$

Multiplying through by $e^{-\mathrm{i}\,\bar{k}\bar{z}}$ and rearranging,

$$w(z) - \frac{1}{2\pi\,\mathrm{i}} \int_{\partial\Omega} \frac{w(\zeta)e^{\mathrm{i}\,\bar{k}(\bar{\zeta}-\bar{z})}}{\bar{z} - \bar{\zeta}}\; d\bar{\zeta} = 0, \quad z \in \mathbb{C}\setminus\overline{\Omega}. \tag{5.79}$$

We will use another modified *Plemelj's Formula*,

$$\lim_{\substack{z\to\partial\Omega\\ \text{outside}}}\left\{\frac{1}{2\,\mathrm{i}}\int_{\partial\Omega}\phi(\zeta)\overline{\mathfrak{g}_k(\zeta-z)}\,d\bar{\zeta}\right\}=\frac{1}{2}\phi(z)+P.V.\,\frac{1}{2\,\mathrm{i}}\int_{\partial\Omega}\phi(\zeta)\overline{\mathfrak{g}_k(\zeta-z)}\,d\bar{\zeta}. \tag{5.80}$$

Now, let z tend toward the boundary $\partial\Omega$ (from the outside) in Equation (5.79) and use (5.80),

$$\begin{aligned}
\lim_{\substack{z\to\partial\Omega\\ \text{outside}}}\left\{w(z)-\frac{1}{2\pi\,\mathrm{i}}\int_{\partial\Omega}\frac{w(\zeta)e^{\mathrm{i}\,\bar{k}(\bar{\zeta}-\bar{z})}}{\bar{z}-\bar{\zeta}}\,d\bar{\zeta}\right\} &= 0\\
w(z)-\lim_{\substack{z\to\partial\Omega\\ \text{outside}}}\left\{\frac{1}{2\pi\,\mathrm{i}}\int_{\partial\Omega}\frac{w(\zeta)e^{\mathrm{i}\,\bar{k}(\bar{\zeta}-\bar{z})}}{\bar{z}-\bar{\zeta}}\,d\bar{\zeta}\right\} &= 0\\
w(z)-\left(\frac{1}{2}w(z)+P.V.\,\frac{1}{2\,\mathrm{i}}\int_{\partial\Omega}w(\zeta)\overline{\mathfrak{g}_k(\zeta-z)}\,d\bar{\zeta}\right) &= 0.
\end{aligned}$$

Multiplying by 2 and rearranging,

$$w(z)+P.V.\;\mathrm{i}\int_{\partial\Omega}w(\zeta)\overline{\mathfrak{g}_k(\zeta-z)}\,d\bar{\zeta}=0,$$

or equivalently,

$$\left(I+\mathrm{i}\,\overline{\mathcal{S}_k}\right)w(z)=0, \tag{5.81}$$

where

$$\overline{\mathcal{S}_k}f(z)=P.V.\int_{\partial\Omega}f(\zeta)\overline{\mathfrak{g}_k(\zeta-z)}\,d\bar{\zeta}. \tag{5.82}$$

This completes the proof of Lemma 5. □

Lemma 5 (with $\Psi_{11}=v$ and $\Psi_{21}=w$), along with the boundary relation given in Equation 5.70, gives us the following theorem.

Theorem 11 (Theorem 3.4.4 of [Knu02])**.** *The system of equations on* $\partial\Omega$

$$\begin{pmatrix}(I-\mathrm{i}\,\mathcal{S}_k) & 0\\ 0 & (I+\mathrm{i}\,\overline{\mathcal{S}_k})\\ (iH_\gamma-1)\nu & -(iH_\gamma+1)\bar{\nu}\end{pmatrix}\Phi=\begin{pmatrix}2e^{\mathrm{i}\,kz}\\ 0\\ 0\end{pmatrix},\quad z\in\partial\Omega. \tag{5.83}$$

has the unique solution $\Phi=(\Psi_{11},\Psi_{21})|_{\partial\Omega}$ *in*

$$\{\Phi\in C^{1+\epsilon}(\partial\Omega)\times C^{1+\epsilon}(\partial\Omega):(\nu\Phi_1-\bar{\nu}\Phi_2)\in C_0^{1+\epsilon}(\partial\Omega)\}.$$

The derivation follows directly from Lemma 5 and the boundary relation (5.70). For the uniqueness part of the proof, I refer the reader to the proof given in [Knu02]. The proof holds even though Knudsen only considers real valued conductivities $\gamma = \sigma$ whereas we consider complex admittivities $\gamma = \sigma + \mathrm{i}\,\omega\epsilon$.

We also need formulas to determine Ψ_{12} and Ψ_{22} on the boundary $\partial\Omega$. In an analogous fashion, we find

Lemma 6. *Let $r > 2$ and assume that the functions $\tilde{v}$ and $\tilde{w}$ satisfy $e^{\mathrm{i}\,k\bar{z}}\tilde{v}$ and $\left(e^{\mathrm{i}\,k\bar{z}}\tilde{w} - 1\right) \in L^r(\mathbb{R}^2)$ respectively. Further assume that $\bar{\partial}\,\tilde{v}$ and $\partial\,\tilde{w}$ in $C^\alpha(\mathbb{R}^2)$ for $0 < \alpha < 1$ are compactly supported in Ω. Then on the boundary, $\partial\Omega$,*

$$\begin{array}{rcl} (I - \mathrm{i}\,\mathcal{S}_{\bar{k}})\tilde{v} & = & 0 \\ (I + \mathrm{i}\,\overline{\mathcal{S}_{\bar{k}}})\tilde{w} & = & 2e^{\mathrm{i}\,k\bar{z}}, \end{array} \tag{5.84}$$

where the operators $\mathcal{S}_{\bar{k}}$ and $\overline{\mathcal{S}_{\bar{k}}}$ are given by,

$$S_{\bar{k}}f(z) = P.V. \int_{\partial\Omega} f(\zeta)\mathfrak{g}_{\bar{k}}(\zeta - z)\, d\zeta \tag{5.85}$$

$$\overline{S_{\bar{k}}}f(z) = P.V. \int_{\partial\Omega} f(\zeta)\overline{\mathfrak{g}_{\bar{k}}(\zeta - z)}\, d\overline{\zeta}. \tag{5.86}$$

The proof of Lemma 6 is analogous to that of Lemma 5. Similarly, we have the following theorem to recover Ψ_{12} and Ψ_{21} on the boundary $\partial\Omega$.

Theorem 12. *The system of equations on $\partial\Omega$*

$$\begin{pmatrix} 0 & (I - \mathrm{i}\,S_{\bar{k}}) \\ (I + \mathrm{i}\,\overline{S_{\bar{k}}}) & 0 \\ (iH_\gamma - 1)\nu & -(iH_\gamma + 1)\bar{\nu} \end{pmatrix} \tilde{\Phi} = \begin{pmatrix} 0 \\ 2e^{\mathrm{i}\,k\bar{z}} \\ 0 \end{pmatrix}, \quad z \in \partial\Omega. \tag{5.87}$$

has the unique solution $\tilde{\Phi} = (\Psi_{12}, \Psi_{22})|_{\partial\Omega}$ in

$$\{\tilde{\Phi} \in C^{1+\epsilon}(\partial\Omega) \times C^{1+\epsilon}(\partial\Omega) : (\nu\tilde{\Phi}_1 - \bar{\nu}\tilde{\Phi}_2) \in C_0^{1+\epsilon}(\partial\Omega)\}.$$

The proof is analogous to that of Theorem 11.

We have chosen not to implement these formulas for the CGO solutions Ψ on the boundary since, according to Knudsen [Knu02], their accurate recovery of the CGO solutions proves to be very difficult. Solving the systems in Equations (5.83) and (5.87) for Ψ_{21} and Ψ_{12} requires that we also recover Ψ_{11} and Ψ_{22} (which are not required for the evaluation of the scattering transform $S(k)$). Unfortunately, the exponential terms in the systems

corresponding to the CGO solutions Ψ_{11} and Ψ_{22} dominate the solution, leaving the terms corresponding to Ψ_{12} and Ψ_{21} corrupted with excessive computational errors. As we already have more practical formulas for recovering Ψ_{12} and Ψ_{21} on the boundary (see Section 5.1.2), we have not fully investigated the implementation of Equations (5.83) and (5.87).

5.3.2 Additional BIE Formulas for the CGO Solutions Ψ_{11} and Ψ_{22}

Although the definitions of the scattering transforms, (5.49) and (5.50), require knowledge of $\Psi_{12}(z,k)$ and $\Psi_{21}(z,k)$ for $z \in \partial\Omega$ (not Ψ_{11} or Ψ_{22}), formulas for Ψ_{11} and Ψ_{22} may be of use to someone someday. Therefore, we include them here. Recall,

$$\bar{\partial}_{\mathrm{z}}\, \Psi_{11}(z,k) = Q_{12}(z)\Psi_{21}(z,k),$$

which comes from the original transformation of rewriting the admittivity equation as a first order system using ∂_{z} and $\bar{\partial}_{\mathrm{z}}$ derivatives. Taking the ∂_{z} derivative of both sides and multiplying by -4,

$$-4\,\partial_{\mathrm{z}}\left(\bar{\partial}_{\mathrm{z}}\, \Psi_{11}(z,k)\right) = -4\,\partial_{\mathrm{z}}\left(Q_{12}(z)\Psi_{21}(z,k)\right),$$

or equivalently, since $4\,\partial_{\mathrm{z}}\,\bar{\partial}_{\mathrm{z}} = \Delta = 4\,\bar{\partial}_{\mathrm{z}}\,\partial_{\mathrm{z}}$,

$$-\Delta\Psi_{11}(z,k) = -4\,\partial_{\mathrm{z}}\left(Q_{12}(z)\Psi_{21}(z,k)\right). \tag{5.88}$$

Using the Green's function for $-\Delta$, we can write the solution for $\Psi_{11}(z,k)$ as,

$$\Psi_{11}(z,k) = e^{\mathrm{i}\,zk} + \int_{\Omega} G_k(z-\zeta)\left[-4\,\partial_{\zeta}\left(Q_{12}(\zeta)\Psi_{21}(\zeta,k)\right)\right]\, d\mu(\zeta). \tag{5.89}$$

Now we need to find a relation to replace the integral over Ω. In order to do so, let w be a solution to

$$-\Delta w = -4\,\partial_{\mathrm{z}}\left(\tilde{Q}_{12}(z)\tilde{\Psi}_{21}(z,k)\right) \tag{5.90}$$

where,

$$\tilde{Q}_{12}(z) = -\frac{1}{2}\,\partial_{\mathrm{z}}\log(\tilde{\gamma}(z)).$$

Multiplying w by (5.88) and subtracting Ψ_{11} multiplied by (5.90), we have

$$0 = \int_{\Omega} w\left[-\Delta_{\zeta}\Psi_{11} + 4\,\partial_{\zeta}\left(Q_{12}\Psi_{21}\right)\right] - \Psi_{11}\left[-\Delta_{\zeta}w + 4\,\partial_{\zeta}\left(\tilde{Q}_{12}\tilde{\Psi}_{21}\right)\right]\, d\mu(\zeta),$$

and applying integration by parts on the Laplacian terms,

$$\begin{aligned} 0 &= -\int_{\partial\Omega} w\frac{\partial\Psi_{11}}{\partial\nu} - \Psi_{11}\frac{\partial w}{\partial\nu}\, dS(\zeta) + \int_\Omega \nabla_\zeta w\cdot\nabla_\zeta\Psi_{11} - \nabla_\zeta\Psi_{11}\nabla_\zeta w\, d\mu(\zeta) \\ &\quad +4\int_\Omega \partial_\zeta\left(Q_{12}\Psi_{21}\right) - \Psi_{11}\,\partial_\zeta\left(\tilde{Q}_{12}\tilde{\Psi}_{21}\right)\, d\mu(\zeta) \\ &= \int_{\partial\Omega}\Psi_{11}\frac{\partial w}{\partial\nu} - w\frac{\partial\Psi_{11}}{\partial\nu}\, dS(\zeta) \\ &\quad +4\int_\Omega \partial_\zeta\left(Q_{12}\Psi_{21}\right) - \Psi_{11}\,\partial_\zeta\left(\tilde{Q}_{12}\tilde{\Psi}_{21}\right)\, d\mu(\zeta). \end{aligned} \tag{5.91}$$

Now, let $\tilde{\gamma}$ be a constant admittivity function, and therefore,

$$\tilde{Q}_{12} = -\frac{1}{2}\,\partial\log\tilde{\gamma} = 0.$$

Thus, equation (5.91) reduces to

$$0 = -\int_{\partial\Omega} w\frac{\partial\Psi_{11}}{\partial\nu} - \Psi_{11}\frac{\partial w}{\partial\nu}\, dS(\zeta) + 4\int_\Omega \partial_\zeta\left(Q_{12}\Psi_{21}\right)\, d\mu(\zeta),$$

or equivalently,

$$0 = -\int_{\partial\Omega} w\Lambda_Q\Psi_{11} - \Psi_{11}\Lambda_{\tilde{Q}}w\, dS(\zeta) + 4\int_\Omega \partial_\zeta\left(Q_{12}\Psi_{21}\right)\, d\mu(\zeta), \tag{5.92}$$

where Λ_Q is a modified Dirichlet-to-Neumann map corresponding to γ and $\Lambda_{\tilde{Q}}$ corresponds to $\tilde{\gamma}$. We would like to interchange the CGO solution Ψ_{11} and the unknown function w in the boundary integral above so that

$$\int_{\partial\Omega}\Psi_{11}\Lambda_{\tilde{Q}}w\, dS(\zeta) = \int_{\partial\Omega} w\Lambda_{\tilde{Q}}\Psi_{11}\, dS(\zeta).$$

Therefore, we consider the following auxiliary problem where v is a solution to

$$\begin{aligned} -\Delta v &= -4\,\partial\left(\tilde{Q}_{12}\tilde{v}\right) \\ v|_{\partial\Omega} &= \Psi_{11}|_{\partial\Omega}. \end{aligned} \tag{5.93}$$

Then, as before, we combine equations (5.90) and (5.93) as follows,

$$0 = \int_\Omega v\left[-\Delta_\zeta w + 4\,\partial_\zeta\left(\tilde{Q}_{12}\tilde{\Psi}_{21}\right)\right] - w\left[-\Delta_\zeta v + 4\,\partial_\zeta\left(\tilde{Q}_{12}\tilde{v}\right)\right]\, d\mu(\zeta).$$

Since $\tilde{\gamma}$ is constant, $\tilde{Q}_{12} = 0$ and therefore the above reduces to

$$0 = -\int_\Omega v\Delta_\zeta w - w\Delta_\zeta v\, d\mu(\zeta).$$

Applying integration by parts on the Laplacian operators,

$$\begin{aligned} 0 &= \int_{\partial\Omega} v\frac{\partial w}{\partial \nu} - w\frac{\partial v}{\partial \nu}\, dS(\zeta) - \int_{\Omega} \nabla_\zeta v \cdot \nabla_\zeta w - \nabla_\zeta v \nabla_\zeta w \, d\mu(\zeta) \\ &= \int_{\partial\Omega} v\frac{\partial w}{\partial \nu} - w\frac{\partial v}{\partial \nu}\, dS(\zeta) \\ &= \int_{\partial\Omega} v\Lambda_{\tilde{Q}} w - w\Lambda_{\tilde{Q}} v \, dS(\zeta). \end{aligned}$$

Then, since $v|_{\partial\Omega} = \Psi_{11}|_{\partial\Omega}$, we have

$$\int_{\partial\Omega} \Psi_{11}\Lambda_{\tilde{Q}} w \, dS(\zeta) = \int_{\partial\Omega} w\Lambda_{\tilde{Q}}\Psi_{11} \, dS(\zeta), \tag{5.94}$$

which will allow us to interchange Ψ_{11} and w in equation (5.92). Now, using equation (5.94) in (5.92) yields

$$0 = -\int_{\partial\Omega} w\Lambda_Q\Psi_{11} - w\Lambda_{\tilde{Q}}\Psi_{11} \, dS(\zeta) + 4\int_{\Omega} w\, \partial_\zeta \left(Q_{12}\Psi_{21}\right) \, d\mu(\zeta). \tag{5.95}$$

Recall that $\tilde{\gamma}$ is a constant and therefore the original equation for w, equation (5.90), reduces to

$$-\Delta w = 0,$$

and thus w is the Green's function for the $-\Delta$ operator. Using this in equation (5.95) gives

$$\begin{aligned} 0 &= \int_{\partial\Omega} G_k(z-\zeta)\left[\Lambda_Q - \Lambda_{\tilde{Q}}\right]\Psi_{11}(\zeta,k)\, dS(\zeta) \\ &\quad + \int_{\Omega} G_k(z-\zeta)\left[-4\,\partial_\zeta\left(Q_{12}(\zeta)\Psi_{21}(\zeta,k)\right)\right] \, d\mu(\zeta). \end{aligned} \tag{5.96}$$

Now replacing the integral over Ω with the corresponding term in (5.89) gives

$$0 = \int_{\partial\Omega} G_k(z-\zeta)\left[\Lambda_Q - \Lambda_{\tilde{Q}}\right]\Psi_{11}(\zeta,k)\, dS(\zeta) + \left(e^{\mathrm{i}\, zk} - \Psi_{11}(z,k)\right).$$

Rearranging the terms gives us the following equation for Ψ_{11},

$$\Psi_{11}(z,k) = e^{\mathrm{i}\, zk} + \int_{\partial\Omega} G_k(z-\zeta)\left[\Lambda_Q - \Lambda_{\tilde{Q}}\right]\Psi_{11}(\zeta,k)\, dS(\zeta).$$

We can also derive a similar formula for $\Psi_{22}(z,k)$. We summarize the results in the following theorem.

Theorem 13. *The exponentially growing solutions* $\Psi_{11}(z,k)$ *and* $\Psi_{22}(z,k)$ *to* (3.10) *can be calculated on the boundary* $\partial\Omega$ *via:*

$$\Psi_{11}(z,k) = e^{\mathrm{i}\,zk} + \int_{\partial\Omega} G_k(z-\zeta)\left[\Lambda_Q - \Lambda_{\tilde{Q}}\right]\Psi_{11}(\zeta,k)\,dS(\zeta), \quad z \in \partial\Omega \tag{5.97}$$

$$\Psi_{22}(z,k) = e^{-\mathrm{i}\,\bar{z}k} + \int_{\partial\Omega} G_k(-\bar{z}+\bar{\zeta})\left[\Lambda_Q - \Lambda_{\tilde{Q}}\right]\Psi_{22}(\zeta,k)\,dS(\zeta), \quad z \in \partial\Omega \tag{5.98}$$

for $z,\ k \in \mathbb{C}$ *where* Λ_Q *and* $\Lambda_{\tilde{Q}}$ *are modified Dirichlet-to-Neumann maps corresponding to* γ *and* $\tilde{\gamma}$ *respectively, and* $\tilde{\gamma}$ *is constant.*

Note that these formulas hold for all $z \in \mathbb{C}$ and therefore we could compare the reconstructed CGO solutions Ψ_{11} and Ψ_{22} from the inverse problem (e.g. from simulated Finite Element data) to the CGO solutions Ψ_{11} and Ψ_{22} that we can solve for via the forward $D_kM = QM$ problem for a prescribed admittivity distribution. This gives us another check along the way to verify that our formulas, as well as our forward solver, are correct. Note that while formulas (5.97) and (5.98) are not needed for the solution of the full nonlinear inverse problem, their addition allows us to recover the trace of the entire $\Psi(z,k)$ matrix for $z \in \partial\Omega$ and $k \in \mathbb{C}\setminus 0$ (along with (5.51) and (5.52)).

6. IMPLEMENTATION OF THE COMPLETE RECONSTRUCTION ALGORITHM FOR CIRCULAR DOMAINS

In this chapter the numerical implementation of each of the steps of the full nonlinear reconstruction algorithm:

$$\Lambda_\gamma \underset{1}{\longrightarrow} u_1|_{\partial\Omega},\ u_2|_{\partial\Omega} \underset{2}{\longrightarrow} \Psi_{12}|_{\partial\Omega},\ \Psi_{21}|_{\partial\Omega} \underset{3}{\longrightarrow} S(k) \underset{4}{\longrightarrow} M(z,0) \underset{5}{\longrightarrow} Q(z) \underset{6}{\longrightarrow} \gamma(z)$$

are presented.

6.1 The Steps of the Full Nonlinear Reconstruction Algorithm

We now have all the necessary steps for a direct reconstruction algorithm:

1. Compute the exponentially growing solutions $u_1(z,k)$ and $u_2(z,k)$ to the admittivity equation from the boundary integral formulas (5.32) and (5.37)

$$\begin{aligned} u_1(z,k)|_{\partial\Omega} &= \left.\frac{e^{ikz}}{ik}\right|_{\partial\Omega} - \int_{\partial\Omega} G_k(z-\zeta)(\Lambda_\gamma - \Lambda_1)u_1(\zeta,k)dS(\zeta) \\ u_2(z,k)|_{\partial\Omega} &= \left.\frac{e^{-ik\bar{z}}}{-ik}\right|_{\partial\Omega} - \int_{\partial\Omega} G_k(-\bar{z}+\bar{\zeta})(\Lambda_\gamma - \Lambda_1)u_2(\zeta,k)dS(\zeta). \end{aligned}$$

2. Compute the off diagonal entries of the CGO solution $\Psi(z,k)$ for $z \in \partial\Omega$ from the boundary integral formulas (5.51) and (5.52)

$$\begin{aligned} \Psi_{12}(z,k) &= \int_{\partial\Omega} \frac{e^{i\bar{k}(z-\zeta)}}{4\pi(z-\zeta)} \left[\Lambda_\gamma - \Lambda_1\right] u_2(\zeta,k)\ dS(\zeta) \\ \Psi_{21}(z,k) &= \int_{\partial\Omega} \overline{\left[\frac{e^{ik(z-\zeta)}}{4\pi(z-\zeta)}\right]} \left[\Lambda_\gamma - \Lambda_1\right] u_1(\zeta,k)\ dS(\zeta). \end{aligned}$$

3. Compute the off-diagonal entries of the scattering matrix $S_\gamma(k)$ from (5.49) and (5.50)

$$\begin{aligned} S_{12}(k) &= \frac{\mathrm{i}}{2\pi}\int_{\partial\Omega} e^{-i\bar{k}z}\Psi_{12}(z,k)(\nu_1 + i\nu_2)dS(z) \\ S_{21}(k) &= -\frac{\mathrm{i}}{2\pi}\int_{\partial\Omega} e^{i\bar{k}\bar{z}}\Psi_{21}(z,k)(\nu_1 - i\nu_2)dS(z). \end{aligned}$$

4. Solve the $\bar{\partial}_k$-equation (3.21) for the matrix $M(z,k)$

$$\bar{\partial}_k M(z,k) = M(z,\bar{k}) \begin{pmatrix} e(z,\bar{k}) & 0 \\ 0 & e(z,-k) \end{pmatrix} S_\gamma(k).$$

5. Reconstruct the matrix potential Q from Theorem 10 using equations (5.59) and (5.60)

$$Q_{12}(z) = \frac{\bar{\partial}_z M_+(Q,z,0)}{M_-(Q,z,0)} \quad Q_{21}(z) = \frac{\partial_z M_-(Q,z,0)}{M_+(Q,z,0)}.$$

6. Use the definition of the matrix potential Q, (3.8) or (3.9) to compute $\log(\gamma)$

$$\log(\gamma(z)) = -\frac{2}{\pi}\int_{\mathbb{C}} \frac{Q_{12}(\zeta)}{\bar{z}-\bar{\zeta}}\, d\mu(\zeta) = -\frac{2}{\pi}\int_{\mathbb{C}} \frac{Q_{21}(\zeta)}{z-\zeta}\, d\mu(\zeta)$$

and exponentiate to recover the admittivity distribution γ.

6.2 Step 0: Implementation of the D-N Map on the Boundary of the Unit Disc:

The first examples that we will look at will be on the unit disc, however, the goal is to work with experimental data where the radius is often not one. We introduce a D-N map with two subscripts, the first corresponding to the admittivity, while the second to the radius of the domain. We may need to use the following relation between the D-N map for a circular domain of radius 1 and admittivity γ, namely $\Lambda_{\gamma,1}$, and the D-N map for a circular domain of radius r and admittivity γ, namely $\Lambda_{\gamma,r}$ [DM10, IMNS04]:

$$\Lambda_{\gamma,1} = r\Lambda_{\gamma,r}, \tag{6.1}$$

when using simulated and experimental data from tanks of non-unitary radii. In addition, the theory of the algorithm was derived with $\gamma \equiv 1$ near the boundary whereas for many practical applications this is not true. We will approximate the value of γ near $\partial\Omega$ by the best constant admittivity approximation to fit the measured data, denoted by γ_{best}, using a complex version of the method presented in [JIEN97]. We will then scale the admittivity γ by:

$$\tilde{\gamma} \equiv \gamma/\gamma_{\text{best}}. \tag{6.2}$$

We may then use the corresponding, scaled, D-N map given by

$$\Lambda_{\tilde{\gamma},1} = \frac{1}{\gamma_{\text{best}}}\Lambda_{\gamma,1}, \tag{6.3}$$

when solving the inverse problem. Therefore, the D-N map corresponding to a circular domain of radius 1 and scaled admittivity $\tilde{\gamma}$ (close to one) can be related to the D-N map corresponding to a circular domain of radius r and original admittivity γ via:

$$\Lambda_{\tilde{\gamma},1} = \frac{r}{\gamma_{\text{best}}} \Lambda_{\gamma,r}. \tag{6.4}$$

Since the admittivity equation (3.3) assumes $\gamma \equiv 1$ on the boundary, the D-N map will need to be scaled by the best constant admittivity γ_{best}. However, as the formulas for the scattering transforms, (5.49) and (5.50), only require that the domain of the potential matrix $Q(z)$ has compact support (not necessarily the unit disc), we can choose to either

(i) scale the D-N map according to the radius r of our practical domain and evaluate the scattering transforms $S_{12}(k)$ and $S_{21}(k)$ for a disc of radius 1 (using (6.4))

(ii) work with the D-N map that corresponds to the radius r of our practical domain and evaluate the scattering transforms $S_{12}(k)$ and $S_{21}(k)$ for a disc of radius r (using (6.3)).

We will work with option (i) now and option (ii) later in Section 7.

The theory requires knowledge of the voltages that arise from any possible current pattern. However, in practice, this is not possible as we are working with a finite number L of electrodes. If we use the *trigonometric basis functions* (described in Appendix B) that are commonly used at Rensselaer Polytechnic Institute and Dartmouth College, there are $L-1$ linearly independent current patterns. Other devices may use different current patterns and therefore have a different number of linearly independent current patterns (but never exceeding $L-1$). For example, there are $L-(n+1)$ linearly independent current patterns for the *skip-n* basis of current patterns commonly used at the University of São Paulo in Brazil [CCG08, VBOM04, CLA09]. The case with skip-n current patterns will be described in Section 6.10.

6.2.1 Discretization of the Dirichlet-to-Neumann Map Λ_γ

Here the discrete approximation to the D-N map for the trigonometric current patterns is explained. Let $T_\ell^j = T(\ell, j)$ denote the value of the j-th trigonometric current pattern

applied on the ℓ-th electrode calculated by,

$$T(\ell, j) = \begin{cases} \mathfrak{M}\cos(j\theta_\ell), & j = 1, \ldots, \frac{L}{2} - 1 \\ \mathfrak{M}\cos(\pi\ell), & j = \frac{L}{2} \\ \mathfrak{M}\sin\left(\left(j - \frac{L}{2}\right)\theta_\ell\right), & j = \frac{L}{2}, \ldots, L-1, \end{cases} \tag{6.5}$$

where $\mathfrak{M}$ is the amplitude of the applied current, $\ell = 1, \ldots, L$ and $\theta_\ell = \frac{2\pi\ell}{L}$. Let V_ℓ^j denote the voltage on the ℓ-th electrode that arises from applying the j-th current pattern. The data, i.e. the current pattern matrix T and the voltage matrix V, need to be normalized so that the following are satisfied.

1. Each current pattern T^j has an ℓ^2 norm of 1,

$$\Phi^j = \frac{T^j}{\|T^j\|_{\ell^2}}, \quad \text{where } \|T^j\|_{\ell^2} = \sqrt{\sum_{\ell=1}^{L} \left(T_\ell^j\right)^2}.$$

   Physically, this is equivalent to ensuring conservation of charge.

2. The voltages over all L electrodes are adjusted so that they sum to zero (for each current pattern Φ^j), and will be denoted by $\tilde{V}^j$

$$\sum_{\ell=1}^{L} \tilde{V}_\ell^j = 0, \quad j = 1, \ldots, L-1.$$

   Physically, this is equivalent to specifying a ground and therefore guaranteeing a unique solution.

3. The adjusted voltages $\tilde{V}$ are then scaled by the ℓ^2 norm of the current patterns

$$v^j = \frac{\tilde{V}^j}{\|T^j\|_{\ell^2}}.$$

   Note that the voltages must be scaled since we normalized the current patterns.

Let $R_{\gamma,r}$ denote the Neumann-to-Dirichlet (current-density-to-voltage) operator corresponding to an admittivity $\gamma(z)$ in a disc of radius r. We relate the N-D map (calculated from the experimental data) to the D-N map (which is needed for the reconstruction of the CGO solutions u_1, u_2, Ψ_{12}, and Ψ_{21}) as follows,

$$\Lambda_{\gamma,r} = \left(\Lambda_{\gamma,r}\right)^{-1}, \tag{6.6}$$

where B^{-1} denotes the inverse of a matrix B. We can model the applied current density $j(z)$ on the $\partial\Omega$ using the *gap model* (See Appendix A),

$$j(z) = \begin{cases} \frac{\Phi_\ell}{A_\ell}, & z \in \partial\Omega \\ 0, & \text{else,} \end{cases}$$

where A_ℓ is the area of the ℓ-th electrode. Let $R^M_{\gamma,r}$ denote the discrete matrix approximation of the N-D map $R_{\gamma,r}$ where the (m,n)-th entry is defined by,

$$R^M_{\gamma,r}(m,n) = \left(\frac{\Phi^m_\ell}{A_\ell}, v^n_\ell\right) = \sum_{\ell=1}^{L} \frac{\Phi^m_\ell v^n_\ell}{A_\ell}. \tag{6.7}$$

Recall that the boundary integral equations (BIEs) for the CGO solutions Ψ_{12} and Ψ_{21} require knowledge of the $\delta\Lambda$ operator defined by

$$\delta\Lambda = \Lambda_\gamma - \Lambda_1.$$

To approximate Λ_1, the N-D map corresponding to a constant admittivity of 1, the forward admittivity problem $\nabla \cdot \gamma\nabla u = 0$ is solved using the Finite Element Method for the prescribed constant admittivity 1 (see Appendix B for details of how to implement the Finite Element Method for the forward admittivity problem). Therefore, the $\delta\Lambda$ operator may be approximated via

$$(\delta\Lambda)^M = \left(R^M_{\gamma,r}\right)^{-1} - \left(R^M_{1,r}\right)^{-1}, \tag{6.8}$$

where the superscript ^{M} is used to emphasize that this is a discrete matrix approximation. See [IMNS04] for a more detailed explanation of the discrete approximation for the D-N map.

6.3 Step 1: Implementation of the BIEs for the Exponentially Growing Solutions $u_1(z,k)$ and $u_2(z,k)$ for z on the Boundary of a Circular Domain:

To reconstruct the exponentially growing solutions $u_1(z,k)$ and $u_2(z,k)$ for z on the boundary of a circular domain (via formulas (5.32) and (5.37)), we follow the approach outlined by DeAngelo and Mueller [DM10].

We wish to discretize (5.32) and (5.37). In fact, we will solve

$$u_1(z,k) - \frac{1}{\mathrm{i}\,k} = \frac{e^{\mathrm{i}\,zk}}{\mathrm{i}\,k} - \frac{1}{\mathrm{i}\,k} - \int_{\partial\Omega} G_k(z-\zeta)\delta\Lambda u_1(\zeta,k)\, dS(\zeta) \tag{6.9}$$

$$u_2(z,k) - \frac{1}{\mathrm{i}\,k} = \frac{e^{-\mathrm{i}\,\bar{z}k}}{-\mathrm{i}\,k} - \frac{1}{\mathrm{i}\,k} - \int_{\partial\Omega} G_k(-\bar{z}+\bar{\zeta})\delta\Lambda u_2(\zeta,k)\, dS(\zeta), \tag{6.10}$$

for $z \in \partial\Omega$ and $k \in \mathbb{C}\setminus 0$. Using the basis of normalized trigonometric current patterns Φ, we expand the the exponential terms $\frac{e^{\mathrm{i}\,kz}}{\mathrm{i}\,k} - \frac{1}{\mathrm{i}\,k}$ and $\frac{e^{-\mathrm{i}\,\bar{z}k}}{-\mathrm{i}\,k} - \frac{1}{\mathrm{i}\,k}$ for values of z that correspond to the positions of the centers of the L electrodes (denoted by z_ℓ):

$$\frac{e^{\mathrm{i}\,z_\ell k}}{\mathrm{i}\,k} - \frac{1}{\mathrm{i}\,k} \approx \sum_{j=1}^{L-1} \alpha_j(k)\Phi_\ell^j, \quad \ell = 1,\ldots,L \tag{6.11}$$

$$\frac{e^{-\mathrm{i}\,\bar{z}_\ell k}}{-\mathrm{i}\,k} - \frac{1}{\mathrm{i}\,k} \approx \sum_{j=1}^{L-1} \beta_j(k)\Phi_\ell^j, \quad \ell = 1,\ldots,L. \tag{6.12}$$

We similarly expand $u_1 - \frac{1}{\mathrm{i}\,k}$ and $u_2 - \frac{1}{\mathrm{i}\,k}$ using the normalized trigonometric basis of current patterns Φ:

$$u_1(z_\ell,k) - \frac{1}{\mathrm{i}\,k} \approx \sum_{j=1}^{L-1} a_j(k)\Phi_\ell^j, \quad \ell = 1,\ldots,L \tag{6.13}$$

$$u_2(z_\ell,k) - \frac{1}{\mathrm{i}\,k} \approx \sum_{j=1}^{L-1} b_j(k)\Phi_\ell^j, \quad \ell = 1,\ldots,L. \tag{6.14}$$

Let $\vec{a}$ denote the column vector $\vec{a}(k) = [a_1(k),\ldots,a_{L-1}(k)]^T$ where here the superscript ^{T} denotes the transpose of a matrix/vector. Similarly define $\vec{b}$, $\vec{\alpha}$, and $\vec{\beta}$. Since

$$\delta\Lambda\left(\frac{1}{\mathrm{i}\,k}\right) = \frac{1}{\mathrm{i}\,k}\delta\Lambda(1) = 0,$$

we have

$$\delta\Lambda\left(u_1\right) = \delta\Lambda\left(u_1 - \frac{1}{\mathrm{i}\,k}\right) \quad \text{and} \quad \delta\Lambda\left(u_2\right) = \delta\Lambda\left(u_2 - \frac{1}{\mathrm{i}\,k}\right), \tag{6.15}$$

and thus we can use the expansions of $u_1 - \frac{1}{\mathrm{i}\,k}$ and $u_2 - \frac{1}{\mathrm{i}\,k}$ in the boundary integrals in (6.9) and (6.10) as follows

$$\begin{aligned} u_1(z_\ell,k) - \frac{1}{\mathrm{i}\,k} &= \frac{e^{\mathrm{i}\,z_\ell k}}{\mathrm{i}\,k} - \frac{1}{\mathrm{i}\,k} - \int_{\partial\Omega} G_k\left(z_\ell - \zeta\right)\delta\Lambda\left[u_1(\zeta,k) - \frac{1}{\mathrm{i}\,k}\right]\, dS(\zeta) \\ u_2(z_\ell,k) - \frac{1}{\mathrm{i}\,k} &= \frac{e^{-\mathrm{i}\,\bar{z}_\ell k}}{-\mathrm{i}\,k} - \frac{1}{\mathrm{i}\,k} - \int_{\partial\Omega} G_k(-\bar{z}_\ell + \bar{\zeta})\delta\Lambda\left[u_2(\zeta,k) - \frac{1}{\mathrm{i}\,k}\right]\, dS(\zeta), \end{aligned}$$

for $\ell = 1,\ldots,L$. As the D-N map corresponds to measurements taken on the electrodes e_ℓ for $\ell = 1,\ldots,L$, we only know how the difference in D-N maps, $\delta\Lambda$, acts for boundary values ζ corresponding to the centers of the electrodes, namely for $\zeta = z_\ell$, $\ell = 1,\ldots,L$. Let $E_{\ell'}$ denote the ℓ'-th subdivision of the boundary $\partial\Omega$ ($\ell' = 1,\ldots,L$) centered at $z_{\ell'}$ with length P/L where P denotes the perimeter of the domain. Splitting the integral over $\partial\Omega$

into a sum of integrals over the subsections $E_{\ell'}$

$$\begin{aligned} u_1(z_\ell,k)-\frac{1}{\mathrm{i}\,k} &\approx \frac{e^{\mathrm{i}\,z_\ell k}}{\mathrm{i}\,k}-\frac{1}{\mathrm{i}\,k}-\sum_{\ell'=1}^{L}\int_{E_{\ell'}} G_k\left(z_\ell-\zeta\right)\delta\Lambda\left[u_1(\cdot,k)-\frac{1}{\mathrm{i}\,k}\right]\Big|_{\zeta_{\ell'}} dS(\zeta) \\ &= \frac{e^{\mathrm{i}\,z_\ell k}}{\mathrm{i}\,k}-\frac{1}{\mathrm{i}\,k}-\sum_{\ell'=1}^{L}\int_{E_{\ell'}} G_k\left(z_\ell-\zeta\right)\ dS(\zeta)\ \delta\Lambda\left[u_1(\zeta_{\ell'},k)-\frac{1}{\mathrm{i}\,k}\right]. \end{aligned}$$

Using the expansions for $u_1-\frac{1}{\mathrm{i}\,k}$ and $\frac{e^{\mathrm{i}\,kz}}{\mathrm{i}\,k}-\frac{1}{\mathrm{i}\,k}$, (6.13) and (6.11) respectively, we have

$$\begin{aligned} \sum_{j=1}^{L-1} a_j(k)\Phi_\ell^j &\approx \sum_{j=1}^{L-1}\alpha_j(k)\Phi_\ell^j-\sum_{\ell'=1}^{L}\int_{E_{\ell'}} G_k\left(z_\ell-\zeta\right)\ dS(\zeta)\ \delta\Lambda\sum_{j=1}^{L-1} a_j(k)\Phi_{\ell'}^j \\ &= \sum_{j=1}^{L-1}\alpha_j(k)\Phi_\ell^j-\sum_{\ell'=1}^{L}\int_{E_{\ell'}} G_k\left(z_\ell-\zeta\right)\ dS(\zeta)\sum_{j=1}^{L-1} a_j(k) f_j\left(\zeta_{\ell'}\right), \end{aligned}$$

where $f_j\left(\zeta_{\ell'}\right)$ denotes the action of the discretized $(\delta\Lambda)^M$ matrix on the j-th normalized trigonometric basis function evaluated at the center of the ℓ'-th electrode ($\ell'=1,\ldots,L$). Let

$$\tilde{\mathbf{G}}_k(\ell,\ell')=\begin{cases} G_k\left(z_\ell,\zeta_{\ell'}\right) & \ell\neq\ell' \\ \frac{1}{\mathrm{d}\theta}\int_{E_{\ell'}} G_k(z_\ell-\zeta)\,dS(\zeta) & \ell=\ell', \end{cases} \tag{6.16}$$

where $\mathrm{d}\theta=|E_{\ell'}|$ is the length of the subdivision $E_{\ell'}$ of the boundary of the unit circle. Then

$$\sum_{j=1}^{L-1} a_j(k)\Phi_\ell^j \approx \sum_{j=1}^{L-1}\alpha_j(k)\Phi_\ell^j-\mathrm{d}\theta\sum_{j=1}^{L-1} a_j(k)\sum_{\ell'=1}^{L}\tilde{\mathbf{G}}_k(\ell,\ell')f_j\left(\zeta_{\ell'}\right). \tag{6.17}$$

Following DeAngelo and Mueller ([DM10]),

$$f_p(\zeta_{\ell'})\approx\left(\Phi(\delta\Lambda)^M\right)(\ell',j), \tag{6.18}$$

i.e., the (ℓ',j) entry in the matrix resulting from multiplication of the normalized current pattern matrix Φ and the discretized difference in D-N maps $(\delta\Lambda)^M$. Using the properties of matrix multiplication, equation (6.17) can be rewritten as

$$\sum_{j=1}^{L-1} a_j(k)\Phi_\ell^j=\sum_{j=1}^{L-1}\alpha_j(k)\Phi_\ell^j-\mathrm{d}\theta\sum_{j=1}^{L-1} a_j(k)\left(\tilde{\mathbf{G}}_k\Phi(\delta\Lambda)^M\right)(\ell,j),$$

or equivalently,

$$\Phi\vec{a}=\Phi\vec{\alpha}-\mathrm{d}\theta\tilde{\mathbf{G}}_k\Phi(\delta\Lambda)^M\vec{a},$$

a matrix equation for the unknown coefficients $\vec{a}$ which are needed in the normalized trigonometric basis expansion of $u_1-\frac{1}{\mathrm{i}\,k}$.

Using the orthonormality of the normalized trigonometric basis functions in the matrix Φ, we multiply both sides of the equation by Φ^T, and then solve

$$(I + A)\vec{a} = \vec{\alpha}, \tag{6.19}$$

where

$$A = \mathrm{d}\theta \Phi^T \tilde{\mathbf{G}}_k \Phi (\delta\Lambda)^M. \tag{6.20}$$

For each value of $k \in \mathbb{C}\backslash 0$, we solve the system (6.19) using GMRES for the unknown coefficients $\vec{a}$ and then reconstruct $u_1 - \frac{1}{\mathrm{i}k}$ for the specified value of k via (6.13).

Numerical experimentation has shown that the standard Green's function for the Laplacian $G_0(z-\zeta)$

$$G_0(z-\zeta) := -\frac{1}{2\pi} \log|z-\zeta|, \tag{6.21}$$

is a good approximation to $G_k(z-\zeta)$ [MS03, DM10]. In this thesis, the G_0 approximation on the boundary $\partial\Omega$ is used in (6.20). In [DM10], the singularity that occurs at $\zeta = z_\ell$ in G_0 is dealt with by setting the value to zero. In that work, an $L \times L$ matrix $\tilde{\mathbf{G}}_0$ is defined whose (ℓ, ℓ') entry is given by,

$$\tilde{\mathbf{G}}_0(\ell,\ell') = \tilde{\mathbf{G}}_0(z_\ell - \zeta_{\ell'}) := \begin{cases} G_0(z_\ell - \zeta_{\ell'}) & \text{if } \arg(z_\ell - \zeta_{\ell'}) \geq \text{tol} \\ 0 & \text{otherwise,} \end{cases} \tag{6.22}$$

where $\ell,\ \ell' = 1, \ldots, L$ and *tol* represents a tolerance threshold that one may adjust. In this thesis, will instead use (6.16), replacing G_k by G_0. As we must compute an integral over the boundary, we make use of the fact that the singularity in G_0 is an integrable singularity. We now deal with the singularity at $z_\ell = \zeta$ by calculating the value of

$$\int_{E_\ell} G_0(z_\ell - \zeta)\, dS(\zeta)$$

analytically for a circular domain. If the electrodes are placed uniformly around the boundary of the domain, we only need to calculate the value of this integral for one value of ℓ. Fixing an electrode e_ℓ, and integrating over the corresponding section of the boundary E_ℓ,

$$\int_{E_\ell} G_0(z_\ell - \zeta)\, dS(\zeta) = -\frac{1}{2\pi} \int_{E_\ell} \log|z_\ell - \zeta|\ dS(\zeta),$$

where $z_\ell = e^{\mathrm{i}\,\theta_\ell}$ is at the center of e_ℓ on E_ℓ. Thus, thus the maximum distance between z_ℓ and ζ on E_ℓ is given by

$$\begin{aligned} |z_\ell - \zeta| &\leq \left| e^{\mathrm{i}\,\theta_\ell} - e^{\mathrm{i}(\theta_\ell - \pi/L)} \right| \\ &= \left| e^{\mathrm{i}\,\theta_\ell} \left(1 - e^{-\,\mathrm{i}\,\pi/L}\right) \right| \\ &= \left| 1 - e^{-\,\mathrm{i}\,\pi/L} \right| \\ &= \sqrt{2 - 2\cos\left(\pi/L\right)}. \end{aligned}$$

Therefore,

$$\begin{aligned} -\frac{1}{2\pi} \int_{E_\ell} \log|z_\ell - \zeta| \; dS(\zeta) &= -\frac{2}{2\pi} \int_0^{\sqrt{2-2\cos(\pi/L)}} \log(x) \; dx \\ &= -\frac{1}{\pi} \left[x\log(x) - x \right] \Big|_{x=0}^{x=\sqrt{2-2\cos(\pi/L)}} \\ &= -\frac{1}{\pi} \sqrt{2 - 2\cos\left(\pi/L\right)} \left[\log\left(\sqrt{2 - 2\cos\left(\pi/L\right)} \right) - 1 \right], \end{aligned}$$

and we can approximate the diagonal entries of the $\tilde{\mathbf{G}}_0$ matrix by

$$\tilde{\mathbf{G}}_0(\ell,\ell) := -\frac{L}{2\pi^2} \sqrt{2 - 2\cos\left(\pi/L\right)} \left[\log\left(\sqrt{2 - 2\cos\left(\pi/L\right)} \right) - 1 \right], \tag{6.23}$$

since $\mathrm{d}\theta = \frac{2\pi}{L}$ is the length of the subdivision E_ℓ containing e_ℓ. Similarly, for a disc of radius R,

$$\tilde{\mathbf{G}}_0(\ell,\ell) := -\frac{L}{2\pi^2} \sqrt{2 - 2\cos\left(\pi/L\right)} \left[\log(R) + \log\left(\sqrt{2 - 2\cos\left(\pi/L\right)} \right) - 1 \right]. \tag{6.24}$$

Figure 6.1 shows the approximation to G_0 given in (6.22) as well as the approximation with the corrected diagonal entry given by using (6.23). Figure 6.2 compares the approximations from (6.22) and (6.24) for a disc of radius 0.150m. Notice that for the unit disc, the diagonal entries of the new G_0 are set to approximately 0.5284 instead of 0, and 0.8302 instead of 0 for the $r = 0.150$m case.

Note that the boundary integral equation (6.10) for u_2 requires $G_0(-\bar{z} + \bar{\zeta})$ instead of $G_0(z - \zeta)$. Due to the definition of G_0 in (6.21),

$$G_0(z - \zeta) := -\frac{1}{2\pi} \log|z - \zeta| = G_0(-\bar{z} + \bar{\zeta}).$$

Therefore, in an analogous fashion, the unknown coefficients $\vec{b}$ for u_2 (using G_0) may be found via

$$(I + A)\vec{b} = \vec{\beta}, \tag{6.25}$$

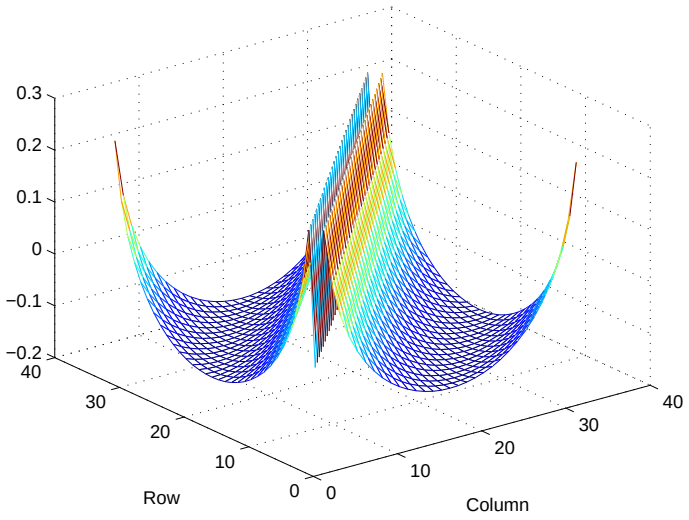

(a) $\tilde{\mathbf{G}}_0$ from (6.22)

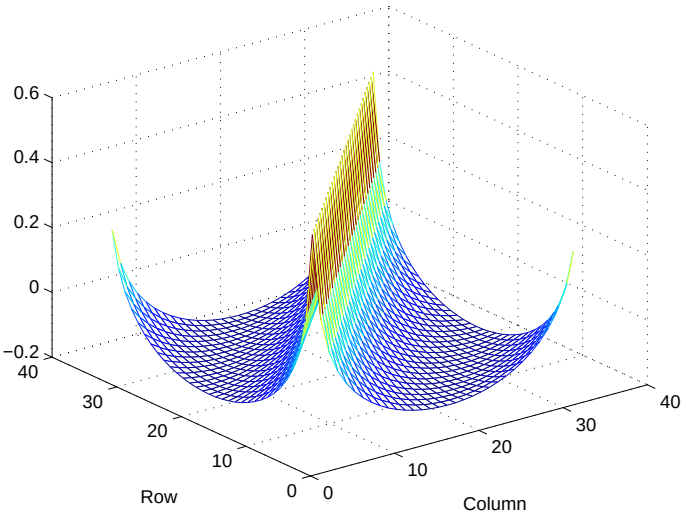

(b) $\tilde{\mathbf{G}}_0$ using (6.23)

Fig. 6.1: Comparison of the $\tilde{\mathbf{G}}_0$ approximation given in (6.22) (a) and the new approximation given in (6.23) for the unit disc (b).

where A is the same matrix defined above in (6.20) and $u_2 - \frac{1}{\mathrm{i}k}$ may be reconstructed via (6.14).

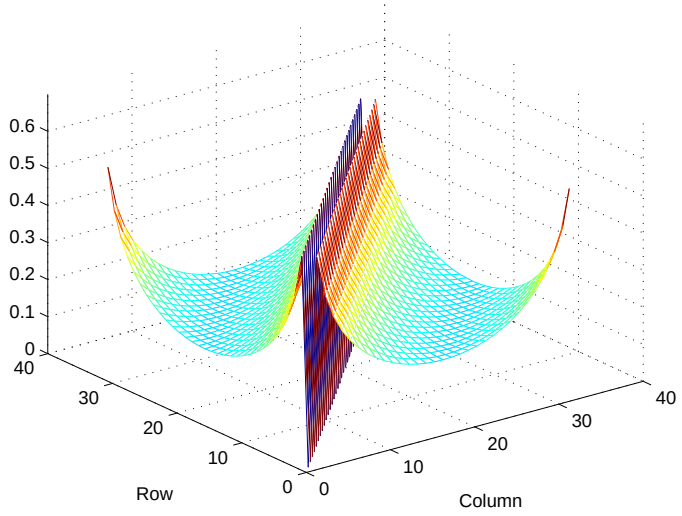

(a) $\tilde{\mathbf{G}}_0$ from (6.22)

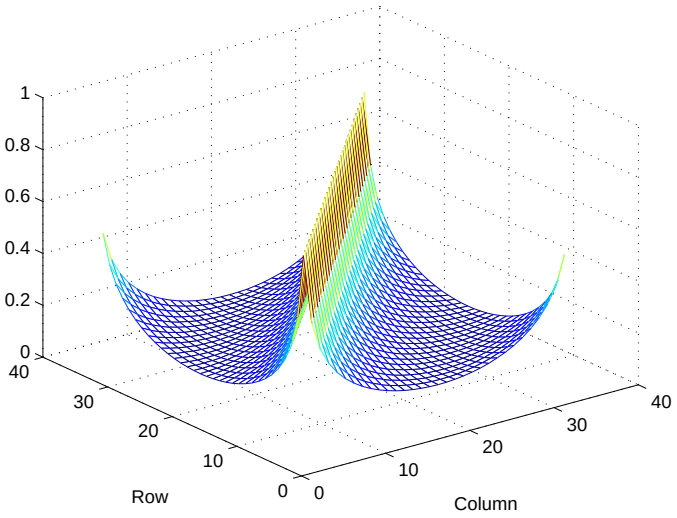

(b) $\tilde{\mathbf{G}}_0$ using (6.24)

Fig. 6.2: Comparison of the $\tilde{\mathbf{G}}_0$ approximation given in (6.22) (a) and the new approximation given in (6.23) for a disc of radius $r = 0.150$m (b).

6.4 Step 2: Implementation of the BIEs for the CGO Solutions $\Psi_{12}(z,k)$ and $\Psi_{21}(z,k)$ for z on the boundary of a Circular Domain:

Now that we have solved for the adjusted exponentially growing solutions $u_1 - \frac{1}{\mathrm{i}k}$ and $u_2 - \frac{1}{\mathrm{i}k}$ on the boundary, we can evaluate the CGO solutions Ψ_{12} and Ψ_{21}. Recall the formulas for

Ψ_{12} and Ψ_{21} on the boundary (5.51) and (5.52)

$$\begin{aligned}\Psi_{12}(z,k) &= \int_{\partial\Omega} \frac{e^{\mathrm{i}\,\bar{k}(z-\zeta)}}{4\pi(z-\zeta)}\delta\Lambda(\zeta)u_2(\zeta,k)\,dS(\zeta)\\ \Psi_{21}(z,k) &= \int_{\partial\Omega} \overline{\left[\frac{e^{\mathrm{i}\,k(z-\zeta)}}{4\pi(z-\zeta)}\right]}\delta\Lambda(\zeta)u_1(\zeta,k)\,dS(\zeta).\end{aligned}$$

Although $u_1 - \frac{1}{\mathrm{i}\,k}$ and $u_2 - \frac{1}{\mathrm{i}\,k}$ were computed above in Step 1, only the action of the difference in D-N maps $\delta\Lambda$ on u_1 and similarly u_2 is needed. However, by (6.15) this does not present a challenge.

When solving for the adjusted exponentially growing solutions $u_1 - \frac{1}{\mathrm{i}\,k}$ and $u_2 - \frac{1}{\mathrm{i}\,k}$ above in Step 1, we already learned how to compute a very similar version of the boundary integral equations for Ψ_{12} and Ψ_{21}! The main difference is that we will not need to use GMRES as we have already calculated the unknown coefficients $\vec{a}$ and $\vec{b}$ that are needed for the evaluation of $\delta\Lambda(\zeta)u_2(\zeta,k)$ and $\delta\Lambda(\zeta)u_1(\zeta,k)$ in the boundary integrals above for Ψ_{21} and Ψ_{12} respectively. In addition, the Faddeev's Green's function $G_k(z-\zeta)$ is now replaced with its ∂_{z} and $\bar{\partial}_{\mathrm{z}}$ derivatives for Ψ_{12} and Ψ_{21} respectively. As it turns out, these functions also arose in the work of Kim Knudsen [Knu02] when he implemented an algorithm based on the global uniqueness result of Brown and Uhlmann for real valued conductivities in $W^{1,p}$ for $p > 2$, [BU97] (see Section 5.3.1 for another set of boundary integral equations derived using methods similar to Knudsen).

The singularities in $\partial_{\mathrm{z}} G_k(-\bar{z}+\bar{\zeta})$ and $\bar{\partial}_{\mathrm{z}} G_k(z-\zeta)$ for $z = \zeta$ are set to zero when implementing the boundary integrals, as was done in the original approximation to the G_0 operator in [DM10], giving the approximation

$$\partial_{\mathrm{z}} G_k(-\bar{z}_n + \bar{\zeta}_{\ell'}) \approx \begin{cases} \frac{e^{\mathrm{i}\,\bar{k}(z_n-\zeta_{\ell'})}}{4\pi(z_n-\zeta_{\ell'})} & \text{if } \arg(z_n-\zeta_{\ell'}) \geq \text{tol} \\ 0 & \text{otherwise,}\end{cases}$$

$$\bar{\partial}_{\mathrm{z}} G_k(z_n - \zeta_{\ell'}) \approx \begin{cases} \overline{\left[\frac{e^{\mathrm{i}\,k(z_n-\zeta_{\ell'})}}{4\pi(z_n-\zeta_{\ell'})}\right]} & \text{if } \arg(z_n-\zeta_{\ell'}) \geq \text{tol} \\ 0 & \text{otherwise,}\end{cases}$$

for $\ell' = 1,\ldots,L$ and $n = 1,\ldots,N_z$ where N_z is the number of evaluation points z along the boundary $\partial\Omega$. For ease of notation, let

$$\begin{aligned}\Gamma(n,\ell') &= \partial_{\mathrm{z}} G_k(-\bar{z}_n + \bar{\zeta}_{\ell'})\\ \tilde{\Gamma}(n,\ell') &= \bar{\partial}_{\mathrm{z}} G_k(z_n - \zeta_{\ell'}).\end{aligned}$$

Then, vectors of CGO solutions Ψ_{12} and Ψ_{21} for z_n along the boundary can be approximated via

$$\Psi_{12} \approx \frac{2\pi}{L}\Gamma\Phi(\delta\Lambda)^M\vec{b} \tag{6.26}$$

$$\Psi_{21} \approx \frac{2\pi}{L}\tilde{\Gamma}\Phi(\delta\Lambda)^M\vec{a} \tag{6.27}$$

and this process is repeated for each value of k.

6.5 Step 3: Evaluation of the Scattering transform $S(k)$

The values of the CGO solutions Ψ_{12} and Ψ_{21} are subsequently used in the evaluation of the scattering transform $S(k)$. The off-diagonal entries of the scattering transform matrix, namely $S_{12}(k)$ and $S_{21}(k)$, were computed inside the square $[-K, K]^2$ (with $k = 0$ not included since the formulas for the CGO solutions do not hold for $k = 0$). Using finite sums, (5.49) and (5.50) can be approximated

$$S_{12}(k) \approx \frac{\mathrm{i}}{N_z}\sum_{n=1}^{N_z} e^{-i\bar{k}z_n}\Psi_{12}(z_n, k)z_n \tag{6.28}$$

$$S_{21}(k) \approx -\frac{\mathrm{i}}{N_z}\sum_{n=1}^{N_z} e^{i\bar{k}\overline{z_n}}\Psi_{21}(z_n, k)\overline{z_n}, \tag{6.29}$$

where z_n denotes the coordinate the n^{th} equally spaced evaluation point around the boundary of Ω (in this case the unit disc) and N_z denotes the total number of such points along the boundary. The factors of 2π in the denominator (originally appearing in (5.49) and (5.50)) cancel with the width of the subintervals $\frac{2\pi}{N_z}$.

6.6 Step 4: Solution of the $\bar{\partial}_k$-equation

In this step the scattering transforms computed in Step 3, from Equations (6.28) and (6.29), are used to set up and solve the $\bar{\partial}_k$-equation (3.21) presented in Theorem 4.1 of Francini [Fra00] (see Theorem 3 in this thesis). We aim to solve the system (3.21) for the CGO solutions $M(z, k)$ over a region Ω containing the support of $Q(z)$. Writing out the terms of

the $\bar{\partial}_k$-equation in more detail, one can see that

$$\begin{aligned}
\bar{\partial}_k M(z,k) &= M(z,\bar{k}) \begin{bmatrix} e(z,\bar{k}) & 0 \\ 0 & e(z,-k) \end{bmatrix} S(k) \\
&= \begin{bmatrix} M_{11}(z,\bar{k}) & M_{12}(z,\bar{k}) \\ M_{21}(z,\bar{k}) & M_{22}(z,\bar{k}) \end{bmatrix} \begin{bmatrix} e(z,\bar{k}) & 0 \\ 0 & e(z,-k) \end{bmatrix} \begin{bmatrix} 0 & S_{12}(k) \\ S_{21}(k) & 0 \end{bmatrix} \\
&= \begin{bmatrix} M_{12}(z,\bar{k})e(z,-k)S_{21}(k) & M_{11}(z,\bar{k})e(z,\bar{k})S_{12}(k) \\ M_{22}(z,\bar{k})e(z,-k)S_{21}(k) & M_{21}(z,\bar{k})e(z,\bar{k})S_{12}(k) \end{bmatrix}
\end{aligned}$$

resulting in the following two systems of equations,

$$\begin{cases} \bar{\partial}_k M_{11}(z,k) = & M_{12}(z,\bar{k})e(z,-k)S_{21}(k) \\ \bar{\partial}_k M_{12}(z,k) = & M_{11}(z,\bar{k})e(z,\bar{k})S_{12}(k) \end{cases}, \tag{6.30}$$

and

$$\begin{cases} \bar{\partial}_k M_{21}(z,k) = & M_{22}(z,\bar{k})e(z,-k)S_{21}(k) \\ \bar{\partial}_k M_{22}(z,k) = & M_{21}(z,\bar{k})e(z,\bar{k})S_{12}(k) \end{cases}. \tag{6.31}$$

Due to the coupling, one can solve two separate systems using the scattering transforms $S_{12}(k)$ and $S_{21}(k)$ computed in Step 3.

We first aim to solve the system in equation (6.30)

$$\begin{cases} \bar{\partial}_k M_{11}(z,k) = & M_{12}(z,\bar{k})e(z,-k)S_{21}(k) \\ \bar{\partial}_k M_{12}(z,k) = & M_{11}(z,\bar{k})e(z,\bar{k})S_{12}(k) \end{cases}$$

using Vainikko's one-grid method generalized for systems. The Generalized Cauchy Integral Formula is used to invert the $\bar{\partial}_k$ operator, taking into account the asymptotics of the CGO solutions $M(z,k)$. This results in

$$\begin{aligned}
M_{11}(z,k) &= 1 + \frac{1}{\pi}\int_{\mathbb{C}} \frac{M_{12}(z,\bar{\tilde{k}})e(z,-\tilde{k})S_{21}(\tilde{k})}{k-\tilde{k}}\, d\mu(\tilde{k}) \\
M_{12}(z,k) &= 0 + \frac{1}{\pi}\int_{\mathbb{C}} \frac{M_{11}(z,\bar{\tilde{k}})e(z,\bar{\tilde{k}})S_{12}(\tilde{k})}{k-\tilde{k}}\, d\mu(\tilde{k})
\end{aligned}$$

or using convolution,

$$\begin{cases} M_{11}(z,k) = & 1 + \frac{1}{\pi k} * \big(M_{12}(z,\bar{k})e(z,-k)S_{21}(k)\big) \\ M_{12}(z,k) = & \frac{1}{\pi k} * \big(M_{11}(z,\bar{k})e(z,\bar{k})S_{12}(k)\big) \end{cases}.$$

The problem is now reduced to solving

$$\begin{cases} 1 = & M_{11}(z,k) - \frac{1}{\pi k} * \big(M_{12}(z,\bar{k})e(z,-k)S_{21}(k)\big) \\ 0 = & M_{12}(z,k) - \frac{1}{\pi k} * \big(M_{11}(z,\bar{k})e(z,\bar{k})S_{12}(k)\big) \end{cases}, \tag{6.32}$$

using Vainikko's one-grid Method. To solve this system, we write functions in MATLAB to implement the action of the operation and use GMRES in a similar fashion as for the

forward $D_k M = QM$ problem (see Chapter 4). We will only need to use one Green's function this time, i.e. the Green's function for the $\bar{\partial}_k$ operator. To deal with the $M(z, \bar{k})$ terms (rather than $M(z, k)$), we solve the system on a grid with the origin at the center and an odd number of grid points in both the horizonal and vertical directions. Then, we merely perform the appropriate flip (**flipud** for a grid that was created using MATLAB's **meshgrid** function) to ensure that we access the correct entries in the CGO solution matrix. Additionally, we we need to solve the problem on the same k-grid for multiple values of z so that we have the solution values $M(z, k)$ over a region that contains Ω in the z-variable. After each solve of the $\bar{\partial}_k$ equation for a specific value of $\tilde{z}$, we store the entry of the matrix $M(\tilde{z}, k)$ corresponding to the $k = 0$ entry is stored in a new matrix $M(\tilde{z}, 0)$ for each value of $\tilde{z}$. This is done for both $M_{11}(z, k)$ and $M_{12}(z, k)$. As the two equations are coupled, they must be solved simultaneously using GMRES. In practice, a finite k-grid is used and therefore the convolution will only be computed over a finite, rather than infinite, grid. One can also think of this as truncating the scattering transform $S(k)$. As it turns out, the numerical evaluation of the scattering transform (from data) can blow up as $|k| \to \infty$ in certain directions. This is consistent with the scattering transform in [Nac96] for real valued conductivities, and the truncation radius has been shown to be a regularization method [KLMS09].

Notice that the multiplier functions in (6.32) do not have compact support even though the scattering transforms decay rapidly to zero as $|k|$ tends towards infinity which could be contributing to the blowup.

The system in equation (6.31)

$$\begin{cases} \bar{\partial}_k M_{21}(z, k) = & M_{22}(z, \bar{k}) e(z, -k) S_{21}(k) \\ \bar{\partial}_k M_{22}(z, k) = & M_{21}(z, \bar{k}) e(z, \bar{k}) S_{12}(k) \end{cases}$$

is solved in an analogous manner as (6.30).

6.7 Step 5: Computation of the Matrix Potential Q via the M to Q Formulas

After solving the $\bar{\partial}_k$-equation via (6.30) and (6.31) in Step 4 above for the CGO solutions $M(z, 0)$, we use Theorem 10 to recover the potential matrix $Q(z)$. Per the theorem,

$$Q_{12}(z) = \frac{\bar{\partial}_z M_+(Q, z, 0)}{M_-(Q, z, 0)} \quad Q_{21}(z) = \frac{\partial_z M_-(Q, z, 0)}{M_+(Q, z, 0)},$$

where M_+ and M_- are formed via (5.61) and (5.62)

$$\begin{aligned} M_+(Q,z,k) &= M_{11}(Q,z,k) + e(z,-k)M_{12}(Q,z,k) \\ M_-(Q,z,k) &= M_{22}(Q,z,k) + e(z,k)M_{21}(Q,z,k). \end{aligned}$$

Therefore the ∂_z and $\bar{\partial}_z$ derivatives of $M_-(z,0)$ and $M_+(z,0)$ respectively are needed. First order centered finite differences are used to approximate the ∂_z and $\bar{\partial}_z$ operators. By definition, the ∂_z and $\bar{\partial}_z$ derivatives of a function $f(z) = f(x,y)$ at a given point (x_j, y_p) are given by,

$$\begin{aligned} \partial_z f(x_j,y_p) &= \frac{1}{2}\left[\frac{\partial}{\partial x} f(x_j,y_p) - \mathrm{i}\,\frac{\partial}{\partial y} f(x_j,y_p)\right] \\ &\approx \frac{1}{2}\left[\frac{f(x_{j+1},y_p) - f(x_{j-1},y_p)}{2h_x} - \mathrm{i}\,\frac{f(x_j,y_{p+1}) - f(x_j,y_{p-1})}{2h_y}\right] \\ &= \frac{1}{4h}\Big[f(x_{j+1},y_p) - f(x_{j-1},y_p) - \mathrm{i}\,f(x_j,y_{p+1}) + \mathrm{i}\,f(x_j,y_{p-1})\Big] \end{aligned}$$

and

$$\begin{aligned} \bar{\partial}_z f(x_j,y_p) &= \frac{1}{2}\left[\frac{\partial}{\partial x} f(x_j,y_p) + \mathrm{i}\,\frac{\partial}{\partial y} f(x_j,y_p)\right] \\ &\approx \frac{1}{2}\left[\frac{f(x_{j+1},y_p) - f(x_{j-1},y_p)}{2h_x} + \mathrm{i}\,\frac{f(x_j,y_{p+1}) - f(x_j,y_{p-1})}{2h_y}\right] \\ &= \frac{1}{4h}\Big[f(x_{j+1},y_p) - f(x_{j-1},y_p) + \mathrm{i}\,f(x_j,y_{p+1}) - \mathrm{i}\,f(x_j,y_{p-1})\Big] \end{aligned}$$

where h_x and h_y denote the stepsize in the x and y directions respectively. For convenience we have taken $h_x = h_y = h$.

The matrices needed to calculate $\bar{\partial}_z f(x,y) = \bar{\partial}_z f(z)$ for a grid with 4 points in each of the x and y directions, i.e., for (x_j, y_p) where $1 \le j,p \le 4$ are described below. Let $f(x_j,y_p) = f_{pj}$, then the following is nearly the $\bar{\partial}_z$ derivative of $f(z)$ for $z = (x_j, y_p)$ on the

grid $1 \leq j, p \leq 4$

$$\begin{bmatrix}
0 & \mathrm{i} & 0 & 0 & 1 & 0 & 0 & 0 & 0 & 0 & 0 & 0 & 0 & 0 & 0 & 0 \\
-\mathrm{i} & 0 & \mathrm{i} & 0 & 0 & 1 & 0 & 0 & 0 & 0 & 0 & 0 & 0 & 0 & 0 & 0 \\
0 & -\mathrm{i} & 0 & \mathrm{i} & 0 & 0 & 1 & 0 & 0 & 0 & 0 & 0 & 0 & 0 & 0 & 0 \\
0 & 0 & -\mathrm{i} & 0 & 0 & 0 & 0 & 1 & 0 & 0 & 0 & 0 & 0 & 0 & 0 & 0 \\
-1 & 0 & 0 & 0 & 0 & \mathrm{i} & 0 & 0 & 1 & 0 & 0 & 0 & 0 & 0 & 0 & 0 \\
0 & -1 & 0 & 0 & -\mathrm{i} & 0 & \mathrm{i} & 0 & 0 & 1 & 0 & 0 & 0 & 0 & 0 & 0 \\
0 & 0 & -1 & 0 & 0 & -\mathrm{i} & 0 & \mathrm{i} & 0 & 0 & 1 & 0 & 0 & 0 & 0 & 0 \\
0 & 0 & 0 & -1 & 0 & 0 & -\mathrm{i} & 0 & 0 & 0 & 0 & 1 & 0 & 0 & 0 & 0 \\
0 & 0 & 0 & 0 & -1 & 0 & 0 & 0 & 0 & \mathrm{i} & 0 & 0 & 1 & 0 & 0 & 0 \\
0 & 0 & 0 & 0 & 0 & -1 & 0 & 0 & -\mathrm{i} & 0 & \mathrm{i} & 0 & 0 & 1 & 0 & 0 \\
0 & 0 & 0 & 0 & 0 & 0 & -1 & 0 & 0 & -\mathrm{i} & 0 & \mathrm{i} & 0 & 0 & 1 & 0 \\
0 & 0 & 0 & 0 & 0 & 0 & 0 & -1 & 0 & 0 & -\mathrm{i} & 0 & 0 & 0 & 0 & 1 \\
0 & 0 & 0 & 0 & 0 & 0 & 0 & 0 & -1 & 0 & 0 & 0 & 0 & \mathrm{i} & 0 & 0 \\
0 & 0 & 0 & 0 & 0 & 0 & 0 & 0 & 0 & -1 & 0 & 0 & -\mathrm{i} & 0 & \mathrm{i} & 0 \\
0 & 0 & 0 & 0 & 0 & 0 & 0 & 0 & 0 & 0 & -1 & 0 & 0 & -\mathrm{i} & 0 & \mathrm{i} \\
0 & 0 & 0 & 0 & 0 & 0 & 0 & 0 & 0 & 0 & 0 & -1 & 0 & 0 & -\mathrm{i} & 0
\end{bmatrix}
\begin{bmatrix} f_{11} \\ f_{21} \\ f_{31} \\ f_{41} \\ f_{12} \\ f_{22} \\ f_{32} \\ f_{42} \\ f_{13} \\ f_{23} \\ f_{33} \\ f_{34} \\ f_{14} \\ f_{24} \\ f_{34} \\ f_{44} \end{bmatrix}$$

$$= \begin{bmatrix}
\mathrm{i}\, f(x_1, y_2) + f(x_2, y_1) \\
-\mathrm{i}\, f(x_1, y_1) + \mathrm{i}\, f(x_1, y_3) + f(x_2, y_2) \\
-\mathrm{i}\, f(x_1, y_2) + \mathrm{i}\, f(x_1, y_4) + f(x_2, y_3) \\
-\mathrm{i}\, f(x_1, y_3) + f(x_2, y_4) \\
-f(x_1, y_1) + \mathrm{i}\, f(x_2, y_2) + f(x_3, y_1) \\
-f(x_1, y_2) - \mathrm{i}\, f(x_2, y_1) + \mathrm{i}\, f(x_2, y_3) + f(x_3, y_2) \\
-f(x_1, y_3) - \mathrm{i}\, f(x_2, y_2) + \mathrm{i}\, f(x_2, y_4) + f(x_3, y_3) \\
-f(x_1, y_4) - \mathrm{i}\, f(x_2, y_3) + f(x_3, y_4) \\
-f(x_2, y_1) + \mathrm{i}\, f(x_3, y_2) + f(x_4, y_1) \\
-f(x_2, y_2) - \mathrm{i}\, f(x_3, y_1) + \mathrm{i}\, f(x_3, y_3) + f(x_4, y_2) \\
-f(x_2, y_3) - \mathrm{i}\, f(x_3, y_2) + \mathrm{i}\, f(x_3, y_4) + f(x_4, y_3) \\
-f(x_2, y_4) - \mathrm{i}\, f(x_3, y_3) + f(x_4, y_4) \\
-f(x_2, y_1) + \mathrm{i}\, f(x_3, y_2) \\
-f(x_2, y_2) - \mathrm{i}\, f(x_3, y_1) + \mathrm{i}\, f(x_3, y_3) \\
-f(x_2, y_3) - \mathrm{i}\, f(x_3, y_2) + \mathrm{i}\, f(x_3, y_4) \\
-f(x_2, y_4) - \mathrm{i}\, f(x_3, y_3)
\end{bmatrix}.$$

However, this ignores the terms that would be present at the boundary which are represented

in red below,

$$\begin{bmatrix} -f(x_0,y_1) - \mathrm{i}\, f(x_1,y_0) + \mathrm{i}\, f(x_1,y_2) + f(x_2,y_1) \\ -f(x_0,y_2) - \mathrm{i}\, f(x_1,y_1) + \mathrm{i}\, f(x_1,y_3) + f(x_2,y_2) \\ -f(x_0,y_3) - \mathrm{i}\, f(x_1,y_2) + \mathrm{i}\, f(x_1,y_4) + f(x_2,y_3) \\ -f(x_0,y_4) - \mathrm{i}\, f(x_1,y_3) + \mathrm{i}\, f(x_1,y_5) + f(x_2,y_4) \\ -f(x_1,y_1) - \mathrm{i}\, f(x_2,y_0) + \mathrm{i}\, f(x_2,y_2) + f(x_3,y_1) \\ -f(x_1,y_2) - \mathrm{i}\, f(x_2,y_1) + \mathrm{i}\, f(x_2,y_3) + f(x_3,y_2) \\ -f(x_1,y_3) - \mathrm{i}\, f(x_2,y_2) + \mathrm{i}\, f(x_2,y_4) + f(x_3,y_3) \\ -f(x_1,y_4) - \mathrm{i}\, f(x_2,y_3) + \mathrm{i}\, f(x_2,y_5) + f(x_3,y_4) \\ -f(x_2,y_1) - \mathrm{i}\, f(x_3,y_0) + \mathrm{i}\, f(x_3,y_2) + f(x_4,y_1) \\ -f(x_2,y_2) - \mathrm{i}\, f(x_3,y_1) + \mathrm{i}\, f(x_3,y_3) + f(x_4,y_2) \\ -f(x_2,y_3) - \mathrm{i}\, f(x_3,y_2) + \mathrm{i}\, f(x_3,y_4) + f(x_4,y_3) \\ -f(x_2,y_4) - \mathrm{i}\, f(x_3,y_3) + \mathrm{i}\, f(x_3,y_5) + f(x_4,y_4) \\ -f(x_2,y_1) - \mathrm{i}\, f(x_4,y_0) + \mathrm{i}\, f(x_3,y_2) + f(x_5,y_1) \\ -f(x_2,y_2) - \mathrm{i}\, f(x_3,y_1) + \mathrm{i}\, f(x_3,y_3) + f(x_5,y_2) \\ -f(x_2,y_3) - \mathrm{i}\, f(x_3,y_2) + \mathrm{i}\, f(x_3,y_4) + f(x_5,y_3) \\ -f(x_2,y_4) - \mathrm{i}\, f(x_3,y_3) + \mathrm{i}\, f(x_4,y_5) + f(x_5,y_4) \end{bmatrix} \approx 4h \begin{bmatrix} \bar\partial_{\mathrm{z}} f(x_1,y_1) \\ \bar\partial_{\mathrm{z}} f(x_1,y_2) \\ \bar\partial_{\mathrm{z}} f(x_1,y_3) \\ \bar\partial_{\mathrm{z}} f(x_1,y_4) \\ \bar\partial_{\mathrm{z}} f(x_2,y_1) \\ \bar\partial_{\mathrm{z}} f(x_2,y_2) \\ \bar\partial_{\mathrm{z}} f(x_2,y_3) \\ \bar\partial_{\mathrm{z}} f(x_2,y_4) \\ \bar\partial_{\mathrm{z}} f(x_3,y_1) \\ \bar\partial_{\mathrm{z}} f(x_3,y_2) \\ \bar\partial_{\mathrm{z}} f(x_3,y_3) \\ \bar\partial_{\mathrm{z}} f(x_3,y_4) \\ \bar\partial_{\mathrm{z}} f(x_4,y_1) \\ \bar\partial_{\mathrm{z}} f(x_4,y_2) \\ \bar\partial_{\mathrm{z}} f(x_4,y_3) \\ \bar\partial_{\mathrm{z}} f(x_4,y_4) \end{bmatrix}.$$

The boundary condition of $f(z)$ outside the mesh, (x_j, y_p) where $1 \le j,p \le 4$, is used to determine $f(x_j,y_p)$ for $j,p = 0,5$. In this case, $f(z) = M_+(z,0)$ and by the definition of $M_+(z,k)$,

$$M_+(z,0) = M_{11}(z,0) + M_{12}(z,0),$$

and thus $M_+ \sim 1$ outside the mesh due to the asymptotic conditions for the CGO solutions M_{11} and M_{12}. Therefore the $\bar\partial_{\mathrm{z}}$ derivative of M_+ can be approximated via

$$\bar\partial_{\mathrm{z}} M_+(z,0) = \frac{1}{4h}\Big(\mathfrak{D}\left[\mathrm{vec}\left(M_+\right)\right] + \mathfrak{B}\Big) \tag{6.33}$$

where

$$\mathfrak{D} = \begin{bmatrix} 0 & \mathrm{i} & 0 & 0 & 1 & 0 & 0 & 0 & 0 & 0 & 0 & 0 & 0 & 0 & 0 & 0 \\ -\mathrm{i} & 0 & \mathrm{i} & 0 & 0 & 1 & 0 & 0 & 0 & 0 & 0 & 0 & 0 & 0 & 0 & 0 \\ 0 & -\mathrm{i} & 0 & \mathrm{i} & 0 & 0 & 1 & 0 & 0 & 0 & 0 & 0 & 0 & 0 & 0 & 0 \\ 0 & 0 & -\mathrm{i} & 0 & 0 & 0 & 0 & 1 & 0 & 0 & 0 & 0 & 0 & 0 & 0 & 0 \\ -1 & 0 & 0 & 0 & 0 & \mathrm{i} & 0 & 0 & 1 & 0 & 0 & 0 & 0 & 0 & 0 & 0 \\ 0 & -1 & 0 & 0 & -\mathrm{i} & 0 & \mathrm{i} & 0 & 0 & 1 & 0 & 0 & 0 & 0 & 0 & 0 \\ 0 & 0 & -1 & 0 & 0 & -\mathrm{i} & 0 & \mathrm{i} & 0 & 0 & 1 & 0 & 0 & 0 & 0 & 0 \\ 0 & 0 & 0 & -1 & 0 & 0 & -\mathrm{i} & 0 & 0 & 0 & 0 & 1 & 0 & 0 & 0 & 0 \\ 0 & 0 & 0 & 0 & -1 & 0 & 0 & 0 & 0 & \mathrm{i} & 0 & 0 & 1 & 0 & 0 & 0 \\ 0 & 0 & 0 & 0 & 0 & -1 & 0 & 0 & -\mathrm{i} & 0 & \mathrm{i} & 0 & 0 & 1 & 0 & 0 \\ 0 & 0 & 0 & 0 & 0 & 0 & -1 & 0 & 0 & -\mathrm{i} & 0 & \mathrm{i} & 0 & 0 & 1 & 0 \\ 0 & 0 & 0 & 0 & 0 & 0 & 0 & -1 & 0 & 0 & -\mathrm{i} & 0 & 0 & 0 & 0 & 1 \\ 0 & 0 & 0 & 0 & 0 & 0 & 0 & 0 & -1 & 0 & 0 & 0 & 0 & \mathrm{i} & 0 & 0 \\ 0 & 0 & 0 & 0 & 0 & 0 & 0 & 0 & 0 & -1 & 0 & 0 & -\mathrm{i} & 0 & \mathrm{i} & 0 \\ 0 & 0 & 0 & 0 & 0 & 0 & 0 & 0 & 0 & 0 & -1 & 0 & 0 & -\mathrm{i} & 0 & \mathrm{i} \\ 0 & 0 & 0 & 0 & 0 & 0 & 0 & 0 & 0 & 0 & 0 & -1 & 0 & 0 & -\mathrm{i} & 0 \end{bmatrix},$$

and

$$\mathfrak{B} = \begin{bmatrix} -\mathrm{i}-1 \\ -1 \\ -1 \\ \mathrm{i}-1 \\ -\mathrm{i} \\ 0 \\ 0 \\ \mathrm{i} \\ -\mathrm{i} \\ 0 \\ 0 \\ \mathrm{i} \\ -\mathrm{i}+1 \\ 1 \\ 1 \\ \mathrm{i}+1 \end{bmatrix}.$$

Since the asymptotic condition for $M_-(z,0)$ is 1 as well, the ∂_{z} derivative of $M_-(z,0)$ can be approximated similarly via

$$\partial_{\mathrm{z}} M_-(z,0) = \frac{1}{4h}\left(\overline{\mathfrak{D}}\left[\mathrm{vec}\left(M_-\right)\right] + \overline{\mathfrak{B}}\right) \tag{6.34}$$

where $\overline{\mathfrak{D}}$ and $\overline{\mathfrak{B}}$ denote the complex conjugates of $\mathfrak{D}$ and $\mathfrak{B}$ respectively.

6.8 Step 6: Recovery of the admittivity $\gamma(z)$

The admittivity distribution $\gamma(z)$ can be recovered from the formula for the matrix potential $Q(z)$ given in (3.6),

$$Q_{12}(z) = -\frac{1}{2}\,\partial_{\mathrm{z}}\left(\log\gamma(z)\right) \qquad Q_{21}(z) = -\frac{1}{2}\,\bar{\partial}_{\mathrm{z}}\left(\log\gamma(z)\right),$$

and subsequently

$$\gamma(z) = \exp\left\{-2\,{\partial_{\mathrm{z}}}^{-1}\left(Q_{12}(z)\right)\right\} \tag{6.35}$$

$$= \exp\left\{-2\,{\bar{\partial}_{\mathrm{z}}}^{-1}\left(Q_{21}(z)\right)\right\}. \tag{6.36}$$

6.8.1 Numerical Implementation of Q to γ Formulas

In order to solve

$$-2Q_{21}(z) = \bar{\partial}_{\mathrm{z}} \log\left(\gamma(z)\right)$$

for the admittivity γ one must first invert the $\bar{\partial}_z$-operator. Letting $v(z) = \log\gamma(z)$ and $f(z) = -2Q_{21}(z)$ we have, by the Generalized Cauchy Integral Formula,

$$\begin{aligned} v(z) &= \frac{1}{\pi}\int_{\mathbb{C}} \frac{f(\zeta)}{z-\zeta}\, d\mu(\zeta) \\ &= (g * f)(z) \end{aligned}$$

where

$$g(z) = \frac{1}{\pi z}.$$

Therefore, we have

$$\begin{aligned} \log\gamma(z) &= \frac{1}{\pi}\int_{\mathbb{C}} \frac{-2Q_{21}(\zeta)}{z-\zeta}\, d\mu(\zeta) \\ &= -2\log\left(\gamma|_{\partial\Omega}\right) + \frac{1}{\pi}\int_{\partial\Omega} \frac{-2Q_{21}(\zeta)}{z-\zeta}\, d\mu(\zeta) \qquad (6.37) \\ &= \frac{1}{\pi z} * \left(-2Q_{21}(z)\right), \qquad (6.38) \end{aligned}$$

due to the compact support of the matrix potential Q and the requirement that $\gamma \equiv 1$ on the boundary. Thus, by the assumption that $\gamma \equiv 1$ outside Ω, there is no contribution along the boundary since $\log(1) = 0$.

Using this formulation, the problem can be solved using Fourier Transforms and Inverse Fourier Transforms. In practice, to evaluate the integral over Ω, both $-2Q_{21}(z)$ and $\frac{1}{\pi z}$ are evaluated on a z-grid where the origin is not a node. We then compute the 2D Fast Fourier Transform of $-2Q_{21}(z)$ and multiply point-wise by the 2D Fast Fourier Transform of $\frac{1}{\pi z}$ since the Fourier transform of a convolution is merely the product of the two Fourier Transforms. We then perform the 2D Inverse Fast Fourier Transform to recover the value of the original integral over Ω. Finally, we exponentiate to recover the admittivity distribution $\gamma(z)$.

6.9 Numerical Results for Trigonometric Current Patterns

In this section several test problems simulating a simplified cross-section of a human torso represented by a circular domain are considered. The text and figures in this section are quoted from our recent paper [HHMV12]. In each example, the admittivity is given by $\gamma = \sigma + \mathrm{i}\,\epsilon$. That is, the imaginary component includes the temporal angular frequency ω.

Since this is a known value, there is no loss of generality in representing γ this way in the simulations. We do not include units or frequency in these examples, since our purpose is to demonstrate that the equations in this work lead to a feasible reconstruction algorithm for complex admittivities.

The complete electrode model (CEM), originally described in [CING89], was implemented in the FEM in order to solve the forward admittivity problem. The CEM takes into account both the shunting effect of the electrodes and the contact impedances between the electrodes and tissue. Thus, the simulations included a simulated contact impedance effect on the electrodes. In our computations, Ω was chosen to be a disk of radius $0.15m$, and the FEM computations were performed on a mesh with 4538 triangular elements and 32 equispaced electrodes $0.029m \times 0.024m$ placed on the boundary. The effective contact impedance was chosen to be $z = 0.0057\Omega m^2$ on all electrodes in our simulations. The current amplitude was chosen to be $\mathfrak{M} = 2mA$, and the applied current patterns are the trigonometric patterns

$$I_\ell^j = \begin{cases} \mathfrak{M}\cos\left(j\theta_\ell\right), & 1 \le \ell \le L, \quad 1 \le j \le \frac{L}{2} \\ \mathfrak{M}\sin\left(\left(\frac{L}{2} - j\right)\theta_\ell\right), & 1 \le \ell \le L, \quad \frac{L}{2} + 1 \le j \le L - 1, \end{cases} \tag{6.39}$$

where $\theta_\ell = \frac{2\pi\ell}{L}$, $|e_\ell|$ is the area of the ℓ^{th} electrode, I_ℓ is the current on the ℓ^{th} electrode, and L denotes the total number of electrodes. As in [IMNS04, DM10], the currents were normalized to have ℓ^2-norm of 1, and the voltages were normalized accordingly. Also, the D-N map was scaled to represent data collected on the unit disk using the relation $\Lambda_{\gamma,1} = r\Lambda_{\gamma,r}$, where the second subscript represents the radius of the disk.

Where indicated, we added 0.01% Gaussian relative noise to the simulated voltages as follows. Denote the (complex-valued) vector of computed voltage for the j-th current pattern by V^j, let $\eta = 0.0001$ denote the noise level, and N a Gaussian random vector (generated by the `randn` commmand in MATLAB) that is unique for each use of the notation N. Denoting the noisy data by $\tilde{V}^j$ we then have $\tilde{V}^j = \mathrm{Re}(\tilde{V}^j) + i\,\mathrm{Im}(\tilde{V}^j)$ where

$$\begin{aligned} \mathrm{Re}(\tilde{V}^j) &= \mathrm{Re}(V^j) + \eta \max|\mathrm{Re}(V^j)|N \\ \mathrm{Im}(\tilde{V}^j) &= \mathrm{Im}(V^j) + \eta \max|\mathrm{Im}(V^j)|N. \end{aligned}$$

We solve the boundary integral equations (5.32) and (5.37) for the traces of the CGO solutions u_1 and u_2 for $k \in [-K, K]^2$, with K varying for each test problem in this work.

The solution $M(z,k)$, to the $\bar{\partial}_k$ equation (3.21), is computed in parallel by the method described in Section 6.6. The low-pass filtering by taking $k \in [-K,K]^2$ results in smooth functions M_{jp}, $j,p = 1,2$, which are differentiated by centered finite differences to recover Q_{21}, as described in Section 6.7. The admittivity γ was then computed by (6.38).

Define the dynamic range of the conductivity, and likewise the permittivity, by

$$\frac{\max \sigma^{(K)} - \min \sigma^{(K)}}{\max \sigma - \min \sigma} \cdot 100\%, \tag{6.40}$$

where the maximum and minimum values are taken on the computational grid for the reconstruction and $\sigma^{(K)}$ denotes the reconstructed conductivity σ that was computed using a scattering transform computed on the truncated k grid.

Example 1

The first test problem is an idealized cross-section of a chest with a background admittivity of $1+0\,\mathrm{i}$. Reconstructions from more realistic admittivity distributions or experimental data are the topic of future work. Figure 6.3 shows the values of the admittivity in the simulated heart and lungs. The scattering transform for the noise-free reconstructions was computed on a 128×128 grid for $k \in [-5.5,5.5]^2$ and can be found in Figure 6.4. Reconstructions of the CGO solutions $M(z,0)$ can be found in Figure 6.5. The reconstructed admittivity, shown in Figure 6.6, has a maximum conductivity and permittivity value of $1.1452 + 0.1802\,\mathrm{i}$, occurring in the heart region and a minimum of $0.8286 - 0.0247\,\mathrm{i}$, occurring in the lung region, resulting in a dynamic range of 79% for the conductivity and 60% for the permittivity when the negative permittivity value is set to 0. Although this decreases the dynamic range, we set the permittivity to 0 when it takes on a negative value in any pixel, since physically the permittivity cannot be less than 0. The reconstruction has the attributes of good spatial resolution and good uniformity in the reconstruction of the background and its value.

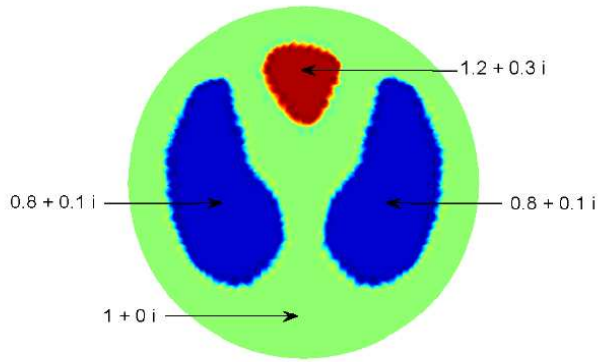

Fig. 6.3: The test problem in Example 1.

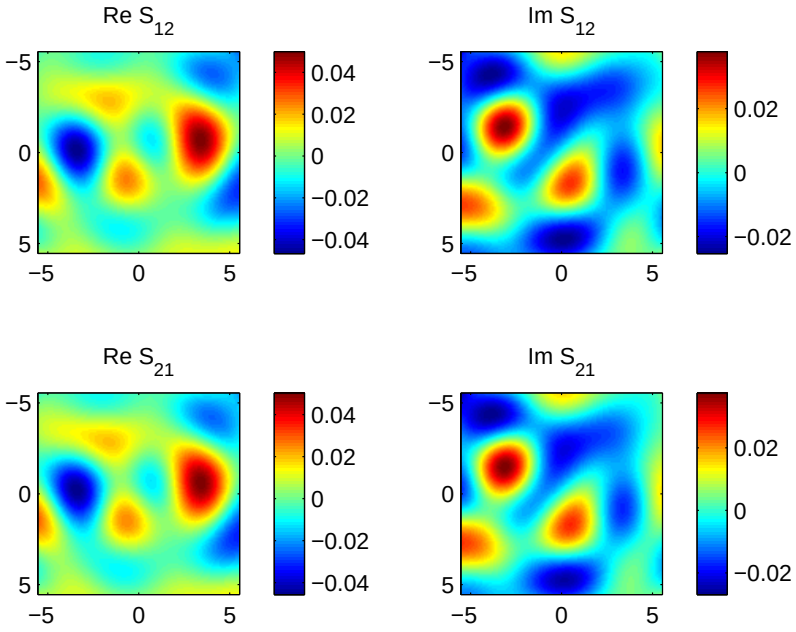

Fig. 6.4: Scattering data for Example 1 with zero added noise using trigonometric current patterns with $K = 5.5$.

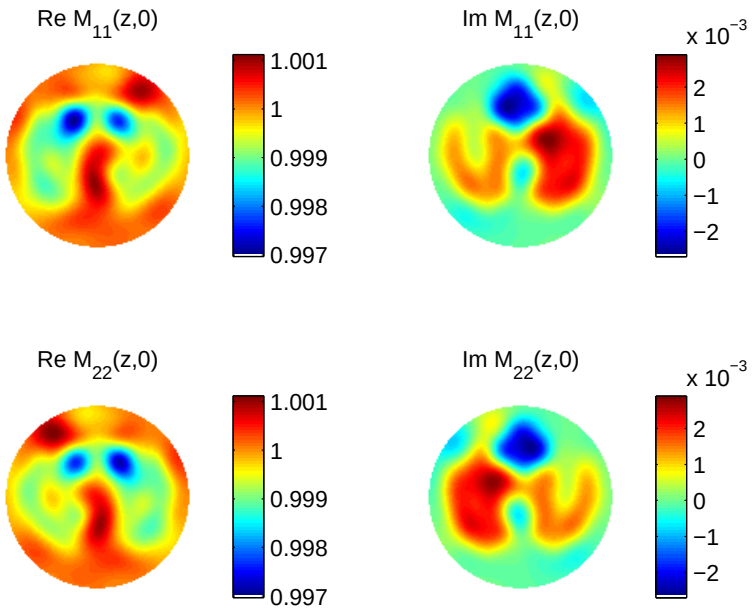

(a) $M_{11}(z,0)$ and $M_{22}(z,0)$

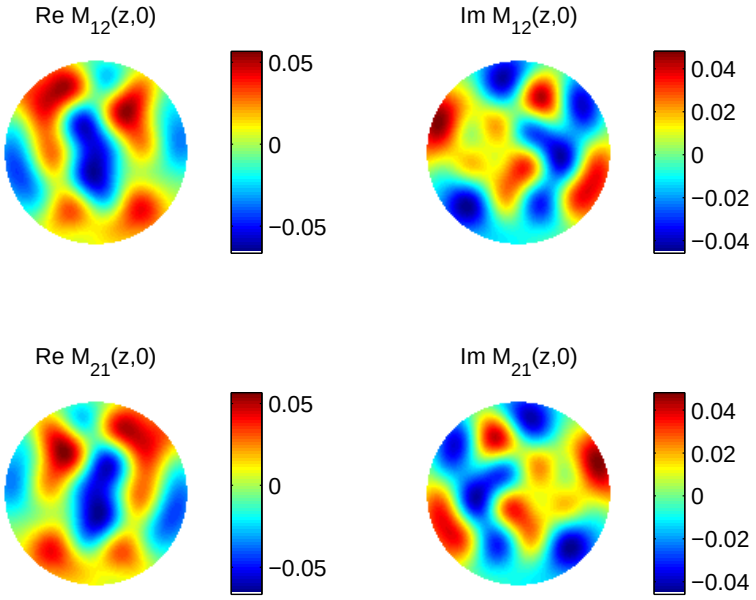

(b) $M_{12}(z,0)$ and $M_{21}(z,0)$

Fig. 6.5: CGO solutions $M(z,0)$ for Example 1 using trigonometric current patterns. Figure (a) shows the CGO solutions $M_{11}(z,0)$ and $M_{22}(z,0)$ for the zero noise case in Example 1 whereas (b) depicts the CGO solutions $M_{12}(z,0)$ and $M_{21}(z,0)$.

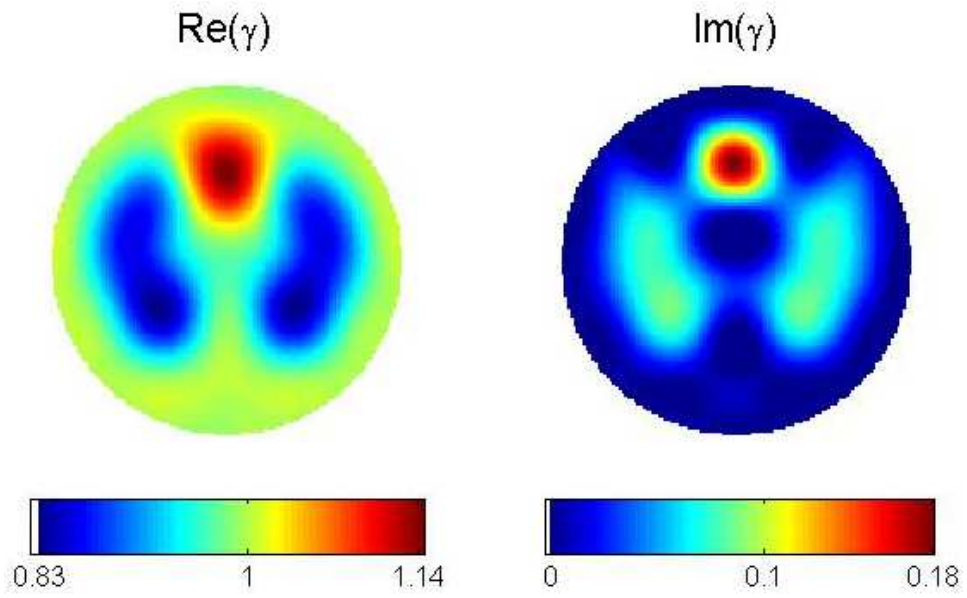

Fig. 6.6: Reconstruction from noise-free data for Example 1 with the real part of γ (conductivity) on the left, and the imaginary part (permittivity) on the right. The cut-off frequency was $K = 5.5$. The dynamic range is 79% for the conductivity, and 60% for the permittivity.

Example 2

This second example was chosen with conductivity values the same as in Example 1, but with permittivity values in which the "lungs" match the permittivity of the background. This is motivated by the fact that at some frequencies, physiological features may match that of the surrounding tissue in the conductivity or permittivity component. This example, purely for illustration, mimics that phenomenon. The admittivity values can be found in Figure 6.7.

Noise-free reconstructions were produced with the scattering transform computed on a 128×128 grid for $k \in [-5.5, 5.5]^2$ shown in Figure 6.8. Figure 6.9 shows the reconstructed CGO solutions $M(z, 0)$. Comparing the CGO reconstructions from Example 1 to those of Example 2, one clearly sees the absence of the "lungs" in the imaginary components of $M_{11}(z, 0)$ and $M_{22}(z, 0)$ in Example 2, shown in Figure 6.9(a), which are clearly present in the the imaginary components of $M_{11}(z, 0)$ and $M_{22}(z, 0)$, shown in Figure 6.5(a). This comparison is not unique to these examples and indicates that the CGO solutions $M(z, k)$ contain valuable information about the underlying admittivity. The reconstructed admittivity is shown in Figure 6.10 and has a maximum value of $1.1429 + 0.1828\,\mathrm{i}$, and minimum

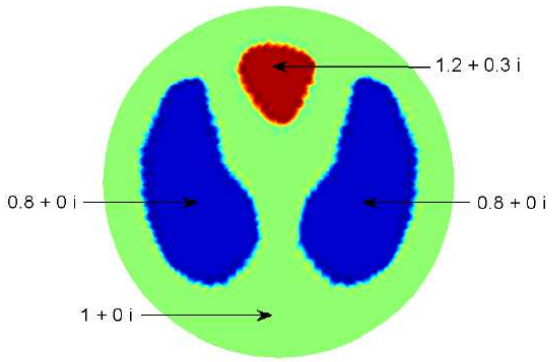

Fig. 6.7: The test problem in Example 2. Notice that in this case, the permittivity of the lungs matches the permittivity of the background, and so only the heart should be visible in the imaginary component of the reconstruction.

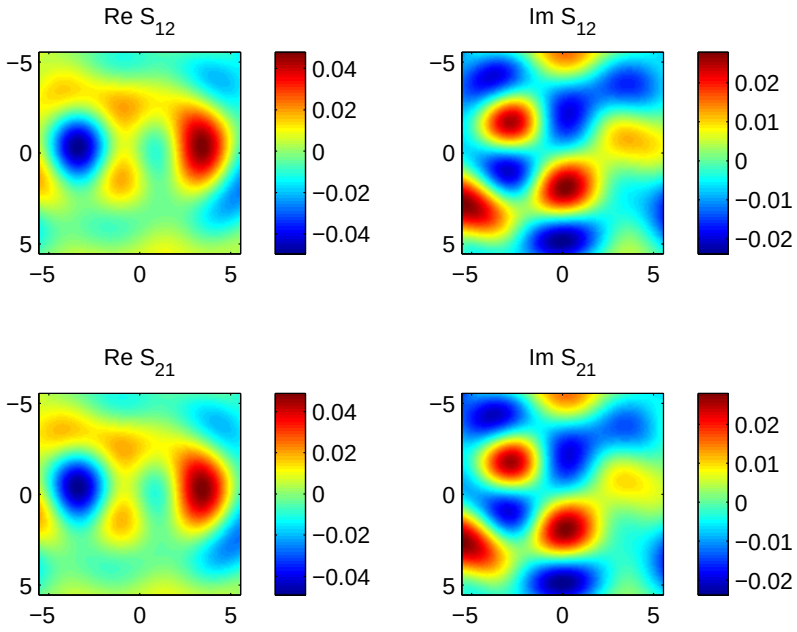

Fig. 6.8: Scattering data for Example 2 with zero added noise using trigonometric current patterns with $K = 5.5$.

value of $0.8271 - 0.0204\,\mathrm{i}$. In this example, the dynamic range is 79% for the conductivity and 61% for the permittivity when the negative permittivity value is set to 0. Again the spatial resolution is quite good, and the background is quite homogeneous, although some small artifacts are present in both the real and imaginary parts.

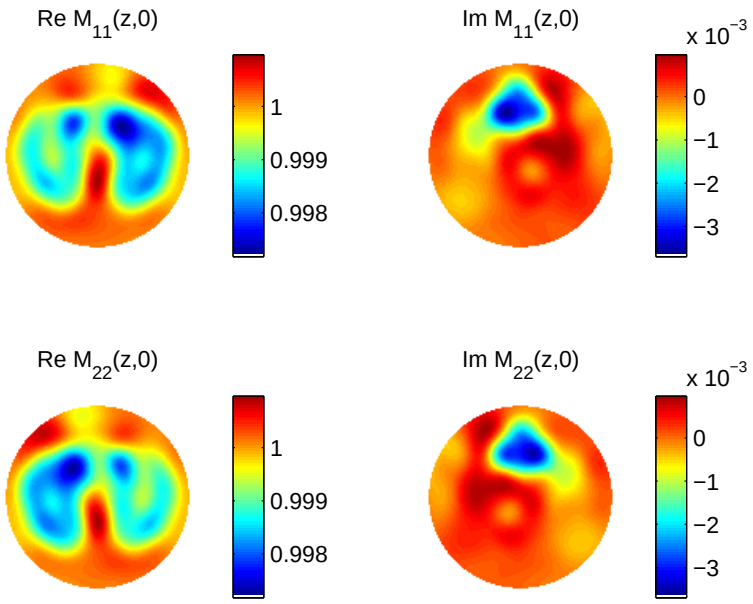

(a) $M_{11}(z,0)$ and $M_{22}(z,0)$

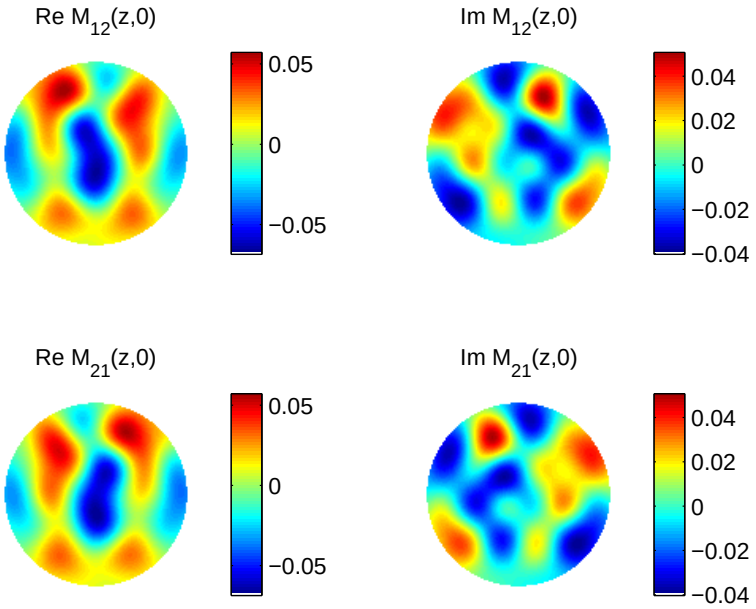

(b) $M_{12}(z,0)$ and $M_{21}(z,0)$

Fig. 6.9: CGO solutions $M(z,0)$ for Example 2 using trigonometric current patterns. Figure (a) shows the CGO solutions $M_{11}(z,0)$ and $M_{22}(z,0)$ for the zero noise case in Example 2 whereas (b) depicts the CGO solutions $M_{12}(z,0)$ and $M_{21}(z,0)$.

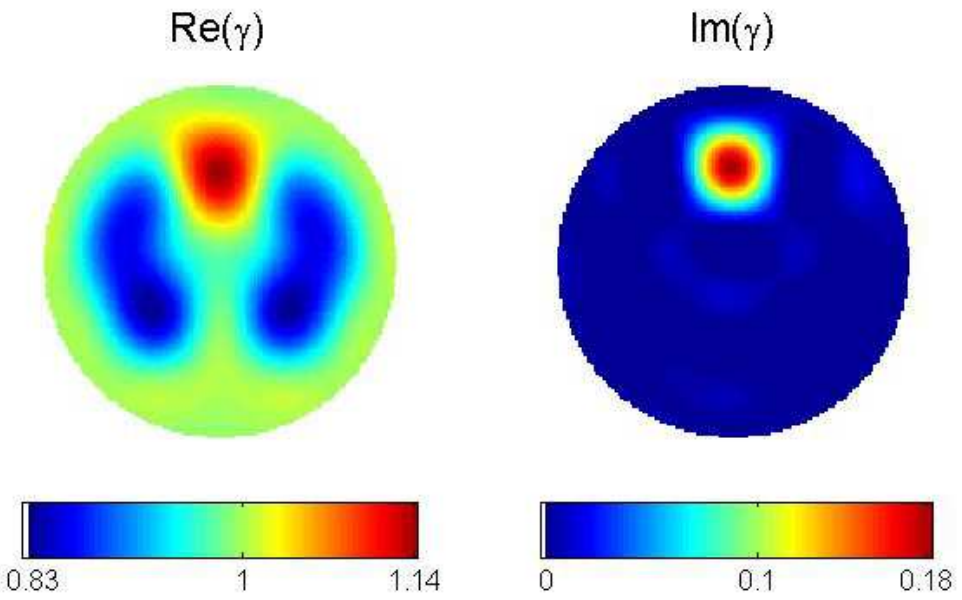

Fig. 6.10: Reconstruction from noise-free data for Example 2 with the real part of γ (conductivity) on the left, and the imaginary part (permittivity) on the right. The cut-off frequency was $K = 5.5$. The dynamic range is 79% for the conductivity, and 61% for the permittivity.

Example 3

Example 3 is an admittivity distribution of slightly higher contrast, and a non-unitary background admittivity of $\gamma_0 = 0.8 + 0.3\,\mathrm{i}$. See Figure 6.11 for a plot of the phantom with admittivity values for the regions. Due to the non-unitary background, the problem was scaled, as was done, for example, in [DM10], by defining a scaled admittivity $\tilde{\gamma} = \gamma/\gamma_0$ to have a unitary value in the neighborhood of the boundary and scaling the D-N map by defining $\Lambda_{\tilde{\gamma}} = \gamma_0 \Lambda_\gamma$, solving the scaled problem, and rescaling the reconstructed admittivity.

Tab. 6.1: Maximum and minimum values in Example 3 with the non-unitary background were found in the appropriate organ region. The table indicates these values of the admittivity in the appropriate region.

	Admitivity of test problem	Reconstruction from noise-free data	Reconstruction from noisy data
heart	1.2 + 0.6 i	1.0246 + 0.5014 i (max)	0.9740 + 0.4679 i (max)
lungs	0.5 + 0.1i	0.5262 + 0.1258 i (min)	0.5390 + 0.1281 i (min)

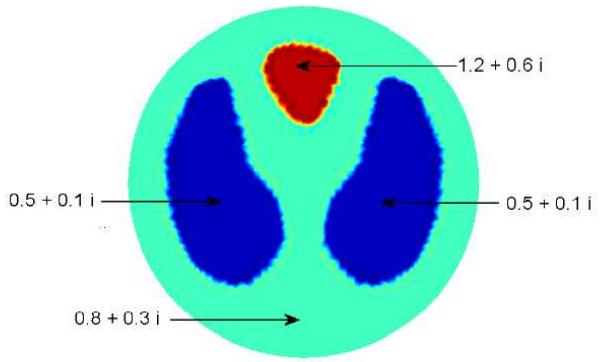

Fig. 6.11: The test problem in Example 3. In this case, the background admittivity is $0.8 + 0.3i$, rather than $1 + 0i$ as in Examples 1 and 2.

The scattering data for the noise-free reconstruction was computed on a 128×128 grid for $k \in [-5.2, 5.2]$ and is shown in Figure 6.12(a). Noisy data was computed as described above in the beginning of this section, and the scattering data was also computed on a 128×128 grid for $|k| \leq 5.5$ and is shown Figure 6.12(b). The reconstructed admittivities are found in Figure 6.13. The maximum and minimum values are given in Table 6.1. In this example, for the noise-free reconstruction, the dynamic range is 71% for the conductivity and 75% for the permittivity. Again the spatial resolution is quite good, and there is little degradation in the image and the reconstructed values in the presence of noise. The scattering transform began to blow up for noisy data, requiring the truncation of the admissible scattering data to a circle of radius 5.5 resulting in a dynamic range of 62% for the conductivity and 68% for the permittivity. For completeness, reconstructions with 0.1% added noise (10 times the published noise level for the ACT III system at RPI) are given in Figure 6.14 with a maximum admittivity $1.0378 + 0.5131\,\mathrm{i}$ and minimum admittivity $0.5428 + 0.0993\,\mathrm{i}$ resulting in a dynamic range of 71% for the conductivity and 83% for the permittivity. The corresponding scattering data was computed on a 128×128 grid with $|k| < 5.2$ and truncated so that the real and imaginary parts did not exceed 0.13 and 0.085 respectively to remove the scattering data corrupted by the noise. A thorough study of the effects of the choice of K and its method of selection is not included in this thesis.

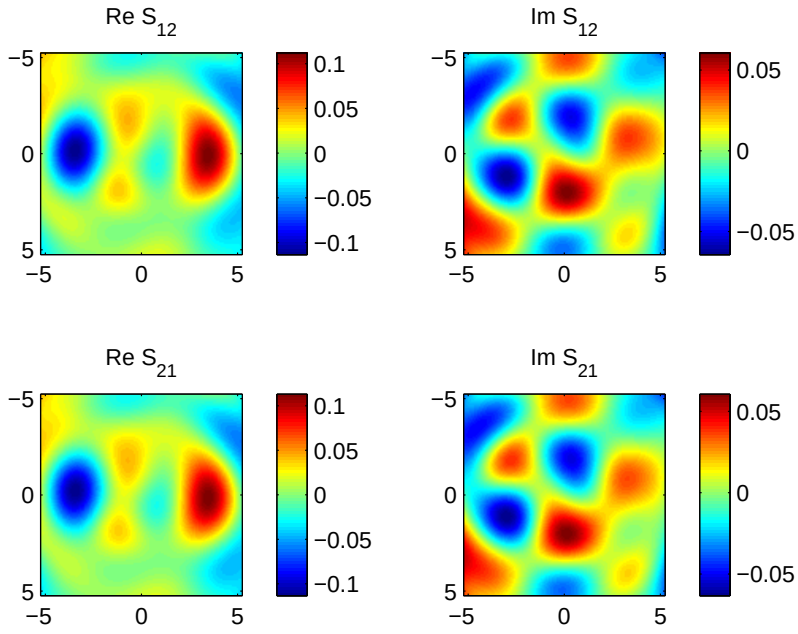

(a) Zero Noise

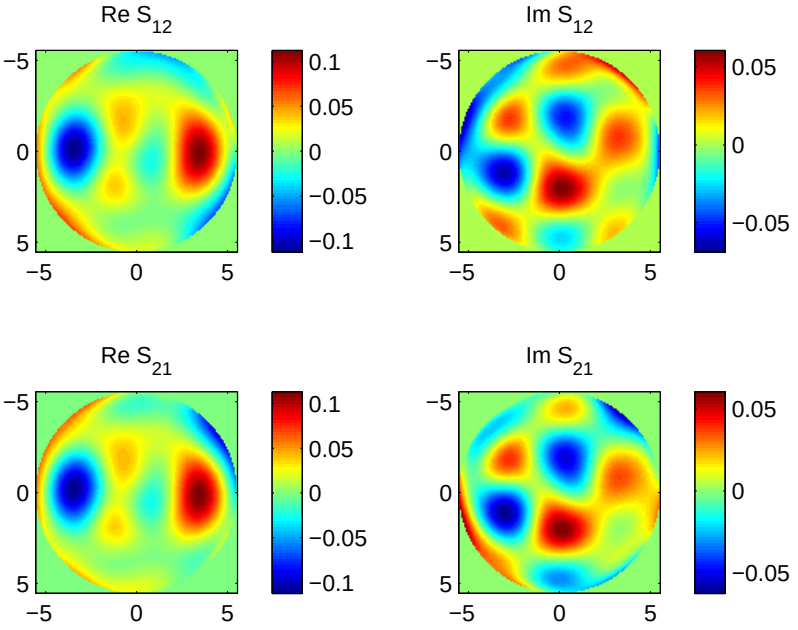

(b) 0.01% Noise

Fig. 6.12: Scattering data for Example 3 with zero and 0.01% added noise using trigonometric current patterns with $K = 5.2$ and $|k| < 5.5$ respectively.

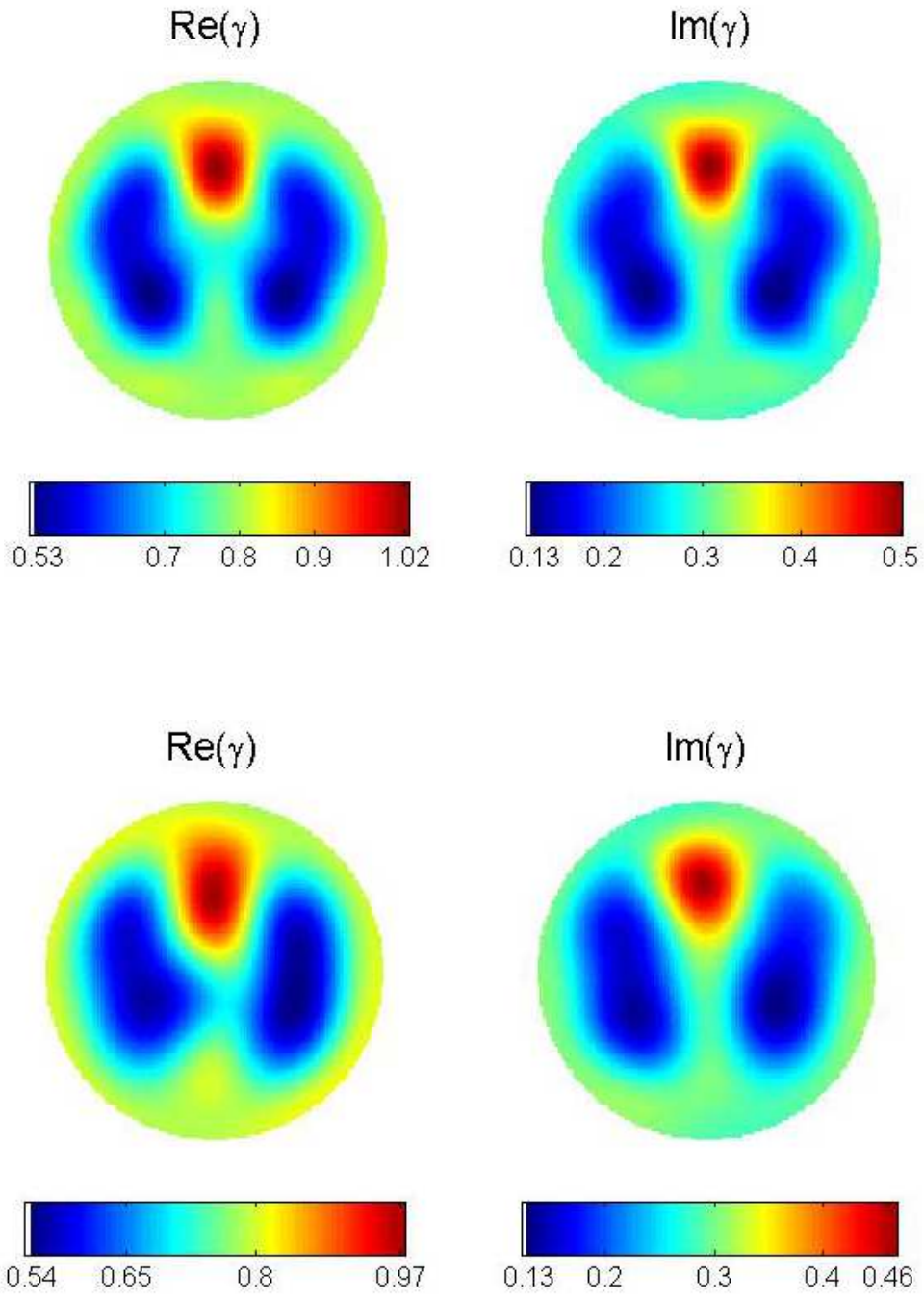

Fig. 6.13: Top row: Reconstruction from noise-free data for Example 3. The cut-off frequency was $K = 5.2$. The dynamic range is 71% for the conductivity, and 75% for the permittivity. Bottom row: Reconstruction from data with 0.01% added noise. The cut-off frequency was $|k| \leq 5.5$. The dynamic range is 62% for the conductivity, and 68% for the permittivity.

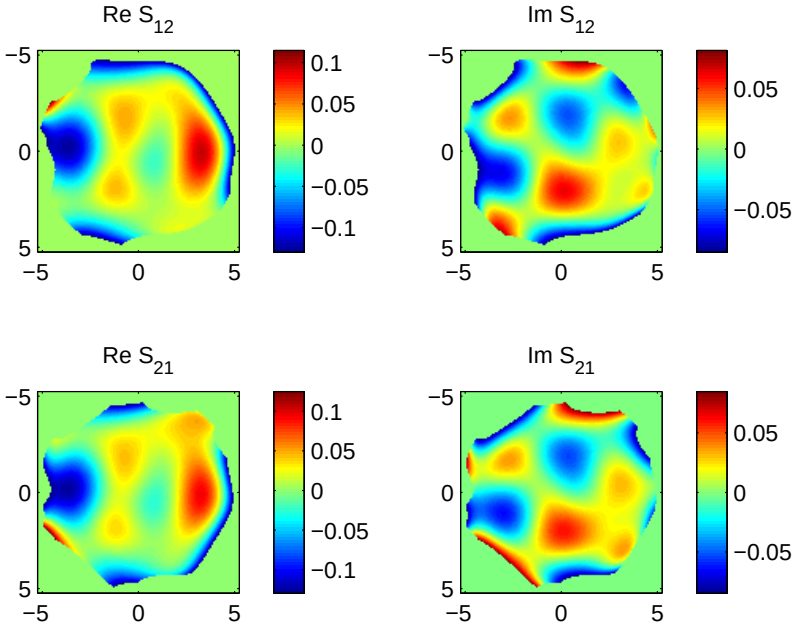

(a) 0.1% Noisy Scattering Data

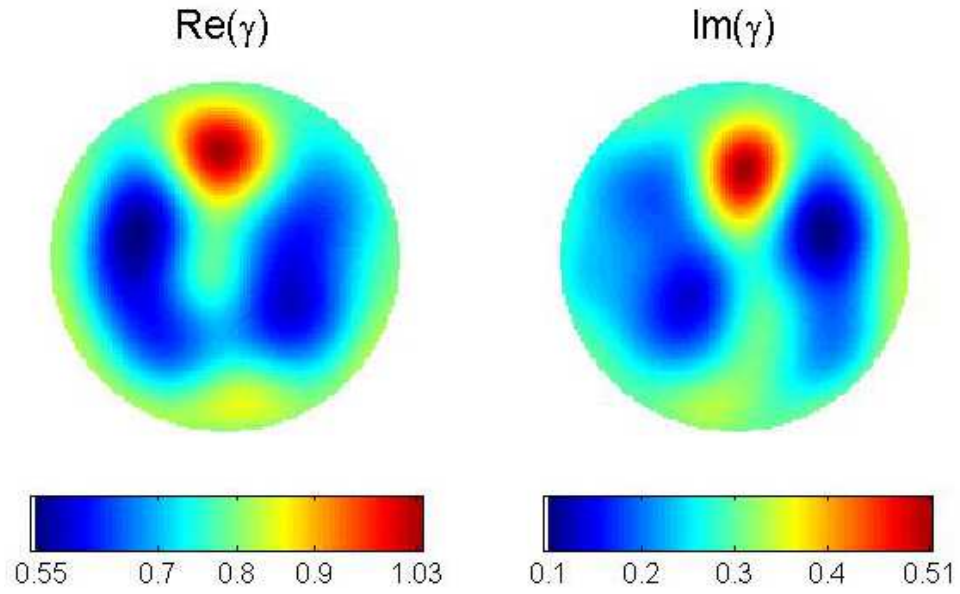

(b) Reconstructed Admittivity from 0.1% Noise

Fig. 6.14: Scattering data for Example 3 with 0.1% added noise (a) and the corresponding admittivity reconstruction (b).

6.10 Numerical Results for Skip Current Patterns

As not all EIT imaging systems use the trigonometric current patterns described above (and used at RPI), we now consider another common class of current patterns, namely skip (or pairwise) current patterns that apply equal and opposite current on two electrodes at a time.

For a system using L electrodes, it is well known that there will be $L-(n+1)$ linearly independent current patterns for a skip n setup. Thus, the j^{th} skip n current pattern J is defined on the ℓ-th electrode by

$$J_\ell^j = \begin{cases} \mathfrak{M} & \ell = j \\ -\mathfrak{M} & \ell = j+(n+1) \\ 0 & \text{otherwise} \end{cases} \tag{6.41}$$

for $1 \le \ell \le L$ and $1 \le j \le L-(n+1)$, where $\mathfrak{M}$ again denotes the amplitude of the applied AC current. Most groups that use skip currently patterns frequently use skip 3. The advantage of skip 3 is that the currents penetrate the domain more than in the skip 0, skip 1, or skip 2 cases and remain stronger than in the skip 4+ cases. Below is the current pattern matrix J for an EIT machine with L electrodes using the skip-3 current patterns,

$$J = \begin{bmatrix} \mathfrak{M} & 0 & \cdots & & & & & 0 \\ 0 & \mathfrak{M} & 0 & \cdots & & & & 0 \\ 0 & 0 & \mathfrak{M} & 0 & \cdots & & & 0 \\ 0 & 0 & 0 & \mathfrak{M} & 0 & \cdots & & 0 \\ -\mathfrak{M} & 0 & 0 & 0 & \ddots & & & 0 \\ 0 & -\mathfrak{M} & 0 & \cdots & & \ddots & & 0 \\ 0 & 0 & -\mathfrak{M} & 0 & \cdots & & \ddots & 0 \\ \vdots & \vdots & 0 & \ddots & & & \ddots & 0 \\ \vdots & \vdots & \ddots & \ddots & \ddots & & & \mathfrak{M} \\ \vdots & \vdots & \ddots & \cdots & & \ddots & & 0 \\ \vdots & \vdots & \ddots & \cdots & & & \ddots & 0 \\ \vdots & \vdots & \ddots & \cdots & & & \ddots & 0 \\ 0 & 0 & \cdots & \cdots & \cdots & \cdots & 0 & -\mathfrak{M} \end{bmatrix} \tag{6.42}$$

an $L \times (L-4)$ matrix.

6.10.1 Implementation

We would like to proceed and solve the boundary integral equations for the CGO solutions u_1 and u_2 in a similar manner as for the trigonometric current patterns (see Section 6.3) using the new D-N map corresponding to the skip-n current patterns. However, this solution method relies on the orthonormality of the normalized trigonometric current pattern matrix Φ, and the normalized skip-n current pattern matrix J is not orthogonal. To deal with this, we need to form an orthonormal basis for $\mathbb{R}^{L-(n+1)}$. The Gram-Schmidt procedure is used to create an orthonormal matrix from the given skip-n current pattern matrix J. One should note that it is not necessary to normalize the skip-n current pattern matrix J before performing the Gram-Schmidt orthonormalization.

Gram-Schmidt Orthonormalization of the Skip-n Current Pattern Matrix

The Gram-Schmidt orthonormalization of the skip-n current pattern matrix for the L electrodes is performed as follows. Let J_{GS} denote the orthonormal current pattern matrix produced by the Gram-Schmidt procedure on the current pattern matrix J. The Gram-Schmidt algorithm takes a set of linearly independent vectors, $\left\{J^j\right\}_{j=1}^{j=L-(n+1)}$, i.e. the columns of J, and produces a set of orthonormal vectors $\left\{J^j_{\text{GS}}\right\}_{j=1}^{j=L-(n+1)}$, i.e. the columns of J_{GS}. To find each vector J^j_{GS}, one begins with the corresponding vector J^j, subtracts off its projection on to the previously formed orthonormal vectors in J_{GS}, then divides by the length of the resulting vector to normalize.

Synthesis of Voltages

A change of bases is performed to "synthesize" the voltages that would occur from an experiment that applies the Gram-Schimdt normalized skip-n current patterns J_{GS}. Once this is done, the same methods used with the normalized trigonometric current patterns can be employed (see Section 6.2.1) with the synthesized voltages and orthonormal Gram-Schmidt current pattern matrix. Note that it is also necessary to "synthesize" the voltages that would occur from an experiment with a constant admittivity distribution of 1 in the domain in order to form the difference in D-N maps $\delta\Lambda$.

We must first compute the coefficients needed to expand the skip-n current pattern matrix J in the new orthonormal Gram-Schmidt matrix J_{GS}. The j^{th} skip-n current pattern can be expanded as

$$J^j = \sum_{p=1}^{L-(n+1)} \mathfrak{C}_{pj}\ J^p_{\text{GS}}$$

where $\mathfrak{C}_{pj} = \left(J^p, J^j_{\text{GS}}\right)$ the discrete inner product.

Once the coefficients $\mathfrak{C}$ are obtained, the voltages that would result from applying the orthonormal Gram-Schmidt current patterns J_{GS} can be synthesized. The voltages $\tilde{V}^j_\ell$ are then normalized, as in Section 6.2.1, so that they sum to zero for each current pattern

$$\sum_{\ell=1}^{L} \tilde{V}^j_\ell = 0, \quad j = 1, \ldots, L-(n+1),$$

and subsequently scaled by the ℓ^2 norm of the original skip-n current pattern matrix J

$$V^j = \frac{\tilde{V}^j}{\|J^j\|_{\ell^2}}.$$

We then synthesize the new voltages V_{GS} from the normalized voltages produced using the following change of bases:

$$V_{\text{GS}} = V\ \mathfrak{C}^{-1}$$

where the superscript $^{-1}$ denotes the inverse of a matrix. Now that we have an orthonormal matrix of current patterns we can form the N-D map as in Section 6.2.1, expand the CGO solutions u_1, u_2, and their exponential terms in the new orthonormal matrix of Gram-Schmidt current patterns J_{GS}, and continue with the algorithm as before. The only remaining difference between the skip-n current pattern method and the trigonometric current pattern method is the number of current patterns used in the expansions (i.e. there are $L-1$ linearly independent trigonometric current patterns whereas there are only $L-(n+1)$ linearly independent orthonormal Gram-Schmidt current patterns from the skip-n current patterns).

To check the validity of this Gram-Schmidt synthesis, the voltages that would occur using the same admittivity and phantom but with the orthonormal Gram-Schmidt current patterns J_{GS} were simulated and compared tot the synthesized voltages. The comparison was done for the skip-3 current patterns. The synthesized voltages V_{GS} (found using the

change of basis) were computed with those produced with the FEM solver for the current patterns J_{GS}. They differed on the scale of 10^{-5} where the max and min for the real part of the voltages are approximately 88 and -153 to give an idea of scale. Therefore, we can be sure that our change of basis is accurate and can proceed with confidence in our inverse solver for the skip-n current patterns.

A Non-Unitary Background Example

In this section reconstructions from simulated data with skip-3 current patterns with current amplitude 2 milliamperes are presented. To generate voltage data, the forward admittivity problem was solved on a circular domain of radius 0.150m with a prescribed admittivity using the FEM as described in Appendix B (modified for the skip-3 current patterns). For the following test problems $L = 32$ electrodes, and thus applied $L - 4 = 28$ linearly independent skip-3 current patterns, were applied. The width and height of the electrodes are 0.025m and 0.029m respectively. The mesh used to generate the Finite Element data has 5,514 triangular elements.

We consider the circular domain shown in Figure 6.15 with a non-unitary background using the admittivity values in Table 6.2.

Tab. 6.2: Maximum and minimum values in the non-unitary background example with skip-3 current patterns were found in the appropriate organ region. The table indicates these values of the admittivity in the appropriate region.

	Admitivity of test problem	Reconstruction from noise-free data	Reconstruction from noisy data
heart	1.1 + 0.6i	0.9521 + 0.4937i (max)	0.9681 + 0.4924i (max)
lungs	0.5 + 0.2i	0.5817 + 0.2427i (min)	0.5729 + 0.2470i (min)
background	0.8+0.4i	0.8+0.4i	0.8+0.4i

Using the simulated voltage data, the discrete D-N map was formed, the boundary integral equations for the exponentially growing solutions u_1 and u_2 were solved, and the traces of the CGO solutions $\Psi_{12}(z, k)$ and $\Psi_{21}(z, k)$ were computed for each z_ℓ on the

boundary of the circular domain (where z_ℓ denotes the center of the ℓ-th electrode). The scattering transforms $S_{12}(k)$ and $S_{21}(k)$ were evaluated on a disc of radius $|k| = 4.3$ where the step size in k was $h_k \approx 0.067$ using 128 evaluation points in each of the k_1 and k_2 directions for both the zero and 0.01% noise cases.

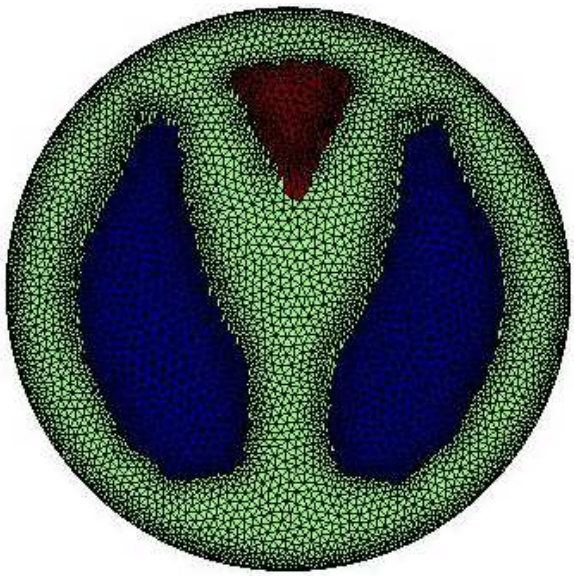

Fig. 6.15: Circular test phantom for the non-unitary background example using skip-3 current patterns.

The $\bar{\partial}_k$-equation was solved on a z grid $[-1.1, 1.1]^2$ with a step size $h_z \approx 0.17$ using 128 evaluation points in each the x and y directions. The $\bar{\partial}_k$-equation was only solved for values of z inside the circle of radius 1.1. The matrix potential Q and admittivity distribution γ were then recovered using the CGO solution matrix $M(z, 0)$. The resulting admittivity distributions for the zero noise and 0.01% noise cases can be found in Figure 6.16. For the zero noise case, the dynamic range is 62% for the conductivity and 63% for the permittivity compared to 66% and 61% for the 0.01% noise case. The heart and lungs are clearly visible and have good spatial resolution. The dynamic ranges for the skip-3 example are less than we saw previously with the trigonometric current patterns. This is not very surprising as the skip-3 current patterns only have $L-4$ linearly independent measurements whereas the trigonometric current patterns have $L - 1$. Examples using skip-3 current patterns on a non-circular domain will be studied in Section 7.2.2.

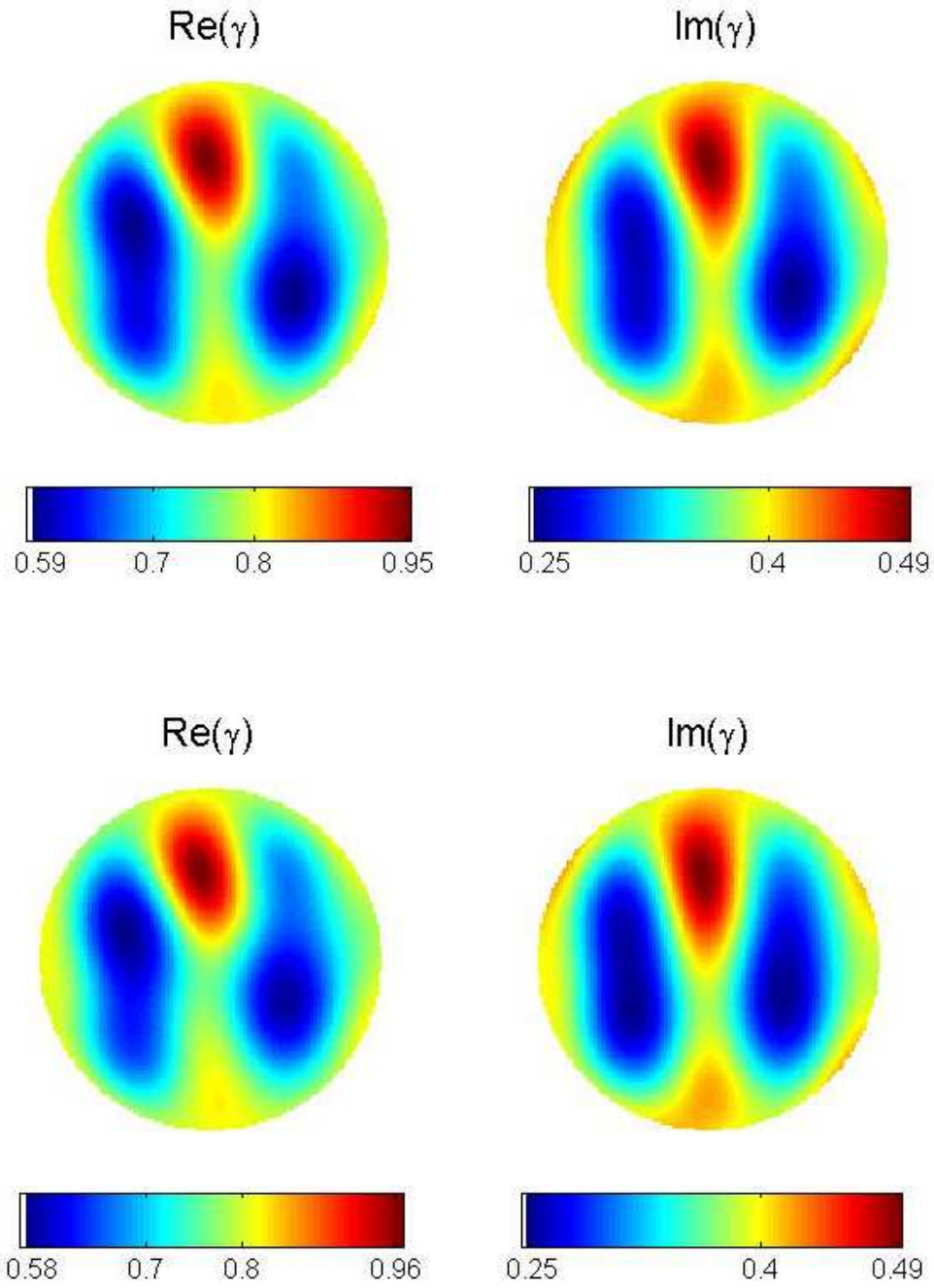

Fig. 6.16: Top row: Reconstruction from noise-free data for the non-unitary example using skip-3 current patterns. The dynamic range is 62% for the conductivity and 63% for the permittivity. Bottom row: Reconstruction from data with 0.01% added noise with skip-3 current patterns. The dynamic range is 66% for the conductivity and 61% for the permittivity.

7. NON-CIRCULAR DOMAINS

In practice, the human chest is not circular and therefore we would like to be able to use our reconstruction algorithm for non-circular domains. In this chapter the necessary modifications are discussed and reconstructions are shown for simulated data on a chest shaped domain.

7.1 Modification of the Inverse Solver

When we relax the assumption that the boundary of the domain is circular the theory behind the algorithm does not change, however, our implementation does. As the domain is no longer circular, it is no longer prudent to scale the Dirichlet-to-Neumann map by the radius of the domain. Previous methods [Mur07, MM09] have scaled the D-N map by the maximum radial value of the non-circular domain and have produced good reconstructions.

It is possible that the reconstructions can be improved by accurately modeling the boundary of the domain and therefore not scaling the D-N map by any radial component. Instead, the evaluation points z for the D-N map and exponentially growing solutions $u_1(z,k)$ and $u_2(z,k)$ will remain the centers of the electrodes on boundary of the non-circular domain and the CGO solutions Ψ_{12} and Ψ_{21} can be evaluated at an $z \in \partial\Omega$. Units are scaled accordingly so that the voltages are represented in volts (V), current in amps (A), height and width of the electrode in meters (m), and the radial components of the boundary in meters (m). As the human chest will always have a radial component less than 1 meter, the magnitude of any point $z \in \partial\Omega$ will be less than 1 and therefore not cause any trouble in Steps 1 and 2 of the reconstruction algorithm (see Sections 6.3 and 6.4). Note that we replace $\mathrm{d}\theta$ in the boundary integral equations for u_1, u_2, Ψ_{12}, and Ψ_{21} with the length of a uniform subdivision of the boundary $\partial\Omega$ calculated by $\frac{P}{L}$ where P denotes the perimeter of the boundary and L the number of electrodes used in the simulated experiment.

We move on to Step 3, the evaluation of the scattering transform. The formulas for the scattering transform $S_{12}(k)$ and $S_{21}(k)$ require knowledge of the outward facing unit

normal vector $\nu = (\nu_1, \nu_2) = \nu_1 + \mathrm{i}\,\nu_2$ and complex conjugate $\overline{\nu}$ respectively,

$$\begin{aligned} S_{12}(k) &= \frac{i}{2\pi}\int_{\partial\Omega} e^{-i\bar{k}z}\Psi_{12}(z,k)(\nu_1 + i\nu_2)dS(z) \\ S_{21}(k) &= -\frac{i}{2\pi}\int_{\partial\Omega} e^{i\bar{k}\bar{z}}\Psi_{21}(z,k)(\nu_1 - i\nu_2)dS(z). \end{aligned}$$

When the boundary is a circle of radius r, the outward facing unit normal vector can be described by the coordinate z on the boundary $\partial\Omega$ divided by its magnitude (i.e. $z/\|z\|$) since it has unit length, faces outward from the boundary, and in fact is normal to the boundary. However, when the boundary is non-circular, as in the case with the chest-shaped domain, we must approximate the outward facing unit normal vector using a parameterization $r(\theta)$ of the boundary for $\theta \in [0, 2\pi)$.

To approximate the unit outward facing normal vector ν to the boundary, we first approximate the unit tangent vector τ to the boundary pointing in the counter-clockwise orientation in θ. To form the approximate tangent vector at a given point $z_0 = x_0 + \mathrm{i}\,y_0 = r(\theta_0)\,e^{\mathrm{i}\,\theta_0}$, we take another point on the boundary $z_+ = x_+ + \mathrm{i}\,y_+ = r(\theta_+)\,e^{\mathrm{i}\,\theta_+}$ where $\theta_+ - \theta_0 = \mathrm{tol} > 0$ for some given tolerance. To form the unit vector from z_0 to z_+ we merely subtract the corresponding entries and divide by the magnitude

$$\tau = \frac{\langle x_+ - x_0,\ y_+ - y_0\rangle}{\|\langle x_+ - x_0,\ y_+ - y_0\rangle\|_2} = \frac{(x_+ - x_0) + \mathrm{i}\,(y_+ - y_0)}{\sqrt{(x_+ - x_0)^2 + (y_+ - y_0)^2}}.$$

We then form the unit outward facing normal vector ν to the boundary at a given point z_0 by

$$\nu = \langle \tau_2, -\tau_1\rangle = \tau_2 - \mathrm{i}\,\tau_1$$

where $\tau = \langle \tau_1,\ \tau_2\rangle = \tau_1 + \mathrm{i}\,\tau_2$.

When evaluating the scattering transforms $S_{12}(k)$ and $S_{21}(k)$ numerically, as in Section 6.5, we approximate the integral by a finite sum

$$S_{12}(k) \approx \frac{\mathrm{i}}{2\pi}\frac{P}{N_z}\sum_{n=1}^{N_z} e^{-i\bar{k}z_n}\Psi_{12}(z_n,k)\nu_n \tag{7.1}$$

$$S_{21}(k) \approx -\frac{\mathrm{i}}{2\pi}\frac{P}{N_z}\sum_{n=1}^{N_z} e^{i\bar{k}\overline{z_n}}\Psi_{21}(z_n,k)\overline{\nu_n}, \tag{7.2}$$

where P denotes the perimeter of the domain (in meters) and ν_n the outward unit facing normal at the evaluation point z_n on the boundary of the domain.

After computing the scattering transform in Step 3 of the algorithm (using the adjusted equations (7.1) and (7.2)), we proceed to Step 4 and solve the $\bar{\partial}_k$-equation as before in Section 6.6. As we will only need to reconstruct the chest-shaped domain, there is no need to reconstruct on the entire square grid. Rather, we just compute at a sufficient number of points outside Ω to ensure that the finite difference approximations for the $\bar{\partial}_{\mathrm{z}}$ and ∂_{z} derivatives of the CGO solutions M are accurate for the entire chest-shaped domain. The parametrization $r(\theta)$ is used to determine whether or not it is necessary to solve the $\bar{\partial}_k$-equation at a given point $z = r\, e^{\mathrm{i}\,\theta}$ in the grid by comparing r to the corresponding radius $r(\theta)$ plus a plump up constant of $2h$ for the same θ value.

In Step 5 the matrix potential $Q(z)$ is computed as before (see Section 6.7) and all unnecessary entries (outside the chest-shaped domain) are set to zero. Finally, in Step 6 the admittivity γ is reconstructed in the same manner as in Section 6.8.

7.2 Numerical Results

In this section reconstructions from simulated finite element data for the chest-shaped test phantom are presented. Reconstructions for a non-unitary background with and without a resistive spine and a conductive tumor in the right lung will be examined. In each example, reconstructions with zero and 0.01% noise in the simulated voltage data for both trigonometric as well as skip-3 current patterns are presented (see Section 6.9 for details regarding how the noise was incorporated).

7.2.1 Simulated Data Examples: Trigonometric Current Patterns

In this section reconstructions from data with trigonometric current patterns with current amplitude 2 milliamperes are presented. To generate voltage data, the forward admittivity problem was solved for a chest shaped domain with a prescribed admittivity using the FEM as described in Appendix B. For the following test problems $L = 32$ electrodes, and thus $L-1 = 31$ linearly independent trigonometric current patterns were applied. The width and height of the electrodes were 0.025m and 0.029m respectively. The mesh used to generate the Finite Element data had 5,785 triangular elements.

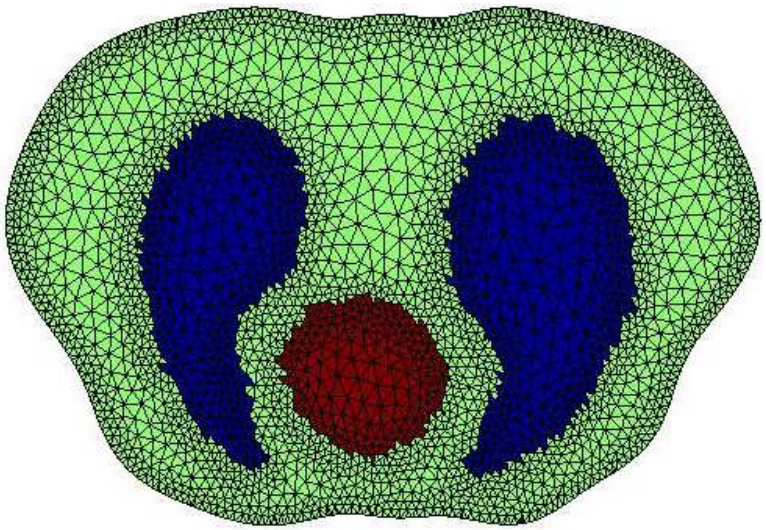

Fig. 7.1: The chest-shaped phantom used in Example 1.

Example 1: A Non-Unitary Background

We first consider the chest-shaped phantom shown in Figure 7.1 with a non-unitary background using the admittivity values in Table 7.1.

Tab. 7.1: Maximum and minimum values in Example 1 with trigonometric current patterns for the non-unitary background were found in the appropriate organ region when applying trigonometric current patterns. The table indicates these values of the admittivity in the appropriate region.

	Admitivity of test problem	Reconstruction from noise-free data	Reconstruction from noisy data
heart	1.1 + 0.6i	1.0239 + 0.5621i (max)	0.9842 + 0.5987i (max)
lungs	0.5 + 0.2i	0.5676 + 0.2435i (min)	0.5720 + 0.2528i (min)
background	0.8+0.4i	0.8+0.4i	0.8+0.4i

Using the simulated voltage data, the discrete D-N map was formed, the boundary integral equations for the exponentially growing solutions u_1 and u_2 were solved, and the traces of the CGO solutions $\Psi_{12}(z,k)$ and $\Psi_{21}(z,k)$ were computed for z on the boundary of the chest-shaped domain. The scattering transforms $S_{12}(k)$ and $S_{21}(k)$ were evaluated on a disc of radius $|k| = 40$ where the step size in k was $h_k \approx 0.63$ using 128 evaluation points in

each of the k_1 and k_2 directions. The scattering transform for the 0.01% noisy data began to blow up near the edges of the disc of evaluation corrupting the data. To deal with the blow up, the scattering data was truncated non-uniformly so that the magnitudes of the real and imaginary parts did not exceed 0.012 and 0.01, respectively. Figure 7.2 shows the scattering transforms used for the zero and 0.01% noisy cases.

The $\bar{\partial}_k$-equation was solved on a z grid $[-0.2, 0.2]^2$ with a step size $h_z \approx 0.003$ using 128 evaluation points in each the x and y directions. The $\bar{\partial}_k$-equation was only solved for values of z that lay inside the chest shaped domain depicted in Figure 7.1 plus an epsilon buffer of $2h_z$ to ensure the accurate computation of the ∂_z and $\bar{\partial}_z$ derivatives of M_+ and M_-. Specifically, an evaluation point $z_0 = R_0\, e^{i\theta_0}$ must satisfy $R_0 < r\,(\theta_0) + 2h_z$ where $r\,(\theta_0)$ is the parameterization of the chest-shaped domain and h_z is the stepsize in the z-grid. The recovered the CGO solutions $M(z, 0)$ can be viewed in Figure 7.3 (the zero noise case is shown here). Notice that $M_{11}(z, 0)$ and $M_{22}(z, 0)$ appear to contain visible information about the shape of the admittivity distribution.

The matrix potential Q and admittivity distribution γ were then recovered using the CGO solution matrix $M(z, 0)$. The resulting admittivity distributions for the zero noise and 0.01% noise cases can be found in Figure 7.4. For the zero noise case, the dynamic range is 76% for the conductivity and 80% for the permittivity compared to 69% and 86% for the 0.01% noise case. The heart and lungs are clearly visible and the right lung is in fact slightly larger than the left as in the test phantom.

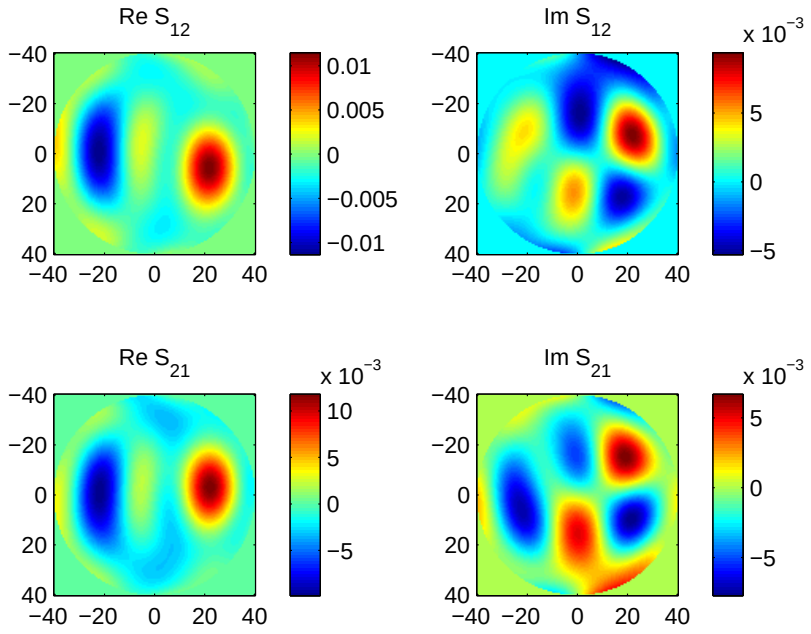

(a) Zero Noise

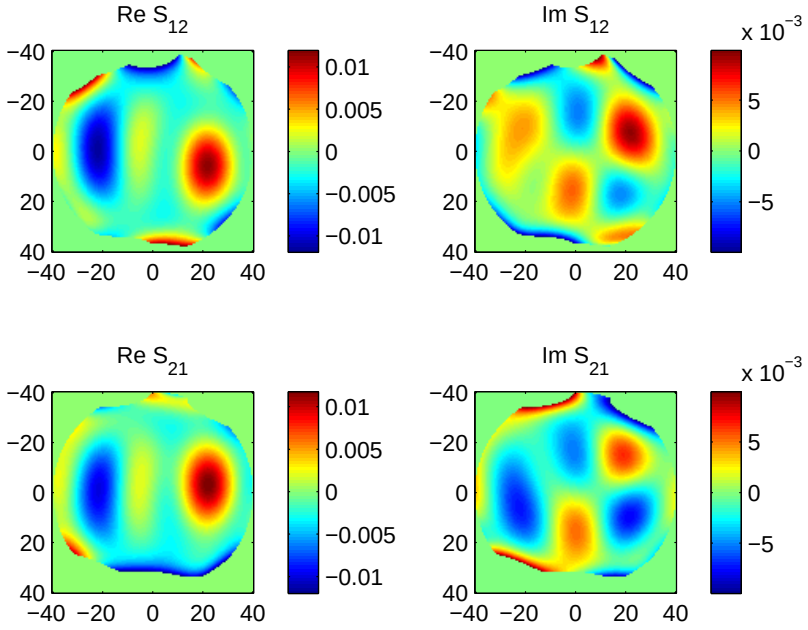

(b) 0.01% Noise

Fig. 7.2: Scattering data for Example 1 using trigonometric current patterns. Figure (a) shows the scattering data used for the zero noise case whereas (b) depicts the scattering data used in the 0.01% noisy case.

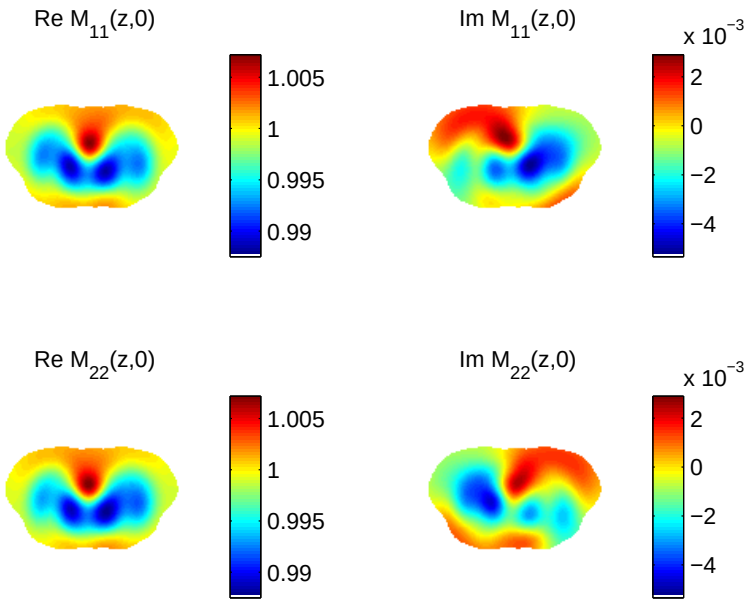

(a) $M_{11}(z,0)$ and $M_{22}(z,0)$

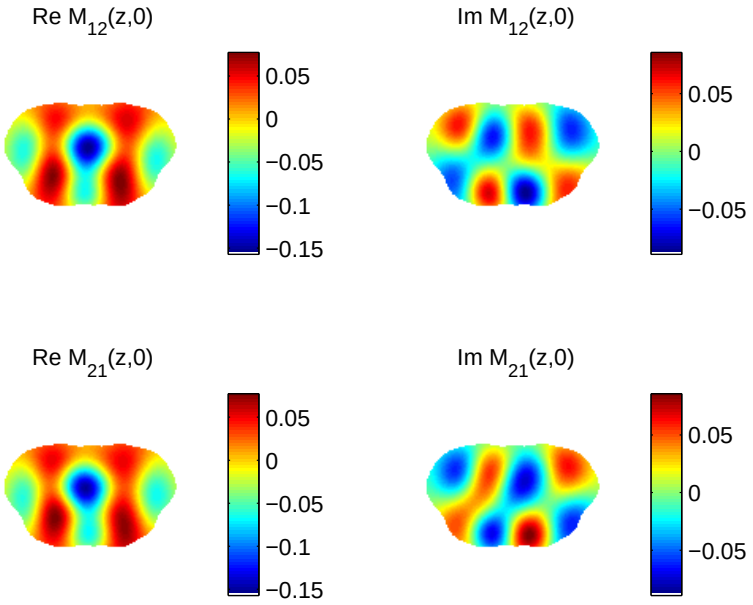

(b) $M_{12}(z,0)$ and $M_{21}(z,0)$

Fig. 7.3: CGO solutions $M(z,0)$ for Example 1 using trigonometric current patterns. Figure (a) shows the CGO solutions $M_{11}(z,0)$ and $M_{22}(z,0)$ for the zero noise case in Example 1 whereas (b) depicts the CGO solutions $M_{12}(z,0)$ and $M_{21}(z,0)$.

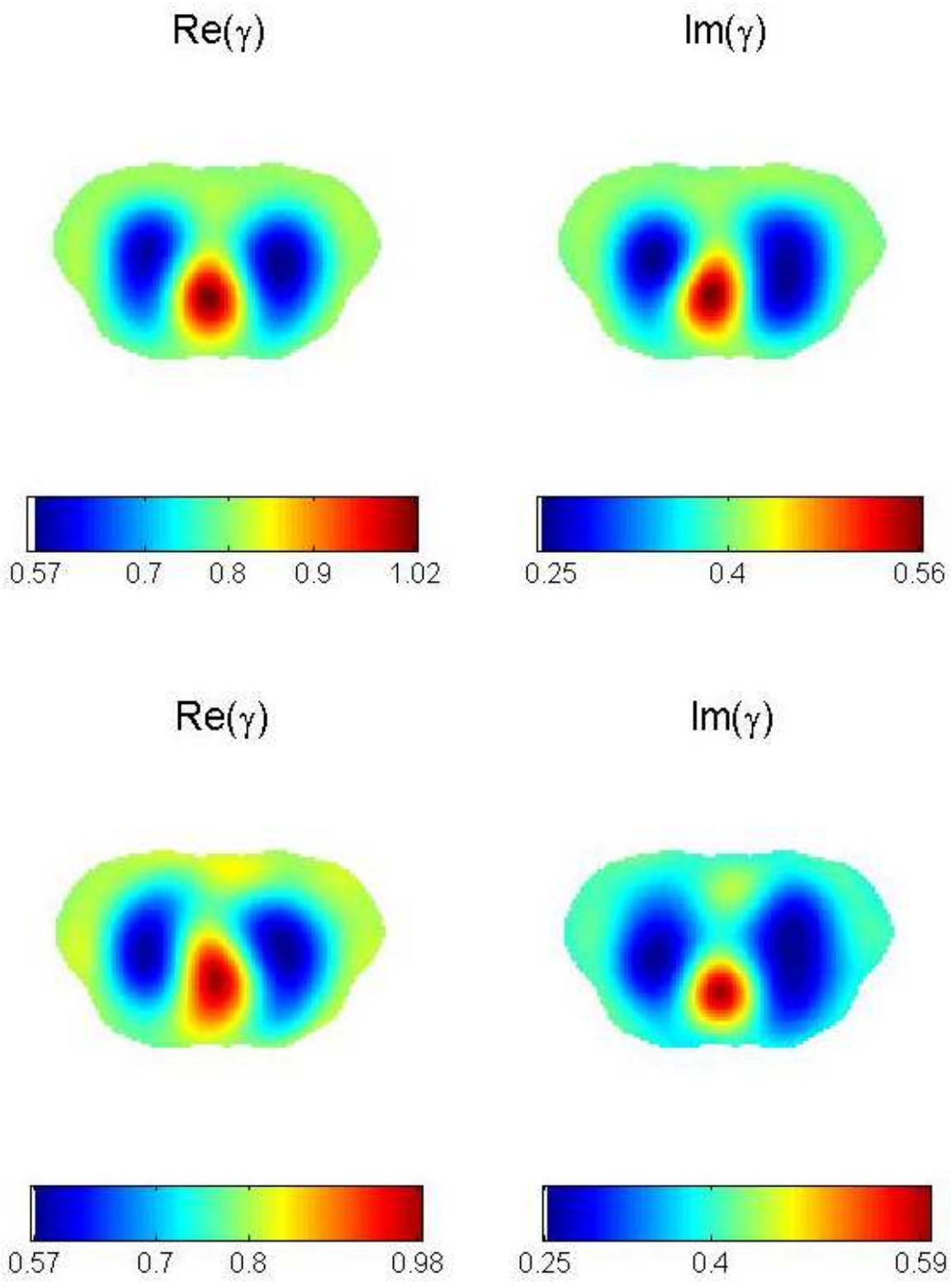

Fig. 7.4: Top row: Reconstruction from noise-free data for Example 1 using trigonometric current patterns. The dynamic range is 76% for the conductivity, and 80% for the permittivity. Bottom row: Reconstruction from data with 0.01% added noise with trigonometric current patterns. The dynamic range is 69% for the conductivity, and 86% for the permittivity.

Example 2: A Resistive Spine

We now consider a test example with a resistive spine using the phantom in Figure 7.5 and admittivity values in Table 7.2.

The scattering transforms were evaluated on the same k grid as in Example 1 with $|k| \leq 40$. This time, the noisy scattering data was truncated so that the magnitude of the real and imaginary parts did not exceed 0.011 and 0.01, respectively. The resulting scattering transforms can be viewed in Figure 7.6.

The $\bar{\partial}_k$-equation was solved as before in Example 1 on the same z grid. Reconstructions of the admittivity distributions for zero and 0.01% noise are shown in Figure 7.7. For the zero noise case, the dynamic range is 50% for the conductivity and 57% for the permittivity compared to 55% and 56% for the 0.01% noise case. These values are clearly lower than in Example 1, however a resistive spine with values approaching 0 is very difficult to reconstruct. The spine is clearly visible in both the zero and 0.01% noise cases even though an artifact that forms a bridge is present. By choosing a larger radius in k for the scattering data, and allowing higher values in the non-uniform truncation of the scattering transform, the bridging will disappear leaving a clearly separated resistive object visible at the top of the reconstruction. However, other artifacts are introduced, e.g., the shapes of the lungs and heart become distorted. Depending on what one is trying to reconstruct, different approaches can be taken.

To emphasize the presence of the spine, Figure 7.8 shows a difference image produced by taking the zero noise reconstruction in Example 2 (Figure 7.7) and subtracting the zero noise reconstruction in Example 1 (which has no spine, see Figure 7.4). In this figure the spine is clearly visible with dynamic range of 40% for the conductivity and 43% for the permittivity. The dynamic range for the conductivity of the spine was computed by taking the minimum value -0.2429 in the difference image Figure 7.8, and dividing it by (0.2-0.8)=-0.6, the value prescribed, and multiplying by 100. The dynamic range for the permittivity of the spine was computed in an analogous fashion.

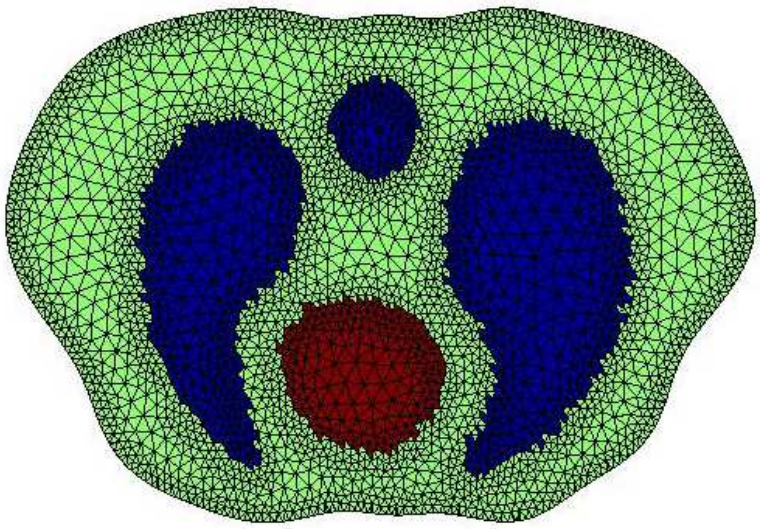

Fig. 7.5: The chest phantom in Example 1 with the addition of a spine.

Tab. 7.2: Maximum and minimum values in Example 2 with the non-unitary background and resistive spine were found in the appropriate organ region when applying trigonometric current patterns. The table indicates these values of the admittivity in the appropriate region.

	Admitivity of test problem	Reconstruction from noise-free data	Reconstruction from noisy data
heart	1.1 + 0.6i	1.0191 + 0.5496i	1.0557 + 0.5382i
lungs	0.5 + 0.2i	0.5653 + 0.2339i	0.5640 + 0.2353i
spine	0.2 + 0.05i	0.5669 + 0.2540i	0.5776 + 0.2281i
background	0.8+0.4i	0.8+0.4i	0.8+0.4i

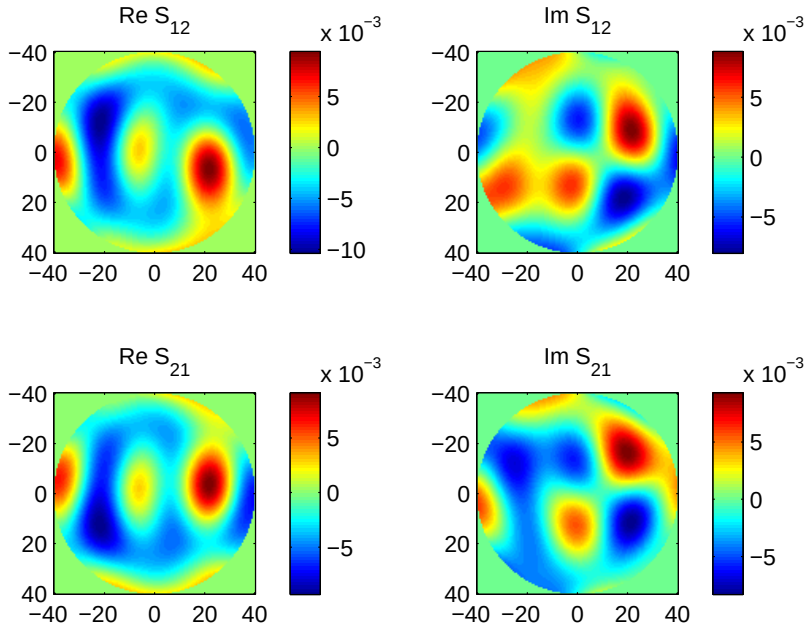

(a) Zero Noise

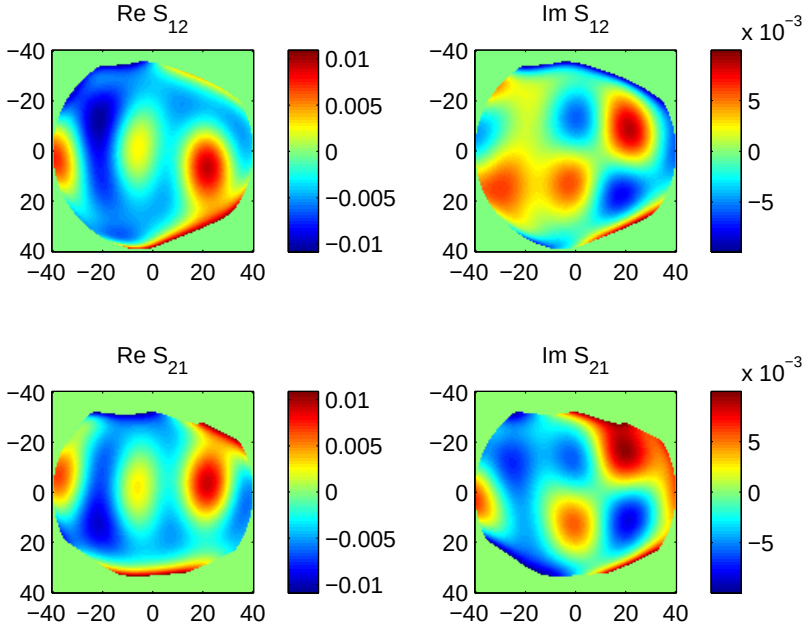

(b) 0.01% Noise

Fig. 7.6: Scattering data for Example 2 using trigonometric current patterns. Figure (a) shows the scattering data used for the zero noise case whereas (b) depicts the scattering data used in the 0.01% noisy case.

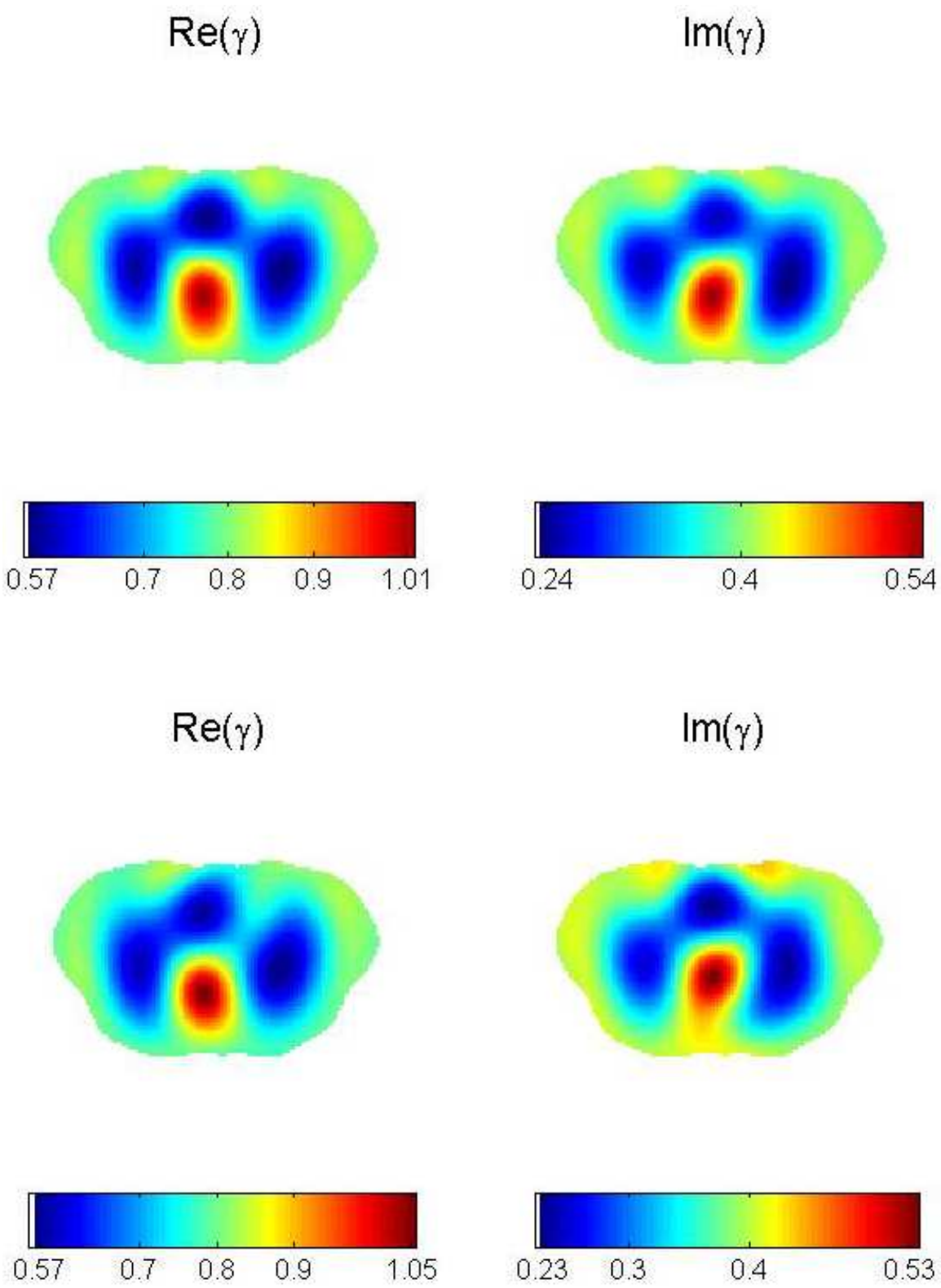

Fig. 7.7: Top row: Reconstruction from noise-free data for Example 2. The dynamic range is 50% for the conductivity, and 57% for the permittivity. Bottom row: Reconstruction from data with 0.01% added noise. The dynamic range is 55% for the conductivity, and 56% for the permittivity.

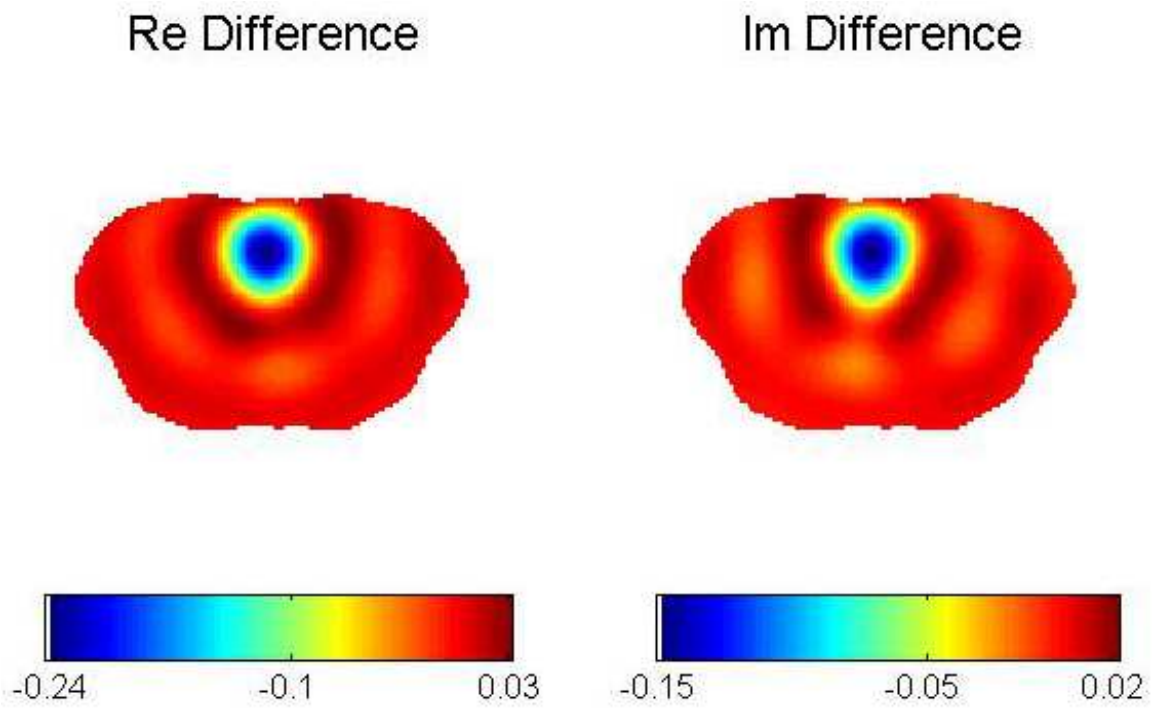

Fig. 7.8: Difference image for the resistive spine in Table 7.2 produced by taking the zero noise reconstruction for Example 2 and subtracting the zero noise reconstruction from Example 1 using trigonometric current patterns. The dynamic range for the spine is 40% for the conductivity, and 43% for the permittivity.

Example 3: A Conductive Tumor

We next consider a test example with a conductive tumor in the right lung using the phantom in Figure 7.9 and admittivity values in Table 7.3.

The scattering transforms were evaluated on the same k grid as in Examples 1 and 2 with the noisy scattering data truncated so that the magnitude of the real and imaginary parts did not exceed 0.011 and 0.009, respectively. The resulting scattering transforms can be viewed in Figure 7.10.

The $\bar{\partial}_k$-equation was solved as before in Examples 1 and 2 on the same z grid. Reconstructions of the admittivity distributions for zero and 0.01% noise are shown in Figure 7.11. For the zero noise case, the dynamic range is 75% for the conductivity and 79% for the permittivity compared to 70% and 96% for the 0.01% noise case. These values are comparable to Example 1, however the tumor is not immediately visible in the right lung. The right lung does appear less resistive than the left and to emphasize the presence of the tumor, Figure 7.12 shows the difference image produced by taking the zero noise reconstruction in Example 3 (Figure 7.11) and subtracting the zero noise reconstruction in Example 1 (which has no tumor, see Figure 7.4). In this figure the tumor is clearly visible and has a dynamic range of 14% for the conductivity, and 12% for the permittivity. The dynamic ranges for the tumor were computed in an analogous fashion (this time using the maximum value in the difference image) as the spine in Example 2.

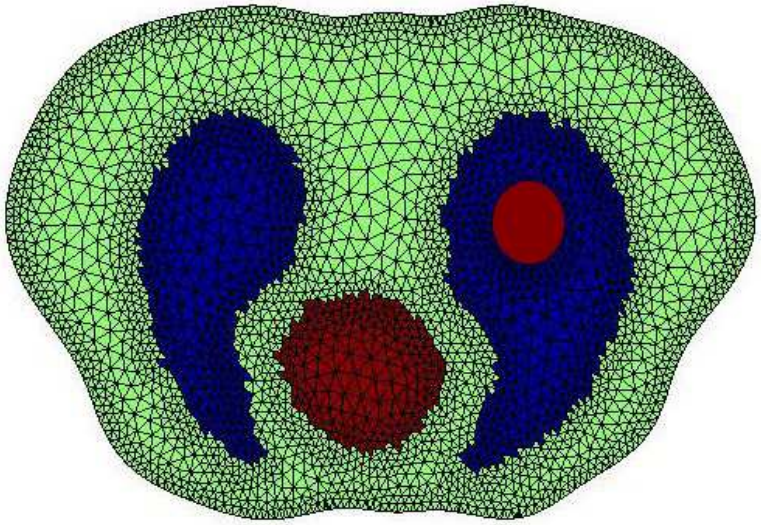

Fig. 7.9: The chest phantom in Example 1 with the addition of a tumor in the right lung.

Tab. 7.3: Maximum and minimum values in Example 3 with the non-unitary background and conductive tumor in the right lung were found in the appropriate organ region when applying trigonometric current patterns. The table indicates these values of the admittivity in the appropriate region.

	Admitivity of test problem	Reconstruction from noise-free data	Reconstruction from noisy data
heart	1.1 + 0.6i	1.0174 + 0.5525 i	0.9921 + 0.6163i
lungs	0.5 + 0.2i	0.5692 + 0.2380 i	0.5698 + 0.2340i
tumor	1.1+ 0.6i	0.6549+ 0.3081i	0.6641 + 0.3073i
background	0.8+0.4i	0.8+0.4i	0.8+0.4i

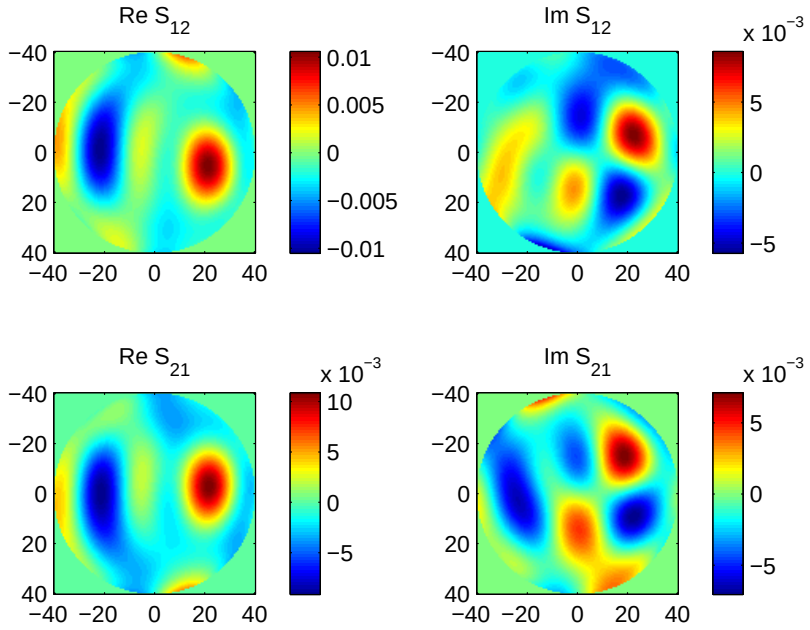

(a) Zero Noise

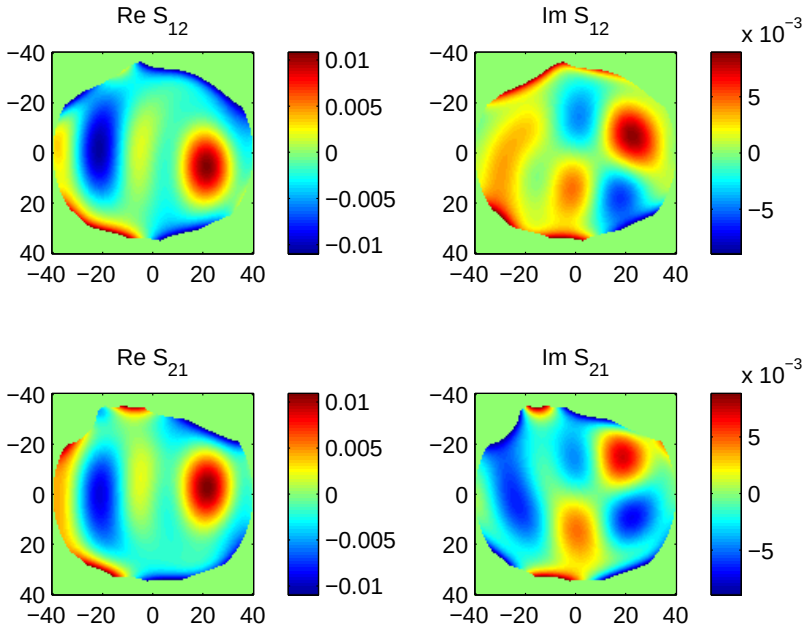

(b) 0.01% Noise

Fig. 7.10: Scattering data for Example 3 using trigonometric current patterns. Figure (a) shows the scattering data used for the zero noise case whereas (b) depicts the scattering data used in the 0.01% noisy case.

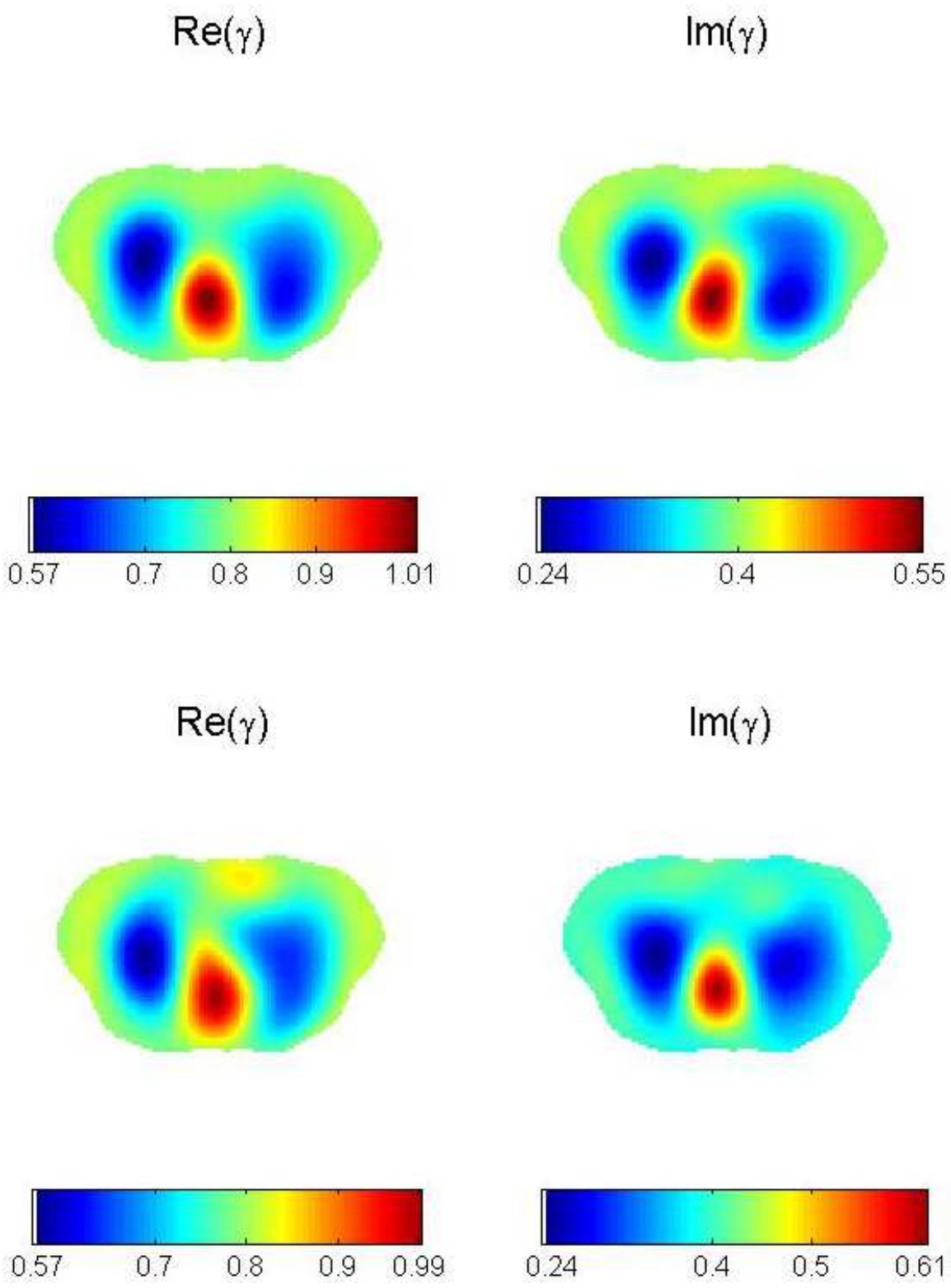

Fig. 7.11: Top row: Reconstruction from noise-free data for Example 3. The dynamic range is 75% for the conductivity, and 79% for the permittivity. Bottom row: Reconstruction from data with 0.01% added noise. The dynamic range is 70% for the conductivity, and 96% for the permittivity.

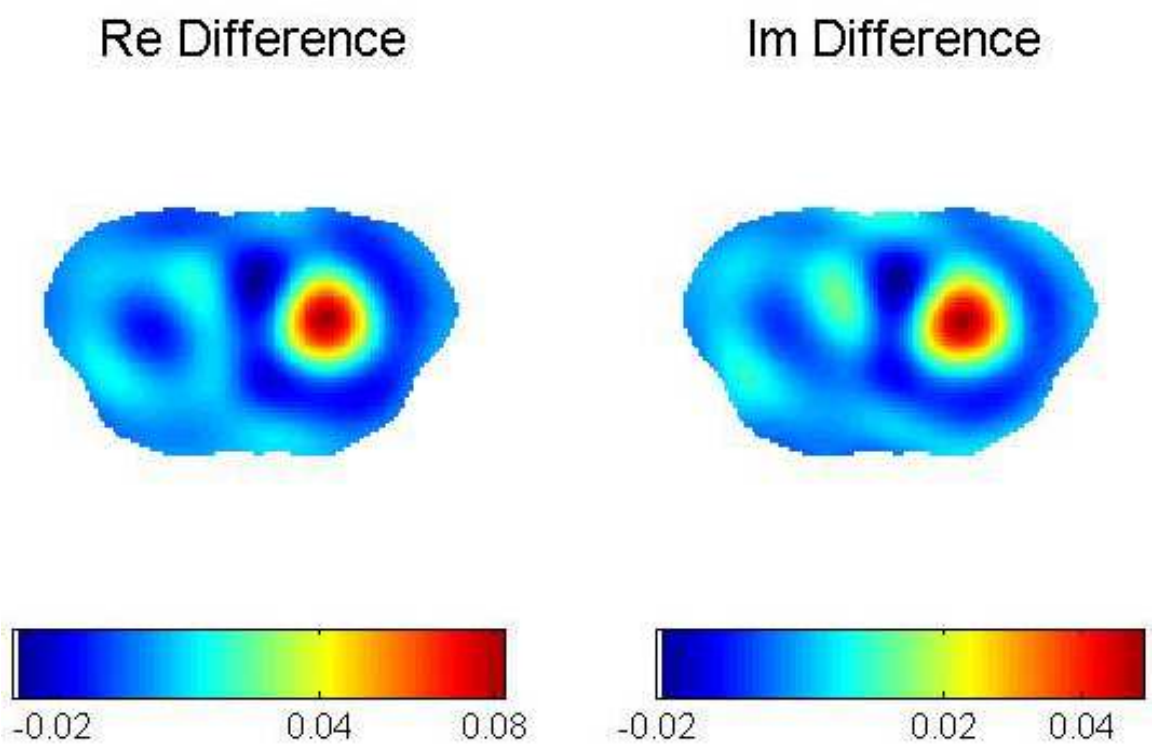

Fig. 7.12: Difference image for the conductive tumor in Table 7.3 produced by taking the zero noise reconstruction for Example 3 and subtracting the zero noise reconstruction from Example 1. The dynamic range for the tumor is 14% for the conductivity, and 12% for the permittivity.

Example 4: Conductive Fluid in the Right Lung

Last we consider a test example with conductive fluid in the right lung using the phantom in Figure 7.13 and admittivity values in Table 7.4.

The scattering transforms were evaluated on the same k grid as in Examples 1-3, this time truncating the noisy scattering data so that the magnitudes of the real and imaginary parts did not exceed 0.01 and 0.009, respectively. The resulting scattering transforms can be viewed in Figure 7.14.

The $\bar{\partial}_k$-equation was solved as before in Examples 1-3 on the same z grid. Reconstructions of the admittivity distributions for zero and 0.01% noise for the fluid example are shown in Figure 7.15. The dynamic ranges for the zero noise case are 79% for the conductivity and 83% for the permittivity compared to 74% and 80% for the 0.01% noise case. These values are again comparable to Example 1, and the fluid is immediately visible and quite pronounced in the right lung. To further emphasize the presence of the fluid, Figure 7.16 shows the difference image produced by taking the zero noise reconstruction in Example 4 (Figure 7.15) and subtracting the zero noise reconstruction in Example 1 (which has no fluid, see Figure 7.4). In this figure the fluid is clearly visible, localized, and has a dynamic range of 54% for the conductivity, and 51% for the permittivity. The dynamic ranges for the fluid were computed in the same manner as the tumor in Example 3.

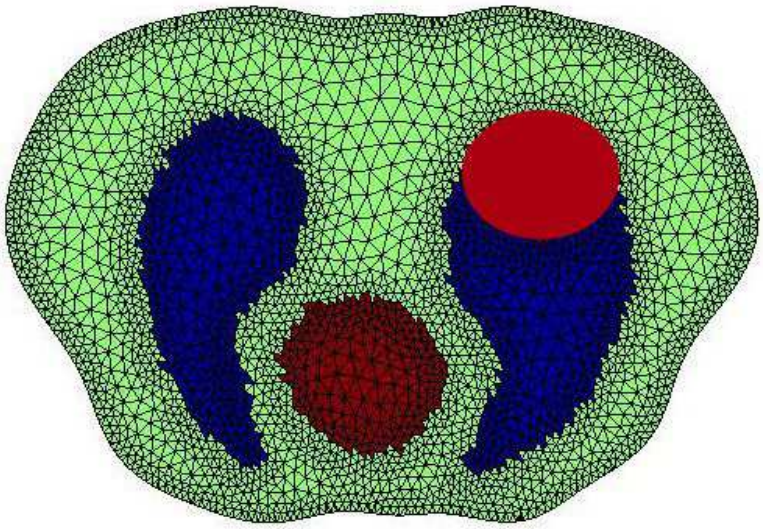

Fig. 7.13: The chest phantom in Example 1 with the addition of conductive fluid in the right lung.

Tab. 7.4: Maximum and minimum values in Example 4 with the non-unitary background and conductive fluid in the right lung were found in the appropriate organ region when applying trigonometric current patterns. The table indicates these values of the admittivity in the appropriate region.

	Admitivity of test problem	Reconstruction from noise-free data	Reconstruction from noisy data
heart	1.1 + 0.6i	1.0459 + 0.5798 i	1.0296 + 0.5529i
lungs	0.5 + 0.2i	0.5748 + 0.2468 i	0.5884 + 0.2339i
fluid	1.1+ 0.6i	0.9707+ 0.4936i	0.9381 + 0.5225i
background	0.8+0.4i	0.8+0.4i	0.8+0.4i

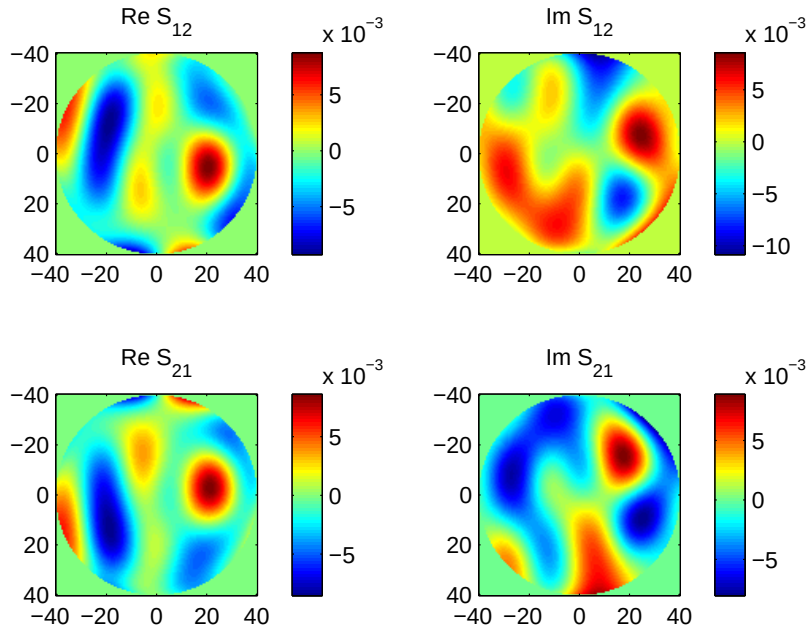

(a) Zero Noise

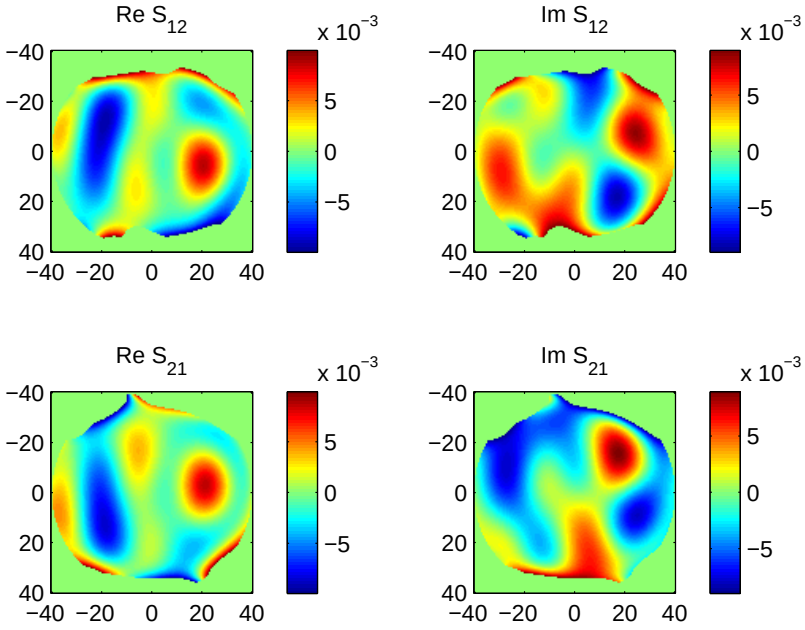

(b) 0.01% Noise

Fig. 7.14: Scattering data for Example 4 using trigonometric current patterns. Figure (a) shows the scattering data used for the zero noise case whereas (b) depicts the scattering data used in the 0.01% noisy case.

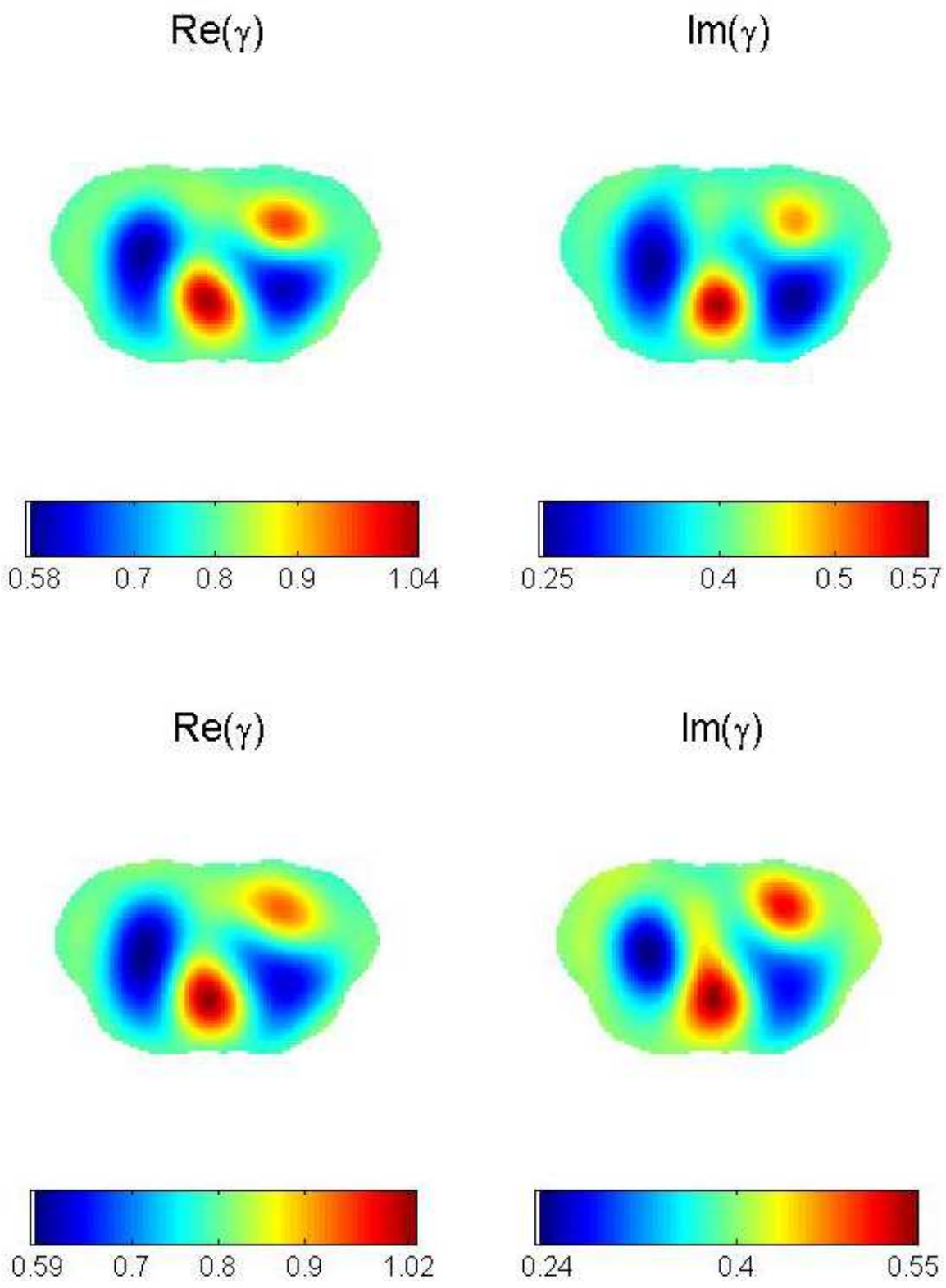

Fig. 7.15: Top row: Reconstruction from noise-free data for Example 4. The dynamic range is 79% for the conductivity, and 83% for the permittivity. Bottom row: Reconstruction from data with 0.01% added noise. The dynamic range is 74% for the conductivity, and 80% for the permittivity.

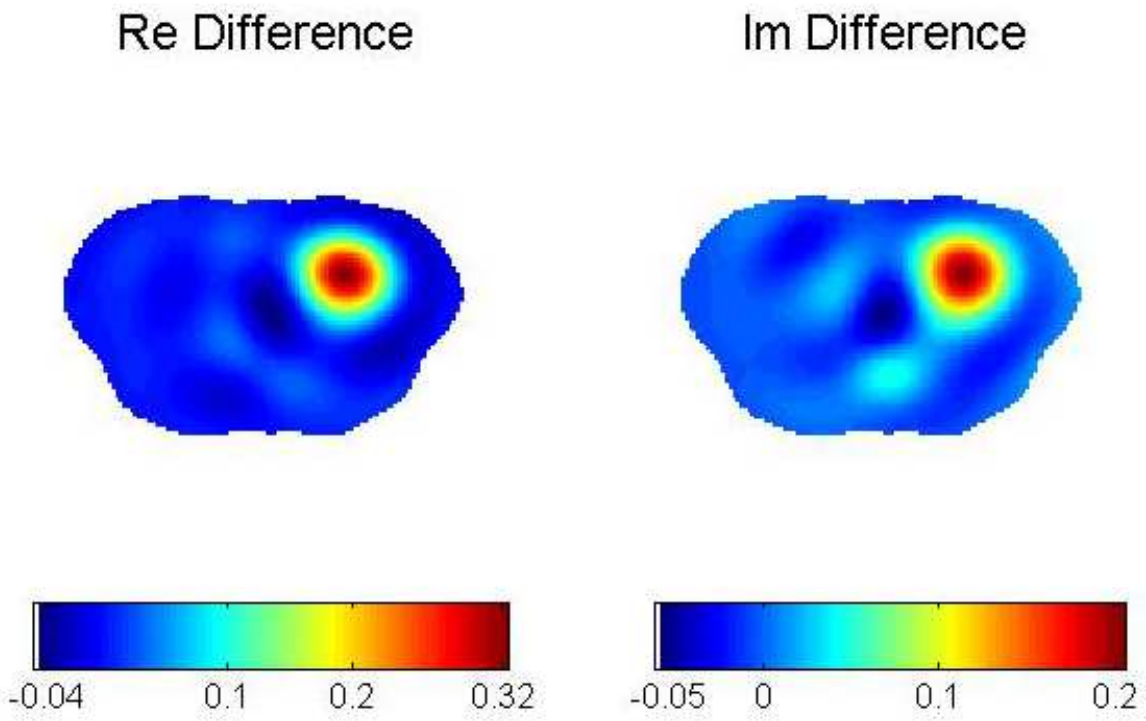

Fig. 7.16: Difference image for the conductive fluid in Table 7.4 produced by taking the zero noise reconstruction for Example 4 and subtracting the zero noise reconstruction from Example 1. The dynamic range for the tumor is 54% for the conductivity, and 51% for the permittivity.

7.2.2 Simulated Data Examples: Skip-3 Current Patterns

In this section reconstructions using skip-3 current patterns with current amplitude 2 milliamperes are presented. To generate voltage data, I again solved the forward admittivity problem was solved for a chest-shaped domain with a prescribed admittivity using a modified version of the FEM formulation described in Appendix B. For the following test problems $L = 32$ electrodes, and thus $L - (3 + 1) = 28$ linearly independent skip-3 current patterns, were applied. The width and height of the electrodes are 0.025m and 0.029m respectively. The same mesh was used to generate the Finite Element data for the skip-3 current patterns as in the case of the trigonometric current patterns. The same test examples used for the trigonometric current patterns in Section 7.2.1 are used for the skip-3 current patterns.

Example 1: A Non-Unitary Background

We first reconsider the phantom shown in Figure 7.1 with the non-unitary background in Example 1 of Section 7.2.1 using the same admittivity values.

Tab. 7.5: Maximum and minimum values in Example 1 with the non-unitary background were found in the appropriate organ region when applying skip-3 current patterns. The table indicates these values of the admittivity in the appropriate region.

	Admitivity of test problem	Reconstruction from noise-free data	Reconstruction from noisy data
heart	1.1 + 0.6i	0.9645 + 0.5158i (max)	0.9606 + 0.5208i (max)
lungs	0.5 + 0.2i	0.5992 + 0.2617i (min)	0.5973 + 0.2613i (min)
background	0.8+0.4i	0.8+0.4i	0.8+0.4i

Using the simulated voltage data, the Gram-Schmidt voltages were synthesized as described in Section 6.10. The discrete D-N map was formed, the boundary integral equations for the exponentially growing solutions u_1 and u_2 were solved, and the traces of the CGO solutions $\Psi_{12}(z, k)$ and $\Psi_{21}(z, k)$ were solved for z on the boundary of the chest-shaped domain. The scattering transforms were evaluated for k in $[-30, 30]^2$ with a step size of

$h_k \approx 0.47$ using 128 evaluation points in each of the k_1 and k_2 directions. The scattering data for the skip-3 current patterns appear to be more prone to blowup than the trigonometric current patterns and therefore demand a smaller truncation radius. For both the zero noise and 0.01% noise cases, the scattering transform S was truncated so that neither the magnitude of the maximum real component nor the maximum imaginary component exceeded 0.012 and 0.011, respectively. The resulting scattering transforms can be viewed in Figure 7.17.

The $\bar{\partial}_k$-equation was solved on the same z grid as before in Examples 1-4 in Section 7.2.1 for the trigonometric current patterns. Reconstructions of the admittivity distributions for zero and 0.01% noise are shown in Figure 7.18. For the zero noise case, the dynamic range is 61% for the conductivity and 64% for the permittivity compared to 61% and 65% for the 0.01% noise case. The right lung is correctly reconstructed to be slightly larger than the left, however there is an artifact present at the upper left part of the right lung in the skip-3 reconstruction as compared to the trigonometric current pattern reconstruction. In addition, the dynamic ranges for the conductivity and permittivity are reduced for the skip-3 current patterns. However, the skip-3 current patterns may have an advantage when it comes to noise. The zero noise and 0.01% noise reconstructions are very similar for the skip-3 current patterns whereas you can see a clear difference for the zero noise and 0.01% noise reconstructions when using the trigonometric current patterns.

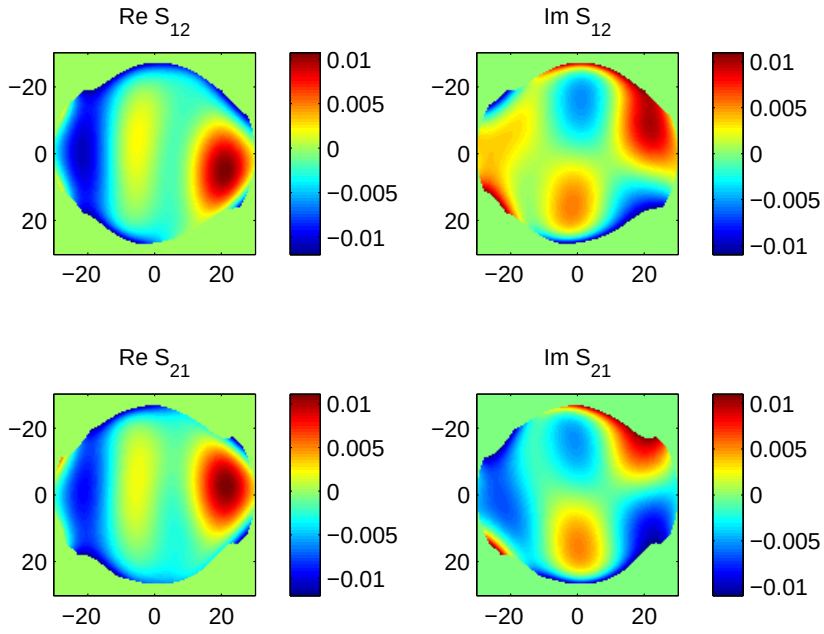

(a) Zero Noise

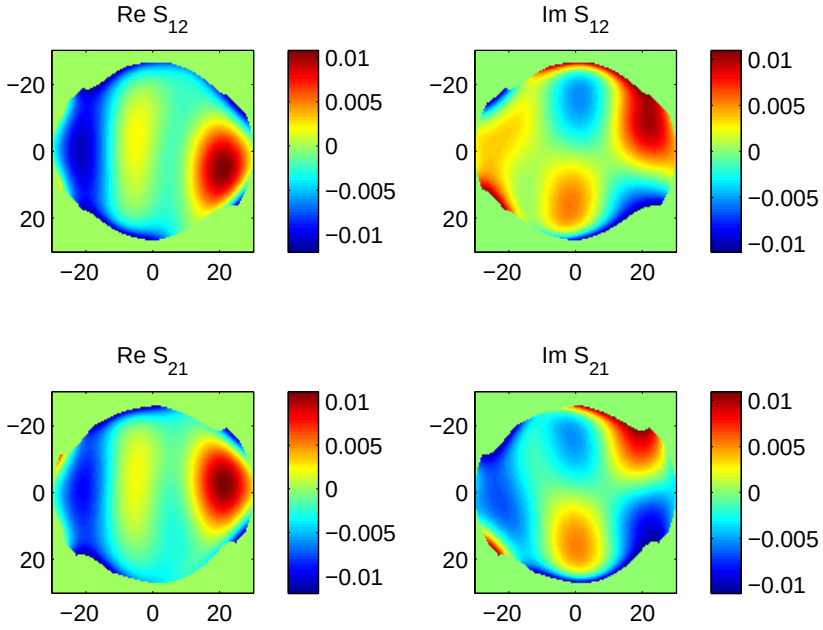

(b) 0.01% Noise

Fig. 7.17: Scattering data for Example 1 for skip-3 current patterns. Figure (a) shows the scattering data used for the zero noise case whereas (b) depicts the scattering data used in the 0.01% noisy case.

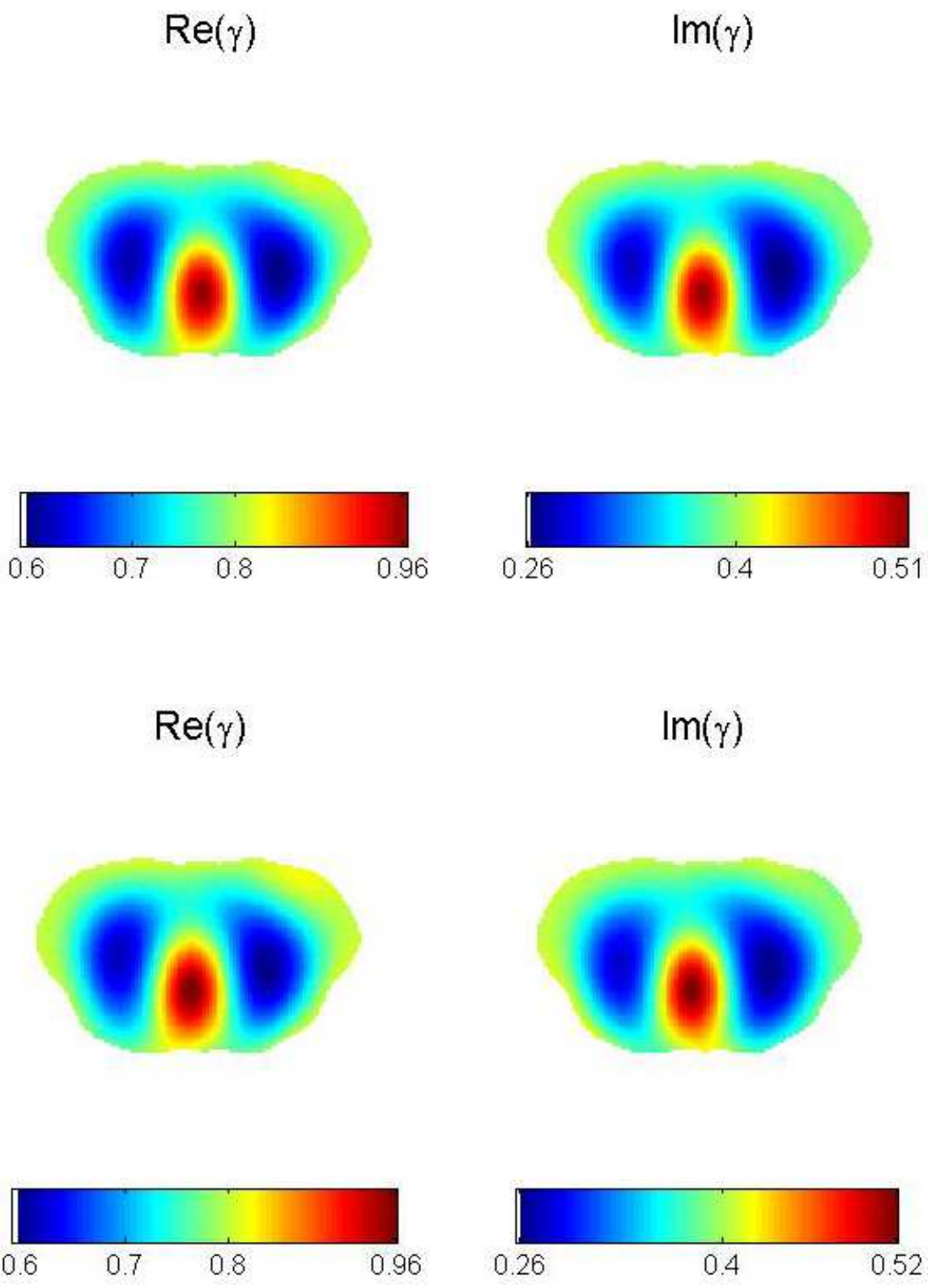

Fig. 7.18: Top row: Reconstruction from noise-free data for Example 1. The dynamic range is 61% for the conductivity, and 64% for the permittivity. Bottom row: Reconstruction from data with 0.01% added noise. The dynamic range is 61% for the conductivity, and 65% for the permittivity.

Example 2: A Resistive Spine

We next revisit the test example with a resistive spine from Section 7.2.1 using the phantom in Figure 7.5 and the same admittivity values.

Tab. 7.6: Maximum and minimum values in Example 2 with the non-unitary background and resistive spine were found in the appropriate organ region when applying skip-3 current patterns. The table indicates these values of the admittivity in the appropriate region.

	Admitivity of test problem	Reconstruction from noise-free data	Reconstruction from noisy data
heart	1.1 + 0.6i	1.0120 + 0.5382i	1.0033 + 0.5370i
lungs	0.5 + 0.2i	0.6028 + 0.2693i	0.6028 + 0.2703i
spine	0.2 + 0.05i	0.6051 + 0.2775i	0.6101 + 0.2742i
background	0.8+0.4i	0.8+0.4i	0.8+0.4i

The scattering transforms were evaluated on the same k grid as in Example 1. For both the zero noise and 0.01% noise cases, the scattering transform S were truncated so that neither the magnitude of the maximum real component nor the maximum imaginary component exceeded 0.02 or 0.015, respectively. The resulting scattering transforms can be viewed in Figure 7.19.

The $\bar{\partial}_k$-equation was solved on the same z grid as the previous chest shaped domain examples. Reconstructions of the admittivity distributions for zero and 0.01% noise are shown in Figure 7.20. For the zero noise case, the dynamic range is 45% for the conductivity and 49% for the permittivity compared to 45% and 48% for the 0.01% noise case. Again, these values are clearly lower than in Example 1 which does not contain a resistive spine. The spine is clearly visible in both the zero and 0.01% noise cases even though the bridging artifact is present. As was the case with the trigonometric current patterns, increasing the radius $|k|$ for the scattering data and allowing higher values in the non-uniform truncation of the scattering transform, decreases the presence of the bridging artifact leaving a better defined separation for resistive object visible at the top of the reconstruction. However, other artifacts are introduced, e.g., the shapes of the lungs and heart become distorted.

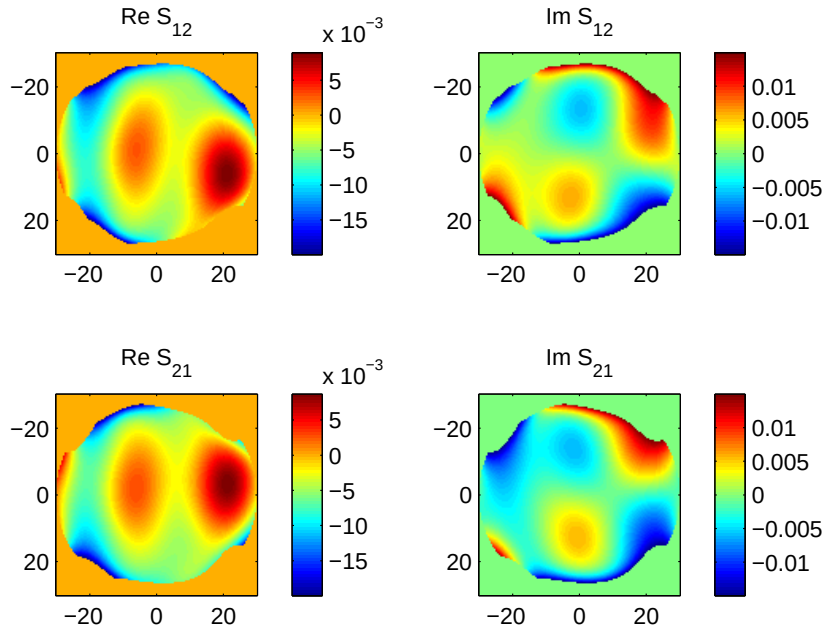

(a) Zero Noise

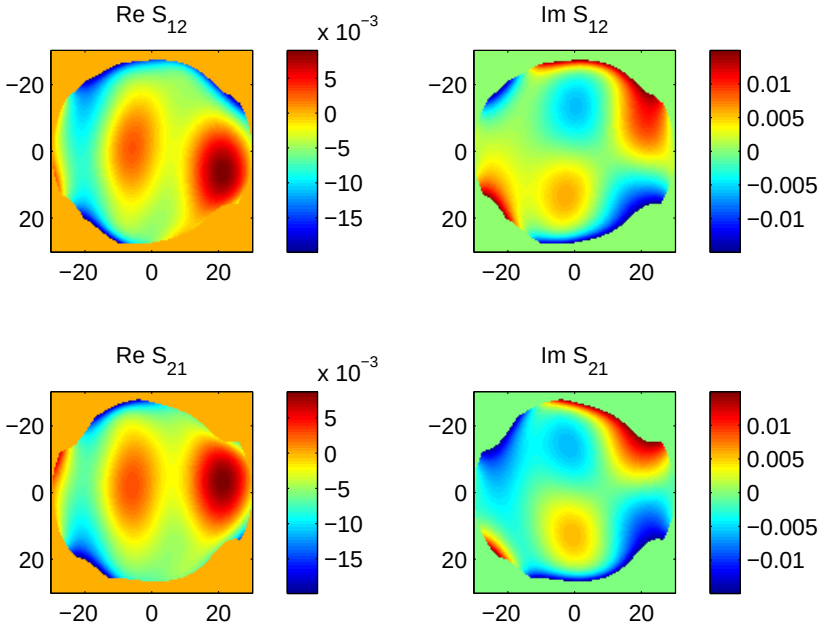

(b) 0.01% Noise

Fig. 7.19: Scattering data for Example 2 with skip-3 current patterns. Figure (a) shows the scattering data used for the zero noise case whereas (b) depicts the scattering data used in the 0.01% noisy case.

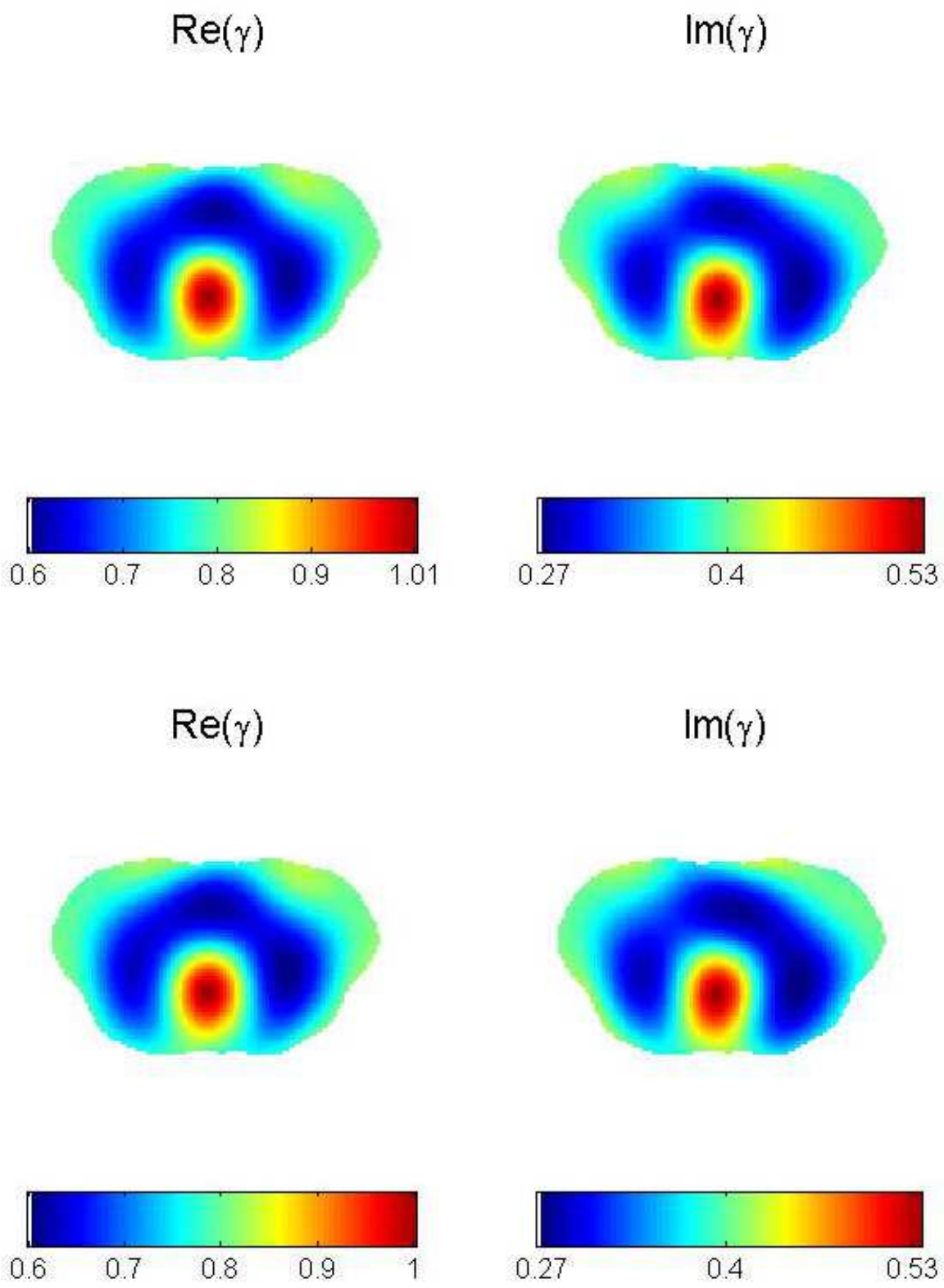

Fig. 7.20: Top row: Reconstruction from noise-free data for Example 2. The dynamic range is 45% for the conductivity, and 49% for the permittivity. Bottom row: Reconstruction from data with 0.01% added noise. The dynamic range is 45% for the conductivity, and 48% for the permittivity.

To emphasize the presence of the spine, Figure 7.21 shows the difference image produced by taking the zero noise reconstruction in Example 2 (Figure 7.20) and subtracting the zero noise reconstruction in Example 1 (which has no spine, see Figure 7.18). In this figure the spine is clearly visible with dynamic range of 22% for the conductivity and 24% for the permittivity.

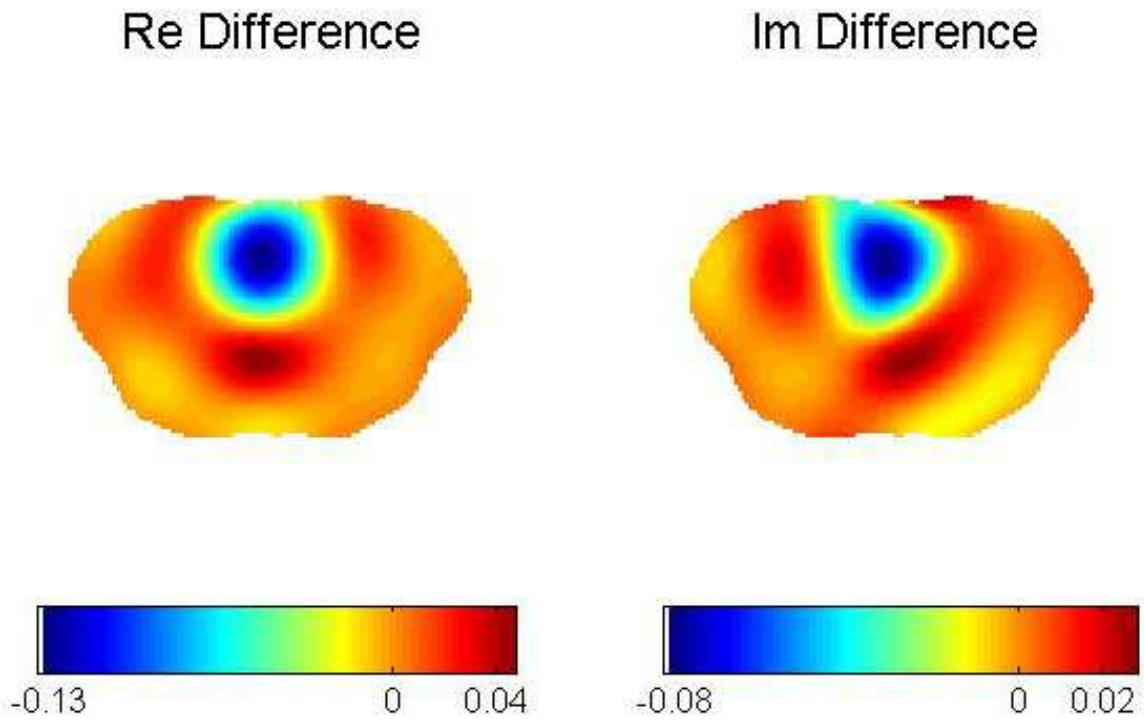

Fig. 7.21: Difference image for the resistive spine in Table 7.6 produced by taking the zero noise reconstruction for Example 2 and subtracting the zero noise reconstruction from Example 1. The dynamic range for the spine is 22% for the conductivity, and 24% for the permittivity.

Example 3: A Conductive Tumor

We next revisit the test example with a conductive tumor in the right lung using the phantom in Figure 7.9 and the same admittivity values as before.

Tab. 7.7: Maximum and minimum values in Example 3 with the non-unitary background and conductive tumor in the right lung were found in the appropriate organ region when applying skip-3 current patterns. The table indicates these values of the admittivity in the appropriate region.

	Admitivity of test problem	Reconstruction from noise-free data	Reconstruction from noisy data
heart	1.1 + 0.6i	0.9384 + 0.4987i	0.9298 + 0.4982i
lungs	0.5 + 0.2i	0.6403 + 0.2901i	0.6381 + 0.2951i
tumor	1.1+ 0.6i	0.6955+ 0.3303i	0.7062 + 0.3392i
background	0.8+0.4i	0.8+0.4i	0.8+0.4i

The scattering transforms were evaluated on the same k grid as in Examples 1 and 2. For both the zero noise and 0.01% noise cases, the scattering transform S were truncated so that neither the magnitude of the maximum real component nor the maximum imaginary component exceeded 0.01. The resulting scattering transforms can be viewed in Figure 7.22.

The $\bar{\partial}_k$-equation was solved on the same z grid as the previous chest shaped domain examples. Reconstructions of the admittivity distributions for zero and 0.01% noise are shown in Figure 7.23. For the zero noise case, the dynamic range is 50% for the conductivity and 52% for the permittivity compared to 49% and 51% for the 0.01% noise case. Again, these values are lower than their trigonometric current pattern counterparts in Example 3 of Section 7.2.1. The bridging artifact between the two lungs is disappointing and regardless of the the scattering transform and truncation criterion tried, this artifact has yet to be removed and may be due to the manner in which the skip current patterns penetrate the domain.

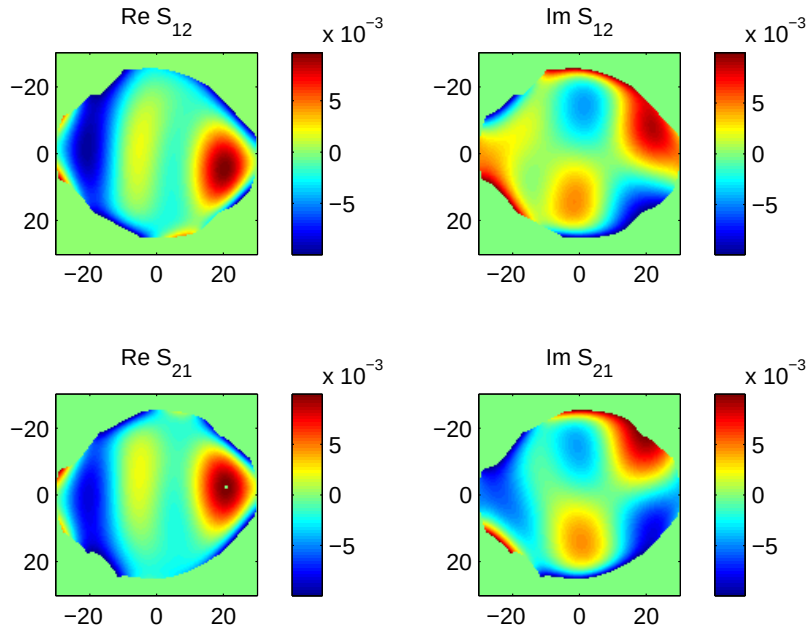

(a) Zero Noise

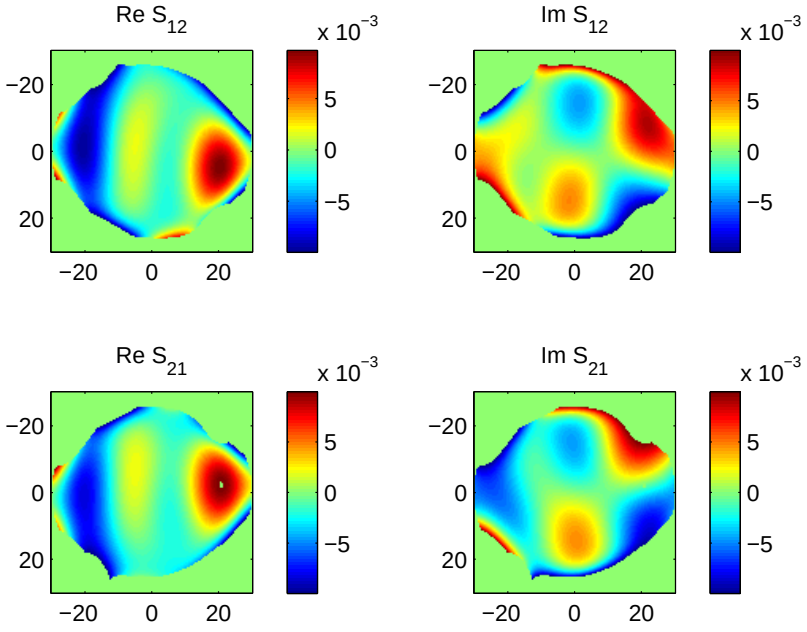

(b) 0.01% Noise

Fig. 7.22: Scattering data for Example 3 with skip-3 current patterns. Figure (a) shows the scattering data used for the zero noise case whereas (b) depicts the scattering data used in the 0.01% noisy case.

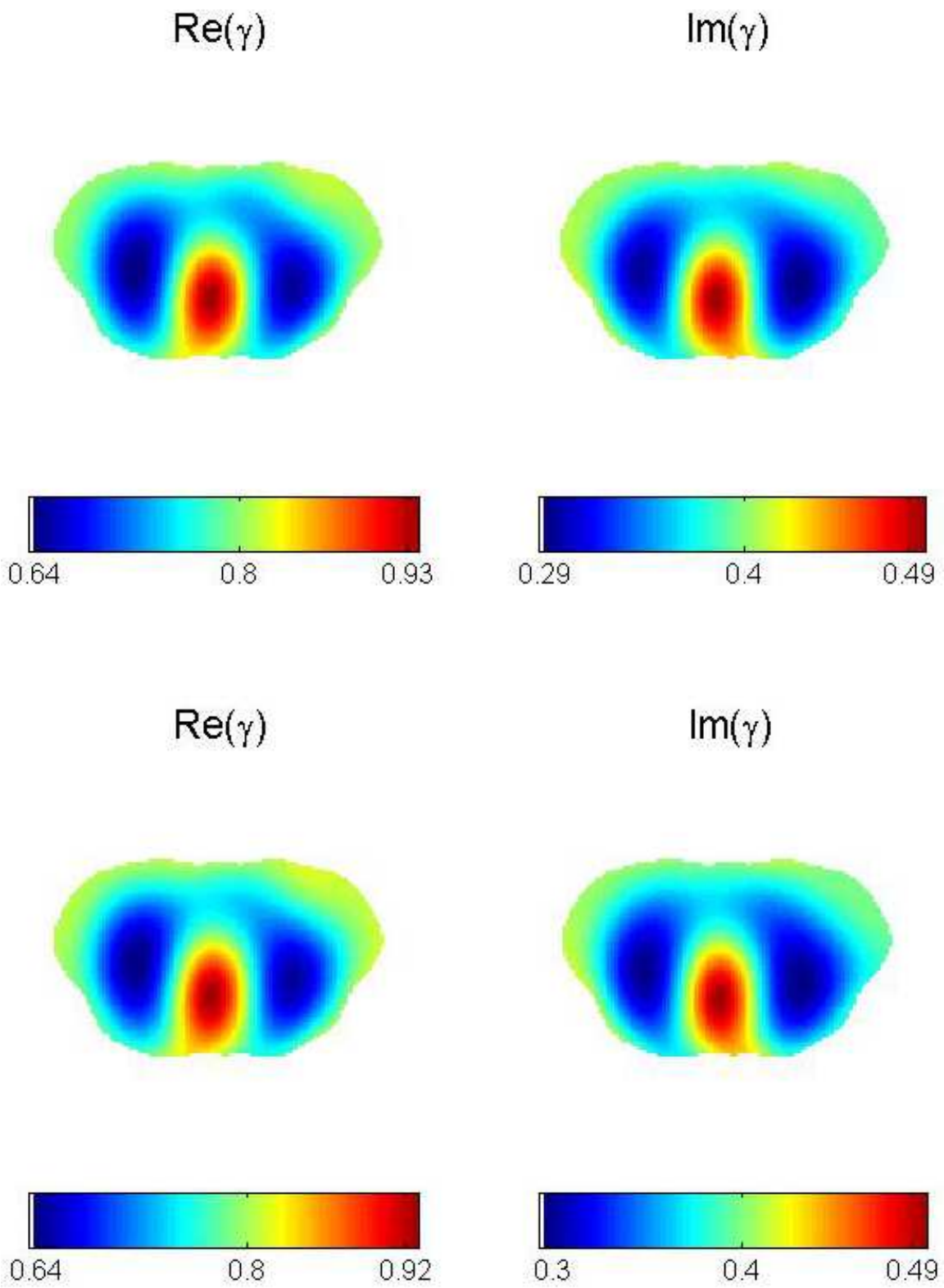

Fig. 7.23: Top row: Reconstruction from noise-free data for Example 3 using skip-3 current patterns. The dynamic range is 50% for the conductivity, and 52% for the permittivity. Bottom row: Reconstruction from data with 0.01% added noise. The dynamic range is 49% for the conductivity, and 51% for the permittivity.

As was the case for the trigonometric current patterns in Section 7.2.1, the the tumor is not immediately visible in the right lung. The right lung does appear less resistive than the left and Figure 7.24 shows the difference image produced by taking the zero noise reconstruction in Example 3 (Figure 7.23) and subtracting the zero noise reconstruction in Example 1 (which has no tumor, see Figure 7.18) therefore emphasizing the presence of the tumor. Admittedly the artifact present in the left lung due to the difference in reconstructed values for Examples 1 and 3 is disappointing, however the tumor is clearly visible, although enlarged, in the right lung and has a dynamic range of 11% for the conductivity, and 10% for the permittivity.

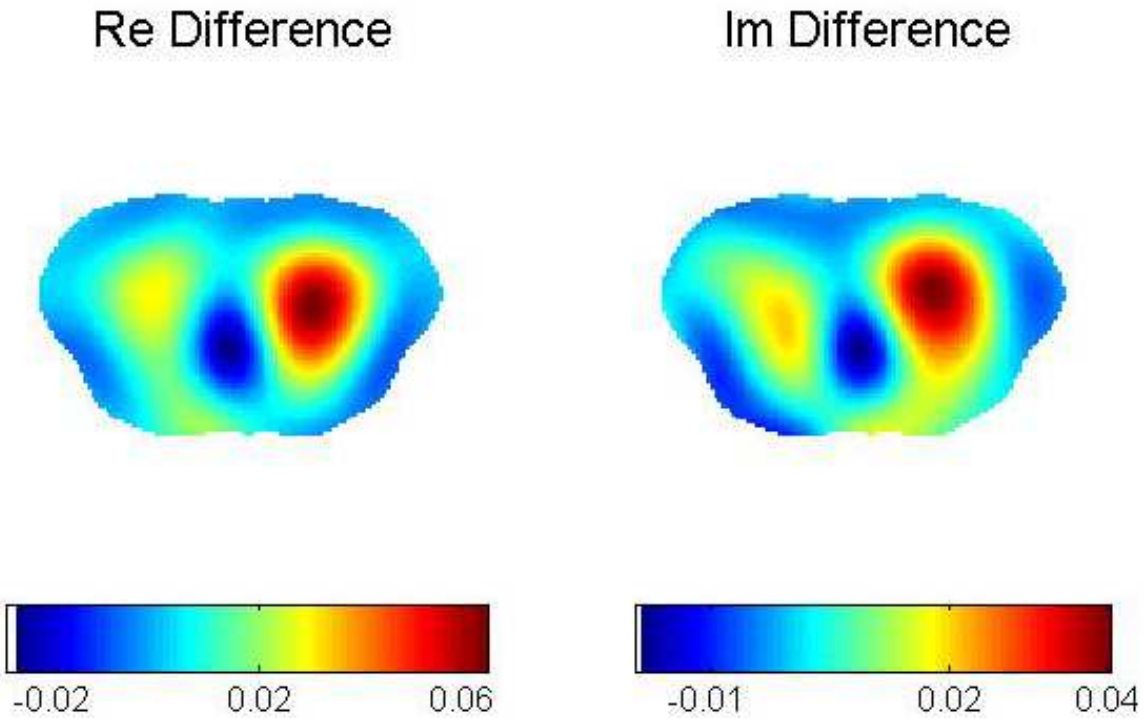

Fig. 7.24: Difference image for the conductive tumor in Table 7.7 produced by taking the zero noise reconstruction for Example 3 and subtracting the zero noise reconstruction from Example 1 using skip-3 current patterns. The dynamic range for the tumor is 11% for the conductivity, and 10% for the permittivity.

8. CONCLUSIONS

In this thesis, the first direct $\bar{\partial}$-algorithm for complex admittivities where the conductivity, σ, and permittivity ϵ are twice differentiable and bounded, is formulated. Formulas connecting the CGO solutions Ψ in the nearly constructive proof given by Elisa Francini [Fra00] to practical voltage data (described in the D-N map) are derived and a direct formula is developed for the recovery of the matrix potential Q from the CGO solutions $M(z,k)$ that only requires knowledge of $M(z,0)$. The reconstruction algorithm is implemented and tested on simulated FEM voltage data for unitary and complex-valued backgrounds on circular and non-circular domains. The method was applied to numerically simulated phantoms with discontinuous admittivity distributions. In all cases, the results were found to display excellent spatial resolution and good dynamic range, even in the presence of noise. This work demonstrates that EIT, with the incorporation of permittivity, is a promising imaging technique for chest imaging.

BIBLIOGRAPHY

[Ale98] G. Alessandrini, *Stable determination of conductivity by boundary measurements*, Appl. Anal. **27** (1998), no. no. 1-3, 153–172.

[ALP05] K. Astala, M. Lassas, and L. Päivärinta, *Calderóns inverse problem for anisotropic conductivity in the plane*, Comm. Partial Differential Equations **30** (2005), 207224.

[ALP11] K. Astala, M. Lassas, and L. Paivarinta, *The borderlines of the invisibility and visibility for Calderon's inverse problem*, (available on arXiv: 1109.2749) **(submitted)** (2011).

[AMP+11] K. Astala, J. L. Mueller, L. Päivärinta, L. Peramaki, and S. Siltanen, *Direct electrical impedance tomography for nonsmooth conductivities*, Inverse Problems and Imaging **5** (2011), no. 3, 531–549.

[AMPS10] K. Astala, J. L. Mueller, L. Päivärinta, and S. Siltanen, *Numerical computation of complex geometrical optics solutions to the conductivity equation*, Applied and Computational Harmonic Analysis **29** (2010), 2–17.

[AP06] K. Astala and L. Päivärinta, *Calderón's inverse conductivity problem in the plane*, Ann. of Math. **163** (2006), 265–299.

[AS91] A. Allers and F. Santosa, *Stability and resolution analysis of a linearized problem in electrical impedance tomography*, Inverse Problems **7** (1991), 515533, linearization using moment methods.

[BB90] D. C. Barber and B. H. Brown, *Inverse problems in partial differential equations*, ch. Progress in electrical impedance tomography, pp. 151–164, SIAM, 1990, backprojection methods.

[BBM94] B. H. Brown, D. C. Barber, and A. H. Morice, *Cardiac and respiratory related electrical impedance changes in the human thorax*, IEEE Trans. Biomed. Eng. **41** (1994), 729–734.

[BBP96] L. Borcea, J. G. Berryman, and G. Papanicolaou, *High contrast impedance tomography*, Inverse Problems **12** (1996), 835858.

[BBR01] J. A. Barceló, T. Barceló, and A. Ruiz, *Stability of the inverse conductivity problem in the plane for less regular conductivities*, J. Differential Equations **173** (2001), 231–270.

[BC80] R. Beals and R. R. Coifman, *Scattering, transformations spectrales, et equations d'evolution non lineaires i,ii*, Seminaire Goulaouic-Meyer-Shwartz **Expose 22** (1980), First paper using dbar for inverse scattering.

[BC85] ———, *Multidimensional inverse scattering*, Proceedings of symposia in pure mathematics **43** (1985), 45–70.

[BC86] ———, *The D-bar approach to inverse scattering and nonlinear evolutions*, Physica **18D** (1986), 242–249.

[BKIS08] G. Boverman, T.J. Kao, D. Isaacson, and Gary J. Saulnier, *An implementation of Calderón's method for 3-D limited view EIT*, IEEE Trans. Med. Imaging **1** (2008), no. 1, 1–10.

[BKM11] J. Bikowski, K. Knudsen, and J. L. Mueller, *Direct numerical reconstruction of conductivities in three dimensions using scattering transforms*, Inverse Problems **27** (2011), no. 1, 015002.

[Blu97] R. Blue, *Real-time three-dimensional Electrical Impedance Tomography*, Ph.D Thesis, R.P.I., Troy, NY, 1997.

[BM04] J. Bikowski and J. L. Mueller, *Electrical impedance tomography and the fast multipole method*, Proceedings of the 2004 SPIE Annual Meeting (P. J. Bones, M. A. Fiddy, and R. P. Millane, eds.), SPIE, 2004, p. 129140.

[BM08] ———, *2D EIT reconstructions using Calderóns method*, Inverse Problems and Imaging **2** (2008), no. 1, 43–61.

[Bor01] L. Borcea, *Nonlinear multigrid for imaging electrical conductivity and permittivity at low frequency*, Inverse Problems **17** (2001), 329–359.

[BT91] C. Berenstein and E. C. Tarabusi, *Inversion formulas for the k-dimensional radon transform in real hyperbolic spaces*, Duke Math. J. **62** (1991), 1–19, backprojection.

[BT03] R. M. Brown and R. H. Torres, *Uniqueness in the inverse conductivity problem for conductivities with 3/2 derivatives in l^p, $p > 2n$*, Anal. Appl. **9** (2003), 1049–1056.

[BU97] R. M. Brown and G. A. Uhlmann, *Uniqueness in the inverse conductivity problem for nonsmooth conductivities in two dimensions*, Communications in Partial Differential Equations **22** (1997), no. 5&6, 1009–1027.

[Buk08] A. Bukhgeim, *Recovering the potential from cauchy data in two dimensions*, J. Inverse Ill-Posed Probl. **16** (2008), 1934.

[Cal80] A. P. Calderón, *On an inverse boundary value problem*, Seminar on Numerical Analysis and its Applications to Continuum Physics (Rio de Janerio), Soc. Brasileira de Matematica, 1980, pp. 67–73.

[CBKM08] A. P. Calderón, A. Bellow, C. E. Kenig, and P. Malliavin, *Selected papers of Alberto P. Calderón with commentary*, illustrated ed., Collected Works Series, ch. Commentary on Calderón's Paper (29), On an Inverse Boundary Value Problem, by Gunther Uhlmann, pp. 623–636, American Mathematical Soc., 2008, ISBN:0821842978, 9780821842973.

[CCG08] E. L. V. Costa, C. N. Chaves, and S. Gomes, *Real-time detection of pneumothorax using electrical impedance tomography*, Crit. Care Med. **36** (2008), 1230–1238.

[CGMS05] N. Coulombe, H. Gagnon, F. Marquis, and Y. Skrobik, *A parametric model of the relationship between EIT and total lung volume*, Physiological Measurement **26** (2005), 401–411.

[CII90] M. Cheney, D. Isaacson, and E. L. Isaacson, *Exact solutions to a linearized inverse boundary value problem*, Inverse Problems **6** (1990), 923–934.

[CIN+90] M. Cheney, D. Isaacson, J. C. Newell, S. Simske, and J. Goble, *Noser: An algorithm for solving the inverse conductivity problem*, Int. J. Imag. Sys. Tech. **2** (1990), 66–75.

[CING89] K.S. Cheng, D. Isaacson, J. C. Newell, and D. G. Gisser, *Electrode models for electric current computed tomography*, IEEE Transactions on Biomedical Engineering **36** (1989), no. 9, 918–924.

[CLA09] E. L. V. Costa, R. G. Lima, and M. B. P. Amato, *Electrical impedance tomography*, Curr Opin Crit Care. **15** (2009), no. 1, 18–24.

[CMGW06] P. Church, J. E. McFee, S. Gagnon, and P. Wort, *Electrical impedance tomographic imaging of buried landmines*, IEEE Transactions on Geoscience and Remote Sensing **44** (2006), no. 9, 2407–2420.

[DBABP99] O. Dorn, H. Berteta-Aguirre, J. G. Berryman, and G. Papanicolaou, *A nonlinear inversion method for 3d-electromagnetic imaging using adjoint fields*, Inverse Problems **15** (1999), 1523–1558.

[DHK11] F. Delbary, P. C. Hansen, and K. Knudsen, *A direct numerical reconstruction algorithm for the 3D Calderón problem*, Journal of Physics: Conference Series (Print) **290** (2011), 012003.

[DM10] M. DeAngelo and J. L. Mueller, *2D D-bar reconstructions of human chest and tank data using an improved approximation to the scattering transform*, Physiological Measurement **31** (2010), 221–232.

[Dob92] D. C. Dobson, *Convergence of a reconstruction method for the inverse conductivity problem*, SIAM J. Appl. Math. **52** (1992), 442458.

[DR95] W. Daily, , and A. Ramirez, *Electrical resistance tomography during in-situ tricholoethylene remediation at the savannah river site*, Appl. Geophys. (1995), no. 33, 329–249.

[DRJ98] W. Daily, , A. Ramirez, and R. Johnson, *Electrical impedance tomography of a perchloroethylene release*, JEEG (1998), no. 2, 189–201.

[DRLN92] W. Daily, A. Ramirez, D. LaBrecque, and J. Nitao, *Electrical resistivity tomography of vadose water movement*, Water Resources Res. (1992), no. 28, 1429–1442.

[DS94] D. C. Dobson and F. Santosa, *An image-enhancement technique for electrical impedance tomography*, Inverse Problems **10** (1994), 317–334.

[EIS+98] P. M. Edic, D. Isaacson, G. J. Saulnier, H. Jain, and J. C. Newell, *An iterative newton-raphson method to solve the inverse admittivity problem*, IEEE Transactions on Biomedical Engineering **45** (1998), no. 7, 899–900.

[Fad66] L. D. Faddeev, *Increasing solutions of the schrödinger equation*, Sov. Phys. Dokl **10** (1966), 1033–5.

[FAS07] D. Freimark, M. Arad, and R. Sokolover, *Monitoring lung fluid contest in chf patients under intravenous diuretics treatment using bio-impedance measurements*, Physiol. Meas. **28** (2007), S269–S277.

[FCI+91] F. Fuks, M. Cheney, D. Isaacson, D. G. Gisser, and J. C. Newell, *Detection and imaging of electric conductivity and permittivity at low frequency*, IEEE Transactions on Biomedical Engineering **38** (1991), no. 11, 1106–1110.

[FHHW02] I. Frerichs, J. Hinz, P. Herrmann, and G. Weisser, *Detection of local lung air content by electrical impedance tomography compared with electron beam ct*, J. Appl. Physiol. **93** (2002), 660–666.

[FPE09] I. Frerichs, S. Pulletz, and G. Elke, *Assessment of changes in distribution of lung perfusion by electrical impedance tomography*, Respiration **77** (2009), 282–291.

[Fra00] E. Francini, *Recovering a complex coefficient in a planar domain from the dirichlet-to-neumann map*, Inverse Problems **16** (2000), 107–119.

[FSPS07] I. Frerichs, G. Schmitz, S. Pulletz, and D Schaedler, *Reproducibility of regional lung ventilation distribution determined by electrical impedance tomography during mechanical ventilation*, Physiol. Meas. **28** (2007), 261–267.

[Ges71] D. B. Geselowitz, *An application of electrocardiographic lead theory to impedance plethysmography*, IEEE Trans. Biomed. Eng. **18** (1971), 38–41.

[GGKM67] C. S. Gardner, J. M. Greene, M. D. Kruskal, and R. M. Miura, *Method for solving the korteweg-de vries equation*, Phys. Rev. Lett. **19** (1967), 1095–1097, First paper using dbar methods for KdV.

[GKLU07] A. Greenleaf, Y. Kurylev, M. Lassas, and G. Uhlmann, *Full-wave invisibility of active devices at all frequencies*, Comm. Math. Phys. **275** (2007), 749789.

[Gla01] Roland Glaser, *Biophysics*, 5th ed., Springer-Verlag, New York, 2001.

[GLU03a] A. Greenleaf, M. Lassas, and G. Uhlmann, *Anisotropic conductivities that cannot be detected in eit*, Physiolog. Meas. (special issue on Impedance Tomography) **24** (2003), 413–420.

[GLU03b] ———, *On nonuniqueness for Calderons inverse problem*, Math. Res. Lett. **10** (2003), no. 5-6, 685–693.

[GLU09] ———, *Invisibility and inverse problems*, Bull. Amer. Math. Soc. **46** (2009), 55–59.

[Ham09] Sarah J. Hamilton, *Simulation of voltages on electrodes for the 2-D EIT forward admittivity problem by the continuum and complete electrode models*, Master's thesis, Colorado State University, 2009.

[HHMV12] S. J. Hamilton, N. L. Herrera, J. L. Mueller, and A. VonHerrmann, *A direct D-bar reconstruction algorithm for recovering a complex conductivity in 2-D*, Inverse Problems, To Appear (2012).

[HVWV02] L.M. Heikkinen, T. Vilhunen, R. West, and M. Vauhkonen, *Simultaneous reconstruction of electrode contact impedances and internal electrical properties: Ii. laboratory experiments*, Meas. Sci. Technol. **13** (2002), 1885–61.

[HWWT91] P. Hua, E.J. Woo, J. G. Webster, and W.J. Tompkins, *Iterative reconstruction methods using regularization and optimal current patterns in electrical impedance tomography*, IEEE Trans. on Med. Imag **10** (1991), no. 4, 621–628.

[IC90] D. Isaacson and M. Cheney, *Current problems in impedance imaging*, Inverse Problems in Partial Differential Equations (Philidelphia) (David Colton, Richard Ewing, and William Rundell, eds.), AMS, SIAM, 1990, pp. 141–150.

[IC91] ———, *Effects of measurement precision and finite numbers of electrodes on linear impedance imaging algorithms*, SIAM J. Appl. Math **51** (1991), 1705–1731.

[II89] D. Isaacson and E. L. Isaacson, *Comment on Calderóns paper: "on an inverse boundary value problem"*, Math. of Comp. **52** (1989), 553–9.

[IIN+07] T. Ide, H. Isozaki, S. Nakata, S. Siltanen, and G. Uhlmann, *Probing for electrical inclusions with complex spherical waves*, Communications on Pure and Applied Mathematics **60** (2007), 14151442.

[IKK+07] U. Z. Ijaz, B. S. Kim, T.J. Kao, A. K. Khambampati, S. K., M. C. Kim, J. C. Newell, D. Isaacson, and K. Y. Kim, *Mammography phantom studies using 3D Electrical Impedance Tomography with numerical forward solver*, Frontiers in the Convergence of Bioscience and Information Technologies (2007), 379–383.

[IMNS04] D. Isaacson, J.L. Mueller, J.C. Newell, and S. Siltanen, *Reconstructions of chest phantoms by the d-bar method for electrical impedance tomography*, IEEE Trans Med Imaging **23** (2004), no. 7, 821–828.

[IMNS06] D. Isaacson, J. L. Mueller, J. C. Newell, and S. Siltanen, *Imaging cardiac activity by the d-bar method for electrical impedance tomography*, Physiol. Mea. **27** (2006), S43–S50.

[IS00] M. Ikehata and S. Siltanen, *Numerical method for finding the convex hull of an inclusion in conductivity from boundary measurements*, Inverse Problems **16** (2000), 1043–1052.

[IS04] ———, *Electrical impedance tomography and mittag-leffers function*, Inverse Problems **20** (2004), 1325–1348.

[JIEN97] H. Jain, D. Isaacson, P. M. Edic, and J. C. Newell, *Electrical Impedance Tomography of complex conductivity distributions with noncircular boundary*, IEEE Transactions on Biomedical Engineering **44** (1997), no. 11, 1051–1060.

[KB92] J. S. Kallman and J. G. Berryman, *Weighted least-squares methods for electrical impedance tomography*, IEEE Trans. Med. Imaging **11** (1992), 284292.

[KINS06] T.J. Kao, D. Isaacson, J. C. Newell, and G. J. Saulnier, *A 3D reconstruction algorithm for EIT using a handheld probe for breast cancer detection*, Physiol. Meas (2006), S1–S11.

[KKSV00] J.P. Kaipio, V. Kolehmainen, E. Somersalo, and M. Vauhkonen, *Statistical inversion and Monte Carlo sampling methods in electrical impedance tomography*, Inverse Problems **16** (2000), no. 5, 1487–1522.

[KLMS09] K. Knudsen, M. Lassas, J. L. Mueller, and S. Siltanen, *Regularized D-bar method for the inverse conductivity problem*, Inverse Problems and Imaging **3** (2009), no. 4, 599–624.

[KMS04] K. Knudsen, J. Mueller, and S. Siltanen, *Numerical solution method for the dbar-equation in the plane*, Journal of Computational Physics **198** (2004), 500–517.

[KNR99] P. W. Kunst, A. Vonk Noordegraaf, and E. Raaijmakers, *Electrical Impedance Tomography in the assessment of extravascular lung water in noncardiogenic acute respiratory failure*, Chest **116** (1999), 1695–1702.

[KNSI07] T. Kao, J. Newell, G. Saulnier, and D. Isaacson, *Radiolucent electrode array for combined EIT and mammography*, World Congress on Medical Physics and Biomedical Engineering (2007), 3893–3896.

[Knu02] K. Knudsen, *On the inverse conductivity problem*, Ph.D. Thesis, Aalborg University, 2002.

[KPH+02] T. E. Kerner, K. D. Paulsen, A. Hartov, S. K. Soho, and S. P. Poplack, *Electrical impedance spectroscopy of the breast: Clinical imaging results in 26 subjects*, IEEE Transactions on Medical Imaging **21** (2002), no. 6, 638–645.

[KT04] K. Knudsen and A. Tamasan, *Reconstruction of less regular conductivities in the plane*, Comm. Partial Differential Equations **29** (2004), 361381.

[KV84] R. Kohn and M. Vogelius, *Determining conductivity by boundary measurements*, Communications on Pure and Applied Mathematics **37** (1984), 289–298.

[KV85] ———, *Determining conductivity by boundary measurements ii. interior results*, Communications on Pure and Applied Mathematics **38** (1985), 643–667.

[KWT83] Y. Kim, J. G. Webster, and W. J. Tompkins, *Electrical impedance imaging of the thorax*, J. Microwave Power **18** (1983), 245–257.

[Leh72] J. Lehr, *A vector derivation useful in impedance plethysmographic field calculation*, IEEE Trans. Biomed. Eng. **19** (1972), 156–157.

[LTU03] M. Lassas, M. Taylor, and G. Uhlmann, *The dirichlet-to-neumann map for complete riemannian manifolds with boundary*, Comm. Geom. Anal. **11** (2003), 207222.

[MAF+10] F. S. Moura, J. C. C. Aya, A. T. Fleury, M. B. P. Amato, and R. G. Lima, *Dynamic imaging in Electrical Impedance Tomography of the human chest with online transition matrix identification*, IEEE Trans. Biomed. Eng. **57** (2010), no. 2, 422–431.

[MCCG06] F. Marquis, N. Coulombe, R. Costa, and H. Gagnon, *Electrical impedance tomography's correlation to lung volume is not influenced by anthropometric parameters*, J. Clinical Monitoring and Computing **20** (2006), 201–207.

[MIN99] J. L. Mueller, D. Isaacson, and J. C. Newell, *A reconstruction algorithm for electrical impedance tomography data collected on rectangular electrode arrays*, IEEE Trans. Biomed. Engr. **49** (1999), 1379–1386.

[MM09] E. K. Murphy and J. L. Mueller, *Effect of domain-shape modeling and measurement errors on the 2-D D-bar method for electrical impedance tomography*, IEEE Trans. Med. Imaging **28** (2009), no. 10, 15761584.

[MS03] J. Mueller and S. Siltanen, *Direct reconstructions of conductivities from boundary measurements*, SIAM Journal of Scientific Computation **24** (2003), no. 4, 1232–1266, http://www.siltanen-research.net/publications.html.

[MSI02a] J. L. Mueller, S. Siltanen, and D. Isaacson, *A direct reconstruction algorithm for electrical impedance tomography*, IEEE Trans. Med. Imag. **21** (2002), no. 6, 555–559.

[MSI02b] ———, *A direct reconstruction algorithm for electrical impedance tomography*, IEEE Trans. Med. Imag. **21** (2002), no. 6, 555–9.

[Mur07] E. K. Murphy, *2-D D-Bar conductivity reconstructions on non-circular domains*, Ph.D. Thesis, Colorado State University, Fort Collins, CO, Fall 2007.

[Nac88] A. I. Nachman, *Reconstructions from boundary measurements*, Ann. of Math. **2** (1988), no. 128, 531576.

[Nac96] ———, *Global uniqueness for a two-dimensional inverse boundary value problem*, Ann. of Math. **2** (1996), no. 143, 71–96.

[NSU88] A. I. Nachman, J. Sylvester, and G. Uhlmann, *An n-dimensional borg-levinson theorem*, Comm. Math. Phys. **115** (1988), 595605.

[Pha11] TMT Pham, *Regional ventilation distribution in the first 6 months of life*, Eur Respir J. **37** (2011), 919–924.

[RDB+96] A. Ramirez, W. Daily, A. Binley, D. LaBrecque, and D. Roelant, *Detection of leaks in underground storage tanks using electrical resistance methods*, J. Envir. Eng. Geophys. **1** (1996), 189–203.

[RDL+93] A. Ramirez, W. Daily, D. LaBrecque, E. Owen, and D. Chesnut, *Monitoring an underground steam injection process using electrical resistance tomography*, Water Resources Research **29** (1993), 73–87.

[RWW04] S. Meng R.M. West, R.G. Aykroyd and R.A. Williams, *Markov chain monte carlo techniques and spatialtemporal modelling for medical eit*, Physiological Measurement **25** (2004), 181–94.

[SCI92] E. Somersalo, M. Cheney, and D. Isaacson, *Existence and uniqueness for electrode models for Electric Current Computed Tomography*, SIAM Journal of Applied Mathematics **52** (1992), no. 4, 1023–1040.

[SCII91] E. Somersalo, M. Cheney, D. Isaacson, and E. Isaacson, *Layer stripping: a direct numerical method for impedance imaging*, Inverse Problems **7** (1991), 899926.

[SGS94] A.V. Shahidi, R. Guardo, and P. Savard, *On the monitoring of pulmonary edema by impedance tomography*, Engineering in Medicine and Biology Society, 1994. Engineering Advances: New Opportunities for Biomedical Engineers. Proceedings of the 16th Annual International Conference of the IEEE **1** (1994), 532–533.

[Sil99] S. Siltanen, *Electrical Impedance Tomography and Faddeev Green's Functions*, Ph.D. Thesis, Helsinki University of Technology, Espoo, Finland, 1999.

[Sim87] S. J. Simske, *An adaptive current determination and a one-step reconstruction technique for a current tomography system*, Master's thesis, R.P.I., Troy, NY, 1987, NOSER algorithm.

[SK57] H. P. Schwan and C. F. Kay, *The conductivity of living tissues*, Annals of the New York Academy of Sciences **65** (1957), 1007–1013.

[SMI00] S. Siltanen, J. Mueller, and D. Isaacson, *An implementation of the reconstruction algorithm of a. nachman for the 2-D inverse conductivity problem*, Inverse Problems **16** (2000), 681–699.

[SMI01] S. Siltanen, J. L. Mueller, and D. Isaacson., *Radon transforms and tomography*, Contemp. Math., vol. 278, ch. Reconstruction of high contrast 2-D conductivities by the algorithm of A. Nachman, pp. 241–254, Amer. Math. Soc., Providence, RI, 2001.

[SNM04] H. Smit, A. Vonk Noordegraaf, and J. T. Marcus, *Determinants of pulmonary perfusion measured by electrical impedance tomography*, Eur. J. Appl. Physiol. **92** (2004), 45–49.

[SSS30] S. Stefanescu, C. Schlumberger, and M. Schlumberger, *Sur la distribution electrique autour dune prise de terre ponctuelle dans un terrain a couches horizontales, homogenes et isotropes*, J. Physics and Radium Ser. (1930), no. 7, 132140.

[SU86] J. Sylvester and G. Uhlmann, *A uniqueness theorem for an inverse boundary value problem in electrical prospection*, Comm. Pure Appl. Math. **39** (1986).

[SU03] Z. Sun and G. Uhlmann, *Anisotropic inverse problems in two dimensions*, Inverse Problems **19** (2003), 1001–1010.

[SV90] F. Santosa and M. Vogelius, *A backprojection algorithm for electrical impedance imaging*, SIAM J. Appl. Math. **50** (1990), 216–243.

[Syl90] J. Sylvester, *An anisotropic inverse boundary value problem*, Comm. Pure Appl. Math. **43** (1990), 201232.

[Syl92] ———, *A convergent layer stripping algorithm for the radially symmetric impedance tomography problem*, Comm. Partial Differential Equations **17** (1992), 19551994.

[TGLA04] F. C. Trigo, R. Gonzalez-Lima, and M. B. P. Amato, *Electrical impedance tomography using the extended kalman filter*, IEEE Trans. Biomed. Engr. **51** (2004), 72–81.

[Uhl99] G. A. Uhlmann, *Developments in inverse problems since Calderóns foundational paper*, Harmonic analysis and partial differential equations, Univ. Chicago Press, Chicago, IL, 1999.

[UW08] G. Uhlmann and J-N. Wang, *Complex geometrical optics solutions and reconstruction of discontinuities*, SIAM J. Appl. Math. **68** (2008), 10261044.

[VBOM04] J. A. Victorino, J. B. Borges, V. N. Okamoto, and G. F. J. Matos, *Imbalances in regional lung ventilation: a validation study on electrical impedance tomography*, Am. J. Respir. Crit. Care Med. **169** (2004), 791–800.

[VKK98] M. Vauhkonen, P. A. Karjalainen, and J. P. Kaipio, *A kalman filter approach to track fast impedance changes in electrical impedance tomography*, IEEE Trans Biomed Eng. **45** (1998), 486493.

[Von09] A. VonHerrmann, *Properties of the reconstruction algorithm and the associated scattering transform for admittivities in the plane*, Ph.D. Thesis, Colorado State University, Fort Collins, CO USA, 2009.

[VVSK99a] P. J. Vauhkonen, M. Vauhkonen, T. Savolainen, and J. P. Kaipio, *Three-dimensional electrical impedance tomography based on the complete electrode model*, IEEE Trans. Biomed. Engr. **46** (1999), 1150–1160.

[VVSK99b] P. J. Vauhkonen, M. Vauhkonen, T. Savolainen, and J. P. Kaipio, *Three-dimensional Electrical Impedance Tomography based on the Complete Electrode Model*, IEEE Transactions on Biomedical Engineering **46** (1999), no. 9, 1150–1160.

[WB95] R. A. Williams and M. S. Beck (eds.), *Process tomography-principles, techniques, and applications*, Butterworth-Heinemann, Oxford, UK, 1995.

[XPB89] C. G. Xie, A. Plaskowski, and M. S. Beck, *8-electrode capacitance system for two-component flow identification*, IEEE Proc. A (1989), no. 136, 173190.

[Yag87] A. E. Yagle, *A layer stripping fast algorithm for the two-dimensional direct current inverse resistivity problem*, IEEE Trans. Geosci. Remote Sensing **25** (1987), 558563.

[YWT87] T.J. Yorkey, J.G. Webster, and W.J. Tompkins, *Comparing reconstruction algorithms for electrical impedance tomography*, IEEE Trans. Biomed. Eng. **34** (1987), 843–852.

[ZRBS] S. Zlochiver, M. M. Radai, and D. Barak-Shinar, *An EIT system for monitoring lung conductivity in chf patients*, www.cardio-inspect.com/EIT_System.pdf.

APPENDIX

A. A DETAILED DERIVATION OF THE ADMITTIVITY EQUATION

The following is taken from my Master's paper [Ham09] and gives a detailed derivation of the admittivity equation (3.3).

A.1 Terminology

Definition: *Electrical impedance* describes the measure of an object's opposition to a sinusoidal alternating current (AC). It extends the concept of resistance in AC circuits by not only describing the relative amplitudes of voltages and currents, but also the changes in their relative phases.

Definition: *Magnetic permeability*, μ, is the degree of magnetization of a material that responds linearly to an applied magnetic field. Materials with high permeabilities allow magnetic flux through more easily than others. (Newtons/Amps^2)

Definition: *Permittivity*, ϵ, is a measure of the ability of a material to store a charge (Farads/meter).

Definition: *Capacitance* is a measure of the amount of electrical charge stored in a material (Farads).

Definition: *Electrical conductivity*, σ, measures the ease with which a steady current can flow.

Definition: The *electrical admittivity*, γ, is a complex value, denoted by $\gamma = \sigma + \mathrm{i}\omega\epsilon$, consisting of the the electrical conductivity (real part) along with the electrical permittivity (frequency dependent imaginary part) where ω is the time frequency of the applied AC

current measured in Hz.

A.2 Maxwell's Equations

In order to describe the propagation of electromagnetic fields through a body, we begin with Maxwell's Equations for free charge and current.

Gauss's Law:

$$\nabla \cdot \vec{D} = \rho_f, \tag{A.1}$$

Gauss's Law for Magnetism:

$$\nabla \cdot \vec{B} = 0, \tag{A.2}$$

Maxwell-Faraday Law or **Faraday's Law of Induction**:

$$\nabla \times \vec{E} = -\frac{\partial \vec{B}}{\partial t}, \tag{A.3}$$

Ampère's Circuital law with Maxwell's Correction:

$$\nabla \times \vec{H} = \vec{J}_f + \frac{\partial \vec{D}}{\partial t}, \tag{A.4}$$

where

$$\vec{D} = \text{electric displacement field}$$

$$\vec{E} = \text{electric field}$$

$$\vec{H} = \text{magnetizing field}$$

$$\vec{B} = \text{magnetic field}$$

$$\rho_f = \text{free charge density}$$

$$\vec{J}_f = \text{free current density}$$

and $\nabla \cdot \vec{A}$ represents the *divergence* of the vector $\vec{A}$, and $\nabla \times \vec{A}$ represents the *curl* of the vector $\vec{A}$. For our problem, $\vec{J}_f = \vec{J}$ is the current density which we apply, on the boundary of the domain we wish to image, during the course of the experiment and use as a boundary condition in the solution to the Forward Problem for the electric potential u.

Gauss's Law explains why opposite charges attract while same charges repel, and that electrical charges create an electrical field which other charges respond to by an electrical force. Gauss's Law for Magnetism states that north and south (magnetic) poles come in pairs which we call 'magnetic dipoles'. Faraday's Law of Induction describes how changing a magnetic field creates an electric field. Ampère's Law states that magnetic fields can be generated by an electrical current and Maxwell's correction ($+\partial\vec{D}/\partial t$) adds that magnetic fields can also be generated by changing an electric field.

In order to apply Maxwell's Equations, we need to impose *constitutive relations*, i.e. relations between $\vec{D}$ and $\vec{E}$, and between $\vec{H}$ and $\vec{B}$. Physically these relations specify how much magnetization and polarization a material acquires when in the presence of electromagnetic fields. Since the currents we apply are of small frequency (28.8-125 kHz), as in [IC90, CCG08, VBOM04, TGLA04, CLA09], we can assume that the following linear *constitutive relations* hold inside the body,

$$\vec{D} = \epsilon(x,\omega)\vec{E} \tag{A.5}$$

$$\vec{B} = \mu(x,\omega)\vec{H} \tag{A.6}$$

$$\vec{J}_f = \sigma(x,\omega)\vec{E} \tag{A.7}$$

where x and ω represent the spatial and frequency dependence of

$$\sigma = \text{electrical conductivity},$$

$$\epsilon = \text{ electrical permittivity},$$

and

$$\mu = \text{magnetic permeability}.$$

In practice, as stated in [IC90], we apply sinusoidal current density patterns (in time) on the boundary of the form,

$$\vec{J}^{\text{source}} = \vec{J}^{\text{source}}(x)\cos(\omega t) = Re\{\vec{J}^{\text{source}} e^{\mathrm{i}\,\omega t}\}. \tag{A.8}$$

Thus, due to Equations (A.5), (A.6), and (A.7) we look for solutions $\vec{E} = \vec{E}(x)e^{\mathrm{i}\,\omega t}$ and

$\vec{B} = \vec{B}(x)e^{\mathrm{i}\,\omega t}$. Using these solutions in Equation (A.3) yields

$$\begin{aligned}
\nabla \times \vec{E} &= -\frac{\partial \vec{B}}{\partial t} \\
&= -\frac{\partial}{\partial t}\left(\vec{B}(x)e^{\mathrm{i}\,\omega t}\right) \\
&= -\mathrm{i}\,\omega\left(\vec{B}(x)e^{\mathrm{i}\,\omega t}\right) \\
&= -\mathrm{i}\,\omega\vec{B}, \qquad \text{(A.9)}
\end{aligned}$$

and in Equation (A.4)

$$\begin{aligned}
\nabla \times \vec{H} &= \vec{J}_f + \frac{\partial \vec{D}}{\partial t} \\
&= \vec{J}_f + \frac{\partial}{\partial t}\left(\epsilon(x,\omega)\vec{E}\right) \\
&= \vec{J}_f + \frac{\partial}{\partial t}\left(\epsilon(x,\omega)\vec{E}(x)e^{\mathrm{i}\,\omega t}\right) \\
&= \vec{J}_f + \epsilon(x,\omega)\vec{E}(x)\,\mathrm{i}\,\omega e^{\mathrm{i}\,\omega t} \\
&= \vec{J}_f + \mathrm{i}\,\omega\left[\epsilon(x,\omega)\vec{E}(x)e^{\mathrm{i}\,\omega t}\right] \\
&= \vec{J}_f + \mathrm{i}\,\omega\vec{D}. \qquad \text{(A.10)}
\end{aligned}$$

It has been shown, in [Gla01], that the magnetic permeability of the human body differs from that of free space ($\mu_0 = 4\pi \times 10^{-7} NA^{-2}$) by less than 10^{-5} and its dependence on time is negligible. Therefore, the change in magnetic permeability in oxygenated vs. deoxygenated blood is a very small number. This small difference results from deoxygenated blood having a higher amount of iron which then reacts to the electric field in a slightly different way. Since the magnetic permeability of the human body is very small we can expand $\vec{E}$ and $\vec{H}$ each in a Taylor Series about $\mu = 0$,

$$\vec{E} = \vec{E}^0 + \mu\vec{E}^1 + \mu^2\vec{E}^2 + \mu^3\vec{E}^3 + \ldots, \qquad \text{(A.11)}$$

$$\vec{H} = \vec{H}^0 + \mu\vec{H}^1 + \mu^2\vec{H}^2 + \mu^3\vec{H}^3 + \ldots. \qquad \text{(A.12)}$$

Substituting these expansions into Equation (A.3) and using the constitutive relation given in Equation (A.6),

$$\begin{aligned}
\nabla \times \left(\vec{E}^0 + \mu\vec{E}^1 + \mu^2\vec{E}^2 + \ldots\right) &= -\frac{\partial}{\partial t}\mu(x,\omega)\left(\vec{H}^0 + \mu\vec{H}^1 + \mu^2\vec{H}^2 + \ldots\right) \\
\nabla \times \vec{E}^0 + \nabla \times \mu\vec{E}^1 + \nabla \times \mu^2\vec{E}^2 + \ldots &= -\frac{\partial}{\partial t}\mu\vec{H}^0 - \frac{\partial}{\partial t}\mu^2\vec{H}^1 - \frac{\partial}{\partial t}\mu^3\vec{H}^2 - \ldots
\end{aligned}$$

Equating terms of order zero in μ gives

$$\nabla \times \vec{E}^0 = 0, \tag{A.13}$$

where $\vec{E}^0$ is the zeroth order electric field. Then, since the curl of $\vec{E}^0$ is zero, there exists an electrical potential u such that

$$\vec{E}^0 = -\nabla u(x,t) \tag{A.14}$$

Using the constitutive relations (A.5) and (A.7) in Equation (A.10) we have,

$$\nabla \times \vec{H} = \sigma(x,\omega)\vec{E} + \mathrm{i}\,\omega\left(\epsilon(x,\omega)\vec{E}\right). \tag{A.15}$$

Since the divergence of a curl is zero, we take the curl of both sides of (A.15) so that

$$\begin{aligned}
0 &= \nabla \cdot \left(\nabla \times \vec{H}\right) \\
&= \nabla \cdot \left(\sigma(x,\omega)\vec{E} + \mathrm{i}\,\omega\epsilon(x,\omega)\vec{E}\right) \\
&= \nabla \cdot (\sigma + \mathrm{i}\,\omega\epsilon)\,\vec{E} \\
&= \nabla \cdot (\sigma + \mathrm{i}\,\omega\epsilon)\left(\vec{E}^0 + \mu\vec{E}^1 + \mu^2\vec{E}^2 + \ldots\right) \\
&= \nabla \cdot (\sigma + \mathrm{i}\,\omega\epsilon)\,\vec{E}^0 + \nabla \cdot (\sigma + \mathrm{i}\,\omega\epsilon)\,\mu\vec{E}^1 + \nabla \cdot (\sigma + \mathrm{i}\,\omega\epsilon)\,\mu^2\vec{E}^2 + \ldots
\end{aligned}$$

Taking the zeroth order equation in μ and using Equation (A.14), we have

$$\begin{aligned}
0 &= \nabla \cdot (\sigma + \mathrm{i}\,\omega\epsilon)\,\vec{E}^0 \\
0 &= \nabla \cdot (\sigma + \mathrm{i}\,\omega\epsilon)\,(-\nabla u) \\
0 &= \nabla \cdot (\sigma + \mathrm{i}\,\omega\epsilon)\,\nabla u,
\end{aligned}$$

or equivalently,

$$\nabla \cdot \gamma\nabla u = 0, \tag{A.16}$$

which describes the electric potential inside the body. We call Equation (A.16) the *Admittivity Equation*.

We now need to impose boundary conditions on the problem. Physically this means that we need to determine what the electric fields look like on the surface of the body that we are imaging. In practice, electrodes are placed on the surface of the body and a

sequence of currents is applied to said electrodes. This produces an (applied) current density distribution on the surface of the body which is represented by the Neumann boundary condition,

$$\gamma \frac{\partial u}{\partial \nu} = j \text{ on } \partial\Omega \tag{A.17}$$

where j is the inward pointing normal component of the current density on the boundary $\partial\Omega$, ν is the outward pointing unit normal vector to $\partial\Omega$, u is the voltage potential, γ is the admittivity (i.e. $\gamma = \sigma + \mathrm{i}\,\omega\epsilon$ where σ is the electrical conductivity, ϵ is the electrical permittivity, and $\omega = 28.8$ kHz is the frequency of the applied current in the data sets that we use with trigonometric current patterns) [IC90, 143] and [SCI92, 1026].

In addition, we know that the voltages on the electrodes correspond to the Dirichlet boundary condition,

$$u = f(x) \text{ on } \partial\Omega \tag{A.18}$$

A.3 Electrode Models

In this section we take a closer look at how to model the applied current density j.

A.3.1 Continuum Model

In the *Continuum Model*, we assume that j is a continuous function and experiments Somersalo et al., [SCI92], suggest that j could have the following form,

$$j(\theta) = \cos(k\theta) \text{ or } j(\theta) = \sin(k\theta)$$

where $k \in \mathbb{Z}$ and $\theta \in [0, 2\pi]$. Then,

$$\nabla \cdot \gamma \nabla u = 0 \tag{A.19}$$

$$\gamma \frac{\partial u}{\partial \nu} = j(\theta) = \begin{cases} \cos(k\theta) \\ \text{or} \\ \sin(k\theta) \end{cases} \tag{A.20}$$

is the *Continuum Model*. Unfortunately, this model does not take into consideration that current is only applied on the electrodes (not in-between them). Due to this naive assumption, the model has been known to overestimate the 'characteristic resistivity' (the voltage on the electrode divided by the current on the electrode) by as much as 25% [SCI92].

A.3.2 Gap Model

In the *Gap Model*, we now consider the placement of the electrodes and assume that the current is constant on each of the electrodes. Let L be the number of electrodes used, and e_l denote the l^{th} electrode. This leads us to the following model,

$$\nabla \cdot \gamma \nabla u = 0 \tag{A.21}$$

$$\gamma \frac{\partial u}{\partial \nu} = j(l) = \begin{cases} \frac{I_l}{|e_l|} & \text{on } e_l \text{ for } l = 1, 2, \ldots, L \\ 0 & \text{off } \bigcup_{l=1}^{L} e_l \end{cases} \tag{A.22}$$

where $|e_l|$ is the area of the l^{th} electrode and I_l is the current on the l^{th} electrode. For a homogeneous tank experiment where we apply trigonometric current patterns, I_l can be computed by

$$I_l^k = \begin{cases} \cos(k\theta_l), & 1 \le l \le L, \quad 1 \le k \le \frac{L}{2} \\ \sin\left(\left(\frac{L}{2} - k\right)\theta_l\right), & 1 \le l \le L, \quad \frac{L}{2} + 1 \le k \le L - 1 \end{cases} \tag{A.23}$$

where $\theta_l = \frac{2\pi l}{L}$. This model has the advantage that it is mathematically easy to work with. While the *Gap Model* is an improvement over the *Continuum Model*, it still overestimates the resistivity by an unacceptable amount.

A.3.3 Shunt Model

In the Gap Model we took into consideration the placement of the electrodes, but we were still ignoring the fact that the metal of the electrodes themselves provide a low-resistance path for the current to pass through. We call this the "shorting or shunting effect of the electrodes" [SCI92, 1027]. The *Shunt Model*, as its name suggests, accounts for this and assumes that

1. the metal is a perfect conductor

2. the potential u is constant on the metal electrodes.

These assumptions bring us to the following model,

$$\nabla \cdot \gamma \nabla u = 0 \tag{A.24}$$

with boundary conditions

$$\int_{e_l} \gamma \frac{\partial u}{\partial \nu} dS = I_l, \;\; l = 1, 2, \ldots, L, \tag{A.25}$$

$$\gamma \frac{\partial u}{\partial \nu} = 0 \;\text{ off }\; \bigcup_{l=1}^{L} e_l \tag{A.26}$$

and

$$u = U_l \;\text{ on } e_l, \text{ for } l = 1, 2, \ldots, L \tag{A.27}$$

where U_l is a the measured voltage on the electrode e_l (a constant that is part of the solution). For a solution to exist, we include the condition for *conservation of charge*

$$\sum_{l=1}^{L} I_l = 0. \tag{A.28}$$

To ensure uniqueness of the solution, we require that the voltages sum to zero (i.e. specify the ground) by

$$\sum_{l=1}^{L} U_l = 0. \tag{A.29}$$

Unfortunately, even with these extra assumptions, the *Shunt Model* still falls short as it does not replicate the experimental data to the level of precision that we can measure. Somersalo et al. [SCI92] point out that, in fact, the discrepancy between the characteristic resistances that can be predicted using the *Shunt Model* and experimental data gets worse as the spatial frequency of the applied current patterns increases. This error increases since a highly resistive layer forms at the interface between the boundary of the domain and the electrodes and higher spatial frequencies contain proportionately more information about the boundary of the domain (since they are more oscillatory and therefore do not penetrate the domain as deeply). We characterize this resistive layer by the quantity z_l, the *effective contact impedance*.

A.3.4 Complete Model

In the *Complete Electrode Model*, as in [IC90], we extend the *Shunt Model* to account for the extra resistance due to an electro-chemical reaction at the electrode-boundary interface. Letting z_l be the *effective contact impedance* on the l^{th} electrode, we have that the voltage

drop across the electrode is equal to the product of the resistance z_l and the current density $\gamma\frac{\partial u}{\partial \nu}$. Therefore we replace Equation (A.27) for the voltage measured on the l^{th} electrode U_l by,

$$u + z_l\gamma\frac{\partial u}{\partial \nu} = U_l \text{ on } e_l \text{ for } l = 1, 2, \ldots, L. \tag{A.30}$$

Thus the *Complete Model* is comprised of the following set of equations,

$$\nabla \cdot \gamma\nabla u = 0 \tag{A.31}$$

with boundary conditions

$$\int_{e_l} \gamma\frac{\partial u}{\partial \nu} dS = I_l, \quad l = 1, 2, \ldots, L, \tag{A.32}$$

$$\gamma\frac{\partial u}{\partial \nu} = 0 \text{ off } \bigcup_{l=1}^{L} e_l \tag{A.33}$$

and

$$u + z_l\gamma\frac{\partial u}{\partial \nu} = U_l \text{ on } e_l \text{ for } l = 1, 2, \ldots, L. \tag{A.34}$$

We also impose the conditions for existence and uniqueness of a solution,

$$\sum_{l=1}^{L} I_l = 0, \tag{A.35}$$

$$\sum_{l=1}^{L} U_l = 0. \tag{A.36}$$

What are the advantages to the *Complete Electrode Model*? Thus far, it does the best job replicating the experimental data and has the ability to predict voltages to the precision that we can measure [IC90].

B. SOLVING THE FORWARD PROBLEM USING THE FINITE ELEMENT METHOD

It is important to understand how to solve the forward admittivity problem using Finite Elements. When determining the values of the exponentially growing solutions of Ψ_{12} and Ψ_{21} for $z \in \partial\Omega$, we need to simulate the voltages corresponding to a constant admittivity distribution (for simplicity here we use $\gamma = 1$ and therefore Λ_1). In addition, we can use a Finite Element Method (FEM) forward solver to simulate data and test our inverse solver.

While Vauhkonen et al. [VVSK99b] look at the 3-D EIT problem, they describe, in detail, how to solve the forward admittivity problem using the Finite Elements Mehtod with the Complete Electrode Model. The following is taken from my Master's paper [Ham09] and will describe the Finite Element Method formulation.

B.1 Finite Element Formulation

Recall the boundary conditions for the Complete Electrode Model given in Section (A.3.4)

$$\int_{e_l} \gamma \frac{\partial u}{\partial \nu}\, dS = I_l, \quad l = 1, 2, \ldots, L, \tag{B.1}$$

$$\gamma \frac{\partial u}{\partial \nu} = 0 \ \text{ off } \ \bigcup_{l=1}^{L} e_l, \tag{B.2}$$

and

$$u + z_l \gamma \frac{\partial u}{\partial \nu} = U_l \ \text{ on } \ e_l \text{ for } l = 1, 2, \ldots, L. \tag{B.3}$$

Somersalo et al., [SCI92], showed that for any (v, V) where $v \in H^1(\Omega)$ and $V \in \mathbb{C}^L$, the *variational form* of the Complete Electrode Model is

$$B_s((u, U), (v, V)) = \sum_{l=1}^{L} I_l \bar{V}_l \tag{B.4}$$

where $B_s : H \times H \to \mathbb{C}$ is the *sesquilinear* form given by

$$B_s((u, U), (v, V)) = \int_\Omega \gamma \nabla u \cdot \nabla \bar{v} dx + \sum_{l=1}^{L} \frac{1}{z_l} \int_{e_l} (u - U_l)(\bar{v} - \bar{V}_l)\, dS. \tag{B.5}$$

B.2 Trigonometric Current Patterns

As trigonometric current patterns are commonly used in experiments, I describe them in more detail here. Let L be the number of electrodes used in the experiment. Then, if we apply trigonometric current patterns we will have $L-1$ linearly independent current patterns. The trigonometric current patterns are defined as,

$$I_l^k = \begin{cases} M\cos(k\theta_l) & k = 1,\ldots,\frac{L}{2} \\ M\sin\left(\left(k-\frac{L}{2}\right)\theta_l\right) & k = \frac{L}{2}+1,\ldots,L-1 \end{cases} \tag{B.6}$$

where $\theta_l = \dfrac{2\pi l}{L}$ for $l = 1, 2, \ldots, L-1$ and M is the amplitude of the applied current pattern.

Figure B.1 shows the first 3 trigonometric current patterns $\cos(x)$, $\cos(2x)$, and $\cos(3x)$ for the case $M = 1$ and $L = 6$ electrodes.

B.3 The Finite Element Scheme

We follow the ideas outlined in [VVSK99b] using the Finite Element Method to formulate our continuous problem as a discrete one. We begin by discretizing our domain $\Omega \subset \mathbb{R}^2$, using tetrahedra, into very small elements. Suppose (u, U) is the solution to the forward admittivity problem using the Complete Electrode Model and that we are applying trigonometric current patterns. Using finite sums, we can approximate the voltage distribution inside our domain with,

$$u^h(\vec{x}) = \sum_{k=1}^{N} \alpha_k \phi_k(\vec{x}), \tag{B.7}$$

and on the electrodes with

$$U^h(\vec{x}) = \sum_{k=N+1}^{N+(L-1)} \beta_{(k-N)} \vec{n}_{(k-N)}, \tag{B.8}$$

where

- the h represents that the solution is discrete
- $L =$ the number of electrodes used in the experiment
- the test functions ϕ_k make up a basis for the finite dimensional space $\mathcal{H} \subset H^1(\Omega)$
- $\vec{n}_j = (1, 0, \ldots, 0, -1, 0, \ldots, 0)^T \in \mathbb{R}^{L\times 1}$ where the -1 is in the $j+1^{\text{st}}$ position

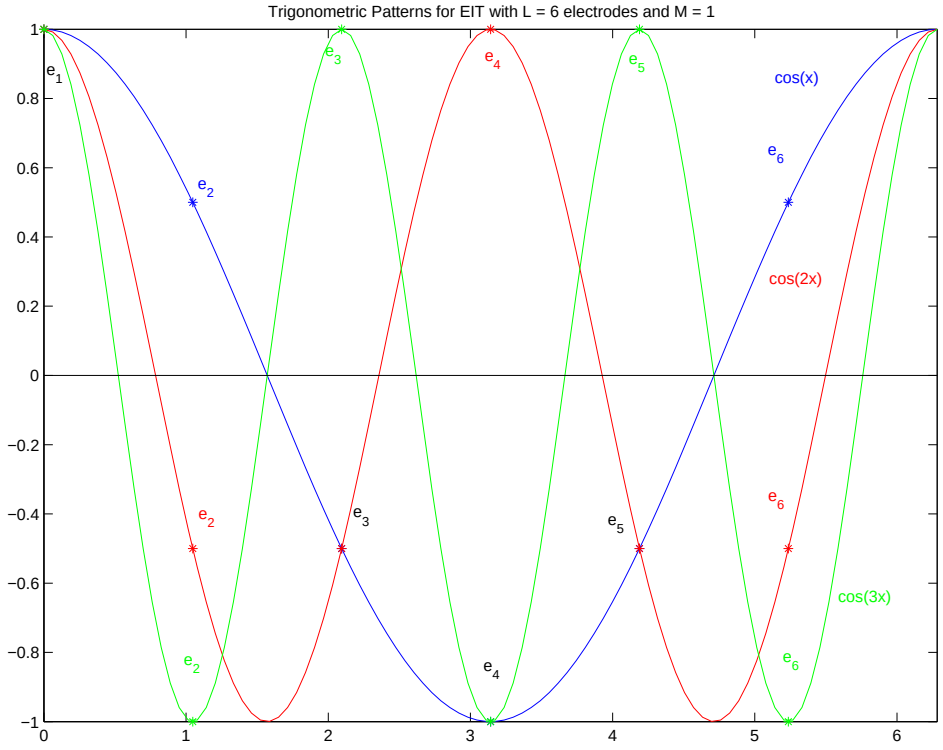

Fig. B.1: The first three trigonometric current patterns

- $N =$ the number of nodes in the finite element mesh
- α_k and $\beta_{(k-N)}$ are coefficients yet to be determined

Notice that this choice of $\vec{n}_{(k-N)}$ satisfies the condition for the ground in Equation (A.36) since, by plugging the $\vec{n}_{(k-N)}$'s into Equation (B.8),

$$\begin{aligned} U^h(\vec{x}) &= \sum_{k=N+1}^{N+(L-1)} \beta_{(k-N)}\vec{n}_{(k-N)} \\ &= \sum_{k=1}^{L-1} \beta_k \vec{n}_k \\ &= \left(\sum_{k=1}^{L-1} \beta_k, -\beta_1, -\beta_2, \ldots, -\beta_{L-1}\right)^T, \end{aligned} \tag{B.9}$$

where T denotes the transpose of a matrix/vector. Let $U_l^h = U^h(e_l)$, and $[\vec{n}_k]_l$ denote the l^{th} component of the vector $\vec{n}_k$. Then,

$$U_l^h = U^h(e_l) = l^{\text{th}} \text{ component of } \left(\sum_{k=1}^{L-1} \beta_k, -\beta_1, -\beta_2, \ldots, -\beta_{L-1}\right)^T,$$

which gives,

$$\begin{aligned} U_1^h &= \sum_{k=1}^{L-1} \beta_k \\ U_2^h &= -\beta_1 \\ U_3^h &= -\beta_2 \\ &\vdots \\ U_L^h &= -\beta_{L-1}. \end{aligned}$$

Then,

$$\begin{aligned} \sum_{l=1}^{L} U_l^h &= \text{ sum of components of } U^h \\ &= 0. \end{aligned}$$

In order to implement the Finite Element Method computationally in MatLab, we first need to expand Equation (B.4) using our approximating functions in Equations (B.7) and (B.8) with $v = \phi_j$ for $j = 1, 2, \ldots, N$ and $V = \vec{n}_j$ for $j = N+1, N+2, \ldots, N+(L-1)$.

Let's look at this is in cases.

Case 1: $1 \leq k, j \leq N$

Here $u^h \neq 0$, $U^h = 0$, $v \neq 0$, but $V = 0$ and thus $B_s((u^h, U^h), (v, V))$ becomes

$$\begin{aligned} B_s((u^h, 0), (v, 0)) &= \int_\Omega \gamma \nabla u^h \cdot \nabla \bar{v} dx + \sum_{l=1}^{L} \frac{1}{z_l} \int_{e_l} u^h \bar{v} \, dS \\ &= \int_\Omega \gamma \nabla \left(\sum_{k=1}^{N} \alpha_k \phi_k(\vec{x}) \right) \cdot \nabla \bar{\phi}_j \, dx + \sum_{l=1}^{L} \frac{1}{z_l} \int_{e_l} \left(\sum_{k=1}^{N} \alpha_k \phi_k(\vec{x}) \right) \bar{\phi}_j \, dS. \end{aligned}$$

Then using Equation (B.4), we have

$$B_s((u^h, 0), (v, 0)) = \sum_{l=1}^{L} I_l(0)_l = 0,$$

which gives,

$$\int_\Omega \gamma \nabla \left(\sum_{k=1}^{N} \alpha_k \phi_k \right) \cdot \nabla \bar{\phi}_j \, dx + \sum_{l=1}^{L} \frac{1}{z_l} \int_{e_l} \left(\sum_{k=1}^{N} \alpha_k \phi_k \right) \bar{\phi}_j \, dS = 0 \;\; 1 \leq j \leq N. \tag{B.10}$$

Looking at the k^{th} term, without the coefficient (we put it back later), we have

$$B_{kj} = \int_\Omega \gamma \nabla \phi_k \cdot \nabla \bar{\phi}_j \, dx + \sum_{l=1}^{L} \frac{1}{z_l} \int_{e_l} \phi_k \bar{\phi}_j \, dS. \tag{B.11}$$

Case 2: $1 \leq k \leq N$ **and** $N + 1 \leq j \leq N + (L - 1)$

Here $u^h \neq 0$, $U^h = 0$, $v = 0$, and $V \neq 0$ and thus $B_s((u^h, U^h), (v, V))$ becomes

$$\begin{aligned} B_s((u^h, 0), (0, V)) &= -\sum_{l=1}^{L} \frac{1}{z_l} \int_{e_l} u^h \bar{V}_l \, dS \\ &= -\sum_{l=1}^{L} \frac{1}{z_l} \int_{e_l} \left(\sum_{k=1}^{N} \alpha_k \phi_k \right) \overline{(\vec{n}_j)_l} \, dS \\ &= -\sum_{l=1}^{L} \frac{1}{z_l} \int_{e_l} \sum_{k=1}^{N} \alpha_k \phi_k \, (\vec{n}_j)_l \, dS. \end{aligned} \tag{B.12}$$

The last line comes from the fact that the entries of $\vec{n}$ are real, which gives $\overline{\vec{n}} = \vec{n}$. In addition we have,

$$(\vec{n}_j)_l = \begin{cases} 1 & l = 1 \\ -1 & l = j + 1 \\ 0 & else. \end{cases} \tag{B.13}$$

Then using Equation (B.4), we have

$$B_s((u^h,0),(0,V)) = \sum_{l=1}^{L} I_l \bar{V}_l = I_1 - I_{j+1},$$

and Equation (B.12) becomes

$$-\sum_{l=1}^{L} \frac{1}{z_l} \int_{e_l} \sum_{k=1}^{N} \alpha_k \phi_k \left(\vec{n}_j\right)_l \, dS = I_1 - I_{j+1} \quad \text{for } N+1 \le j \le N+(L-1). \tag{B.14}$$

Looking at the k^{th} term, without the coefficient (again we put it back later), we have

$$\begin{aligned} C_{kj} &= -\sum_{l=1}^{L} \frac{1}{z_l} \int_{e_l} \phi_k \left(\vec{n}_j\right)_l \, dS \\ &= -\left[\frac{1}{z_1} \int_{e_1} \phi_k \, dS - \frac{1}{z_{j+1}} \int_{e_{j+1}} \phi_k \, dS \right]. \end{aligned} \tag{B.15}$$

Case 3: $N \le k \le N+(L-1)$ **and** $1 \le j \le N$

Here, $u^h = 0$, $U^h \neq 0$, $v \neq 0$, and $V = 0$ and thus $B_s((u^h,U^h),(v,V))$ becomes,

$$\begin{aligned} B_s((0,U^h),(v,0)) &= -\sum_{l=1}^{L} \frac{1}{z_l} \int_{e_l} U^h \bar{v}_l \, dS \\ &= -\sum_{l=1}^{L} \frac{1}{z_l} \int_{e_l} \left(\sum_{k=N+1}^{N+(L-1)} \beta_{(k-N)} \vec{n}_{(k-N)} \right)_l \bar{\phi}_j \, dS. \end{aligned} \tag{B.16}$$

Then using Equation (B.4), we have

$$B_s((0,U^h),(v,0)) = \sum_{l=1}^{L} I_l(0)_l = 0,$$

and Equation B.16 becomes

$$-\sum_{l=1}^{L} \frac{1}{z_l} \int_{e_l} \left(\sum_{k=N+1}^{N+(L-1)} \beta_{(k-N)} \vec{n}_{(k-N)} \right)_l \bar{\phi}_j \, dS = 0 \quad 1 \le j \le N. \tag{B.17}$$

Looking at the k^{th} term, without the coefficient (again we put it back later), we have

$$\begin{aligned} \tilde{C}_{kj} &= -\sum_{l=1}^{L} \frac{1}{z_l} \int_{e_l} \left(\phi_{(k-N)}\right)_l \vec{\phi}_j \, dS \\ &= -\left[\frac{1}{z_1} \int_{e_1} \bar{\phi}_j \, dS - \frac{1}{z_{j+1}} \int_{e_{j+1}} \bar{\phi}_{j+1} \, dS \right]. \end{aligned} \tag{B.18}$$

Case 4: $N \leq k, j \leq N + (L-1)$

Here, $u^h = 0$, $U^h \neq 0$, $v = 0$, and $V \neq 0$ and thus $B_s((u^h, U^h), (v, V))$ becomes,

$$\begin{aligned} B_s((0, U^h), (0, V)) &= \sum_{l=1}^{L} \frac{1}{z_l} \int_{e_l} U^h \bar{V}_l \, dS \\ &= \sum_{l=1}^{L} \frac{1}{z_l} \int_{e_l} \left(\sum_{k=N+1}^{N+(L-1)} \beta_{(k-N)} \vec{n}_{(k-N)} \right)_l \left(\bar{\vec{n}}_j \right)_l \, dS. \end{aligned} \tag{B.19}$$

Then using Equation (B.4), we have

$$B_s((0, U^h), (0, V)) = \sum_{l=1}^{L} I_l \left(\bar{\vec{n}}_j \right)_l = I_1 - I_{j+1},$$

and Equation B.16 becomes

$$\sum_{l=1}^{L} \frac{1}{z_l} \int_{e_l} \left(\sum_{k=N+1}^{N+(L-1)} \beta_{(k-N)} \vec{n}_{(k-N)} \right)_l \left(\bar{\vec{n}}_j \right)_l \, dS = I_1 - I_{j+1} \quad 1 \leq j \leq N. \tag{B.20}$$

Looking at the k^{th} term, without the coefficient (again we put it back later), we have

$$\begin{aligned} D_{kj} &= \sum_{l=1}^{L} \frac{1}{z_l} \int_{e_l} \left(\vec{n}_{(k-N)} \right)_l \left(\bar{\vec{n}}_j \right)_l \, dS \\ &= \sum_{l=1}^{L} \frac{1}{z_l} \int_{e_l} \left(\vec{n}_{(k-N)} \right)_l \left(\vec{n}_j \right)_l \, dS. \end{aligned} \tag{B.21}$$

If $j = k - N$, Equation (B.21) becomes,

$$\begin{aligned} D_{jj} &= \sum_{l=1}^{L} \frac{1}{z_l} \int_{e_l} \left(\vec{n}_j \right)_l \left(\vec{n}_j \right)_l \, dS \\ &= \frac{1}{z_1} \int_{e_1} dS + \frac{1}{z_{j+1}} \int_{e_{j+1}} dS \\ &= \frac{|e_1|}{z_1} + \frac{|e_{j+1}|}{z_{j+1}}, \end{aligned} \tag{B.22}$$

where $|e_1|$ and $|e_{j+1}|$ denote the area of the 1^{st} and $j+1^{\text{st}}$ electrodes respectively.

If $j \neq k - N$,

$$\begin{aligned} D_{kj} &= \frac{1}{z_1} \int_{e_1} dS - 0 \\ &= \frac{|e_1|}{z_1}. \end{aligned} \tag{B.23}$$

Thus for $N \leq k, j \leq N + (L-1)$,

$$D_{kj} = \begin{cases} \frac{|e_1|}{z_1} + \frac{|e_{j+1}|}{z_{j+1}} & j = k - N \\ \frac{|e_1|}{z_1} & j \neq k - N. \end{cases} \tag{B.24}$$

We can combine Equations (B.10), (B.14), (B.17), and (B.20) into a system written as,

$$A\vec{b} = \vec{f} \tag{B.25}$$

where $\vec{b} = (\vec{\alpha}, \vec{\beta})^T \in \mathbb{C}^{N+L-1}$ (where $\vec{\alpha} = (\alpha_1, \alpha_2, \ldots, \alpha_N)$ and $\vec{\beta} = (\beta_1, \beta_2, \ldots, \beta_{L-1})$) and $A \in \mathbb{C}^{(N+L-1)\times(N+L-1)}$ is of the form,

$$A = \begin{pmatrix} B & C \\ \tilde{C} & D \end{pmatrix}, \tag{B.26}$$

and the data vector

$$\vec{f} = (\mathbf{0}, \tilde{I})^T, \tag{B.27}$$

where $\mathbf{0} \in \mathbb{C}^{1\times N}$ and $\tilde{I} = (I_1 - I_2, I_1 - I_3, \ldots, I_1 - I_L) \in \mathbb{C}^{1\times(L-1)}$.

Solving Equation (B.25) for the unknown coefficients $\vec{b}$,

$$\vec{b} = A^{-1}\vec{f}, \tag{B.28}$$

gives the solution to the forward admittivity problem with the Complete Electrode Model. The coefficients in the vector $\vec{\alpha}$ represent the voltages throughout the domain, while those in $\vec{\beta}$ are used to find the voltages on the electrodes by

$$U^h = \mathcal{C}\vec{\beta}, \tag{B.29}$$

where,

$$\mathcal{C} = \begin{pmatrix} 1 & 1 & 1 & \ldots & 1 \\ -1 & 0 & 0 & \ldots & 0 \\ 0 & -1 & 0 & \ldots & 0 \\ & & \ddots & & \\ 0 & 0 & 0 & \ldots & -1 \end{pmatrix}, \tag{B.30}$$

and $\mathcal{C}$ is an $L \times (L-1)$ matrix.